Active chatter control in high-speed milling processes

Active chatter control in high-speed milling processes

Niels van Dijk

Active chatter control in high-speed milling processes

Niels van Dijk

This work is supported by the Ministry of Economic Affairs, Agriculture and Innovation within the framework of Innovation Oriented Research Programmes (IOP) Precision Technology.

The research reported in this thesis is part of the research program of the Dutch Institute of Systems and Control (DISC). The author has successfully completed the educational program of the Graduate School DISC.

A catalogue record is available from the Eindhoven University of Technology Library.
ISBN: 978-90-386-2430-3

Typeset by the author with the LaTeX 2_ε documentation system

Cover Design: Liane Design, www.lianedesign.nl.
Reproduction: Ipskamp drukkers, Enschede, the Netherlands.

Active chatter control in high-speed milling processes

PROEFSCHRIFT

ter verkrijging van de graad van doctor aan de
Technische Universiteit Eindhoven, op gezag van de
rector magnificus, prof.dr.ir. C.J. van Duijn, voor een
commissie aangewezen door het College voor
Promoties in het openbaar te verdedigen
op dinsdag 15 februari 2011 om 16.00 uur

door

Niels Johannes Maria van Dijk

geboren te Deurne

Dit proefschrift is goedgekeurd door de promotor:

prof.dr. H. Nijmeijer

Copromotor:
dr.ir. N. van de Wouw

Contents

Summary

Active chatter control in high-speed milling processes

In present day manufacturing industry, an increasing demand for high-precision products at a high productivity level is seen. High-speed milling is a manufacturing technique which is commonly exploited to produce high-precision parts at a high productivity level for the aeroplane, automotive and mould and dies industry.

The performance of a manufacturing process such as high-speed milling, indicated by the material removal rate, is limited by the occurrence of a dynamic instability phenomenon called chatter. The occurrence of chatter results in an inferior workpiece quality due to heavy vibrations of the cutter. Moreover, a high level of noise is produced and the tool wears out rapidly. Although different types of chatter exist, regenerative chatter is recognised as the most prevalent type of chatter. The occurrence of (regenerative) chatter has such a devastating effect on workpiece quality and tool wear that it should be avoided at all times.

The occurrence of chatter can be visualised in so-called stability lobes diagrams (SLD). In an SLD the chatter stability boundary between a stable cut (i.e. without chatter) and an unstable cut (i.e. with chatter) is visualised in terms of spindle speed and depth of cut. Using the information gathered in a SLD, the machinist can select a chatter free operating point.

In this thesis two problems are tackled. Firstly, due to e.g. heating of the spindle, tool wear, etc., the SLD may vary in time. Consequently, a stable working point that was originally chosen by the machinist may become unstable. This requires a (controlled) adaptation of process parameters such that stability of the milling process is ensured (i.e. chatter is avoided) even under such changing process conditions. Secondly, the ever increasing demand for high-precision products at a high productivity level requires dedicated shaping of the chatter stability boundary. Such shaping of the SLD should render working points (in terms of spindle speed and depth of cut) of high productivity feasible, while avoiding chatter. These problems require the design of dedicated control strategies that ensure stable high-speed milling operations with increased performance.

In this work, two chatter control strategies are developed that guarantee high-speed chatter-free machining operations. The goal of the two chatter control strategies is, however, different.

The first chatter control strategy guarantees chatter-free high-speed milling operations by automatic adaptation of spindle speed and feed (i.e. the feed is not stopped during the spindle speed transition). In this way, the high-speed milling process will remain stable despite changes in the process, e.g. due to heating of the spindle, tool wear, etc. To do so, an accurate and fast chat-

ter detection algorithm is presented which predicts the occurrence of chatter before chatter marks are visible on the workpiece. Once the onset of chatter is detected, the developed controller adapts the spindle speed and feed such that a new chatter-free working point is attained. Experimental results confirm that by using this control strategy chatter-free machining is ensured. It is also shown experimentally that the detection algorithm is able to detect chatter before it is fully developed. Furthermore, the control strategy ensures that chatter is avoided, thereby ensuring a robust machining operation and a high surface quality.

The second chatter control strategy is developed to design controllers that guarantee chatter-free cutting operations in an a priori defined range of process parameters (spindle speed and depth of cut) such that a higher productivity can be attained. Current (active) chatter control strategies for the milling process cannot provide such a strong guarantee of a priori stability for a predefined range of working points. The methodology is based on a robust control approach using μ-synthesis, where the most important process parameters (spindle speed and depth of cut) are treated as uncertainties. The proposed methodology will allow the machinist to define a desired working range (in spindle speed and depth of cut) and lift the SLD locally in a dedicated fashion.

Finally, experiments have been performed to validate the working principle of the active chatter control strategy in practice. Hereto, a milling spindle with an integrated active magnetic bearing is considered. Based on the obtained experimental results, it can be stated that the active chatter control methodology, as presented in this thesis, can indeed be applied to design controllers, which alter the SLD such that a pre-defined domain of working points is stabilised. Results from milling tests underline this conclusion. By using the active chatter controller working points with a higher material removal rate become feasible while avoiding chatter.

To summarise, the control strategies developed in this thesis, ensure robust chatter-free high-speed milling operations where, by dedicated shaping of the chatter stability boundary, working points with a higher productivity are attained.

Samenvatting

Active chatter control in high-speed milling processes

De hedendaagse maakindustrie wordt gekenmerkt door toenemende eisen ten aanzien van nauwkeurigheid voor hoogwaardige producten die bovendien zo efficient mogelijk geproduceerd moeten worden. Hogesnelheidsfrezen is een productie techniek die vaak wordt toegepast voor het vervaardigen van producten met een hoge nauwkeurigheid en hoge productiviteit voor de vliegtuigindustrie, autoindustrie en de vervaardiging van matrijzen.

De verspaningssnelheid, een maat voor de productiviteit van een bewerkingsproces, wordt vaak beperkt door een dynamisch instabiliteitsfenomeen genaamd chatter. Chatter gaat gepaard met het hevig trillen van de frees, hetgeen resulteert in een inferieure kwaliteit van het oppervlak van een werkstuk. Daarnaast genereert chatter veel (onaangenaam) geluid en slijt de frees snel. Er zijn verschillende oorzaken aan te wijzen voor het ontstaan van chatter. Echter, het zogenaamde regeneratieve effect is een van de meest voorkomende oorzaken van chatter. Het optreden van chatter heeft een dusdanig negatieve impact op de kwaliteit van een werkstuk, als ook slijtage aan de frees, dat het te allen tijde vermeden dient te worden.

De grens tussen een stabiele freesbewerking (geen chatter) en een instabiele freesbewerking (met chatter) kan worden gevisualiseerd in een stabiliteitsdiagram. Hierin wordt de stabiliteitsgrens gekarakteriseerd in termen van snede diepte en toerental. Op basis van het stabiliteitsdiagram kan de operator van een freesmachine een werkpunt kiezen dat resulteert in een stabiele freesbewerking zonder chatter.

In dit proefschrift worden twee problemen omtrent het voorkomen van chatter besproken. Allereerst, door, bijvoorbeeld, temperatuursveranderingen in de spindel, slijtage van de frees, etc, varieert het stabiliteitsdiagram als functie van de tijd. Hierdoor kan het voorkomen dat een oorspronkelijk gekozen werkpunt instabiel wordt. Om ervoor te zorgen dat, ondanks veranderingen in het proces, het freesproces stabiel blijft, is een gecontrolleerde aanpassing van de kenmerkende parameters van het freesproces noodzakelijk. Ten tweede, om te kunnen voldoen aan de steeds groeiende vraag naar een efficient bewerkingsproces voor hoogwaardige producten, is een lokale aanpassing van het stabiliteitsdiagram noodzakelijk. Door een specifieke lokale aanpassing van het stabiliteitsdiagram worden werkpunten, die een hoge productiviteit representeren maar die oorspronkelijk in chatter zouden resulteren, gestabiliseerd. Om de twee hiervoor besproken problemen op te lossen, dienen regelstrategieën te worden ontworpen zodanig dat freesbewerkingen kunnen worden uitgevoerd zonder dat chatter optreedt en die resulteren in een significante toename van de productiviteit van het freesproces.

In dit onderzoek zijn twee regelstrategieën ontwikkeld welke een stabiele

hogesnelheidsfreesbewerking garanderen. Echter, de beide regelstrategieën zijn ontwikkeld met een geheel verschillend doel.

In de eerste regelstrategie wordt een automatische aanpassing van het toerental en de voeding gegenereerd, waarbij de voeding niet wordt gestopt gedurende de toertental aanpassing. Hierdoor blijft het hogesnelheidsfreesproces stabiel (geen chatter) ondanks veranderingen in het proces zoals, bijvoorbeeld, temperatuursveranderingen in de spindel, slijtage van de frees, etc. Om chatter nauwkeurig en voldoende snel te detecteren is een detectie algoritme ontwikkeld dat in staat is om groeiende chatter trillingen te detecteren voordat de typische chatter markeringen zichtbaar zijn op het werkstuk. Wanneer de groei van chatter trillingen wordt gedetecteerd, past de ontworpen regelaar het toerental zodanig aan dat een nieuw stabiel werkpunt wordt bereikt. Door middel van experimenten is aangetoond dat met deze regelstrategie freesbewerkingen zonder chatter kunnen worden gegarandeerd. Daarnaast is aangetoond dat met het ontwikkelde detectie algoritme het mogelijk is om de groei van chatter te detecteren voordat chatter markeringen zichtbaar zijn op het werkstuk. Omdat de regelstrategie chatter voorkomt kan een robuuste freesbewerking met een hoge oppervlaktenauwkeurigheid worden gegarandeerd.

De tweede regelstrategie resulteert in regelaars die a priori een set van werkpunten (toerental en snede diepte) stabiliseert zodaning dat, voor elk van de werkpunten in de set, een chatter-vrije freesbewerking kan worden uitgevoerd. Op deze manier kan de productiviteit van het hogesnelheidsfreesproces aanzienlijk worden verhoogd. Een dusdanige a priori stabiliteitsgarantie voor een set van werkpunten is nog niet eerder beschreven in de literatuur met betrekking tot het freesproces. De aanpak is gebasseerd op robuuste regeltechniek via μ-synthese. Hiertoe zijn het toerental en de snede diepte als onzekerheden meegenomen in de regelaarsynthese. De gepresenteerde regelstratgie geeft de operator van een freesmachine de vrijheid om een vooraf gedefinieerde set van werkpunten te stabiliseren zodat het stabileitsdiagram lokaal wordt aangepast.

Experimenten, die zijn uitgevoerd met de actieve chatter regelstrategie, tonen aan dat de regelstrategie kan worden toegepast in de praktijk. Hiertoe is een freespindel, die is uitgerust met een actief magneetlager, gebruikt. Op basis van de experimenten kan worden geconcludeerd dat het mogelijk is om, met de ontworpen regelstrategie, een regelaar te ontwerpen die het stabiliteitsdiagram lokaal aanpast zodanig dat een set van werkpunten (toerental en snede diepte) wordt gestabiliseerd. Dezelfde conclusies kunnen worden getrokken uit de resultaten van freestesten. Wannneer de actieve chatter regelstrategie wordt gebruikt, kunnen werkpunten worden gekozen die een hogere productiviteit representeren en bovendien waarvoor geen chatter optreedt.

Samenvattend kan worden gesteld dat met de regelstrategieën, zoals ontwikkeld in dit proefschrift, een robuuste freesbewerking kan worden uitgevoerd waarbij werkpunten die een hogere productiviteit representeren kunnen worden gekozen doordat het stabiliteitsdiagram lokaal is aangepast.

Nomenclature

General Notation

$\dot{a}$	time derivative
$\underline{a}$	vector
$\mathbf{A}$	matrix
$\mathbb{B}$	n_K-dimensional open ball with radius one
$\mathbb{C}$	set of all complex numbers
$\mathcal{D}_\tau$	delay operator
E	expectation operator
$\partial f(\underline{x})$	Clarke subdifferential of f with respect to $\underline{x}$
$\mathbb{R}$	set of all real numbers
$\mathbb{Z}$	set of all integer numbers
$\nabla f(\underline{x})$	classical gradient of f with respect to $\underline{x}$

Latin Letters

$\bar{a}_p$	maximal axial depth of cut	mm
$\hat{a}$	predicted acceleration	ms^{-2}
$\tilde{a}$	perturbation on the periodic movement of measured acceleration	ms^{-2}
a	measured acceleration	ms^{-2}
a^*	periodic movement of measured acceleration	ms^{-2}
a_e	radial depth of cut	mm
a_p	axial depth of cut	mm
$a_{p,\mathsf{max}}$	critical axial depth of cut	mm
$\underline{B}_i$	sample from $\mathbb{B}$	
$b_x,\ b_y$	damping in x/y direction	Ns/m
c	constant for selecting controller input	
$c_x,\ c_y$	stiffness in x/y direction	N/m
$\underline{d}$	descent direction	
d	diameter of the cutter	mm
d_{tol}	tolerance on descent direction	
$\underline{e}$	process noise vector	
e	Gaussian white noise	
f_{chat}	dominant chatter frequency	Hz
$\hat{f}_{\mathsf{chat}}$	estimated dominant chatter frequency	Hz
$\underline{F}_a$	actuator force	N
$\underline{F}_t$	force acting at tooltip	N
f_s	sampling frequency	Hz
f_z	chip load (feed per tooth)	mm/tooth

F_{rad}	radial force	N
F_{tang}	tangential force	N
f_C	range of chatter frequencies	Hz
f_c	basic chatter frequency	Hz
f_{SP}	range of spindle revolution frequency harmonics	Hz
f_{sp}	spindle speed frequency	Hz
$F_{t,x_{\mathsf{meas}}}, F_{t,y_{\mathsf{meas}}}$	measured cutting forces in x/y direction	N
f_{TPE}	range of tooth passing frequency harmonics	Hz
f_{tpe}	tooth passing frequency	Hz
$\mathbf{G}$	spindle-actuator dynamics transfer function matrix	
$\mathbf{G}_d$	set of gradients	
$\mathbf{G}_s$	scaled frequency response function matrix	
G_d	transfer function nominal delay approximation	
g_j	screen function	
$\overline{\mathbf{H}}$	averaged cutting force matrix	N/mm^2
h_j	chip thickness at tooth j	mm
$h_{j,\mathsf{dyn}}$	dynamic chip thickness at tooth j	mm
$h_{j,\mathsf{stat}}$	static chip thickness at tooth j	mm
$\underline{i}_c$	controller output	A
$\mathbf{I}$	identity matrix	
i	imaginary number	
i_0	bias current AMB	A
j	tooth number	
J_c	spindle speed selection cost function	
J_p, J_u	detection algorithm cost functions	
$\underline{K}$	Kalman gain	
$\underline{K}_p$	controller parameter vector	
$\mathbf{KS}$	control sensitivity transfer function matrix	A/m
$\mathbf{K}$	controller transfer function matrix	A/m
$\mathbf{K}_a$	actuator gain matrix	N/A
$\mathbf{K}_i$	AMB force-current matrix	N/A
$\mathbf{K}_s$	AMB force-displacement matrix	N/m
K_p	controller weighting gain	m/A
K_r	radial cutting force parameter	N/mm$^{1+x_F}$
K_t	tangential cutting force parameter	N/mm$^{1+x_F}$
$m_{a,x}, m_{a,y}$	spindle/actuator mass in x/y direction	kg
$m_{t,x}, m_{t,y}$	tool mass in x/y direction	kg
n	spindle speed	rpm
n_c	number of controller states	
n_d	order of perturbation model	
n_g	number of subgradients	
n_K	number of controller parameters	
n_L	number of spindle speed harmonics	

n_u	number of uncertain spindle modes	
$n_{\mathbb{C}}, n_{\mathbb{R}}$	number of complex/real eigenvalues	
n_{pd}	Padé approximation order	
n_x	number of states of spindle model	
$\underline{p}$	uncertainty model input	
$\mathbf{P}$	generalised plant	
$\underline{q}$	uncertainty model output	
$\mathbf{Q}$	estimation covariance matrix	
q	shift operator	
$\underline{r}$	reference input signal	m
$\mathbf{R}_e$	process covariance matrix	
R_w	innovation covariance	$\mathrm{m^2 s^{-4}}$
r_ω, r_ζ	relative uncertainty in eigenfrequency/damping	
$\mathbf{S}$	direction cosine matrix	
s	Laplace operator	
S_{xx}	power spectral density of signal x	
$\mathbf{T}$	transformation matrix	
T	period time	s
t	time	s
T_r	residual covariance	
T_s	sampling period	s
$\underline{u}_P$	generalised plant input vector	
u	input signal	
$\underline{v}_a$	vibration at the actuator	m
$\underline{v}_P$	generalised plant output vector	
$\underline{v}_t$	vibration of the tool	m
$\underline{v}_t^*$	periodic movement of the cutter	m
$\underline{v}_{pd}$	Padé approximated displacements	m
$\tilde{\underline{v}}_t$	perturbation on the periodic movement of the cutter	m
v_0	nominal gap displacement AMB	m
$\mathbf{W}_{KS}$	controller performance weighting matrix	
w	observation noise	
W_d	transfer function of weighting function for delay interval approximation	
$\underline{x}$	state vector	
$\underline{x}^*, \underline{\xi}^*$	periodic solution	
$\tilde{\underline{x}}, \tilde{\underline{\xi}}$	perturbations about periodic solution	
x_F	exponent of cutting force model	
x	feed direction	
$\underline{y}$	controller input signal	m
y	normal direction	
$\underline{z}$	performance variable	

z	number of teeth	

Greek Letters

α, α_c	step-size	
γ	positive constant	
$\delta_{a_p}, \delta_\tau, \delta_\omega, \delta_\zeta$	scalar uncertainty	
$\mathbf{\Delta}$	uncertainty set	
$\mathbf{\Delta}_c$	complex structured uncertainty set	
$\hat{\mathbf{\Delta}}$	extended uncertainty set	
ϵ	fraction of incomplete waves	rad
ϵ_s	gradient sampling radius	
ε	prediction error periodic part	ms^{-2}
ε_m	prediction error	ms^{-2}
$\zeta_{a,x}, \zeta_{a,y}$	dimensionless damping ratio of spindle/actuator combination in x/y direction	
$\zeta_{t,x}, \zeta_{t,y}$	dimensionless damping ratio of tool in x/y direction	
η, η_c	forgetting factor	
$\underline{\theta}$	parameter vector	
$\kappa(\omega)$	frequency dependent delay upper bound	
λ	eigenvalue	
μ	Floquet multiplier	
$\mu_{\mathbf{\Delta}}$	structured singular value	
$\nu_{s,x}, \nu_{s,y}$	averaged value of FRF magnitude in x/y direction	
$\underline{\xi}$	controller state vector	
$\rho_l(\omega)$	over-approximated delay upper bound	
$\bar{\sigma}$	largest singular value	
σ	standard deviation	
$\bar{\tau}$	delay upper bound	s
$\underline{\tau}$	delay lower bound	s
τ	delay	s
$\underline{\varphi}_p$	vector of sine and cosine series	
$\underline{\varphi}_u$	vector of perturbation measurements	
ϕ_e	exit angle	rad
ϕ_j	tooth angle of tooth j	rad
ϕ_p	pitch angle	rad
ϕ_s	entry angle	rad
χ	root of discrete time transfer function	
ω	frequency	rad/s
$\omega_{a,x}, \omega_{a,y}$	natural frequency of spindle/actuator combination in x/y direction	rad/s
$\omega_{t,x}, \omega_{t,y}$	natural frequency of tool in x/y direction	rad/s

Abbreviations

AMB	active magnetic bearing
AR	auto-regressive
ARMA	auto-regressive moving average
BJ	Box-Jenkins model
CRAC	chatter recognition and control
DDE	delay-differential equations
DOF	degree of freedom
FRF	frequency response function
HSM	high-speed milling
LQG	linear quadratic Gaussian
LTI	linear time invariant
MA	moving average
MIMO	multi input multi output
MRR	material removal rate
NC	numerical control
NLMS	normalised least mean square
ODE	ordinary differential equation
PRBS	pseudo random binary sequence
PSD	power spectral density
SDM	semi-discretisation method
SIMO	single input multi output
SISO	single input single output
SK	Sanathanan-Koerner
SLD	stability lobes diagram
SSV	spindle speed variation
TDS	time domain simulations

1

Introduction

1.1 High-speed milling

An important production step in the manufacturing of mechanical parts is performed using cutting techniques. In cutting, material is removed from a workpiece using a tool by creating chips of the metal which is cut. Turning and milling operations are probably the most well-known cutting techniques. With the development of spindles that could rotate much faster while retaining a relatively good stiffness in the 1980s, high-speed milling (HSM) became a well-established technique in the present day manufacturing industry [156]. Different definitions are used in literature to define a distinction between conventional milling and HSM. Sometimes the absolute spindle speed is used, which may be an unclear definition since the dimension of the spindle is not given [146]. This leads to another definition, where the product of the mean bearing diameter D_m in mm and the spindle speed n in rpm is determined. In [3], a milling operation is defined as high-speed when the product $D_m n$ exceeds $0.5 \cdot 10^6$ mm/min. A third definition is related to the tool and spindle dynamics and stability of the process, see [146]. Herein, a milling operation is defined as high-speed when the tooth passing frequency approaches a substantial fraction of the dominant (most flexible) natural frequency of the spindle-tool dynamics.

In any case, HSM is e.g. used to produce monolithic aluminum structure parts for the aerospace industry [67, 156] where more than 90% of the original workpiece is machined. Other applications include the fabrication of moulds and dies [161, 164] and parts for the automotive industry [116]. The application of HSM in the manufacturing of mechanical parts, in especially the latter two applications, where often long and slender tools are used, is especially beneficial

Table 1.1: Main business indicators for the manufacturing of aircraft and spacecrafts, automotive applications and mould and dies in the European Union (EU) and the Netherlands (NL) in million euros for the year 2006 [46, 48].

		total industry	aerospace	automotive	mould and die
Turnover	EU	7,984,000	89,066.9	780,000.5	88,645.0
	NL	407,184[1)]	1,034.9	9,908.4	5,937.5
Added value at factor cost[2)]	EU	2,004,000	29,964.3	143,991.5	33,003.6
	NL	74,148[1)]	348.9	2,662.6	1,847.3
Machining cost	EU	300,600	4,494.6	21598.7	4,495.5
	NL	11,122.2	52.3	399.4	277.1

[1)] *values over* 2004

[2)] *for definition see [47]*

due to the (relatively) high rotational speed of the tool. Therewith, relatively small radial depth of cuts/feed per tooth can be chosen which results in small cutting forces without compromising on the material removal rate (MRR), which is beneficial when machining e.g. thin walled structures.

Next, the relevance of the economic manufacturing sector in the European Union (EU) and the Netherlands (NL) is briefly discussed. The turnover and value added at factor cost for the manufacturing of aircraft and spacecrafts, automotive applications and mould and dies in the European Union (EU) and the Netherlands (NL) for the year 2006 are listed in Table 1.1. Also the main business indicators for the total industry of the non-financial economy (which, next to the listed figures, also includes other types of industry) are listed. It can be seen that the industries for which high-speed milling operations are used as a production step in the manufacturing of parts, is a significant part of the total industry. Therewith, economic growth can be realised when productivity of the HSM process is increased. Machining operations account for 15% of the value of all manufactured mechanical parts [21]. Based on these numbers, the total (annual) machining cost can be determined, see Table 1.1. By developing new methodologies for machining technologies, the total machining costs can be reduced. It is expected that this may lead to an increase in the value added at factor cost. Moreover, this will also have impact on the turnover of milling machine manufacturers. Hence, increasing productivity, while maintaining quality/accuracy, is one of the main drivers of the research in this work.

(a) No chatter. (b) Chatter.

Figure 1.1: Detail of a workpiece without and with chatter marks.

1.2 Chatter

Chatter is the most obscure and delicate of all problems facing a machinist [153]. Although this statement was made by F.W. Taylor over 100 years ago, it still remains valid today. Chatter is an instability phenomenon that not only occurs in milling but also in other machining processes such as turning, drilling and grinding. Chatter results in large vibrations between the tool and the workpiece which in turn results in a nonsmooth surface of the workpiece. This can be seen in Figure 1.1, where pictures of the resulting workpiece for a cut with and without chatter are given. Next to a nonsmooth surface, chatter results in rapid wear of spindle and tool and the production of a significant amount of noise. In principle there are four mechanisms that describe the occurrence of chatter [172]. Firstly, chatter may occur due to variable friction between tool and workpiece [27]. Secondly, mode-coupling chatter exists when vibrations in e.g. the feed direction generate vibrations in the direction normal to the feed direction [27, 81]. A third mechanism is due to thermo-mechanical effects on the chip formation [172]. The aforementioned methods are often defined as primary chatter. The fourth mechanism that describes the occurrence of chatter, and is often defined as secondary chatter, is regenerative chatter. Regenerative chatter occurs due to regeneration of waviness of the surface of the workpiece. Due to the fact that the spindle system is not infinitely stiff, during cutting, the cutter vibrates and leaves a wavy surface behind on the workpiece. The next tooth on the cutter encounters the waviness, left behind by the previous tooth of the cutter, and generates its own wavy surface. Consequently, a phase difference is present between the two waves which results in a (rapidly) varying chip thickness. As a result, the forces acting on the cutter vary. By increasing the axial depth of cut a_p, the regenerative effect becomes dominant and, in turn, chatter occurs. This results in the jumping in and out of cut of the cutter which results in a nonsmooth surface. At high spindle speeds, the primary chatter mechanisms diminish and chatter due to regeneration of the waviness of the surface is most prone to occur [144]. Therefore, the focus in this work

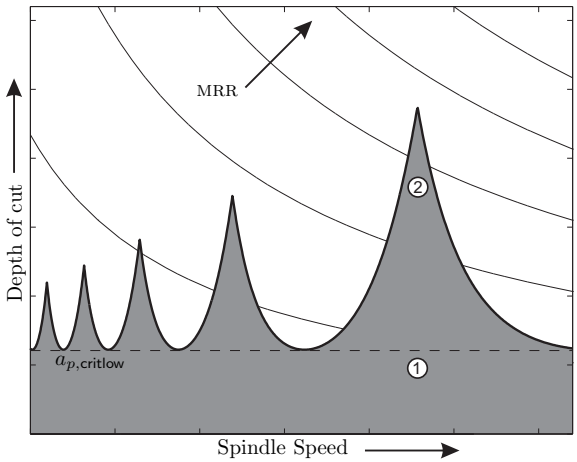

Figure 1.2: Schematic representation of a typical stability lobes diagram of a milling process. Working point 1 is considered a conservative choice. When more accurate milling models are available, working point 2 may be chosen.

lies on the prevalent type of chatter, i.e. regenerative chatter.

Pioneering work of Tlusty [157] and Tobias [159, 160] resulted in the first stability analysis for the orthogonal cutting process. Merritt [108] illustrates that chatter stability analysis can be characterised by a feedback loop. The result of the stability analysis is the so-called stability lobes diagram (SLD). In an SLD the chatter stability boundary between a stable cut (i.e. without chatter) and an unstable cut (i.e. with chatter) is visualised in terms of spindle speed n and depth of cut a_p. A typical SLD is given in Figure 1.2. By using a stability lobes diagram, a machinist may select chatter free milling conditions directly, whilst ensuring a high MRR, where MRR $\propto a_p n$. From the SLD it can be seen that a depth-of-cut $a_{p,\text{critlow}}$ exists such that the cut is stable (i.e. chatter-free) for all spindle speeds and all $a_p \leq a_{p,\text{critlow}}$. Furthermore it can be seen that the lobes become broader and higher as the spindle speed increases as opposed to low spindle speeds. At low spindle speeds a relatively small change in spindle speed may lead to a relatively large change in the phase difference between two consecutive teeth [8]. Due to the broader lobes at high spindle speeds, the productivity can be substantially increased when the lobes are accurately predicted by choosing a working point in a lobe (see point 2 in Figure 1.2). As a result, when high-speed milling became commercially available in the 1990s, a renewed interest in studying chatter phenomena in high-speed machining was seen in machining research field.

1.3 Chatter prediction

In order to avoid chatter, a working point should be selected which guarantees stable cutting conditions as predicted from the stability lobes diagram [8]. As described above, early stability analyses presented by Tlusty, Tobias and Merritt were based on a model of the orthogonal cutting process where the cutting force does not depend on time. For the milling process, however, the stability analysis becomes more complicated due to the rotating tool, the fact that cutters with multiple teeth are used and multi-degree of freedom spindle dynamics [172]. The set of equations that describe the milling process is then modelled by a set of non-autonomous delay-differential equations (DDE). Numerous models have been developed to describe the milling process. In Chapter 2, a more in-depth discussion regarding the modelling of the milling process for the purpose of chatter prediction will be presented. Comprehensive reviews on models describing the milling process can be found in [8, 49].

Chatter is predicted by analysing the stability properties of the model. One way to do so is by performing time domain simulations, see e.g. [158]. However, in general, performing simulations is time-consuming and, moreover, the border between a stable and unstable cut is not always clear from the simulation data [49]. Altintas and Budak present a fast analytical method to determine stability of the milling process [6] based on the Nyquist criterion. Herein, the non-autonomous term in the DDE milling model is approximated by averaging the cutting forces over one revolution. In order to evaluate the stability properties of the non-autonomous model describing the milling process, e.g. the semi-discretisation method (SDM), presented in [72, 75], can be used.

1.4 Chatter control

In the previous section, it has been discussed that one way of dealing with chatter in machining is to construct a stability lobes diagram (SLD) based on a model of the machining process. Such a SLD may be used to select working points which, on the one hand, guarantee a high MRR and, on the other hand, avoid the occurrence of chatter. In facing this trade-off, one encounters the following two problems:

- firstly, by selecting a working point (spindle speed, depth of cut and feed) that lies below the chatter boundary the process is stable and may exhibit a high MRR (high up in a lobe). However, due to temperature effects, wear and tear of the milling machine and tool, the SLD may (slowly) vary/shift over time. As a result, an initially chosen working point may become unstable. Hence, working points of high MRR (high up in a lobe) are generally not robust against the occurrence of chatter;
- secondly, some workpiece materials require specific cutting speeds (or

spindle speeds) which may result in a rather limited MRR if no lobe is located at this spindle speed.

Therefore, to fulfill the demands of both high productivity and high accuracy in a machining process and to overcome the above two problems, automated chatter control strategies may be highly beneficial [100].

In literature, basically three types of chatter control approaches can distinguished, namely spindle speed modulation, spindle speed selection and alteration of the spindle dynamics. These approaches will be discussed in the next sections.

1.4.1 Spindle speed modulation

The goal of spindle speed modulation is to disturb the regenerative effect by continuously varying the spindle speed. This can be done via sinusoidal or random spindle speed variation (SSV), see [4, 7, 70, 79, 80, 96, 139, 177]. In [174], instead of spindle speed variation the rake angle in case of turning is continuously varied by means of an oscillating cutter. Yang *et al.* [175] combine both SSV and variation of the rake angle into a multiple time-varying parameter method for chatter suppression in turning. In general, the modulation parameters need to be specifically determined for each application. Therefore, Kubica and Ismail [89] propose an algorithm based on fuzzy logic control that online adjusts the modulation parameters to guarantee chatter free machining.

While most of the work focuses on experimental implementation, the works in [74, 76, 149] illustrate the influence of the variation amplitude and frequency for sinusoidal SSV on the stability lobes diagram. It is shown that the optimal modulation period is equal to two times the spindle speed period.

The application of spindle speed modulation is limited by the inertia (and actuation power) of the spindle system and can therefore in general not be used in high-speed machining. Another way of disturbing the regenerative waviness, that is not limited by the inertia of the spindle, can be realised by using tools with a non-equidistant tooth distribution. While this strategy can be used at high speed, it is not desirable due to fact that the chip load is unevenly distributed over the teeth causing more wear on those teeth.

1.4.2 Spindle speed selection

As described above, an initially chosen working point may become unstable due to changing process conditions. This can be overcome by adjusting the process parameters (spindle speed, depth of cut and/or chip load) of the machining process such that a stable working point is assured even in changing process conditions. This strategy consists of two parts, namely the detection of (onset) of chatter and the control algorithm that selects the new setpoint for the process parameter(s).

In the majority of the strategies presented in literature, adaptation of the spindle speed is proposed. The new spindle speed is selected by relying on the fact that stable machining is guaranteed when a tooth passing frequency equals the dominant chatter frequency. As a result, the spindle speed selection strategy requires an accurate detection of chatter and an accurate estimate of the dominant chatter frequency. Both the detection of (the onset of) chatter and the estimation of the chatter frequency should, preferably, be available before any chatter marks are visible on the workpiece. Current chatter detection methods, see [11, 23, 29, 51, 145, 147], might work well for low spindle speeds but they either utilise too much computational time to be able to detect chatter before it has already developed towards the fully grown stage or are not able to estimate the dominant chatter frequency. A notable exception is the work presented in [42], where an online chatter detection methodology in case of turning is presented. Based on a discrete autoregressive moving average model, chatter modes are estimated from the vibration signal. Since in case of milling the vibration signal also consists of spindle speed related frequencies, see [77], the method presented in [42] cannot directly be used for the milling process.

Weck *et al.* [170] filter the tooth passing excitation frequency from the measured power spectrum of measured spindle torque. A new setpoint is then calculated by setting the spindle speed equal to the measured chatter frequency. The so-called chatter recognition and control (CRAC) system, where chatter is identified by considering the audio spectrum of a cut, is presented in [28, 143–145]. Due to lack of computational efficiency in these detection and control algorithms the feed should stopped once chatter is detected. This implies that at that moment chatter is fully grown and the workpiece already exhibits chatter marks [145]. Next, the new spindle speed setpoint is determined such that it equals the dominant chatter frequency in the audio spectrum. After setting the new spindle speed setpoint, the feed is resumed and the process continues until chatter no longer occurs. A similar approach is presented in [151]. Soliman and Ismail [148] present the first experimental results where feed is not interrupted during a spindle speed change. Once chatter is detected, the spindle speed is ramped up until the detection variable, described in [79], becomes smaller than the detection threshold. Ramping up the spindle speed does not ensure that the nearest stable working point is found. Moreover, when an initial working point is close to the maximum operating spindle speed no new spindle speed may be found. Liang *et al.* [95] compare adaptation of feed, spindle speed and a combination of spindle speed and feed using a fuzzy logic controller. Results show that chatter cannot be suppressed by feed adjustment alone. In [43], new spindle speed and feedrate setpoints are based on a heuristic search for stable machining conditions.

Experimental results using the methods described above are only shown up to a spindle speed of approximately 6000 rpm (so for relatively low spindle

speeds). In [49], a computationally efficient method is developed that can be used in the case of high-speed milling. All methods, discussed above, rely on the fact that stable machining is guaranteed when a tooth passing frequency equals the dominant chatter frequency. Setting a spindle speed harmonic equal to the dominant chatter frequency in general implies that chatter vibrations will be bounded but are not likely to be minimised. Therefore, important improvements can be made by automatically searching for a spindle speed setpoint that lowers the vibrations associated with chatter.

1.4.3 Alteration of spindle dynamics

Another way of addressing the chatter problem is to alter the dynamics of the spindle-bearing, toolholder and tool system. This is a completely different approach as compared to the chatter control methods discussed before. By altering the dynamics of the spindle, the SLD can be altered such that a higher MRR becomes feasible. In this thesis, when referring to the spindle dynamics, we mean to indicate the dynamics of spindle-toolholder system as well as the tool dynamics. Basically, two methodologies are known in literature to alter the spindle dynamics; namely, altering the spindle dynamics either in a passive or an active manner. In the following sections, both approaches will be discussed.

1.4.3.1 Passive chatter control

In early studies on chatter prediction, it has been observed that machining stability can be enhanced by increased damping of the whole system. Therefore, passive vibration control techniques generally aim to increase damping. Several kinds of dampers are used, such as Lanchester dampers [63], impact dampers [41, 138], tuned mass dampers [128, 168, 176] or vibration absorbers [92, 97, 130, 141, 152]. As an example, in [92] a passive vibration control system using a dynamic vibration absorber mounted on a cutting tool has been developed to suppress vibrations in turning operations. The dynamic vibration absorber has to satisfy two conditions: 1) the natural frequency of the dynamic vibration absorber should be close to the natural frequency of the tool and 2) the dynamic vibration absorber should have a larger damping ratio than the tool. Whereas in most cases a single damper is used, Yang *et al.* [176] present an optimisation strategy for multiple tuned mass dampers to maximise the minimum value of the real part of the tooltip frequency response function, which is beneficial for stability, see [157, 160]. In [86] and [182], the development of a so-called multi-fingered centrifugal damper, which is inserted inside a hollow tool, is discussed. As a result of centrifugal forces the flexible fingers press against the inner surface of the hollow tool which constrains the bending of the tool.

Passive dampers are relatively cheap and easy to implement and do not require external energy. More importantly, passive control methods never destabilise the system. However, drawbacks regarding the use of passive damping

techniques are the fact that the amount of damping which is practically achievable is rather limited. Furthermore, vibration absorbers need accurate tuning with respect to their natural frequencies and, consequently, lack robustness with respect to changing machining conditions. Also, passive vibration control methods find very limited application in milling as compared to turning operations. This is due to the nature of milling operations in which the cutting tools rotate at high speed, whereas in turning operations the cutting tool is fixed. Hence, in the latter case it is more convenient to add passive dampers to damp tool vibrations.

An approach taken from a different perspective, which also could be considered as a passive chatter suppression technique, is presented by Maeda *et al.* [101]. Herein, the configuration of a spindle is designed based on the specification of the workpiece material and the tools used during cutting. An algorithm determines the distribution of the bearings along the spindle such that the spindle modes are altered in such a way that a peak in the stability lobes diagram is located at a desired spindle speed. During each optimisation step the frequency response function (FRF) of the spindle tooltip dynamics is calculated using a Timoshenko beam based finite element model. The obtained mass, damping and stiffness matrices are integrated into the Altintas-Budak stability analysis method [6] to determine the objective function value, i.e. the critical depth of cut at the desired spindle speed. A major disadvantage of this approach is that once the optimal hardware design is found and implemented, there is no possibility anymore to alter the spindle dynamics. This could be a problem when stability boundaries start to shift due to heat generation, tool wear, etc. or when one would like to employ the machine at different spindle speeds.

1.4.3.2 Active chatter control

Chatter mitigation by active controller design is growing research field. Active control of the spindle dynamics involves the design of a mechatronic system which consists of an actuator/sensor system and a control law which calculates the forces that should be applied to the spindle or tool. Active control of chatter in machining processes has been proposed in different ways.

Firstly, different control laws are used. Examples are model-based control procedures based on LQG and/or optimal control [22, 36, 37, 113, 140, 154], $\mathcal{H}_\infty$-norm based control [90, 103, 104] and μ-synthesis [21, 83–85, 87], and non-model-based active damping procedures, see [124], based on positive position feedback [180], acceleration feedback [122, 123] and velocity feedback [24, 57].

Secondly, several kinds of actuators are applied, such as active vibration absorbers [58, 103, 113], active magnetic bearings [21, 83, 91], piezo-electric actuators [30, 37, 119, 129, 180], Tefenol-D actuators [40, 118, 122, 123] and electro-rheological fluids [137, 166, 167]. An extensive overview of the use of active materials in machining processes can be found in [120].

Early attempts in controlling chatter using active control methodologies are performed by Comstock [26], Nachtigal [112] and Glaser and Nachtigal [59]. Comstock introduces an impedance control method to reduce tool vibrations in single-point turning. In [59, 112] the effect of active damping on a boring bar with hydraulic actuation is investigated.

The first experimental results of active chatter control for the milling process are given in [37]. Herein, the theoretical results of [36] are demonstrated on an experimental system, denoted as the *smart spindle unit*, which consists of piezoelectric actuators where the tool-vibrations are measured using strain gauges. A linear quadratic Gaussian (LQG) controller is used to alter machine dynamics such that damping of the dominant tool mode is enhanced. Using a model of the *smart spindle unit*, an active damping approach based on $\mathcal{H}_\infty$-norm based control is proposed in [90]. Results from time-domain simulations, where the cutting forces acting at the tool are modelled as an external disturbance without taking the regenerative effect into account, illustrates that an increase in the depth of cut is possible.

In [57], active damping control using velocity-feedback is applied to turning operations and in [58] an extension to milling operations is proposed. Results are illustrated using a hardware-in-the-loop simulator. Hereto, the cutting forces are simulated using a mathematical model of the regenerative effect and are interfaced to a beam which represents the structural dynamics of the turning/milling machine.

A static and dynamic compensation of tool deflections is presented in [30]. A tripod which consists of three piezoelectric actuators is build around a spindle unit. Static tool deflection is compensated based on a priori knowledge of the tool's and the spindle's stiffness. Dynamic tool deflection is attenuated by measuring the tool deflection with eddy current sensors. After identification of this disturbance, a compensation signal is calculated, which is phase shifted by 180° and applied to the milling spindle by the piezoelectric actuators.

Ries *et al.* [129] introduce a commercial milling spindle with additional piezoelectric actuators which induce forces at the outer ring of the front bearing. Herewith, a controller is designed which increase damping which leads to an increase of the critical depth of cut.

Another possibility is to use active magnetic bearings (AMB) in milling spindles as presented by Fittro and Knospe in [54, 55, 87, 88]. The dynamic compliance at the tooltip of the spindle is minimised, using on μ-synthesis techniques. Henceforth, the set of machining parameters, that is, spindle speed and depth-of-cut, for which stable cutting holds is enlarged. A similar approach is presented by Kern *et al.* [83], where active damping is applied for a milling spindle equipped with an AMB in addition to the ball bearings. A controller for a single spindle speed is designed using μ-synthesis. The eigenfrequency of the milling machine depends on the spindle speed and is modelled as an uncertainty. This strategy is extended in [84], where controllers are designed

for two different spindle speeds. To apply active damping in the entire spindle speed range, gain-scheduling is applied for spindle speeds that differ from the two design spindle speeds.

An approach taking a different perspective is presented in [180]. Herein, it is assumed that chatter originates from workpiece flexibilities. Active damping is applied by using piezoelectric actuators and sensors, which are mounted to the thin-walled workpiece.

In some sense, all aforementioned active chatter control approaches aim to attenuate chatter vibrations by applying damping to the spindle or the tool in an active way. In general one can say that damping the machine or workpiece dynamics, either passively or actively, results in a uniform increase of the stability boundary for all spindle speeds. To enable more dedicated shaping of the stability boundary (e.g. lifting the SLD locally around a specific spindle speed), the regenerative effect should be taken into account during chatter controller design, which is one of the main points lacking in the aforementioned control methodologies.

A first approach where the regenerative effect is included in the controller design is presented in [140]. An optimal state feedback-observer controller combination with integral control in the case of turning was designed while taking the regenerative effect into account. The regenerative effect, modelled using a delay term, is written as a rational function via Padé approximation. In [106], the nonlinear continuous-time delay differential model describing the milling process is converted to a discrete time representation. A high-order delay-free model is obtained by adding delay states to the system description and computing the system's monodromy matrix. A controller is then determined based on LQG techniques. Recently, Chen and Knospe [21] developed three different chatter control strategies, based on μ-synthesis, for the case of turning: speed-independent control, speed-specified control and speed-interval control. The experimental setup consists of an AMB on an actuator platform that is connected to the tool platform via a leaf spring.

Although the experimental setup discussed in [21] exhibits some aspects encountered in high-speed milling, a comprehensive active chatter control strategy tailored to the full complexity of the HSM process is missing to this date. Moreover, except for the work in [83, 84], all research on active chatter control is limited to low spindle speeds (i.e. below 5000 rpm).

1.5 Goals and main contributions of the thesis

From the discussion in the previous sections, it becomes clear that chatter must be avoided at all times. Based on the stability lobes diagram, a machinist is able to select the optimal process parameters which should render a chatter-free milling operation while ensuring a high MRR. In this work, two chatter control approaches will be presented, which enable the increase or maintain

of machining efficiency and/or increase the robustness of the milling process against chatter. Below the main goals of the two control approaches will be discussed in more detail.

Due to changes in temperature of the milling spindle, wear and tear of the milling spindle and/or tool, the lobes in the SLD may shift over time. Then it may very well happen that an originally selected, chatter-free, working point, chosen high in the lobe (with a high MRR, see point 2 in Figure 1.2), becomes unstable. This should be prevented by detecting the occurrence of chatter while it is a pre-mature stage (i.e. when no chatter marks are visible on the workpiece yet) and adjusting the spindle speed and feed such that the process remains stable. The first main goal of this thesis can be formulated as follows:

> *A chatter detection and control algorithm should be developed, which, firstly, detects chatter in a premature phase, and, secondly, by automatic adaptation of spindle speed and feed, guarantees a robust high-speed milling operation despite changing process conditions, such as e.g. an increase of temperature of the spindle or wear of the tool.*

Based on the discussion above the first contributions of this work is given as follows:

- Current chatter detection methods might work well for low spindle speeds but they either utilise too much computational time to be able to detect chatter before it has already developed towards the fully grown stage or are not able to estimate the dominant chatter frequency. Therefore, in this work, a novel chatter detection algorithm is presented, that detects chatter when it is in a pre-mature stage, i.e. no chatter marks are visible on the workpiece yet, and, moreover, gives an accurate estimate of the dominant chatter frequency.

- Current chatter control techniques, which alter the process parameters to prevent the occurrence of chatter due to changing process conditions (such as temperature changes and wear of the spindle/tool), guarantee stable machining by setting a tooth passing frequency equal to the dominant chatter frequency. However, setting a spindle speed harmonic equal to the dominant chatter frequency in general implies that chatter vibrations will be bounded but are not likely to be minimised. Therefore, in this work, a chatter control strategy is presented that automatically lowers the cutter vibrations associated with chatter via real-time adaptation of spindle speed and feed.

The continuously increasing demand for high-precision products at a high productivity level, as seen in the present day manufacturing industry [114], asks for the design of dedicated control strategies, which are able to actively alter the chatter stability boundary and therewith enable high material removal rates. The second main goal of this thesis can be formulated as follows:

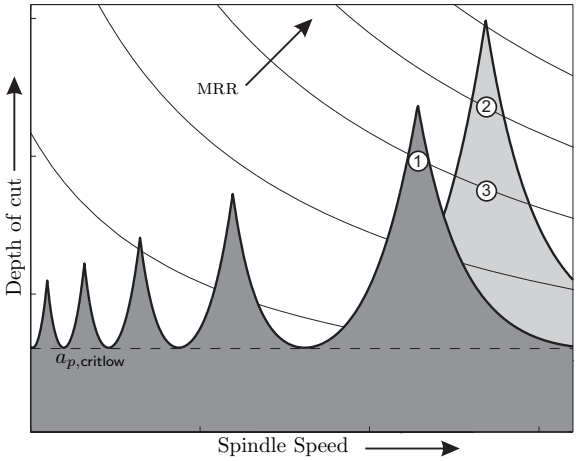

Figure 1.3: Stability lobes diagram with (light grey area) and without (dark grey area) active chatter control.

> *An active control strategy should be developed which alters the stability lobes diagram in a selective spindle speed range, and, therewith ensures a priori chatter-free milling operations for a predefined domain of process parameters (spindle speed and depth-of-cut) such that (chatter-free) operating points of higher* MRR *become feasible.*

To illustrate the demand for such *lobe shaping*, consider the SLD for a given spindle-toolholder-tool and workpiece material combination as given by the dark grey area in Figure 1.3. Herein, next to the SLD, isolines for a constant MRR are given. The productivity for this typical spindle-toolholder-tool and workpiece combination can be increased by designing an active chatter controller, which alters the stability lobes such that the controlled SLD is generated as indicated by the light grey area in Figure 1.3. In that case, an initial operating point, point 1, can be shifted into the new stability lobe, i.e. point 2 in Figure 1.3, which implies a larger MRR and machining productivity. Increasing demands for improved surface quality and high-precision products also trigger the desire for lobe shaping. In general, these demands can be fulfilled by reducing the cutting forces, i.e. reducing the depth-of-cut a_p or chip load f_z. Ideally, this is done without compromising on productivity. Hereto, consider once again Figure 1.3, where it is assumed that the originally selected working point 1 results in a bad surface quality. To improve the surface quality, without reducing the MRR, a point along the isoline of the MRR for point 1, for a smaller depth of cut, should be chosen, e.g. point 3 in Figure 1.3. However, without altering the spindle dynamics this would not be possible. Along the same line of reasoning, lobe shaping via active chatter control is motivated by limited

spindle speed ranges in which tools operate properly and without excessive wear [12]. Due to complex geometries or specific material properties, tools are often limited to operate in a narrow spindle speed range which is favourable in terms of tool life time.

Based on the discussion above, the following goals and main contributions of this work regarding active chatter controller design can be formulated:

- A (model-based) active chatter controller methodology for the high-speed milling process is presented, which can guarantee chatter-free cutting operations in an a priori defined range of process parameters such as spindle speed and depth of cut, where a model of the regenerative effect will be taken into account during the controller design. From the discussion in Section 1.4.3 it becomes clear that current chatter control strategies for the milling process cannot provide such a strong guarantee of a priori stability for a predefined range of working points. In general, the existing techniques require a posteriori calculation of the set of stable working points.

- For an active control approach, it is important to limit the amount of actuator forces needed to stabilise the milling process. A comprehensive analysis will illustrate the choice of the controller input signal that significantly reduces the amount of actuator forces needed to stabilise the milling process in the pre-defined domain of operating points. In addition, a bound on the actuator forces will be incorporated as a performance criterion during the controller design.

- It is well known that the spindle dynamics vary due to heat generation and gyroscopic effects in angular contact ball bearings. Therefore, during controller synthesis robustness against changing process conditions (i.e. modelling uncertainties) will be taken into account.

- The active control methodology will be based on robust-control design techniques. Standard robust control techniques will result in relatively high-order controllers, which may be undesirable from an implementation perspective. Therefore, additionally, in this work a fixed structure active chatter control design procedure, while considering the infinite-dimensional model of the milling process, is presented.

- A important aspect is the implementation of the active chatter control strategy on an actual experimental setup, where more complex models (and uncertainties) of the spindle dynamics need to be taken into account during controller synthesis. In this work, controllers are tested on an experimental setup where an AMB is integrated in the spindle. Using the designed controller, milling tests are performed and a proof of principle of the active chatter control methodology is provided.

Summarising, it can be said that, with the two chatter control strategies, an increase in the robustness as well as efficiency of the milling process will be realised.

1.6 Outline of the thesis

Chapter 2 discusses a comprehensive model of the milling process. The milling process is introduced in detail in Section 2.2. The model describing the milling process consists of three submodels. Firstly, a model of the tooth path is presented in Section 2.3. Secondly, the cutting force model is presented in Section 2.4. Finally, a model describing the spindle and actuator dynamics is described in Section 2.5. Assembling the submodels, results in a total model of the milling process discussed in Section 2.6. Moreover, a stability analysis of the model will be discussed in Section 2.7, which can be used to construct model-based stability lobes diagrams. Finally, a discussion on the frequencies that appear in the vibration signals during chatter will be discussed in Section 2.8.

Chapter 3 presents the control strategy which automatically adjusts spindle speed and feed by minimising the vibrations associated with chatter. Hereto, Section 3.2 presents a novel detection algorithm, based on a parametric model of the milling process, which is able to detect chatter when it is in a premature stage, i.e. when no chatter marks are visible on the workpiece yet, and, moreover, gives an accurate estimate of the dominant chatter frequency. The automatic spindle speed selection algorithm is presented in Section 3.3. Experimental results using the detection and control strategy are discussed in Section 3.4.

The active chatter control synthesis methodology, which enables dedicated shaping of the SLD in specific spindle speed ranges, is presented in Chapters 4, 5 and 6.

Section 4.2 presents the problem statement of the active chatter control problem. Then, in Section 4.3 a comprehensive analysis is performed to select an appropriate feedback signal for the active chatter controller input, such that the actuator forces are significantly reduced. The model of the milling process as presented in Chapter 2 cannot be directly used in the robust controller design procedure. Therefore, in Section 4.4 some model simplifications will be discussed in order to construct a model suitable for controller design. Section 4.5 present the robust control design procedure, based on a μ-synthesis approach. Results of the proposed strategy, when applied to an illustrative example using a relatively simple model for the spindle-toolholder-tool dynamics, are presented in Section 4.6.

In Chapter 5, a fixed structure active chatter control design procedure for the milling process without approximating the infinite-dimensional delay term (as done in Chapter 4) is discussed. The fixed structure controller design is

based on a μ-synthesis approach. Using this controller synthesis technique, controllers of relatively low order when compared to the controllers obtained using the methodology from Chapter 4 are designed, as described in Section 5.1. The algorithm for synthesising the controllers is presented in Section 5.2. Results, using the algorithm for fixed structure controller design and a relatively simple model for the spindle-toolholder-tool dynamics, are discussed in Section 5.3.

Experimental results, where the active chatter control strategy, as proposed in Chapter 4, is tested for an actual high-speed milling spindle, which is equipped with an AMB, are presented in Chapter 6. The main goals of the experiments are given in Section 6.1. The experimental setup is presented in Section 6.2. Parameters of the cutting force model and a model of the spindle-actuator dynamics will be determined experimentally and the resulting model is discussed in Section 6.3. Controller design for the experimental setup is presented in Section 6.4. A closed-loop model-based stability analysis is performed in Section 6.5. The results of milling tests with the controllers implemented on the experimental setup are discussed in Section 6.6.

Finally, conclusions and recommendations for future research are presented in Chapter 7.

2

Modelling the milling process

2.1 Introduction

This chapter presents a comprehensive model of the milling process which can be used to predict the occurrence of regenerative chatter. Moreover, the model serves as a basis for the control design methodologies that will be presented in the remainder of this work. Extensive overviews regarding modelling the milling process for the prediction of regenerative chatter can be found in [5, 8, 49].

In Section 2.2, the basic structure of the milling process will be presented. In the Sections 2.3, 2.4 and 2.5, the tooth path model, cutting model and model of the spindle and actuator dynamics will be presented, respectively. Combining the submodels gives the total milling model, which will be presented in Section 2.6. Stability properties of the model will be discussed in Section 2.7. Finally, a discussion on the frequencies that appear in the vibration signals during chatter will be discussed in Section 2.8.

2.2 The milling process

In the milling process, material is removed from the workpiece by a combination of rotation of a milling cutter and horizontal motion of this cutter in the feed (x) direction into the workpiece. In Figure 2.1(a), a three-dimensional schematic overview of the milling process can be found. Typical parameters

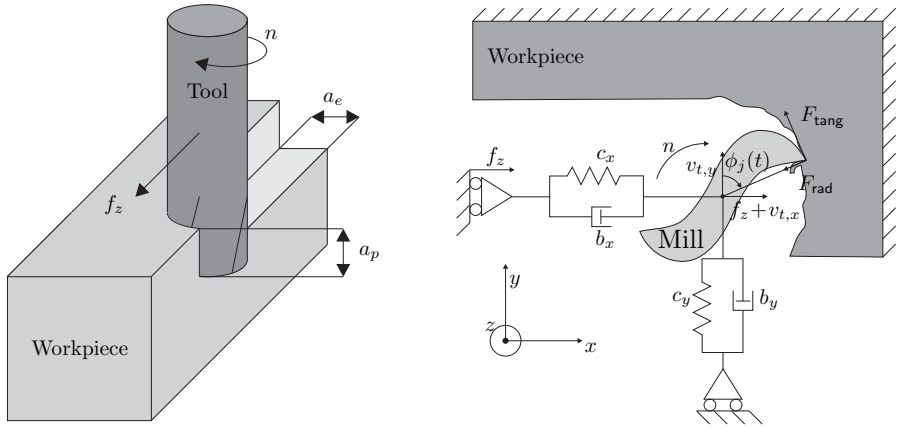

(a) 3D-view. (b) Top view.

Figure 2.1: Schematic representation of the milling process.

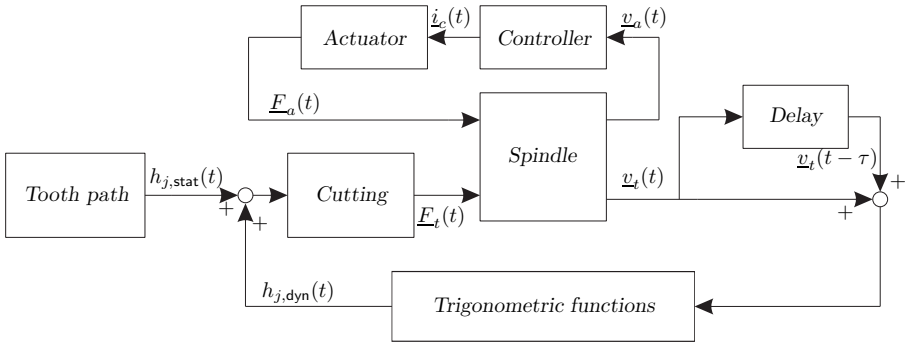

Figure 2.2: Block diagram of the milling process.

that characterise the milling process, which are shown in the figure, are the spindle speed n, the chip load f_z, the axial depth of cut a_p and the radial depth of cut a_e. Here, chip load refers to the thickness of the material which is removed by one tooth of the milling cutter. Unlike in the turning process, in the milling process the chip thickness is not constant, but a periodic function of time. This is a result of the combination of the movement in the feed direction and the rotating cutter.

In Figure 2.1(b), a schematic representation of the milling process is given, where, for illustrative purposes, it is assumed that the dynamics of the milling machine can be characterised by a single mode. In such a case, the spindle-toolholder-tool combination is modelled as a 2-DOF mass-spring-damper system

in x- and y-direction with spring constants c_x and c_y and damping constants b_x and b_y, respectively. In general, however, the dynamics of the spindle dynamics will be more complex. The tangential and radial forces on the tool are denoted by F_{tang} and F_{rad}, respectively. The angle that tooth j makes with the normal y-direction is described by $\phi_j(t)$. A block diagram of the milling process, with controller, is given in Figure 2.2. Below, each of the blocks in this figure will be explained in more detail. As can be seen from the block diagram in Figure 2.2, the milling process is a closed-loop position-driven process (even without the controller). The setpoint of the milling process is the predefined motion of the tool with respect to the workpiece, given in terms of the static chip thickness $h_{j,\mathsf{stat}}(t)$. The static chip thickness is a result of a model of the tooth path (and is generated by the nominal motion in feed direction and the imposed rotation of the tool). However, the total chip thickness also depends on the interaction between the cutter and the workpiece. Since in general the machine tool is not infinitely stiff, the interaction between the cutter and the workpiece leads to cutter vibrations resulting in a dynamic displacement $\underline{v}_t(t) = \begin{bmatrix} v_{t,x}(t) & v_{t,y}(t) \end{bmatrix}^T$ of the tool which is superimposed on the predefined tool motion. This results in a wavy surface on the workpiece. The next tooth encounters the wavy surface left behind by the previous tooth and generates its own waviness. This is called the regenerative effect and results in the block *Delay* in Figure 2.2, see [108, 157]. The difference between the current and previous wavy surface is denoted as the dynamic chip thickness

$$h_{j,\mathsf{dyn}}(t) = \begin{bmatrix} \sin\phi_j(t) \cos\phi_j(t) \end{bmatrix} \big(\underline{v}_t(t) - \underline{v}_t(t-\tau) \big), \tag{2.1}$$

defined in the radial direction where $\begin{bmatrix} \sin\phi_j(t) \cos\phi_j(t) \end{bmatrix}$ are the trigonometric functions as given in the block diagram in Figure 2.2 and the delay τ given as

$$\tau = \frac{60}{zn}. \tag{2.2}$$

Herein, n is the spindle speed in revolutions per minute (rpm) and z the number of teeth. Hence, the total chip thickness of tooth j, $h_j(t)$, is the sum of the static and dynamic chip thickness: $h_j(t) = h_{j,\mathsf{stat}}(t) + h_{j,\mathsf{dyn}}(t)$. In the next sections, the components of the milling model, more specifically the tooth path model, cutting force model and spindle and actuator dynamics, will be described in more detail.

2.3 Tooth path model

The tooth path is the trajectory of a milling cutter tooth when it cuts through the material. Traditionally, for the two-dimensional case, i.e. when the mill is modelled in the plane of the machine bed, the tooth path is modelled as a circular arc. However, the real tooth path is trochoidal. In [52], a model of

the milling process is presented where the tooth path model is described using a trochoidal path. Results in [52] illustrate that the effect of the trochoidal tooth path model on the stability lobes diagram (SLD) becomes relevant when considering low immersion levels (i.e. the ratio a_e/d, with d the diameter of the cutter, is small). Since high-speed milling (HSM) is often applied for rough machining, the focus in this work lies on full immersion cuts, where the full width of the cutter is used for cutting (i.e. $a_e = d$). Then it is sufficient to model the tooth path using a circular tooth path and the static chip thickness is given as, see [5]:

$$h_{j,\mathsf{stat}}(t) = f_z \sin \phi_j(t) \tag{2.3}$$

with f_z the chip load in mm/tooth and $\phi_j(t)$ the rotation angle of the j-th tooth of the tool with respect to the y (normal) axis (see Figure 2.1(b)).

2.4 Cutting force model

The cutting force model (indicated by the *Cutting* block in Figure 2.2) relates the cutting forces acting at the tool tip of the machine spindle to the total chip thickness. It is common to use an empirical model for the cutting force model. In this work, it is assumed that the cutting tool is straight-fluted with zero helix-angle. Consequently, it is sufficient to only consider cutting forces in feed (x)- and normal (y)-direction [5]. The cutting forces in tangential and radial direction for a single tooth j are described by the following exponential cutting force model, see [150, 156]:

$$\begin{aligned} F_{\mathsf{tang},j}(t) &= g_j\big(\phi_j(t)\big) K_t \, a_p \, h_j(t)^{x_F}, \\ F_{\mathsf{rad},j}(t) &= g_j\big(\phi_j(t)\big) K_r \, a_p \, h_j(t)^{x_F}, \end{aligned} \tag{2.4}$$

where $0 < x_F \leq 1$ and $K_t, K_r > 0$ are cutting parameters which depend on the workpiece material and the cutter, and a_p is the axial depth of cut. The parameters are different for each workpiece material and tool combination. The usage of an exponential dependency of the cutting force on the chip thickness has the benefit that the stability lobes diagram will depend on the chip load f_z which is the case in practice. The cutting force only acts on the cutter when the corresponding tooth is in cut. Hereto, the function $g_j\big(\phi_j(t)\big)$ describes whether a tooth is in or out of cut:

$$g_j\big(\phi_j(t)\big) = \begin{cases} 1, & \phi_s \leq \phi_j(t) \leq \phi_e \wedge h_j(t) > 0, \\ 0, & \text{else}, \end{cases} \tag{2.5}$$

where ϕ_s and ϕ_e are the entry and exit angle of the cut, respectively. Via trigonometric functions, the cutting force can easily be converted to x(feed)- and y(normal)-direction (see Figure 2.1(b)). Hence, cutting forces in x- and

y-direction, $F_{t,x}$ and $F_{t,y}$, respectively, can be obtained by summing over all z teeth:

$$\begin{aligned}\underline{F}_t(t) = a_p \sum_{j=0}^{z-1} g_j\left(\phi_j(t)\right)\Bigg(\Big(h_{j,\mathsf{stat}}(t) \\ + \left[\sin\phi_j(t) \;\; \cos\phi_j(t)\right]\left(\underline{v}_t(t) - \underline{v}_t(t-\tau)\right)\Big)^{x_F}\mathbf{S}(t)\begin{bmatrix}K_t\\K_r\end{bmatrix}\Bigg),\end{aligned} \tag{2.6}$$

where $\underline{F}_t(t) = \begin{bmatrix}F_{t,x}(t) & F_{t,y}(t)\end{bmatrix}^T$ and

$$\mathbf{S}(t) = \begin{bmatrix}-\cos\phi_j(t) & -\sin\phi_j(t)\\ \sin\phi_j(t) & -\cos\phi_j(t)\end{bmatrix}.$$

2.5 Spindle dynamics and actuator dynamics

The cutting forces interact with the spindle rotor and tool dynamics (block *Spindle* in Figure 2.2). For the purpose of active chatter control, which will be discussed in more detail in Chapters 4, 5 and 6, an actuator is implemented in the spindle rotor. The controller output $\underline{i}_c(t)$ is dictated to the actuator which, in turn, generates a force $\underline{F}_a(t)$ on the spindle.

In general, the spindle rotor, toolholder and tool dynamics (jointly called the spindle dynamics) can be modelled by a linear multi-input-multi-output (MIMO) model. The model has four inputs and four outputs. The inputs consist of the cutting forces $\underline{F}_t(t) = \begin{bmatrix}F_{t,x}(t) & F_{t,y}(t)\end{bmatrix}^T$ acting at the tool-tip in x-/y-direction and the actuator forces $\underline{F}_a(t) = \begin{bmatrix}F_{a,x}(t) & F_{a,y}(t)\end{bmatrix}^T$ in x-/y-direction induced at some point in the spindle, which generally differs from the location at which the cutting forces are acting (the tooltip). This leads to an inherent flexibility between the location of the actuator/sensor system and the location at which cutting forces act. The outputs of the spindle rotor dynamics model are the displacements $\underline{v}_t(t) = \begin{bmatrix}v_{t,x}(t) & v_{t,y}(t)\end{bmatrix}^T$ of the tooltip and displacements $\underline{v}_a(t) = \begin{bmatrix}v_{a,x}(t) & v_{a,y}(t)\end{bmatrix}^T$ measured at some position on the spindle, the latter of which are used for feedback. The state-space equations describing the rotor dynamic model (spindle, toolholder and tool dynamics) are given as follows:

$$\begin{aligned}\dot{\underline{x}}(t) &= \mathbf{A}\underline{x}(t) + \mathbf{B}_t\underline{F}_t(t) + \mathbf{B}_a\underline{F}_a(t),\\ \underline{v}_t(t) &= \mathbf{C}_t\underline{x}(t), \quad \underline{v}_a(t) = \mathbf{C}_a\underline{x}(t),\end{aligned} \tag{2.7}$$

where $\underline{x} \in \mathbb{R}^{n_x}$ is the state vector (the order n_x of this model primarily depends on the order of the spindle-tool dynamics model), $\mathbf{A} \in \mathbb{R}^{n_x \times n_x}$, $\mathbf{B}_t, \mathbf{B}_a \in \mathbb{R}^{n_x \times 2}$

and $\mathbf{C}_t, \mathbf{C}_a \in \mathbb{R}^{2\times n_x}$. The state-space matrices describing the model of the spindle dynamics can be either obtained using experimental data, after which a parametric model is fit onto the data, or using a finite element approach [3]. In this work, the model of the spindle dynamics will be based on the experimental approach. In addition, the workpiece is considered rigid in this work. However, workpiece flexibilities can be incorporated in the state-space model in (2.7) describing the spindle dynamics.

Next to the spindle rotor, toolholder and tool dynamics, an actuator model should be included. In this work, two different actuator models will be considered, namely

1. a linear actuator model, given by

$$\underline{F}_a(t) = \mathbf{K}_a \underline{i}_c(t) \tag{2.8}$$

   with controller output $\underline{i}_c(t)$;

2. a model of an active magnetic bearing (AMB).

The linear actuator model is considered as a generic class of actuator models for which the active chatter control design procedure will be illustrated. Next to the generic linear actuator model, the active chatter control design procedure will also be developed for a model incorporating a specific actuator model for an active magnetic bearing (AMB). As described in Chapter 1 an AMB is a common type of actuator applied to rotor dynamic systems and in [83] feasibility of using such actuator in the scope of high-speed milling has been shown. This motivates to pay special attention to this kind of actuator (model). The nonlinear model of an AMB driven in differential mode is given as follows [136]:

$$F_{a,k}(t) = k_{\mathsf{amb},k}\left(\frac{(i_0 + i_{c,k}(t))^2}{(v_0 - v_{a,k}(t))^2} - \frac{(i_0 - i_{c,k}(t))^2}{(v_0 + v_{a,k}(t))^2}\right),\ k = x, y, \tag{2.9}$$

where $k_{\mathsf{amb},k}$ are the specific AMB coefficients, i_0 is the so-called pre-magnetising current (to compensate for gravity, etc.), v_0 the corresponding nominal gap displacement and $i_{c,k}(t)$ is the controller output (i.e. the input currents to the actuator) and $v_{a,k}(t)$ the bearing displacements. In general, the displacements in the actuator journal $v_{a,k}(t)$ are significantly smaller than the gap width v_0. In addition, the controller output $\underline{i}_c(t)$ will be limited by the controller design methodology. Then, for control design the nonlinear model of the AMB may be linearised about $\underline{i}_c(t) = \underline{v}_a(t) = 0$, which has already been successfully performed for many applications as is described in [136]. This results in the following linear model of the AMB:

$$\underline{F}_a(t) = \mathbf{K}_i \underline{i}_c(t) + \mathbf{K}_s \underline{v}_a(t), \tag{2.10}$$

where

$$\mathbf{K}_i = \mathrm{diag}\big(4k_{\mathsf{amb},x}\frac{i_0}{v_0^2}, 4k_{\mathsf{amb},y}\frac{i_0}{v_0^2}\big), \tag{2.11}$$

$$\mathbf{K}_s = \mathrm{diag}\big(4k_{\mathsf{amb},x}\frac{i_0^2}{v_0^3}, 4k_{\mathsf{amb},y}\frac{i_0^2}{v_0^3}\big). \tag{2.12}$$

Note that both the actuator models, that will be used for controller design, are actually linear models. However, in the remainder of this thesis, the model in (2.8) will be referred to as the linear actuator model, whereas the model in (2.10) will be referred to as the AMB model, as the model exhibits special properties since it depends on the vibrations $\underline{v}_a(t)$ of the spindle rotor.

Combining the actuator model with the model describing the spindle, toolholder and tool dynamics in (2.7), gives the total model of the spindle-actuator dynamics.

2.6 Total milling model

In the previous sections, the submodels for the static chip thickness, cutting force and spindle rotor, toolholder, tool and actuator dynamics for the different blocks representing the milling model as given in Figure 2.2 are introduced. Substitution of the cutting force model, given in (2.6) into the model of the spindle rotor, toolholder and tool dynamics, given in (2.7), yields the total milling model:

$$\begin{aligned}\dot{\underline{x}}(t) = \mathbf{A}\underline{x}(t) + \mathbf{B}_t a_p \sum_{j=0}^{z-1} g_j\big(\phi_j(t)\big)\Bigg(\Big(h_{j,\mathsf{stat}}(t) + \\ \big[\sin\phi_j(t)\ \ \cos\phi_j(t)\big]\,\mathbf{C}_t\big(\underline{x}(t) - \underline{x}(t-\tau)\big)\Big)^{x_F}\mathbf{S}(t)\begin{bmatrix}K_t\\K_r\end{bmatrix}\Bigg) \\ + \mathbf{B}_a\underline{F}_a(t), \quad \underline{v}_a(t) = \mathbf{C}_a\underline{x}(t).\end{aligned} \tag{2.13}$$

In addition, the appropriate actuator model, i.e. either (2.8) or (2.10), should be added to the total milling model (2.13). It can be seen that the model describing the milling process is set of nonlinear, time-dependent delay differential equations (DDE). In the next section, the stability properties of the model will be analysed.

2.7 Stability of the milling process

In this section, the stability analysis exploited to determine chatter boundaries in the stability lobes diagram is briefly addressed. In the milling process the static chip thickness is periodic with period time τ. In general, the uncontrolled

(i.e. $\underline{F}_a(t) = 0$) milling model (2.13) has a periodic solution $\underline{x}^*(t)$ with period time τ [52]. To validate this fact let us assume the following decomposition of $\underline{x}(t)$ can be made:

$$\underline{x}(t) = \underline{x}^*(t) + \underline{\tilde{x}}(t), \tag{2.14}$$

where $\underline{x}^*(t)$ is a τ-periodic motion that can be considered as the ideal motion when no chatter occurs, and $\underline{\tilde{x}}(t)$ the perturbation term [77]. When no chatter occurs, $\underline{\tilde{x}}(t) = 0$ and the nominal tool motion is described by the following ordinary differential equation (ODE):

$$\dot{\underline{x}}^*(t) = \mathbf{A}\underline{x}^*(t) + \mathbf{B}_t a_p \sum_{j=0}^{z-1} g_j\big(\phi_j(t)\big) h_{j,\mathsf{stat}}(t)^{x_F} \mathbf{S}(t) \begin{bmatrix} K_t \\ K_r \end{bmatrix}, \tag{2.15}$$

which follows from (2.13) by exploiting the fact that $\underline{x}^*(t) = \underline{x}^*(t-\tau),\ \forall t$, since it is assumed that $\underline{x}^*(t)$ is τ-periodic. This is a linear system with a periodic excitation with period time τ. Hence, when $\mathbf{A}$ has no eigenvalues at $il2\pi f_{tpe}$, for $f_{tpe} := \frac{1}{\tau}$ and all $l \in \mathbb{Z}$, the solution $\underline{x}^*(t)$ exists, is unique and is τ-periodic [53]. Now the occurrence of chatter can be studied by investigating the stability of the periodic solution $\underline{x}^*(t)$. More specifically, the periodic solution is (at least locally) asymptotically stable when no chatter occurs and when chatter occurs it is unstable. Hence, to study the chatter stability boundary, the uncontrolled milling model is linearised about the periodic solution $\underline{x}^*(t)$ which yields the following linearised dynamics in terms of the perturbations $\underline{\tilde{x}}(t)$:

$$\dot{\underline{\tilde{x}}}(t) = \mathbf{A}\underline{\tilde{x}}(t) + a_p \mathbf{B}_t \sum_{j=0}^{z-1} \mathbf{H}_j(t) \mathbf{C}_t (\underline{\tilde{x}}(t) - \underline{\tilde{x}}(t-\tau)), \tag{2.16}$$

where

$$\mathbf{H}_j(t) = g_j\big(\phi_j(t)\big) x_F (f_z \sin\phi_j(t))^{x_F - 1} \mathbf{S}(t) \begin{bmatrix} K_t \\ K_r \end{bmatrix} \big[\sin\phi_j(t) \ \ \cos\phi_j(t)\big]. \tag{2.17}$$

As can be seen from (2.16), (2.17), the linearised model is a delayed, periodically time-varying system. For a linear periodic DDE, as in (2.16), stability properties can be examined using extended Floquet theory for DDEs [53, 64]. In general, a linear periodic DDE has an infinite-dimensional state-space. For an autonomous DDE system this leads to an infinite number of characteristic roots. For a periodic DDE system the so-called characteristic multipliers (or Floquet multipliers) μ, with $\mu = e^{\lambda\tau}$, with λ the characteristic exponent, are determined. The number of Floquet multipliers is infinite. However, it can be proved, see [53], that the number of Floquet multipliers is countable and the Floquet multipliers are located in a compact subset of the complex plane and have only one cluster point $\mu = 0$. When all the Floquet multipliers have magnitude smaller than one, i.e. $|\mu| < 1$, the equilibrium point $\underline{\tilde{x}}(t) = 0$ in (2.16)

is (globally) asymptotically stable. Since stability of $\underline{x}^*(t)$ is studied using a linearisation of (2.13) around $\underline{x}^*(t)$, this, in turn, implies that $\underline{x}^*(t)$ is a local asymptotically stable solution of (2.13). If one or more Floquet multipliers lie outside the unit disk, the equilibrium point $\underline{\tilde{x}}(t) = 0$ in (2.16) is unstable. This implies that the periodic solution $\underline{x}^*(t)$ is unstable and chatter will occur.

Based on the discussion above, it can be seen that stability of the milling process is based on the calculation of the relevant characteristic multipliers μ. Several approximation methods have been proposed in literature to determine a finite number of characteristic multipliers [16, 35, 73, 75, 102]. In this work stability is assessed using the semi-discretisation method of [75]. The main point of semi-discretisation is that only the delay term is discretised, instead of the actual time domain terms.

2.8 Chatter frequencies

In the final part of this chapter, briefly, the frequencies that are typically present in the spectrum of the cutter vibrations $\underline{v}_t(t)$, for the case with and without chatter, are discussed. The same reasoning holds for the vibrations $\underline{v}_a(t)$ measured at the actuator location.

As discussed before, in the milling process, the static chip thickness $h_{j,\mathsf{stat}}(t)$ is periodic. The motion $\underline{v}_t(t)$ of the cutter can therefore be described by a periodic motion $\underline{v}_t^*(t) = \mathbf{C}_t\underline{x}^*(t)$, which is, in case of a concentric tool, periodic with period time $T = \tau = \frac{1}{f_{tpe}} = \frac{60}{zn}$. Here, f_{tpe} denotes the tooth passing frequency, z is the number of teeth on the cutter and n the spindle speed in revolutions per minute (rpm). In practice, the axis of rotation does not coincide with the geometric axis, and, consequently, the motion $\underline{v}_t(t)$ is periodic with the spindle speed $T = \frac{1}{f_{sp}} = \frac{60}{n}$ [78], with f_{sp} the spindle speed frequency. This effect is called runout. Then the following frequencies appear in the vibration signals when no chatter occurs [77]: for the case without runout,

- (multiples of) the tooth passing excitation frequency,

$$f_{TPE} = l f_{tpe}, \text{ with } l \in \mathbb{Z}^+, \tag{2.18}$$

and for the case with runout,

- (multiples of) the spindle speed frequency,

$$f_{SP} = l f_{sp}, \text{ with } l \in \mathbb{Z}^+, \tag{2.19}$$

and, moreover, the damped natural frequencies of the spindle-toolholder and tool dynamics.

As described above, when the periodic solution $\underline{x}^*(t)$ loses its stability (e.g. with an increasing axial depth-of-cut), a set of Floquet multipliers cross the

unit disk. Then three different cases can be distinguished, namely for $|\mu| = 1 \wedge \mathrm{Im}(\mu) \neq 0$, $\mu = -1$ and $\mu = 1$. When $|\mu| = 1 \wedge \mathrm{Im}(\mu) \neq 0$, a new periodic motion with frequency f_c is superimposed on the original periodic motion. In the remainder of this work, f_c is denoted as the basic chatter frequency. This type of instability is denoted as a secondary Hopf bifurcation, and it is in most cases responsible for the occurrence of chatter in milling. The basic chatter frequency f_c is related to the Floquet multipliers via

$$f_c = \frac{\mathrm{Im}(\ln(\mu))}{2\pi T}, \tag{2.20}$$

where $T = \tau$ in case of no runout and $T = z\tau$ for the case with runout [49, 77]. For a secondary Hopf bifurcation, the frequency of the new motion f_c is incommensurable to the frequency of the original solution (f_{tpe} in case of no runout or f_{sp} in case of runout). Hence, this results in a quasi-periodic motion of the tool. Consequently, in an unstable cut, the following chatter frequencies f_C occur additionally due to a secondary Hopf bifurcation [77]:

$$f_C = \pm f_c + l\frac{1}{T}, \text{ with } l = 0, \pm 1, \pm 2, \ldots. \tag{2.21}$$

When $\mu = -1$, a so-called period doubling bifurcation occurs and the frequency of the new motion is exactly half the frequency of the original motion. Then, the following chatter frequencies due to a period doubling bifurcation occur:

$$f_C = (l + \tfrac{1}{2})\frac{1}{T}, \text{ with } l = 0, \pm 1, \pm 2, \ldots. \tag{2.22}$$

The final case is when $\mu = 1$ and is denoted by period one chatter. For the case without runout, period one chatter will never arise in the vibration signals, see [78]. For the case with runout, the frequencies coincide with the harmonics of the spindle speed frequencies. Consequently, the chatter frequencies due to a period one bifurcation are given as

$$f_C = l f_{sp}, \text{ with } l = 0, \pm 1, \pm 2, \ldots. \tag{2.23}$$

When chatter occurs, the energy of the vibration at the frequencies related to f_C significantly increases. Since the chatter frequencies represent a large set of discrete frequencies, one of these frequencies will generally lie close to a natural frequency of the spindle-toolholder and tool dynamics and will, consequently, be dominant in the vibration signals. This frequency will be called the dominant chatter frequency f_{chat} in the remainder of this thesis. In practice, basically three stages in the development of chatter can be identified. In the first phase, no chatter is occurring. This implies that the frequency spectrum of the vibration signals only consists of spindle speed related frequencies and no

chatter marks are visible on the workpiece. In the second phase, the frequency spectrum of the vibration signals consists of spindle speed related frequencies and the dominant chatter frequency. However, no chatter marks are visible on the workpiece yet. This phase is called onset of chatter. The third phase is called full grown chatter. In this phase, the frequency spectrum consists of spindle speed related frequencies and chatter frequencies f_C. Moreover, chatter marks are visible on the workpiece. At high spindle speeds full grown chatter typically arises within a time span of approximately 100 ms.

3

Chatter control by automatic in-process spindle speed selection

3.1 Introduction

In machine shops, generally a working point (in terms of spindle speed n and depth of cut a_p) is chosen such that the milling operations remain stable for the entire spindle speed range. This is illustrated in Figure 3.1. A working point will generally be chosen below the line indicated by $a_{p,\mathsf{critlow}}$, resulting in e.g. working point 1 in Figure 3.1. Improved modelling of the milling process, using e.g. models as discussed in Chapter 2, results in a more accurate prediction of the peaks in the stability lobes diagram (SLD). As a consequence, a working point in the peak of a lobe may be chosen (point 2 in Figure 3.1). In this way the material removal rate (MRR) can be significantly increased. However, due to temperature effects, wear and tear of the milling machine, the SLD may (slowly) vary/shift over time. As a result, an initially chosen working point may become unstable. This is illustrated in Figure 3.1, where the working point 2 becomes unstable due to shifting of the SLD. This asks for a control strategy that ensures robust stability of the process, despite the (slow) varying nature of the SLD, by e.g. automatically changing the spindle speed to point 3 in Figure 3.1.

As described in Chapter 1, there basically exist three methods to overcome or avoid chatter. From these three methods, only two are applicable in case of high-speed milling (HSM), namely spindle speed selection and active or passive altering of the machine dynamics. In this chapter, a novel chatter control method based on spindle speed selection will be presented. By automatic

Parts of this chapter originally appeared in [31] and [32]

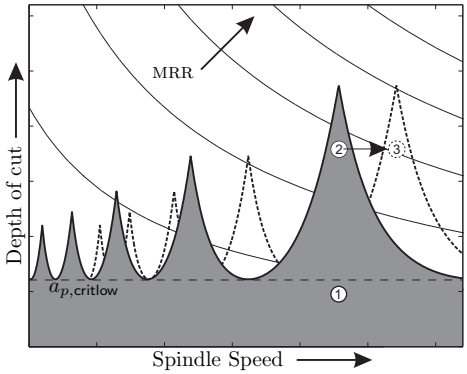

Figure 3.1: Schematic representation of automatic spindle speed selection procedure. Working point 1 *is considered a conservative choice. Due to better modelling working point* 2 *may be chosen, which may become unstable over time due to shifting of the stability lobes. A spindle speed adaptation towards working point* 3 *ensures a robustly stable milling operation.*

adaptation of spindle speed and feed a chatter-free high-speed milling operation, which is robust for changing process conditions (e.g. due to heating of the spindle or tool wear, etc.), is guaranteed. An important part of this chatter control strategy is the detection of (onset of) chatter. The model of the milling process, as discussed in Chapter 2 cannot readily be employed for the spindle speed selection control strategy (due to the fact that temperature effects etc, are not included in the model). Therefore, a novel chatter detection algorithm is presented that is able to track (slow) varying changes in the milling process and automatically detects the onset of chatter in an online fashion and in a pre-mature phase such that visible chatter marks on the workpiece are avoided. Experiments on a state-of-the-art high-speed milling machine underline the effectiveness of the proposed detection and control strategies.

In Section 3.2, the novel detection algorithm is described. In Section 3.3, the automatic chatter control strategy by means of automatic spindle speed selection is described. Experimental results using the detection and the control strategy are discussed in Section 3.4.

3.2 Chatter detection

In this section, the real-time chatter detection strategy will be presented. The main objectives of the chatter detection are, firstly, to detect onset of chatter in an early stage of its growth and, secondly, to identify the dominant chatter

frequency f_{chat} which is essential in the desired control strategy (see Section 3.3). Moreover, the chatter detection procedure must be able to track changing (uncertain) process conditions, e.g. due to heating of the spindle or tool wear, which are difficult to incorporate in the model as discussed in Chapter 2. This asks for a parametric modelling approach of the milling process, which will be presented Section 3.2.1. Based on the outcome of the detection method, a control action (in this case adjusting spindle speed and feed) will be effected to ensure that the process remains stable and full grown chatter is avoided. The detection and control action must be performed in real-time due to the rapid growth of chatter (typically within 100 ms) for high spindle speeds. Therefore, existing chatter detection procedures, as e.g. discussed in [7, 110], which require the computation of the frequency spectrum of the vibrations and hence are computationally inefficient, can therefore not applied in the case of high-speed milling. Note, once more, that the goal of the detection strategy focuses on the detection of onset of chatter and the corresponding chatter frequency, rather than identifying the parameters of the milling process as presented in the previous chapter.

In Section 3.2.2, the estimation of the parameters of the model will be presented. The real-time implementation of the estimation of the parameters is presented in Section 3.2.3. Finally, the procedure for detection of the onset of chatter is discussed in Section 3.2.4.

3.2.1 Parametric modelling of the milling process

Clearly, the choice of an appropriate sensor is essential in a detection and control system. In [49] an experimental comparative study has been presented, using a wide range of sensors (accelerometer, dynamometer, eddy current sensors and a microphone). Results show that the use of an accelerometer, mounted near the lower bearing of a milling spindle is preferable from a detection performance as well as cost effectiveness point of view. Therefore, here, one accelerometer mounted near the lower bearing of a milling spindle will be used for chatter detection. This section presents a parametric model of the milling process, using the measured acceleration $a(t)$, without the necessity constructing a complete cutting process model as presented in Chapter 2.

As described in Chapter 2, the movement of the cutter $\underline{v}_t(t)$ can be decomposed into a periodic part $\underline{v}_t^*(t)$ and a perturbation part $\tilde{\underline{v}}_t(t)$. The same decomposition can be used for the acceleration $a(t)$: $a(t) = a^*(t) + \tilde{a}(t)$. The digital representation of the milling process can then be written as an output error model [98], which is of the following form:

$$a(kT_s) = G(q)u(kT_s) + H(q)e(kT_s). \tag{3.1}$$

Herein the sequence $a(kT_s)$, $k = 0, 1, \ldots$ is the digital representation of the continuous signal $a(t)$ with sampling interval T_s, $u(kT_s)$ the input signal, $e(kT_s)$

Gaussian white noise with zero-mean and variance σ^2, $G(q)$ and $H(q)$ are rational minimum-phase transfer functions which are a function of the shift operator q. In the remainder, the sampling interval T_s is omitted for notational convenience, i.e $a(k) := a(kT_s)$. The signal model of the periodic component $a^*(k)$ can now be denoted as $a^*(k) = G(q)u(k)$, and the signal model of the perturbation part $\tilde{a}(k)$ can be denoted as $\tilde{a}(k) = H(q)e(k)$. A common model structure for (3.1) is the Box-Jenkins (BJ) model, see e.g. [98]. Its general formulation is as follows:

$$a(k) = \frac{B(q)}{F(q)}u(k) + \frac{C(q)}{D(q)}e(k). \tag{3.2}$$

Here, $e(k)$ is again Gaussian white noise of zero-mean and variance σ^2 and $u(k)$ is the input, due to the spindle speed related perturbation, which can be composed by a discrete cosine/sine series, with the spindle speed as the fundamental frequency, given by

$$u(k) = \sum_{l=1}^{n_L} \underline{u}^l(k) = \sum_{l=1}^{n_L} \begin{bmatrix} \cos(l\omega(k)kT_s) \\ \sin(l\omega(k)kT_s) \end{bmatrix}. \tag{3.3}$$

Herein, $\omega(k) = \frac{2\pi n(k)}{60}$, with $n(k)$ the measured spindle speed in rpm and n_L the number of harmonics under consideration.

In the case of milling, the periodic movement of the cutter can be modelled as an input-output relation between the spindle speed related perturbation $u(k)$ and $a^*(k)$ without any dynamics, i.e. $F(q) = 1$ in (3.2). The reasoning behind this is the fact that the spindle speed dependency of the model is not considered as part of the regenerative effect (i.e. the spindle speed related vibrations do not enter the feedback path of the milling process, as given in Figure 2.2). The model of the periodic part can therefore be considered as a moving average (MA) process. As described in Chapter 2, when chatter occurs, the frequency spectrum consists of spindle speed and chatter frequencies. The chatter frequencies close to a machine spindle resonance will have a significantly larger amplitude than the other chatter frequencies. Therefore, the signal model of the perturbation part $\tilde{a}(k)$ can be considered as a so-called *narrow-band signal* of which the frequency and amplitude may vary in time. Commonly, a *narrow-band signal* can be modelled as an auto-regressive moving average (ARMA) process. Since we are interested in the resonance (frequency and amplitude) of the model, which can be modelled as a time-varying auto regressive (AR) signal model, we take $C(q) = 1$ in (3.2). Taking the considerations stated above into account, the total signal model can be given as

$$a(k) = \sum_{l=1}^{n_L} \underline{B}^l(q)\underline{u}^l(k) + \frac{1}{D(q)}e(k), \tag{3.4}$$

where $\underline{B}^l(q)$ is defined as,

$$\underline{B}^l(q) = \left[B^l_{\cos},\ B^l_{\sin}\right] \tag{3.5}$$

and $B^l_{\cos}$ and $B^l_{\sin}$ are zero-th order transfer functions (i.e. do not depend on q). The chatter vibrations (= regenerative effect) are modelled by $D(q)$ since the chatter-related vibration $\tilde{a}(k) = \frac{1}{D(q)}e(k)$. Hence, it is expected that properties of $D(q)$ will predict the onset of chatter.

3.2.2 Identification of the parametric milling model

The rational transfer functions $\underline{B}^l(q),\ l = 1, 2, \ldots, n_L$, and $D(q)$ in (3.2) are unknown and are to be determined with an estimation procedure. The unknown coefficients of $\underline{B}^l(q)$ and $D(q)$ are gathered in the parameter vector $\underline{\theta}$, i.e. denote $\underline{B}^l(q)$ as $\underline{B}^l(q, \underline{\theta})$ and $D(q)$ as $D(q, \underline{\theta})$. The one-step ahead predictor for the parametric milling model in (3.4) is given as

$$\hat{a}(k, \underline{\theta}) = D(q, \underline{\theta}) \sum_{l=1}^{n_L} \underline{B}^l(q, \underline{\theta}) \underline{u}^l(k) + (1 - D(q, \underline{\theta}))\, a(k). \tag{3.6}$$

The prediction error is defined as the difference between the measured and the predicted acceleration:

$$\varepsilon_m(k, \underline{\theta}) := a(k) - \hat{a}(k, \underline{\theta}) = D(q, \underline{\theta}) \varepsilon(k, \underline{\theta}), \tag{3.7}$$

with

$$\varepsilon(k, \underline{\theta}) := a(k) - \hat{a}^*(k) = a(k) - \sum_{l=1}^{n_L} B^l(q, \underline{\theta}) u^l(k). \tag{3.8}$$

Herein, the one-step ahead predictor from (3.6) is used. The two transfer functions $\underline{B}^l(q, \underline{\theta})$ and $D(q, \underline{\theta})$ can be estimated independently as will be shown below. This is desirable, firstly, to reduce the complexities of the one-step-ahead prediction and, secondly, from a computational point of view. Hereto, the parameter vector $\underline{\theta}$ is decomposed into two separate vectors, $\underline{\theta}_p$ for the periodic transfer functions $\underline{B}^l(q, \underline{\theta}_p)$ and $\underline{\theta}_u$ for the perturbation transfer function $D(q, \underline{\theta}_u)$, i.e. $\underline{\theta} = \left[\underline{\theta}_p^T,\ \underline{\theta}_u^T\right]^T$.
The first prediction scheme estimates the periodic part of the accelerations:

$$\hat{a}^*(k, \underline{\theta}_p) = \sum_{l=1}^{n_L} \underline{B}^l(q, \underline{\theta}_p) u^l(k), \tag{3.9}$$

with cost function

$$J_p(\underline{\theta}_p) = E\left[\varepsilon^2(k, \underline{\theta}_p)\right], \tag{3.10}$$

where $E[.]$ denotes the expectation operator. The second prediction scheme estimates the perturbation part of the measured accelerations:

$$\hat{\tilde{a}}(k,\underline{\theta}_u)=\hat{a}(k,\underline{\theta})-\hat{a}^*(k,\underline{\theta}_p)=(1-D(q,\underline{\theta}_u))\varepsilon(k)=:\hat{\varepsilon}(k,\underline{\theta}_u) \tag{3.11}$$

with cost function

$$J_u(\underline{\theta}_p,\underline{\theta}_u) = E\left[(\varepsilon(k,\underline{\theta}_p) - \hat{\varepsilon}(k,\underline{\theta}_u))^2\right]. \tag{3.12}$$

Note that J_u is a function of both $\underline{\theta}_p$ and $\underline{\theta}_u$. However, below it will be shown that the cost functions J_u and J_p can be minimised independently. Moreover, $J_u(\underline{\theta}_p,\underline{\theta}_u) = E\left[\varepsilon_m^2(k,\underline{\theta})\right]$. Furthermore, note that by minimising $J_p(\underline{\theta}_p)$ the goal is to minimise $E\left[\varepsilon^2\right]$ which reflects the quality of the estimated $a^*(k)$ of the spindle speed related accelerations. Moreover, the minimisation of J_u, i.e. of $E[(\varepsilon(k,\underline{\theta}_p) - \hat{\varepsilon}(k,\underline{\theta}_u))^2] = E[\varepsilon_m(k)^2] = E[(a(k) - \hat{a}(k,\underline{\theta}))^2]$, aims at good prediction of the overall acceleration signal.

The two-step prediction scheme approach, outlined above, may only be applied when the estimated signals $\hat{a}^*(k)$ and $\hat{\tilde{a}}(k)$ fulfill the property of orthogonality and have zero-mean. Hereto, consider the expected value of $\hat{a}^*(k)$ and $\hat{\tilde{a}}(k)$ to be defined as follows

$$E\left[\begin{bmatrix} \hat{a}^*(k,\underline{\theta}_p) \\ 1 \end{bmatrix} \hat{\tilde{a}}(k-\beta,\underline{\theta}_u)\right] = \begin{bmatrix} \sigma_{pu}^2\delta(\beta) \\ 0 \end{bmatrix}, \tag{3.13}$$

with covariance σ_{pu}^2, β the time shift operator and $\delta(\beta) = 1$ for $\beta = 0$ and $\delta(\beta) = 0$ for $\beta \neq 0$. For the property of orthogonality to hold, in practice, it is required that $\sigma_{pu}^2 \ll 1$. To show that this is indeed the case, (3.9) and (3.11) are substituted into (3.13) which gives

$$E\left[\begin{bmatrix} \sum_{l=1}^{n_L} \underline{B}^l(q,\underline{\theta}_p)\underline{u}^l(k) \\ 1 \end{bmatrix} \hat{\varepsilon}(k-\beta,\underline{\theta}_u)\right] = \begin{bmatrix} \sigma_{pu}^2\delta(\beta) \\ 0 \end{bmatrix}. \tag{3.14}$$

From the definition of the input vector $u^l(k)$ in (3.3) and $\hat{a}^*(k)$ in (3.9), it is clear that the first prediction scheme estimates the periodic movement of the cutter at specific (spindle speed related) frequencies. Moreover, in general, as described in Section 2.8, the (dominant) chatter frequency, which largely determines $\hat{\tilde{a}}(k) = \hat{\varepsilon}(k)$, differs from the spindle speed related frequencies. Then, as is known from Fourier theory, sinusoidal signals with different frequency fulfill the orthogonality property, i.e. $\int_{-\pi}^{\pi} \sin(mx)\sin(nx)dx = \pi\delta_{mn}$ for $m \neq n$, with $m, n \in \mathbb{Z}$, and δ_{mn} the Kronecker delta. Note that the condition of orthogonality may be violated in case period one chatter occurs. Then the chatter frequency coincides with a spindle speed harmonic. For full immersion cuts, which are considered in this work, the range of spindle speeds for which period one chatter occurs is, especially in practice, very small. Hence, it can be concluded that, in practice, $\sigma_{pu}^2 \ll 1$ and $a^*(k)$ and $\tilde{a}(k)$ can be estimated

independently. When no chatter occurs, the estimation error $\varepsilon(k)$ of the first prediction scheme will, in theory, be equal to white noise. Then our assumption that the perturbation signal $\tilde{a}(k)$ is a narrow-band signal, does not hold. However, from the discussion in Section 2.8 and as will be shown in the experimental results in Section 3.4, in practice, the regenerative effect is already visible during stable cutting. This implies that the (dominant) chatter frequency will already be present in the perturbation signal $\tilde{a}(k)$. Therefore, in practice, the assumption that the perturbation signal is a narrow-band-signal still holds when no chatter occurs.
The problem now is to find parameter vectors $\underline{\theta}_p, \underline{\theta}_u$ in (3.9) and (3.11) such that the prediction error $\varepsilon_m(k, \underline{\theta})$ is minimised[1)]. The optimally estimated parameter vectors $\underline{\theta}_p^o$ and $\underline{\theta}_u^o$ are defined as,

$$\underline{\theta}_p^o = \arg\min J_p(\underline{\theta}_p), \tag{3.15}$$

and

$$\underline{\theta}_u^o = \arg\min J_u(\underline{\theta}_p^o, \underline{\theta}_u). \tag{3.16}$$

To solve the estimation problem, normally a set of measurement data is collected. This data is then processed off-line, using e.g. a least square estimator. This off-line approach cannot be used for the chatter control system proposed for three reasons. Firstly, knowledge on the state of the system (i.e. stable/unstable) is required at each time instant in order to detect chatter in an online and real-time fashion. Secondly, from the estimation parameters $\underline{\theta}_u$ the chatter frequency will be estimated which is necessary for the control design that will be presented in Section 3.3. Thirdly, the properties of the milling process may vary during the milling operation. Moreover, during a control action the spindle speed changes which results in a change of the milling process.
The next section describes the identification procedure that is able to deal with the time-varying properties of the milling process and that can be implemented in real-time.

3.2.3 Recursive identification of the parametric milling model

Adaptive and recursive identification methods are designed to deal with time-varying characteristics of dynamic processes (such as the milling process) and can be implemented in real-time. To cope with the time-varying regenerative process and to be able to track variations in the process properties, an adaptive and recursive identification method is used to obtain parameter vectors $\underline{\theta}_p^o$ and $\underline{\theta}_u^o$ such that the cost functions $J_p(\underline{\theta}_p)$ and $J_u(\underline{\theta}_p, \underline{\theta}_u)$ are minimised.

[1)] Note that the minimisation of ε^2 in $J_p(\underline{\theta}_p) = E\left[\varepsilon^2(k, \underline{\theta}_p)\right]$ is only an intermediate step in the estimation process.

A major drawback of the use of recursive methods are the asymptotic properties of the estimation parameters. For fast changing time-variant systems, these drawbacks have disturbing side-effects on the convergence time of an algorithm. Moreover, the condition of orthogonality (3.14) may be violated, resulting in biased estimation of $B^l(q,\underline{\theta})$ and $D(q,\underline{\theta})$. Therefore, it is crucial to select an algorithm with excellent convergence and tracking properties.

The first prediction scheme is solved by application of the widely used normalised least mean square (NLMS) algorithm. The NLMS algorithm is known for its simplicity and ease of computation [66].

The NLMS algorithm is given by

$$\underline{\theta}_p(k+1) = \eta\underline{\theta}_p(k) + 2\alpha\frac{\underline{\varphi}_p(k)\varepsilon(k)}{\|\underline{\varphi}_p(k)\|^2}, \tag{3.17a}$$

$$\varepsilon(k) = a(k) - \underline{\varphi}_p(k)^T\underline{\theta}_p(k), \tag{3.17b}$$

$$\underline{\varphi}_p(k) = \left[\underline{u}^1(k)^T, \underline{u}^2(k)^T, \ldots, \underline{u}^{n_L}(k)^T\right]^T, \tag{3.17c}$$

$$\underline{\theta}_p(k) := \left[\underline{B}^{1\,T}, \underline{B}^{2\,T}, \ldots, \underline{B}^{n_L\,T}\right]^T \tag{3.17d}$$

with $\underline{\theta}_p(0) = \underline{0}$, and where $\underline{u}^l(k)$ as in (3.3) and $\underline{B}^l$ as defined by (3.5). The estimated periodic part of the vibrations is then obtained via $\hat{a}^*(k) = \underline{\varphi}_p^T(k)\underline{\theta}_p(k)$. Moreover, η is the so-called forgetting factor which enables exponential windowing of the data. Without the forgetting factor, the algorithm is only able to track slow-varying properties in the process. Typical values for η lie in the range $\eta \in [0.95, 0.9999]$. The step size is denoted with α. The NLMS algorithm is convergent in the mean square if and only if $0 < \alpha \leq 2$, see [66]. To prevent overshoot of the optimal solution α is normally chosen as $0 < \alpha \leq 1$. Furthermore, the term $\|\underline{\varphi}_p(k)\|^2$ will be constant when the spindle speed is constant, due to the fact that $\underline{\varphi}_p(k)$ consists of sine and cosine series with frequencies related to the spindle speed. However, in practice the spindle speed is measured and will be changed during a control action. Therefore, $\|\underline{\varphi}_p(k)\|^2$ will not be constant over the entire process and is computed recursively. A schematic overview of the first prediction scheme is given in Figure 3.2(a).

The second prediction scheme can be written into a form that allows for the application of the Kalman filter. The discrete-time state-space description of the Kalman filter is defined as follows:

$$\begin{aligned} \underline{x}(k+1) &= \mathbf{A}(k)\underline{x}(k) + \underline{e}(k), \\ y(k) &= \mathbf{C}(k)\underline{x}(k) + w(k) \end{aligned} \tag{3.18}$$

with $\underline{x}(0) = \underline{0}$, $\mathbf{\Sigma}_0 = E[\underline{x}(0)\underline{x}^T(0)]$ and $\underline{e}(k)$ and $w(k)$ are assumed to be zero-mean Gaussian white process and measurement noise processes, respectively,

which are uncorrelated with covariances and cross-covariance defined by

$$E\begin{bmatrix}\underline{e}(k)\\ w(k)\end{bmatrix}\left[\underline{e}^T(k), w^T(k)\right] = \begin{bmatrix}\mathbf{R}_e(k) & \underline{0}\\ \underline{0}^T & R_w(k)\end{bmatrix}. \tag{3.19}$$

Furthermore it is assumed that the noise processes $\underline{e}(k)$, $w(k)$ are uncorrelated with the initial state vector $\underline{x}(0)$, i.e. $E[\underline{e}(k)\underline{x}^T(0)] = \mathbf{0}$ and $E[w(k)\underline{x}^T(0)] = \underline{0}^T$. By taking $\mathbf{A}(k) = \mathbf{I}$, the state-space model of the Kalman filter is transformed into a *random-walk state model* such that it models a nonstationary movement of the state vector $\underline{x}$, see [66, Chp. 6]. In this way, the variation of the chatter frequency due to the slowly varying changes in the milling process (such as e.g. temperature effects, etc.) is taken into account. Next, denote

$$\underline{\varphi}_u(k) := [\varepsilon(k-1), \varepsilon(k-2), \ldots, \varepsilon(k-n_d)]^T, \tag{3.20}$$

where $\varepsilon(k)$ is the error of the first prediction scheme (see (3.17)) which serves as an input to the second prediction scheme. Then choose $\mathbf{C}(k) = -\underline{\varphi}_u^T(k)$, $y(k) = \hat{\tilde{a}}(k) = \hat{\varepsilon}(k)$, $\underline{x}(k) = \underline{\bar{\theta}}_u(k)$ with $\underline{\bar{\theta}}_u(k)$ the true parameter vector, and using the definition of $\hat{\varepsilon}(k)$ (see (3.11)) the state-space model (3.18) can be written as follows

$$\begin{aligned}\underline{\bar{\theta}}_u(k+1) &= \underline{\bar{\theta}}_u(k) + \underline{e}(k),\\ \hat{\varepsilon}(k) &= -\underline{\varphi}_u^T(k)\underline{\bar{\theta}}_u(k) + w(k),\end{aligned} \tag{3.21}$$

with

$$\underline{\bar{\theta}}_u(k) = [\bar{d}_1, \bar{d}_2, \ldots, \bar{d}_{n_d}]^T, \tag{3.22}$$

and n_d denotes the order of $D(q, \underline{\theta}_u)$ and $\bar{d}_i$, $i = 1, 2, \ldots, n_d$ the true parameters of the polynomial $D(q, \underline{\theta}_u)$, i.e. $D(q, \underline{\bar{\theta}}_u) = 1 + \bar{d}_1 q^{-1} + \bar{d}_2 q^{-2} + \ldots + \bar{d}_{n_d} q^{-n_d}$. n_d is typically set to 4 to be able to *monitor* two chatter frequencies. In this way, chatter frequencies related to either a mode of the spindle dynamics or a tool mode can be determined. It should be noted that, in the state-space description above, the fact that $D(q, \underline{\theta}_u)$ is a monic transfer function is used.

Based on the state-space model of the perturbation vibrations, discussed above, the Kalman filter based on the one-step prediction, which estimates the state vector $\bar{\theta}_u$ can be written as follows, [132]: Given observation $\varepsilon(k)$ and state-space model in (3.21) the identification process can be recursively solved by repeating, for $k > 0$:

$$T_r(k) = R_w + \underline{\varphi}_u(k)\mathbf{Q}(k-1)\underline{\varphi}_u^T(k) \tag{3.23a}$$

$$\underline{K}(k) = -\mathbf{Q}(k-1)\underline{\varphi}_u(k)T_r(k)^{-1}, \tag{3.23b}$$

$$\varepsilon_m(k) = \varepsilon(k) + \underline{\varphi}_u^T(k)\underline{\theta}_u(k), \tag{3.23c}$$

$$\underline{\theta}_u(k+1) = \underline{\theta}_u(k) + \underline{K}(k)\varepsilon_m(k), \tag{3.23d}$$

$$\mathbf{Q}(k) = \mathbf{Q}(k-1) + \mathbf{R}_e(k) - \underline{K}(k)T_r(k)\underline{K}_r^T(k), \tag{3.23e}$$

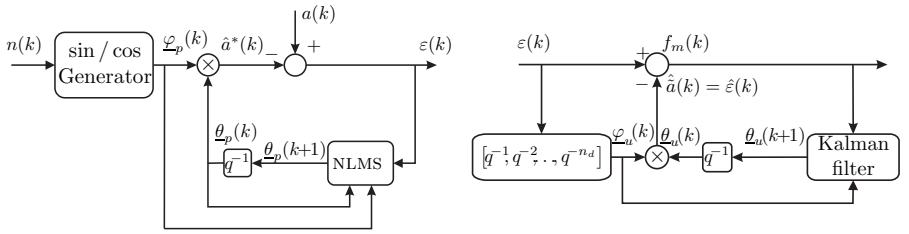

(a) NLMS algorithm. (b) Kalman filter.

Figure 3.2: Schematic overview of the recursive identification algorithms.

with residual covariance $T_r \in \mathbb{R}$, Kalman gain $\underline{K} \in \mathbb{R}^{n_d \times 1}$, the estimated covariance matrix $\mathbf{Q} \in \mathbb{R}^{n_d \times n_d}$ and initial conditions $\underline{\theta}_u(0) = 0$ and $\mathbf{Q}(0) = \mathbf{\Sigma}_0$. The convergence rate and tracking properties of the estimation algorithm can be tuned with the appropriate values for process covariance matrix $\mathbf{R}_e$ and observation covariance R_w. In this particular application, these parameters will be kept constant during the identification procedure. A schematic overview of the second prediction scheme is visualised in Figure 3.2(b). The values of the tuneable parameters will in general differ for each milling machine.

Resuming, this section has presented two algorithms to sequentially estimate the parameters of the parametric model (3.4) of the milling process. The properties of the estimated chatter-related vibrations $\hat{\tilde{a}}(k)$ will be used to predict the occurrence of onset of chatter. The variables employed for chatter detection will be presented in the next section.

3.2.4 Detection of onset of chatter

As discussed above, the properties of $\hat{\tilde{a}}(k)$ will predict the onset of chatter since $\hat{\tilde{a}}(k)$ reflects the signal content of the measured acceleration signal related to the chatter vibrations. Therefore, the detection of onset of chatter is now transformed into the determination of the state of the time-varying auto-regressive signal model $\hat{\tilde{a}}(k) = (1 - D(q, \underline{\theta}_u))\varepsilon(k)$, i.e. the model of the perturbation part. Hence, the detection criterion should indicate the time-varying *strength* of the estimated perturbation signal $\hat{\tilde{a}}(k, \underline{\theta}_u)$.

In literature the following variables are often used in combination with a threshold on the variable as a detection criterion for chatter in case of parametric modelling of the milling process, see e.g. [43]:

- the roots $\underline{\chi}$ of $D(q, \underline{\theta}_u)$;
- the peak value of the power spectral density (PSD) function of $\hat{\tilde{a}}(k)$.

Here a third detection quantity is considered, namely:

- the variance of the perturbation (chatter) part $a(k) - \hat{a}^*(k)$ of the measured acceleration $a(k)$.

The first variable, i.e. the roots of the transfer function $D(q, \underline{\theta}_u)$, directly represents stability of the model which represents the chatter-related vibrations and can therefore be used as a detection variable. The latter two variables represent the energy of the chatter-related vibrations, estimated via $\hat{\tilde{a}}(k)$. When the energy of the estimated chatter-related vibrations $\hat{\tilde{a}}(k)$ is small, no chatter occurs, whereas when the energy increases above a certain threshold chatter is likely to occur. Next the detection variables will be discussed in more detail.

The dominant root of $D(q, \underline{\theta}_u)$ is defined as the root χ with the largest absolute value denoted by $\bar{\chi}$. When $|\bar{\chi}|$ will be come larger than 1, the model $D(q, \underline{\theta}_u)$ will be come unstable and chatter is to occur. The estimated dominant chatter frequency, $\hat{f}_{\mathsf{chat}}$, needed for control and for the second detection variable, is determined from the dominant root $\bar{\chi}$ by,

$$\hat{f}_{\mathsf{chat}}(k) = \mathrm{Im}\left(\frac{ln(\bar{\chi})}{2\pi} f_s\right), \tag{3.24}$$

where $f_s = \frac{1}{T_s}$ denotes the sampling frequency. However, when $|\bar{\chi}| > 1$, and consequently chatter is to occur, the identification results of the milling model will be biased. This results in an unreliable reconstruction of $\hat{\tilde{a}}(k)$. One way to prevent this unstable identification process is to reflect the unstable roots with the unit circle. The reflected distance to the unit circle can be defined arbitrarily. Here, a distance of $\delta_f = 0.001$ to the unit circle is chosen. This implies that when the amplitude of a root becomes equal to $1 + \delta_f$ the pole is reflected with the unit disk, along the line between 0 and the pole, such that the amplitude of the becomes equal to $1 - \delta_f$.

The peak value of the PSD function of $\hat{\tilde{a}}(k)$ is located at the dominant chatter frequency. The peak value of the PSD function of $\hat{\tilde{a}}(k)$ can be calculated directly by

$$\begin{aligned} S_{\hat{\tilde{a}}\hat{\tilde{a}}}(\hat{f}_{\mathsf{chat}}(k), \underline{\theta}_u) &= \left| \frac{1}{D(e^{-i2\pi \hat{f}_{\mathsf{chat}}(k) T_s}, \underline{\theta}_u)} \right|^2 \\ &= \left| \frac{1}{1 + \sum_{l=1}^{n_d} d_l(k) e^{-i2\pi \hat{f}_{\mathsf{chat}}(k) l T_s}} \right|^2 . \end{aligned} \tag{3.25}$$

The final variable for chatter detection considered is the variance of the perturbation part of the measured acceleration (3.11). The estimation error of the first prediction scheme contains all information about the non-spindle

speed related frequencies, whereas the information in the estimated chatter vibrations $\hat{\tilde{a}}(k)$ is limited due to the chosen order n_d of $D(q, \underline{\theta}_u)$. Therefore, the variance is σ^2 calculated from the estimation error $\varepsilon(k) = a(k) - \hat{a}^*(k)$ of the first prediction scheme, i.e. $\sigma_\varepsilon^2 = E\left[\varepsilon^2(k)\right]$. It is expected that the three detection variables (dominant root $\bar{\chi}$ of $D(q, \underline{\theta}_u)$, the PSD value of $\hat{\tilde{a}}(k)$ at the estimated dominant chatter frequency $\hat{f}_{\mathsf{chat}}$ and the variance of the perturbation part $\sigma_\varepsilon^2 = E\left[\varepsilon^2(k)\right]$) will perform differently for an unstable milling process, but comparable for a stable milling process. The choice of which detection variable and threshold to use will be based on experimental results with the detection algorithm, which are presented in Section 3.4.

3.3 Chatter control by spindle speed selection

As described before, basically three methods exist to overcome or avoid chatter, namely continuous spindle speed variation, passively or actively altering the machine dynamics and adjusting the spindle speed. In this chapter, the strategy to adjust the spindle speed and feed to avoid chatter is applied. The following chapters of this thesis describe chatter control by actively altering the machine dynamics. Chatter control by automatic spindle speed selection can be implemented on a state-of-the-art high-speed milling machine without any major changes to the machine, by using the feed override and spindle override functions of the machine. In this section, two methods are presented that automatically adjust the spindle speed in case (the onset of) chatter occurs. Hereto, the detection method of Section 3.2 is used. The detection method gives both an indication that (the onset of) chatter occurs and an estimation of the dominant chatter frequency, which is used for the purpose of control.
In Figure 3.3, a schematic representation of the closed loop including the milling process, chatter detection and chatter control is depicted. An initial working point (spindle speed and depth of cut) is chosen by the machinist based on a model-based stability lobe diagram (SLD), see Chapter 2, or practical experience. This working point is used in the NC program. During the milling process, this spindle speed is maintained as long as (the onset of) chatter is not detected using the detection method presented in Section 3.2. When (the onset of) chatter is detected, a new spindle speed setpoint is computed and sent to the HSM machine using the spindle speed override function to ensure the avoidance of (fully grown) chatter. Simultaneously, the feed is adapted to ensure a constant feed per tooth. The internal speed and feed controllers of the HSM machine will be used to control the spindle speed and feed to its setpoint.

The detection method gives an indication whether or not (the onset of) chatter occurs. Furthermore, the dominant chatter frequency f_{chat} is computed. This chatter frequency is used to compute a new spindle speed setpoint in a chatter-free zone in the case (the onset of) chatter occurs. Hereto, also

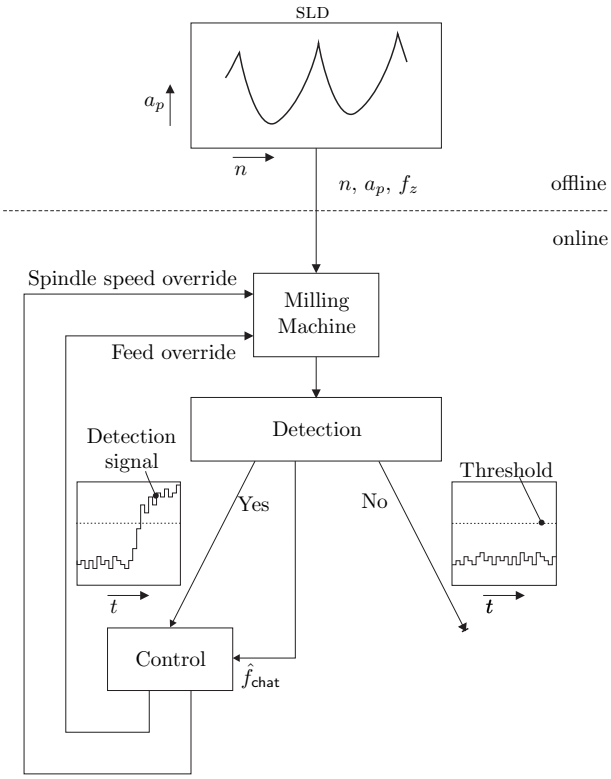

Figure 3.3: Schematic representation of the closed loop including the milling process, chatter detection and chatter control.

the actual spindle speed should be known since it is needed in the detection method and, as will be shown below, it is needed in the computation of the new spindle speed setpoint. The new spindle speed setpoint can be chosen based on two criteria, namely robustness against chatter and the minimisation of the perturbation vibrations of the cutter. Here, robustness is referred to as the selection of a spindle speed as far away from the stability boundary as possible (for fixed depth of cut a_p). The chatter controller as depicted in Figure 3.3 is basically a setpoint generator in closed loop with the HSM machine and the detection algorithm. The internal speed controller of the HSM machine is used to control the spindle speed to its setpoint. In Section 3.3.1, a control strategy is presented that focuses on robustness against chatter whereas Section 3.3.2 presents a control strategy that minimises the perturbation vibrations of the cutter and at the same time guarantees a robust milling performance.

3.3.1 Control strategy 1

In the first control strategy, a new spindle speed is chosen such that the estimated dominant chatter frequency $\hat{f}_{\mathsf{chat}}$ coincides with a (higher harmonic of) the new tooth pass excitation frequency f_{tpe}. The control strategy follows the methodology as presented in [151]. This strategy is also successfully applied for high spindle speeds and by changing the spindle speed in an online fashion in [49].

The chatter frequency is related to the phase difference between two subsequent waves by, see [5]:

$$\epsilon + p = f_{\mathsf{chat}}(k)\frac{60}{zn(k)}, \tag{3.26}$$

with p the (integer) lobe-number, ϵ the fraction of incomplete waves between two subsequent cuts and $n(k)$ the measured current spindle speed in rpm. The new spindle speed is computed such that $\epsilon = 0$, see [151]. Hereto, first the new lobe number is computed by

$$p_{\mathsf{new}}(k) = \left\{ \frac{60\hat{f}_{\mathsf{chat}}(k)}{zn(k)} \right\}, \tag{3.27}$$

where $\{.\}$ means rounding towards the nearest integer and the estimated chatter frequency $\hat{f}_{\mathsf{chat}}$ is provided by the detection method presented in Section 3.2. The new spindle speed is then computed by

$$n_{\mathsf{new}}(k) = \frac{60\hat{f}_{\mathsf{chat}}(k)}{p_{\mathsf{new}}(k)z}. \tag{3.28}$$

Using this method, the spindle speed is directed towards the centre of the lobe, see the schematic overview in Figure 3.1 as discussed in the introduction of this chapter. This fact can be explained as follows. In the milling process the highest depth of cut can be obtained (corresponding to a peak in the SLD) when the dynamic chip thickness $h_{j,\mathsf{dyn}}(t) = \underline{v}_t(t) - \underline{v}_t(t-\tau)$ is equal to zero. This relation can be transformed to the frequency domain as follows

$$H_{j,dyn}(i\omega) = (1 - e^{-i\omega\tau})V_t(i\omega) =: Q(i\omega)V_t(i\omega). \tag{3.29}$$

Hence, the difference between the tooltip displacements of the present and previous cut is actually characterised by a filter, denoted by $Q(i\omega)$, with zeros at $l\omega\tau = l\omega\frac{1}{f_{tpe}}$, $l = 0, 1, 2, \ldots$. Then, by altering the spindle speed n, which is directly related to delay τ via $\tau = \frac{60}{zn}$, i.e. $\tau_{\mathsf{new}} = \frac{p_{\mathsf{new}}}{\hat{f}_{\mathsf{chat}}}$ leading to (3.28), such that the tooth-passing frequency becomes equal to the dominant chatter frequency and due to the filter properties of the $Q(i\omega)$, this results in the

dynamic chip thickness to be zero at the new spindle speed, which implies that a peak in the SLD exists in the SLD at that spindle speed (see Chapter 2).

The exact centre of the lobe may not be exactly characterised by (3.28). As mentioned in [49], if the initial working point is in the lower part of a lobe, the new setpoint lies near the centre of the lobe. However, in the peak of the lobe (i.e. for high depth of cut a_p), $n_{\mathsf{new}}(k)$ as in (3.28) is generally not (exactly) at the centre of the lobe and, consequently, it may happen that the new setpoint may cross the next lobe.

When the spindle speed is changed, this will lead to a new chatter frequency and, hence, the setpoint is changed accordingly. Therefore, the setpoint will be updated constantly as long as the cut is being marked as exhibiting chatter. When the cut is marked as not exhibiting chatter, the most recently computed setpoint is maintained. Therefore, the spindle speed can still change although chatter has already been eliminated.

3.3.2 Control strategy 2

The first control strategy, presented in the previous section, avoids chatter occurrence by setting the tooth-passing frequency equal to the chatter frequency resulting in a zero phase difference ϵ between two subsequent teeth motions. While this approach is robust for changes in the milling process, no guarantees can be given for the performance in terms of the level of vibrations of the process. Therefore, a second control strategy is proposed, where the goal is to minimise the total perturbation vibrations $\tilde{a}(k)$ (which are deemed responsible for chatter marks on the workpiece) and maintain robustness of performance by adapting the spindle speed and feed. This strategy can be seen as an extremum seeking control strategy and generally no guarantees can be given on whether a global minimum is found.

Essential in the development of this second control strategy is the existence of a deterministic relation between perturbation vibrations and the spindle speed. Moreover, knowledge on the relation between the perturbation vibrations and parameters of the milling process parameters, such as spindle speed, depth-of-cut, feed rate etc., is necessary to design a suitable controller. In general no exact model can be found that analytically describes the relation between perturbation vibration and parameters of the milling process. Therefore, this relation is determined empirically. Hereto, milling experiments at a Mikron 700 HSM are performed for several spindle speeds n at a constant depth-of-cut of $a_p = 3.5$ mm and feed per tooth $f_z = 0.2$ mm/tooth. The cut has been made in aluminium 6082 using a Jabro Tools JH421 cutter (2 flute cutter with a diameter of 10 mm and length of 57 mm) mounted in a Kelch HSK40 shrink-fit holder. The acceleration is measured during the cut using an accelerometer which is mounted near the lower spindle bearing. The measured accelerations are processed off line using a MATLAB/SIMULINK [107]

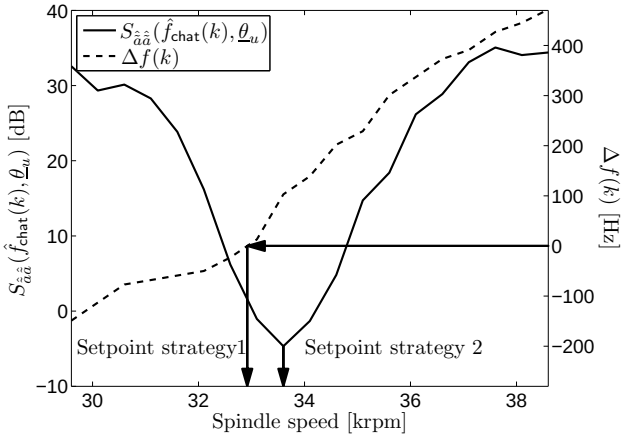

Figure 3.4: Power spectral density $S_{\hat{\tilde{a}}\hat{\tilde{a}}}(\hat{f}_{\mathsf{chat}}(k), \underline{\theta}_u)$ (solid) and $\Delta f(k)$ (dashed) based on measured accelerations for a spindle speed sweep from 29600 to 38600 rpm at a constant depth of cut.

implementation of the detection method presented in Section 3.2. Figure 3.4 presents the resulting relation of the perturbation vibration, in terms of the PSD $S_{\hat{\tilde{a}}\hat{\tilde{a}}}(\hat{f}_{\mathsf{chat}}(k), \underline{\theta}_u)$ of $\hat{\tilde{a}}(k)$ at the chatter frequency, which is presented in Section 3.2.4, as a function of the spindle speed for one specific depth of cut and feed per tooth. In the same figure, the difference between the estimated dominant chatter frequency $\hat{f}_{\mathsf{chat}}(k)$ and the coinciding higher harmonic of the tooth passing frequency, defined as $p_{\mathsf{new}}(k) f_{tpe}$, with $p_{\mathsf{new}}(k)$ as in (3.27). The difference is denoted as $\Delta f(k) = p_{\mathsf{new}}(k) f_{tpe} - \hat{f}_{\mathsf{chat}}(k)$. From Figure 3.4, it can be seen that in the first control strategy, presented in the previous section, the point where Δf crosses the zero axis is calculated (in this case $n_{\mathsf{new}} = 32900$ rpm). Note that $\Delta f(k)60/(p_{new}(k)z)$ is actually the difference between original and new spindle speed setpoint. For the second control strategy the minimum value of the empirically obtained function should be found resulting in a new spindle speed setpoint of $n_{\mathsf{new}} = 33600$ rpm. Both spindle set points are positioned relatively close to each other, which implies that lowering the perturbation vibrations will also result in robust chatter prevention, since the resulting setpoint will also lie near the centre of a lobe. The minimum value of the objective function, as given in Figure 3.4, will be determined via an extremum seeking control like algorithm which will be described in the following section. Note that one of the advantages of applying extremum seeking control, is the fact that the objective function does not need to be known explicitly, since it will be evaluated at each sample instant based on measurements.

3.3.2.1 Control design

As outlined in the previous section, it is in general difficult to determine an analytical relation between the spindle speed and the perturbation vibrations. The model of the milling process, as presented in Chapter 2, could be employed if all disturbances in the milling process would be known and could be accurately modelled, which is in general a harsh operation. Therefore, here an extremum seeking type of controller is designed that will aim to minimise the estimated perturbation vibrations of the mill by adapting the spindle speed. The controller will, therefore, utilise a feedback control scheme to determine the optimal spindle speed that coincides with the minimum value of $S_{\hat{\bar{a}}\hat{\bar{a}}}(\hat{f}_{\mathsf{chat}}(k), \underline{\theta}_u)$ defined in (3.25). The feedback signal is therefore $S_{\hat{\bar{a}}\hat{\bar{a}}}(\hat{f}_{\mathsf{chat}}(k), \underline{\theta}_u)$. The inputs of the controller are the initial spindle speed set point n_0, the PSD $S_{\hat{\bar{a}}\hat{\bar{a}}}(\hat{f}_{\mathsf{chat}}(k), \underline{\theta}_u)$ of $\hat{\bar{a}}(k)$ and the estimated dominant chatter frequency $\hat{f}_{\mathsf{chat}}(k)$. The controller output is the new spindle speed setpoint $n_{\mathsf{new}}(k)$. The desired spindle speed is calculated according to

$$n_{\mathsf{new}}(k) = n_0(1 + \theta_c(k)), \tag{3.30}$$

where $n_{\mathsf{new}} \in [n_{\mathsf{min}}, n_{\mathsf{max}}]$, $\theta_c \in \mathbb{R}$ and n_0 is the initial spindle speed, $\theta_c(k)$ is the controller parameter and where n_{min} and n_{max} represent the minimum and maximum spindle speed of a milling machine. The control objective is to minimise the predefined cost function $J_c(\theta_c)$, defined by $J_c(\theta_c) = \min_{\theta_c} S_{\hat{\bar{a}}\hat{\bar{a}}}(\hat{f}_{\mathsf{chat}}(k), \underline{\theta}_u)$, as function of θ_c. The dependency of objective function J_c on θ_c is introduced by the definition of the new spindle speed in (3.30) and the fact that the objective function J_c implicitly depends on the spindle speed as shown in Figure 3.4. From Figure 3.4, it can be concluded that the selected cost function $J_c(\theta_c)$, as function of the spindle speed, has a (dominant) parabolic shape with a minimum within one lobe. It is therefore reasonable to consider the determination of the minimum value of the cost function with respect to $\theta_c(k)$ as an identification problem and evidently the optimal value for the parameter θ_c (and thus also for the spindle speed n), is defined as $\underline{\theta}_c^o = \arg\min J_c(\theta_c)$. To automatically obtain the optimal θ_c^o at which the cost function has a minimum value, the well-known Normalised Least Means Square algorithm (NLMS) [66] is used. The properties of the NLMS algorithm are already outlined in Section 3.2.3. The control algorithm is given by (3.30) with the following adaptation law:

$$\theta_c(k+1) = \theta_c(k) - 2\alpha_c \frac{\sqrt{S_{\hat{\bar{a}}\hat{\bar{a}}}(\hat{f}_{\mathsf{chat}}(k), \underline{\theta}_u)}}{\epsilon_0 + |\upsilon(k)|} \mathrm{sign}(\Delta f(k)), \tag{3.31}$$

where $\Delta f(k) = p_{\mathsf{new}}(k) f_{tpe}(k) - \hat{f}_{\mathsf{chat}}(k)$, $\epsilon_0 = 1 \cdot 10^{-12}$ to prevent for dividing by zero in case of singularity in $\upsilon(k)$, with initial condition $\theta_c(0) = 0$ and $\upsilon(k)$

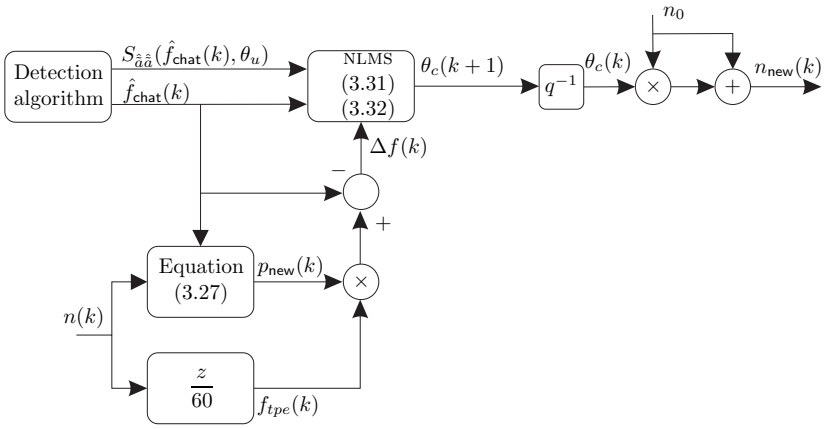

Figure 3.5: Schematic overview of the adaptive chatter controller.

the exponential moving average of $S_{\hat{\tilde{a}}\hat{\tilde{a}}}(\hat{f}_{\mathsf{chat}}(k), \underline{\theta}_u)$ given by

$$\upsilon(k) = (1-\eta_c)\upsilon(k-1) + \eta_c S_{\hat{\tilde{a}}\hat{\tilde{a}}}(\hat{f}_{\mathsf{chat}}(k), \underline{\theta}_u), \tag{3.32}$$

with initial condition $\upsilon(0) = 0$, η_c the smoothing factor, α_c a tuneable parameter that determines the step size, $S_{\hat{\tilde{a}}\hat{\tilde{a}}}(\hat{f}_{\mathsf{chat}}(k), \underline{\theta}_u)$ the time-varying PSD of $\hat{\tilde{a}}(k)$ at the chatter frequency $\hat{f}_{\mathsf{chat}}(k)$ (see (3.25)) and $p_{\mathsf{new}}(k)$ as defined in (3.27). A schematic overview of the proposed controller is given in Figure 3.5.

3.3.3 Properties of the control strategies

For both control strategies, as presented in the previous sections, it is assumed that the initial working point is stable. Due to (slowly) varying process conditions, such as e.g. changing temperature in the milling spindle, the initial working point may become unstable and a control action should be invoked.

The first control strategy outlined in Section 3.3.1 calculates a new spindle set point and overrides the internal controller of the milling machine without directly measuring the performance of the milling process. However, the status of the process is indirectly obtained via the chatter detection procedure and the spindle speed setpoint is updated as long as onset of chatter is occurring. Since the spindle speed setpoint is explicitly based on the estimated chatter frequency, an error in the parameters of the chatter detection error influences the quality of this strategy. The new setpoint will introduce a step-wise change in the setpoint for the HSM's spindle speed controller and the performance will therefore strongly depend on the internal spindle speed controllers of the HSM and the dynamic behaviour of the closed-loop spindle system. Note that

Table 3.1: Parameters of the identification algorithms given by Equations (3.17) and (3.23).

α [-]	η [-]	$\mathbf{R}_e$ [-]	R_w $[m^2 s^{-4}]$
0.5	0.9995	$3 \cdot 10^{-5}\mathbf{I}$	$8 \cdot 10^{-4}$

the HSM milling machine has suitable internal controllers and an optimised trajectory generator.

The main objective of the second control strategy outlined in section 3.3.2 is to lower the perturbation vibrations by finding the optimal spindle speed. The adaptive proportional controller calculates iteratively the optimal spindle speed trajectory using a feedback scheme. In fact the algorithm represents a trajectory generator for the HSM's spindle speed controller. The control parameters α_c and η_c should be tuned such that the controller is insensitive for time delay in the HSM's control system. The parameter values have to be tuned during the experiments. For time-varying delays in the machine's control system, the value of α_c should chosen quite conservatively (i.e. $\alpha_c < 1$), which can lead to deterioration in the settling time of the control action. In the second control strategy, the new setpoint is implicitly based on the estimated parameters of the chatter detection algorithm. This makes the second spindle speed selection algorithm less sensitive to errors in the chatter detection process.

3.4 Experiments

Experiments have been performed to test the detection and control method in practice. All experiments are performed on a Mikron HSM 700 milling machine. The acceleration is measured at the non-rotating part of the spindle near the lower spindle bearing using an accelerometer, type Brüel & Kjær 4382. The detection and control algorithms are implemented on a dSpace system with a sample time of $T_s = 1 \cdot 10^{-4}$ s. The parameters of the recursive identification algorithms, described in Section 3.2, determined for the experiments are listed in Table 3.1. All cuts have been made in aluminium 6082 using a Jabro Tools JH421 cutter (2 flute cutter with a diameter of 10 mm and length of 57 mm) mounted in a Kelch HSK40 shrink-fit holder. Firstly, experiments are performed to validate the detection method experimentally (Section 3.4.1). Secondly, experimental results for the two control strategies are presented (Section 3.4.2).

3.4.1 Detection

Experiments have been performed to validate the detection method experimentally. First, a detection criterion has to be selected, i.e. a detection variable in

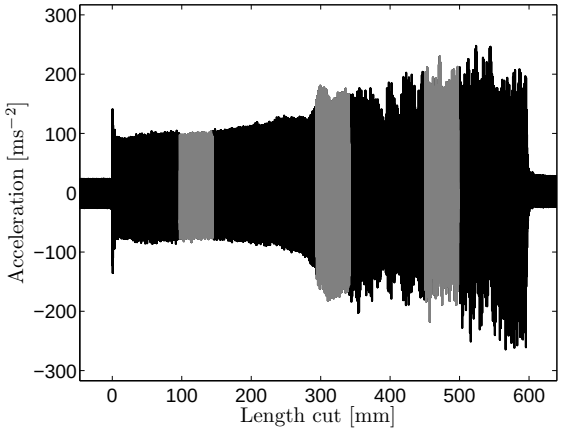

(a) Acceleration.

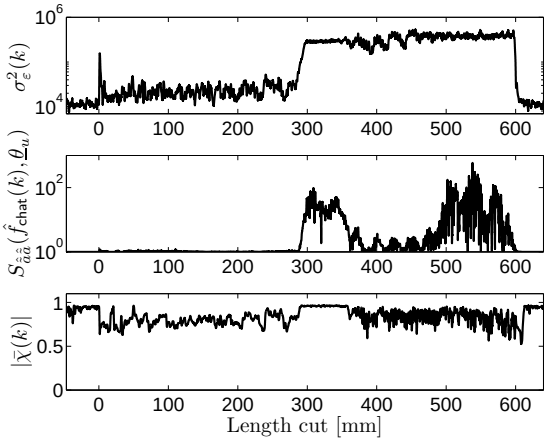

(b) Detection variables.

Figure 3.6: Experimental results of chatter detection method. Chatter is first detected after 288 mm. The grey colouring in Figure 3.6(a) is explained in the caption of Figure 3.7.

---

combination with a threshold. In Section 3.2.4, three possible detection variables were described, namely 1) variance of the estimation error ε in (3.8) of the first prediction scheme $\sigma_\varepsilon^2(k)$, 2) $S_{\hat{a}\hat{a}}(\hat{f}_{\mathsf{chat}}(k), \underline{\theta}_u)$, the PSD of $\hat{a}(k)$ at the estimated dominant chatter frequency $\hat{f}_{\mathsf{chat}}(k)$ and 3) the absolute value of the dominant root $\bar{\chi}(k)$ of $D(q, \underline{\theta}_u)$.

To validate the effectiveness of these detection variables, the experimental

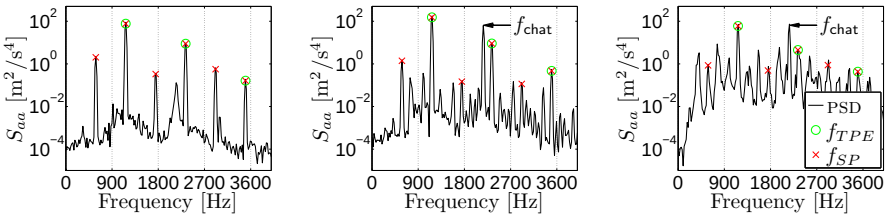

(a) No chatter. (b) Onset of chatter. (c) Full grown chatter.

Figure 3.7: Power spectral densities for three parts of the measured acceleration as indicated in grey in Figure 3.6(a).

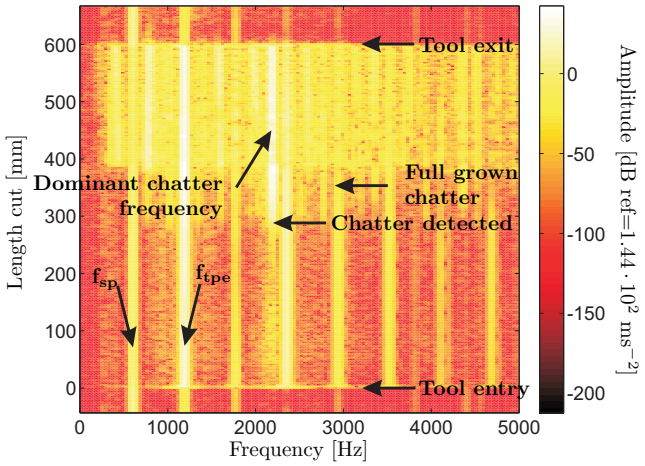

Figure 3.8: Spectrogram of the measured acceleration at the lower spindle bearing. Brighter colours represent a larger magnitude of the frequency component.

results obtained using these detection variables are compared to the surface of the workpiece (by inspection of the workpiece surface, the occurrence of chatter can be determined a posteriori).

A full immersion cut has been made at a spindle speed of 35000 rpm where the axial depth of cut increases from 2.0 to 3.0 mm over a length of 600 mm, which results in the occurrence of chatter during the cut. In Figure 3.6, the acceleration measured at the lower spindle bearing and the three detection variables are depicted. From Figure 3.6(b), it can be seen that the variance $\sigma_\varepsilon^2(k)$ increases upon tool entering. The entering of a tool in the material can be seen as an impulse excitation in the force acting on the tip of the mill. This implies that next to spindle speed frequencies also other frequencies are

present in the acceleration signal. These other frequencies are not predicted by the first prediction scheme and therefore the estimation error of the first prediction scheme $\varepsilon(k)$ increases. After tool impact the variance decreases again. At approximately 288 mm a significant increase is seen in the variance. By inspection of the workpiece, see Figure 3.9, it can be seen that the first chatter marks are visible around 293 mm. Hence, the increase in the detection signal indicates the occurrence of the *onset* of chatter, as is expected. The variance of the estimation error of the first prediction scheme does not decrease and holds approximately the same value, which reflects the marks seen on the workpiece surface, indicating the occurrence of (the onset of) chatter.

When considering the second detection variable, i.e. the PSD function of $\hat{\tilde{a}}(k)$ at the dominant chatter frequency denoted by $S_{\hat{\tilde{a}}\hat{\tilde{a}}}(\hat{f}_{\mathsf{chat}}(k), \underline{\theta}_u)$, no significant increase in the detection signal is seen upon tool entering. This can be clarified by realising that the detection signal is calculated at a single frequency, i.e. the estimated dominant chatter frequency $\hat{f}_{\mathsf{chat}}(k)$. As with the first detection variable, a significant increase in the detection signal is seen at approximately 288 mm indicating the onset of chatter as described above. However, after this increase, a subsequent decrease in the detection signal occurs. This can be explained as follows. By further increasing the depth of cut, the milling process becomes unstable. This implies that the roots of the estimated perturbation model will move further away from the unit circle resulting in a decrease of $S_{\hat{\tilde{a}}\hat{\tilde{a}}}(\hat{f}_{\mathsf{chat}}(k), \underline{\theta}_u)$. So, after the detection signal crosses a user-defined threshold and chatter is said to occur, the signal will become smaller than the threshold and chatter is no longer detected. This is not in agreement with the marks on the workpiece as can be seen in Figure 3.9.

The third detection variable, i.e. the absolute value of the dominant root $\bar{\chi}(k)$ of $D(q, \underline{\theta}_u)$, $|\bar{\chi}(k)|$ varies between zero and one. Before tool entering the value of the detection variable lies close to one, indicating that the system is close to instability. However, this is not the case, since the tool is not yet in cut. When the rotating tool is not in cut, only spindle speed related frequencies are present in the acceleration signal. These are filtered out by the first prediction scheme. Therefore, the perturbation signal is a broad-band signal and the assumption that the regenerative effect is a narrow-band signal does not hold. Consequently, the estimation of the perturbation signal becomes unstable (but bounded due to the fact that the poles are reflected along the unit disk, as explained in Section 3.2.4). When the tool enters the material, a drop in the detection signal, $|\bar{\chi}(k)|$, is seen. This can be explained by realising that in practice the regenerative effect already is present in the measured acceleration spectrum. Consequently, the spectrum of the perturbation signal contains one or more frequencies not coinciding with a spindle speed harmonic. Then, the assumption that the perturbation signal (modelled by $\tilde{a}(k)$) is a narrow-banded signal is valid and the identification process will be able to estimate the parameters of the perturbation model $\hat{\tilde{a}}(k)$. The fact that this is indeed the case is

visualised in the spectrogram in Figure 3.8 where the Fourier transform of the measured acceleration signal $a(k)$ is given as a function of the cutting length. It can be seen that already an extra frequency, i.e. a frequency that does not coincide with a spindle speed related frequency, is present in the acceleration signal just after tool impact, although this frequency contribution is very small in amplitude. Hence, the perturbation signal $\tilde{a}(k)$ is a narrow-band signal and the detection algorithm is able to estimate the perturbation motions. As in the other two detection variables, at approximately 288 mm a (small) increase is seen in the detection signal (see plot for $\bar{\chi}(k)$ in Figure 3.6(b)). Although the dominant root $|\bar{\chi}(k)|$ shows an increase in amplitude during onset of chatter, the signal is noisy and it would not be easy to determine a robust detection threshold. When the depth of cut is further increased, the unstable poles of $D(q, \underline{\theta}_u)$ are reflected inside the unit circle, as described in Section 3.2.4, which results in a decrease in the detection signal.

Based on the discussion above, the variance of the estimation error of the first prediction scheme, $\sigma^2_{\varepsilon}(k)$ is taken as detection signal. Although multiple variables can be combined into one detection quantity, the single variable (estimation error of the first prediction scheme) performed satisfactorily for all experiments. By setting the detection threshold to $\sigma^2_{\varepsilon,0} = 6.678 \cdot 10^4$ [m^{2}s^{-4}], chatter is detected after cutting approximately 288 mm of material. For automatic control it is desirable to select the threshold automatically. One way to do so would, for example, be to select the threshold based on amplitude of the first spindle speed harmonic. The automatic selection of algorithm parameters is an extensive topic for further research and is therefore not considered here in further detail.

Resuming, it can be said that all three detection variables perform well in case of a stable milling operation and, moreover, during onset of chatter. This justifies the application of the peak value of the PSD of the estimated perturbation vibrations $\hat{\tilde{a}}(k)$ at the chatter frequency and the roots of $D(q, \underline{\theta}_u)$ in the second control strategy that is presented in Section 3.3.2.

In Figure 3.7, the power spectral density of the measured acceleration is given for the three stages of the development of chatter as described in Section 2.8. From Figure 3.7(a) it can be seen that when no chatter is occurring, the dominant frequencies in the frequency spectrum of the measured acceleration signal only consists of spindle speed related frequencies. When onset of chatter occurs, which is detected by the chatter detection algorithm, the frequency spectrum of the measured acceleration signal consists of spindle speed related frequencies and the dominant chatter frequency, see Figure 3.7(b). In the case of full grown chatter (Figure 3.7(c)), the frequency spectrum consists of spindle speed related frequencies and chatter frequencies f_C.

In Figure 3.8, a spectrogram of the acceleration signal is shown. The spindle-speed and tooth-passing related frequencies can clearly be distinguished from the spectrogram. Furthermore, when chatter is detected after 288 mm,

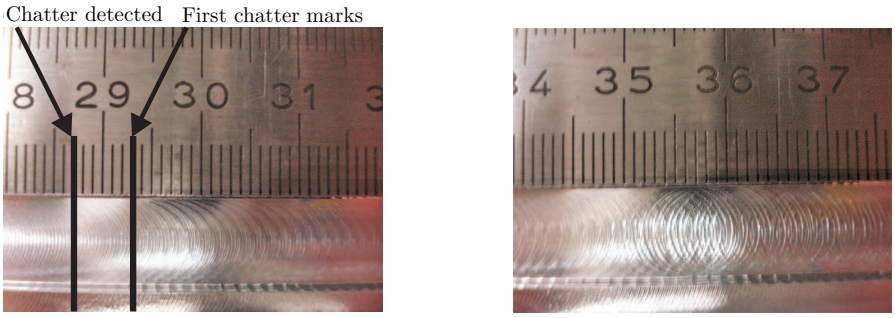

(a) from 280 to 320 mm.

(b) from 340 to 375 mm.

Figure 3.9: Detail of the workpiece for a single cut without control at a spindle speed of 35000 *rpm with increasing depth of cut from* 2.0 *to* 3.0 *mm.*

only the dominant chatter frequency is present in the frequency spectrum next to the spindle-speed related frequencies. At approximately 360 mm chatter is fully grown. It can be seen that at that moment all chatter frequencies are present in the frequency spectrum.

In Figure 3.9, top views of the resulting workpiece are depicted. It can be seen that at the moment chatter is detected no clear chatter marks are visible on the workpiece. The first (small) chatter marks appear at 293 mm. From Figure 3.9(b), it can be seen that chatter is fully grown at 352 mm. Hence, it can be concluded that the results of the detection method in Figure 3.6 coincide very well with the path that is left behind by the cutter. Furthermore, it can be seen that chatter is detected in a very early stage (even before chatter marks are visible on the workpiece). Consequently, once the onset of chatter is detected there is still time to control the spindle speed away from the chatter instabilities.

3.4.2 Control

In order to apply the control strategies presented in Section 3.3, the hand terminal of the Mikron HSM 700 is modified such that the feed override and spindle speed override can be controlled using an external electric potential. This means that the spindle speed can be changed within an interval ranging from 50% to 120% of the initial spindle speed n_0 and the feed can be modified within an interval ranging from 0% to 100% of the initial feed. Hence, using this particular setup, it is not possible to increase the spindle speed while maintaining a constant chip load. Therefore, when the spindle speed in increased, the chip load decreases with maximally 20%. Since the initial chip load is set to

0.2 mm/tooth, the minimal chip load is 0.16 mm/tooth, which is still sufficient for cutting aluminium. One major disadvantage of using the override as control input is the possibly large time-delay between control input and actuation moment, due to a generally lower priority that is assigned to override control in the HSM's control system. For this typical milling machine it is determined that the delay varies between $40 - 70$ ms. The presence of such delay may adversely affect the control performance.

In Figure 3.10, the results are depicted for a full immersion cut where the depth of cut is increased from 2.0 to 3.0 mm with an initial spindle speed of 35000 rpm. The total path length is 600 mm which is cut in about 2.6 s. In this way, the process is forced into an unstable region. This can be seen as a worst-case scenario, since the goal of the control strategy is to ensure chatter-free milling for, relatively low-frequent, time-varying changes of the stability lobes diagram. The same cut is repeated two times. The first cut is performed using controller strategy 1 (Section 3.3.1) whereas the second cut is made using control strategy 2 (Section 3.3.2). The parameters for the second control strategy are chosen as $\alpha_c = 0.7$ and $\eta_c = 0.3$.

In the Figures 3.10(a) and 3.10(b), the measured acceleration is depicted together with the sign of $\Delta f(k) = p_{\mathsf{new}}(k) f_{tpe}(k) - \hat{f}_{\mathsf{chat}}(k)$, which indicates the direction in which the spindle speed should be changed. The variance σ_ε^2 of $\varepsilon(k)$ (i.e. the detection signal) is depicted in Figures 3.10(c) and 3.10(d). As can be seen, chatter is detected just before a major increase of the acceleration is observed (compare Figures 3.10(c) and 3.10(d) with 3.10(a) and 3.10(b)). This implies that chatter is detected during its onset and before the workpiece is damaged as is already shown in Section 3.4.1. The spindle speed and the spindle speed setpoint provided by the controllers are shown in Figures 3.10(e) and 3.10(f). When the variance σ_ε^2 exceeds the threshold, the cut is marked as exhibiting chatter. As described in the previous section, an increase in the detection signal $\sigma_\varepsilon^2(k)$ is seen when the tool enters the material. However, the response due to tool entering is damped out relatively fast and therefore no control action is induced. When chatter is detected, a new setpoint for the spindle speed is computed and sent to the spindle speed override function of the hand terminal. In this particular case, a decrease in spindle speed is desired. It can be seen that the setpoint of the first control strategy overshoots the eventual setpoint. This is due to, firstly, delay in the control system and, secondly, the fact that the chatter frequency differs at different spindle speed. In order to prevent high-frequent oscillation of the setpoint, due to changes in $\mathrm{sign}(\Delta f(k))$, a low-pass filter is added to the estimated chatter frequency.

After the setpoint is reached, for both control strategies, the cut remains stable even when the depth of cut is increased further. It can be observed that it takes some time for the spindle speed to reach the setpoint. The settling time of the closed-loop spindle system is due to: 1) delay in the controller of the Mikron HSM700 (typically between 40 and 70 ms) and 2) the large inertia

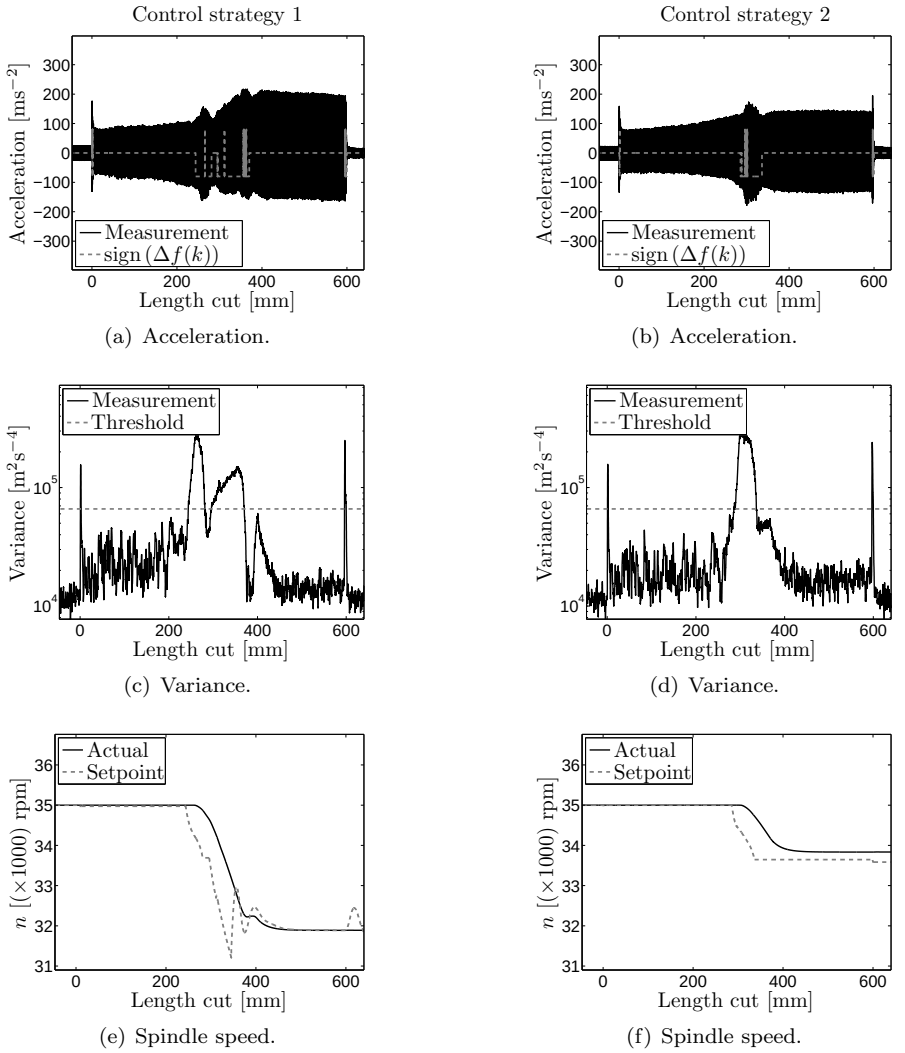

(a) Acceleration. (b) Acceleration.

(c) Variance. (d) Variance.

(e) Spindle speed. (f) Spindle speed.

Figure 3.10: Experimental results of the control strategies for a cut at 35000 rpm with increasing a_p from 2.0 to 3.0 mm in 2.6 s. Left figures: control strategy 1; right figures: control strategy 2.

of the spindle in combination with the standard spindle-speed controller of the Mikron HSM700 which is not specifically tuned for tracking relatively fast changes in spindle-speed. The setpoint that is computed by control strategy 1 varies rapidly as is depicted in Figures 3.10(e). In order to decrease the

variation of the setpoint, the cut-off frequency of the low-pass filter can be lowered. However, the actual spindle speed does not have these large variations due to the relatively low bandwidth of the closed-loop spindle system. The spindle speed is adjusted smoothly towards the chatter-free area. However, a mismatch between the setpoint and actual spindle speed for the second control strategy is seen. This is probably due to lack of integral control of the internal spindle speed controller of the milling machine.

As can be seen in Figure 3.10(a), the amplitude of the acceleration at the end of the cut is about 200 m/s^2 in case control strategy 1 is chosen. For the case where the control strategy 2 is switched on, the amplitude of the acceleration is about 145 m/s^2 (see Figure 3.10(b)). When the controller is switched off the acceleration signal is very noisy with spikes up to 260 m/s^2 (see Figure 3.6). Therefore, using the controller, the acceleration at the spindle bearing is decreased and is even further decreased when control strategy 2 is used (compare Figure 3.10(a) and 3.10(b)). Although, the amplitude of the accelerations with and without control do not differ that much, the frequency spectrum is totally different. This can be seen from Figure 3.11, where the measured acceleration signal, for each control strategy, is shown in a spectrogram. In case the controller is switched off, the frequency spectrum consists of spindle speed related frequencies and chatter frequencies, see Figure 3.8. However, it can clearly be seen that no chatter frequencies are visible in the frequency spectrum of the acceleration in case the controllers are switched on. Note that the dominant chatter frequency is visible during the spindle speed transition. This is mainly due to the delay in the internal spindle speed controllers of the milling machine. However, the dominant chatter frequency disappears from the acceleration spectrum before full grown chatter is to occur. By using control strategy 1, the second harmonic of the new tooth passing frequency f_{tpe} is set to the dominant chatter frequency (which is clearly visible in Figure 3.11(a)). From the spectrogram of the measured acceleration for the second control strategy (Figure 3.11(b)) it can be seen that (a higher harmonic of) tooth passing frequency does not coincide with the dominant chatter frequency.

In Figure 3.12, the results, for the case where the controllers are switched on, are shown in the spindle-speed/depth-of-cut parameter space. Here, the cut moves from a low to a higher value for the depth of cut. It can be seen that for both control strategies the controller ensures that the working point moves away from instability and ensures a stable cut.

Pictures of a detail of the workpiece are shown in Figure 3.13. For sake of clarity also a picture of a cut with the controller switched off is shown. Clearly, when the controller is switched off, the wall of the workpiece is nonsmooth, whereas the wall of the workpiece remains smooth when the controller has been switched on. When the controller is switched on, no chatter marks can be seen on the workpiece after the setpoint has been reached. Some (small) chatter marks appears on the workpiece. As described before, this is due to the

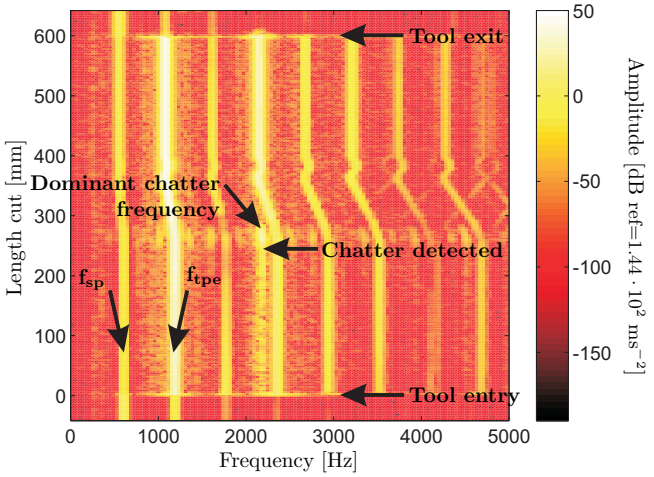

(a) Control strategy 1.

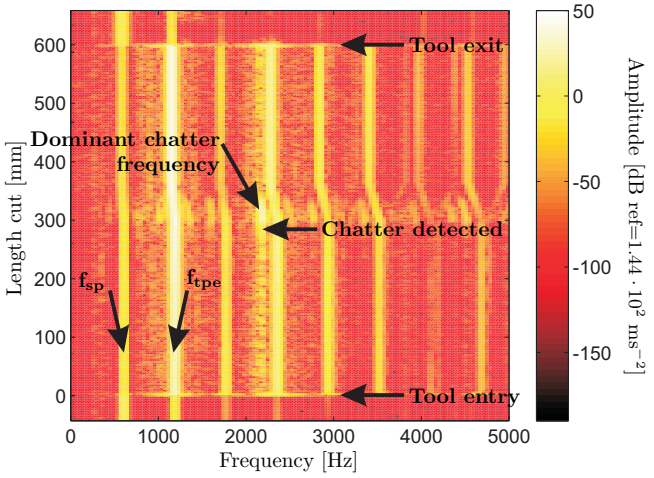

(b) Control strategy 2.

Figure 3.11: Spectrogram of the acceleration measured at the lower spindle bearing for both control strategies.

relatively large time-delay present in the control system of the milling machine. Furthermore, the spindle speed is changed in an online fashion, while the milling continues (i.e. the feed remains nonzero). If the feed would have been stopped, this would have led to a significant increase of production time.

Hence, it can be concluded that the proposed control strategies work in practice. The control strategies ensure stable working points while the feed re-

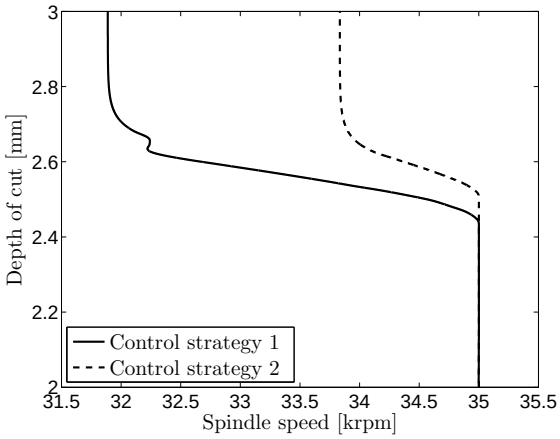

Figure 3.12: Results of the experiments with the controllers switched on.

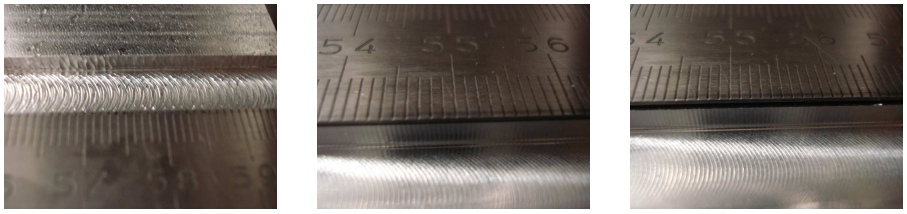

(a) Control off. (b) Control strategy 1. (c) Control strategy 2.

Figure 3.13: Detail of the workpiece with and without chatter control. The depth of cut is increasing from 2.0 to 3.0 mm and the spindle speed is 35000 rpm.

mains nonzero. Moreover, the detection and control algorithms are fast enough to be used at high spindle speeds.

3.5 Discussion

In this chapter, two control strategies are presented that guarantee chatter-free high-speed milling operations by automatic adaptation of spindle speed and feed (i.e. the feed is not stopped during the spindle speed transition). In this way, the high-speed milling process will remain stable despite possible changes in the process, e.g. due to heating of the spindle, tool wear, etc. The first control strategy eliminates chatter by setting the tooth passing frequency equal to the dominant chatter frequency. The goal of the second chatter control strategy

is to minimise the total chatter vibrations by spindle speed adaptation. For both control strategies an accurate and robust chatter detection algorithm is required. Therefore, this chapter presents a novel chatter detection algorithm that automatically detects chatter in an online fashion and in a pre-mature stage, such that no chatter marks are visible on the workpiece yet when it is detected. Experimental results show that by using the control strategies chatter-free machining is ensured. It is shown that the detection algorithm is indeed able to detect chatter before it is fully developed. Furthermore, both control strategies ensure that chatter is avoided, thereby ensuring robust machining and a high surface quality. Furthermore, where the first control strategy only ensures the avoidance of chatter, the second control strategy also minimises the chatter vibrations.

To improve the results even further, firstly, the control action should be introduced directly to the internal spindle speed controller of the HSM, instead of via the hand terminal, such that the delay in the controller is minimised. Secondly, the internal spindle speed controller of the HSM should be tuned properly, to be able to improve the tracking of the desired spindle speed setpoints.

Moreover, the tuning of the presented detection and control strategy is machine specific. To even further enhance practical applicability (for entire machine parks), it is foreseen that automatic tuning, e.g. exploiting recent work on identification methods based on recursive lattice predictors as presented in [39], will be beneficial.

Finally, while in this chapter the chatter detection procedure is used for chatter control purposes, the strategy can also be used for the efficient, in-process experimental determination of stability lobes diagrams. In this way, the effect of modelling inaccuracies in the milling model on model-based stability lobes diagrams can be overcome.

4

Active chatter control design using μ-synthesis

4.1 Introduction

As described in the Chapter 1, it is preferable to be able to shape the stability lobes diagram (SLD) such that the efficiency (i.e. the material removal rate (MRR)) of the milling process can be increased, while ensuring chatter-free milling operations. In this chapter, an active chatter controller design methodology for the high-speed milling process is presented, which can guarantee chatter-free cutting operations in an a priori defined range of process parameters such as spindle speed and depth of cut. The methodology developed in this chapter is based on a robust control approach using μ-synthesis. Hereto, the most important process parameters (depth of cut and spindle speed) are treated as uncertainties. Next to uncertainties in the process parameters, an additional uncertainty in the spindle dynamics will be taken into account in the controller design. In this way, for example, the effect of changing bearing stiffness as function of the the spindle speed, which typically seen in milling spindles [1, 50], can be taken into account.

In Figure 4.1, a schematic overview of the active chatter control procedure approach can be found. The dashed box, given in the figure, indicates the area of working points which should be stabilised by a controller (i.e. the working points that should result in chatter-free milling operations). The controller

The work presented in this chapter is partly discussed in [33] and [34]

should then be designed such that it alters the SLD such that the area of desired working points becomes stable. The newly obtained SLD is given by the light grey area.

Note that the control goal in this chapter is entirely different from the one in Chapter 3. In Chapter 3, the goal was to make the milling process robust (in the sense of avoiding chatter) for changing process conditions by automatically detecting chatter and adapting spindle speed and feed. However, the control strategy proposed in Chapter 3 is unable to alter the SLD and hence did not attain an increase in milling efficiency. As outlined above, the goal of the control strategy in this chapter is exactly the adaptation of the SLD by feedback in order to make working points of higher MRR feasible while avoiding chatter.

The chapter is organised as follows. Section 4.2 presents the problem statement of the active chatter control problem. Then, Section 4.3 describes the selection of an appropriate feedback signal for control. The nonlinear, time-varying DDE model of the milling process as presented in Chapter 2 cannot be directly used in the robust controller design procedure. Therefore, in Section 4.4 some model simplifications will be discussed in order to construct a model suitable for controller design using μ-synthesis techniques. Section 4.5 presents the robust control design procedure. Results of the proposed strategy, when applied to illustrative examples, are presented in Section 4.6. In the examples, for illustrative purposes, relatively simple models of the spindle-toolholder-tool and actuator dynamics will be considered. In Chapter 6, controllers will be designed considering the full complexity of an experimental setup. Note that, as opposed to the discussion in the previous chapter, the spindle dynamics is considered as time-invariant throughout the remainder of this thesis. Finally, a discussion of the presented results will be given in Section 4.7.

4.2 Problem statement

Consider the nonlinear time-varying delay differential equations (DDE) describing the dynamics of the milling process, as presented in Equation (2.13) in Chapter 2, given as follows:

$$\begin{aligned}\dot{\underline{x}}(t) = \mathbf{A}\underline{x}(t) + \mathbf{B}_t a_p \sum_{j=0}^{z-1} g_j\big(\phi_j(t)\big)\Bigg(\Big(h_{j,\mathsf{stat}}(t) + \\ \big[\sin\phi_j(t)\ \ \cos\phi_j(t)\big]\,\mathbf{C}_t\big(\underline{x}(t) - \underline{x}(t-\tau)\big)\Big)^{x_F}\mathbf{S}(t)\begin{bmatrix}K_t\\K_r\end{bmatrix}\Bigg) \\ + \mathbf{B}_a\underline{F}_a(t), \quad \underline{v}_a(t) = \mathbf{C}_a\underline{x}(t),\end{aligned} \tag{4.1}$$

with $\underline{F}_a(t)$ the forces generated by the actuator that are acting at the spindle and $\underline{v}_a(t)$ the displacements measured at some position on the spindle, which are available for feedback, see also Figure 4.2. Recall that, as described in

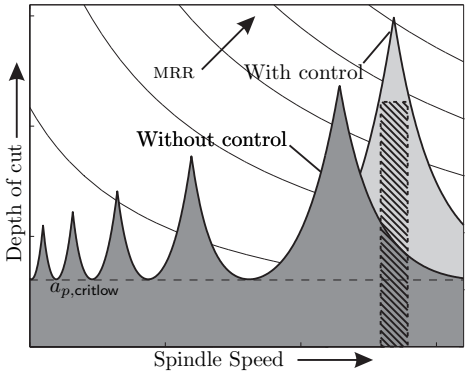

Figure 4.1: Schematic representation of the active chatter control procedure. A controller should be designed which stabilises the dashed area, such that the SLD *with active chatter control encloses the desired area of working points. Moreover, lines with a constant material removal rate (*MRR*) are shown.*

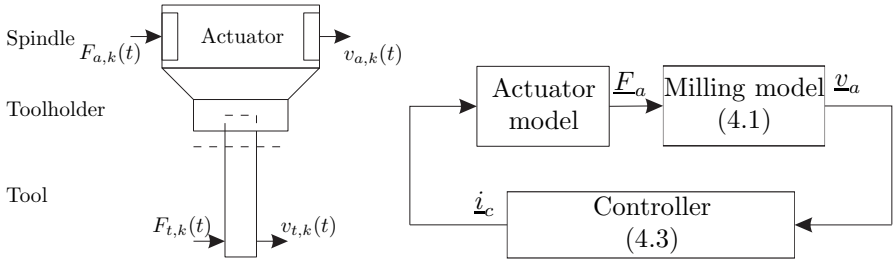

(a) Spindle dynamics. (b) Block diagram.

Figure 4.2: Schematic overview of spindle dynamics and block diagram of the closed-loop milling process.

Chapter 2, the stability lobes diagram (SLD) is determined using the model which describes the perturbation vibrations about the periodic solution of the milling process. Therefore, the controller design, as presented in this chapter, will be based on the model which is linearised about the periodic solution with uncertainties in depth of cut a_p and spindle speed n which results in an uncertainty in the delay τ. Moreover, chatter is defined as the loss of stability of this periodic solution and stability of the milling process is based on the stability of the model describing the perturbations of the milling process around the periodic solution. Using the decomposition $\underline{x}(t) = \underline{x}^*(t) + \tilde{\underline{x}}(t)$, with the periodic solution $\underline{x}^*(t)$ and the perturbation $\tilde{\underline{x}}(t)$, the linearised uncertain

model of the milling process can then be given as follows:

$$\begin{aligned}\dot{\underline{\tilde{x}}}(t) &= \mathbf{A}\underline{\tilde{x}}(t) + a_p\mathbf{B}_t\sum_{j=0}^{z-1}\mathbf{H}_j(t)\mathbf{C}_t(\underline{\tilde{x}}(t)-\underline{\tilde{x}}(t-\tau)) + \mathbf{B}_a\underline{\tilde{F}}_a(t),\\ \underline{\tilde{v}}_a(t) &= \mathbf{C}_a\underline{\tilde{x}}(t),\end{aligned} \tag{4.2}$$

with uncertainty sets $a_p \in [0, \bar{a}_p]$ and $\tau \in [\underline{\tau}, \bar{\tau}]$ and $\mathbf{H}_j(t)$ as given by (2.17). Herein, similar to the decomposition of the state vector, the following decomposition of the vector of actuator forces is used; $\underline{F}_a(t) = \underline{F}_a^*(t) + \underline{\tilde{F}}_a(t)$. More detail about the decomposition of the actuator forces will be discussed in Section 4.3. The aim of this chapter is to design a finite-dimensional linear controller $\mathbf{K}$, which guarantees:

- robust stability of the milling process (4.2) for the given uncertainties in depth of cut a_p, time delay τ, and possible uncertainty in the spindle dynamics;
- performance by minimising the total amount of actuator energy needed to stabilise the uncertain milling process.

The controller design will be employed for both the linear actuator model as well as the AMB actuator model which relates the current commands $\underline{i}_c(t)$, generated by the controller, to forces $\underline{F}_a(t)$ acting at the spindle, as presented in Section 2.5. As described in Chapter 1, an AMB is a common type of actuator applied to rotor dynamic systems and in [83] feasibility of using such actuator in the scope of high-speed milling has been shown. This motivates to pay special attention to this kind of actuator (model).

Hereby, it is assumed that the controller $\mathbf{K}$, with controller input $\underline{y}(t) \in \mathbb{R}^2$ and output current $\underline{i}_c \in \mathbb{R}^2$, has the following state-space description,

$$\begin{aligned}\dot{\underline{\xi}}(t) &= \mathbf{A}_c\underline{\xi}(t) + \mathbf{B}_c\underline{y}(t),\\ \underline{i}_c(t) &= \mathbf{C}_c\underline{\xi}(t) + \mathbf{D}_c\underline{y}(t).\end{aligned} \tag{4.3}$$

Herein, $\underline{\xi} \in \mathbb{R}^{n_c}$, $\mathbf{A}_c \in \mathbb{R}^{n_c\times n_c}$, $\mathbf{B}_c \in \mathbb{R}^{n_c\times 2}$, $\mathbf{C}_c \in \mathbb{R}^{2\times n_c}$ and $\mathbf{D_c} \in \mathbb{R}^{2\times 2}$ with n_c the order of the controller. The choice of the controller input signal $\underline{y}(t)$ will be discussed in Section 4.3. The linearised uncertain model of the milling process, given by (4.2), cannot be directly used in the standard robust controller design procedure. Therefore, after discussing the selection of the controller input signal $\underline{y}(t)$, two model simplifications will be presented in Section 4.4 such that the infinite-dimensional time-varying model (4.2) is transformed into a finite-dimensional linear time-invariant (LTI) model. In this way, the model can be used in a robust control design procedure, which will be presented in Section 4.5.

4.3 Controller input signal

An important part of any control system is the choice of the feedback signal used for control.

From the discussion in Section 2.7 it becomes clear that the nominal solution of the milling model is periodic with period time τ. Moreover, chatter is defined as the loss of stability of this periodic solution and stability of the milling process is based on the stability of the model describing the perturbations of the milling process around the periodic solution. Then, two possibilities arise in selecting the feedback signal which serves as an input to the controller $\mathbf{K}$, namely:

1. full output feedback, i.e. the total (measured) displacements $\underline{v}_a(t)$ are used for feedback;

2. perturbation feedback, i.e. the perturbation (chatter) vibrations $\tilde{\underline{v}}_a(t) = \underline{v}_a(t) - \mathbf{C}_a\underline{x}^*(t)$ are used as feedback signal, where $\underline{x}^*(t)$ denotes the periodic solution of the nominal model given by (4.1).

In Section 4.5, the design of a linear dynamic output feedback control law characterised by the transfer function $\mathbf{K}(s)$ and with a state-space description as defined in (4.3), is pursued. Next, the controller input signal $\underline{y}(t)$ will be denoted as

$$\underline{y}(t) = \underline{v}_a(t) - c\underline{v}_a^*(t) \tag{4.4}$$

where $\underline{v}_a^*(t) = \mathbf{C}_a\underline{x}^*(t)$ is the periodic solution at the measured output. Moreover, c is a constant indicating whether full output ($c = 0$) or perturbation feedback ($c = 1$) is applied.

The implication of the choice for either one of the two controller input signals will be demonstrated next for the actuator models as presented in Section 2.5.

4.3.1 Controller input signal: linear actuator model

It can easily be shown that the stability properties of the closed loop, in case of the linear actuator model $\underline{F}_a(t) = \mathbf{K}_a\underline{i}_c(t)$, presented in Section 2.5, are the same for both choices of the feedback signal (either $c = 0$, or $c = 1$ in (4.4)).

First, it will be shown that the chatter-free τ-periodic solution $(\underline{x}^*(t), \underline{\xi}^*(t))$ will be different for both choices of the controller input signal. To show this, consider the following decompositions of the state vectors $\underline{x}(t)$ and $\underline{\xi}(t)$:

$$\underline{x}(t) = \underline{x}^*(t) + \tilde{\underline{x}}(t),\ \underline{\xi}(t) = \underline{\xi}^*(t) + \tilde{\underline{\xi}}(t). \tag{4.5}$$

Then, let us combine (4.1) with (4.3) and $\underline{F}_a(t) = \mathbf{K}_a \underline{i}_c(t)$ and substitute $\underline{x}(t) = \underline{x}^*(t)$ and $\underline{\xi}(t) = \underline{\xi}^*(t)$. Using the fact that $\underline{x}^*(t)$ is τ-periodic (i.e. $\underline{x}^*(t) = \underline{x}^*(t-\tau)\ \forall t$), this results in the following closed-loop dynamics:

$$\begin{aligned}\begin{bmatrix}\dot{\underline{x}}^*(t)\\ \dot{\underline{\xi}}^*(t)\end{bmatrix} &= \underbrace{\begin{bmatrix}\mathbf{A}+\mathbf{B}_a\mathbf{K}_a\mathbf{D}_c\mathbf{C}_a(1-c) & \mathbf{B}_a\mathbf{K}_a\mathbf{C}_c\\ \mathbf{B}_c\mathbf{C}_a(1-c) & \mathbf{A}_c\end{bmatrix}}_{\mathbf{A}_{cl}}\begin{bmatrix}\underline{x}^*(t)\\ \underline{\xi}^*(t)\end{bmatrix}\\ &\quad + a_p\begin{bmatrix}\mathbf{B}_t\\ \mathbf{0}\end{bmatrix}\sum_{j=0}^{z-1} g_j\big(\phi_j(t)\big)h_{j,\mathsf{stat}}(t)^{x_F}\mathbf{S}(t)\begin{bmatrix}K_t\\ K_r\end{bmatrix}.\end{aligned} \tag{4.6}$$

It can be seen that the *closed-loop* dynamics governing the periodic solution in (4.6) is a LTI system with a τ-periodic disturbance since both $\mathbf{S}(t)$ and $h_{j,\mathsf{stat}}(t)$ are periodic with τ. Then it can be concluded that when full output feedback is applied (i.e. $c = 0$), with the assumption that $\mathbf{A}_{cl}$ has no eigenvalues at $il2\pi f_{tpe}$, for $f_{tpe} := \frac{1}{\tau}$ and all $l \in \mathbb{Z}$, the solution $\underline{x}^*(t), \underline{\xi}^*(t)$ exists, is unique and is τ-periodic [53]. Note that this solution differs from the periodic solution of the *open-loop* dynamics given in (2.15). The conditions imposed on the eigenvalues of $\mathbf{A}_{cl}$ will in general be satisfied, since the controller has to render the closed-loop system stable also for $a_p = 0$ (i.e. the eigenvalues of $\mathbf{A}_{cl}$ will lie in the open left half plane). However, when $c = 1$, and consequently perturbation feedback is applied, the eigenvalues of $\mathbf{A}_{cl}$ are given by the eigenvalues of $\mathbf{A}$ and $\mathbf{A}_c$. Then, there exists a unique, τ-periodic, solution $\underline{x}^*(t), \underline{\xi}^*(t)$ when $\mathbf{A}$ has no eigenvalues at $il2\pi f_{tpe}$, for $f_{tpe} := \frac{1}{\tau}$, $l \in \mathbb{Z}$, and $\mathbf{A}_c$ has no eigenvalues with real part equal to zero. The conditions imposed on $\mathbf{A}$ will typically be satisfied since, in general, the spindle exhibits damping and is therefore described by an asymptotically stable system. Consequently, under such conditions, in case of perturbation feedback, $\underline{\xi}^*(t) = \underline{0}$ is the only solution of (4.6) satisfying $\underline{\xi}^*(t) = \underline{\xi}^*(t-\tau)\ \forall t$. Therewith, the periodic solution $\underline{x}^*(t)$ of (4.6) becomes equal to the solution of the *open-loop* periodic solution of (2.15). Hence, in case of perturbation feedback (i.e. $\underline{y}(t) = \underline{v}_a(t) - \underline{v}_a^*(t)$) the periodic solution $\underline{x}^*(t)$ will be equal to that of the uncontrolled system (and $\underline{\xi}^*(t) = \underline{0}$, i.e. the nominal control action $\underline{i}_c^*(t) = \mathbf{C}_c\underline{\xi}^*(t) + \mathbf{D}_c\underline{y}^*(t)$ is zero). On the other hand, for full output feedback (i.e. $\underline{y}(t) = \underline{v}_a(t)$) the periodic solution $\underline{x}^*(t)$ will be different from that of the uncontrolled system (and $\underline{\xi}^*(t)$ will in general be non-zero, i.e. the steady-state control action $\underline{i}_c^*(t) = \mathbf{C}_c\underline{\xi}^*(t) + \mathbf{D}_c\underline{y}^*(t) = \mathbf{C}_c\underline{\xi}^*(t) + \mathbf{D}_c\mathbf{C}_a\underline{x}^*(t)$ does not vanish).

Secondly, it can be shown that for both choices of the feedback signal the linearisation of (4.1) with (4.3), and $\underline{F}_a(t) = \mathbf{K}_a\underline{i}_c(t)$, about $\underline{x}^*(t), \underline{\xi}^*(t)$ is given

by

$$\begin{bmatrix}\dot{\underline{\tilde{x}}}(t)\\ \dot{\underline{\tilde{\xi}}}(t)\end{bmatrix} = \begin{bmatrix}\mathbf{A}+\mathbf{B}_a\mathbf{K}_a\mathbf{D}_c\mathbf{C}_a & \mathbf{B}_a\mathbf{K}_a\mathbf{C}_c\\ \mathbf{B}_c\mathbf{C}_a & \mathbf{A}_c\end{bmatrix}\begin{bmatrix}\underline{\tilde{x}}(t)\\ \underline{\tilde{\xi}}(t)\end{bmatrix} + a_p\begin{bmatrix}\mathbf{B}_t\\ \mathbf{0}\end{bmatrix}\sum_{j=0}^{z-1}\mathbf{H}_j(t)\mathbf{C}_t(\underline{\tilde{x}}(t)-\underline{\tilde{x}}(t-\tau)), \tag{4.7}$$

with $\mathbf{H}_j(t)$ as defined in (2.17). Clearly, for both choices of the control input signal, the resulting SLD will be the same (since the perturbation dynamics (4.7) does not depend on the constant c). Moreover, in the case of perturbation feedback ($c = 1$) the nominal control action vanishes in steady-state, which is not the case for full output feedback ($c = 0$). As a result, the choice for perturbation feedback is favourable from the point of view of bounding the control action.

4.3.2 Controller input signal: AMB model

A similar analysis can be performed for the model incorporating the model of an AMB. For an AMB it is important to limit the input current in order not to exceed the maximum amount of carrying force. Therefore, in this work, only perturbation feedback in case of the AMB actuator model will be considered. Namely, as discussed above, in case of perturbation feedback, the required actuator forces are significantly smaller as compared to the full output feedback case, which results in a smaller input current for the AMB. In Section 2.5, a linearised model of a nonlinear AMB model has been discussed. Based on the discussion above, it can be stated that when perturbation feedback is applied, the assumptions, for which the linearisation is a good approximation of the nonlinear AMB model, as discussed in Section 2.5, remain valid. Recall that the linear model of the AMB is given as follows:

$$\underline{F}_a(t) = \mathbf{K}_i\underline{i}_c(t) + \mathbf{K}_s\underline{v}_a(t), \tag{4.8}$$

where

$$\mathbf{K}_i = \operatorname{diag}\big(4k_{\mathsf{amb},x}\frac{i_0}{v_0^2}, 4k_{\mathsf{amb},y}\frac{i_0}{v_0^2}\big), \tag{4.9}$$

$$\mathbf{K}_s = \operatorname{diag}\big(4k_{\mathsf{amb},x}\frac{i_0^2}{v_0^3}, 4k_{\mathsf{amb},y}\frac{i_0^2}{v_0^3}\big). \tag{4.10}$$

Herein, where $k_{\mathsf{amb},k},\ k \in \{x, y\}$ are the specific AMB coefficients, i_0 is the so-called pre-magnetising current (to compensate for gravity, etc.), v_0 the corresponding nominal gap displacement and $\underline{i}_c(t)$ is the controller output (i.e. the input currents to the actuator) and $\underline{v}_a(t)$ the measured bearing displacements.

As before, first the existence of a periodic solution $\underline{x}^*(t)$ with period time τ is proven for the case with the AMB model. Hereto, consider the milling model, given by (4.1), with the AMB model, given in (4.8), and a linear control law, given by (4.3) with $\underline{y}(t) = \underline{\tilde{v}}_a(t)$. When a periodic solution of period τ exists, it holds that $\underline{x}^*(t) = \underline{x}^*(t-\tau)\ \forall t$. Then, in order to prove existence of a periodic solution, substitute $\underline{x}(t) = \underline{x}^*(t)$ into the model, i.e. $\underline{\tilde{x}}(t) = 0$. Consequently, the dynamics governing the periodic solution $(\underline{x}^*(t), \underline{\xi}^*(t))$ can be written as follows:

$$\begin{aligned}\dot{\underline{x}}^*(t) = \mathbf{A}\underline{x}^*(t) + \mathbf{B}_t a_p \sum_{j=0}^{z-1} g_j\big(\phi_j(t)\big) h_{j,\mathsf{stat}}(t)^{x_F} \mathbf{S}(t) \begin{bmatrix} K_t \\ K_r \end{bmatrix} \\ + \mathbf{B}_a \mathbf{K}_i \mathbf{C}_c \underline{\xi}^*(t), + \mathbf{B}_a \mathbf{K}_s \mathbf{C}_a \underline{x}^*(t),\end{aligned} \tag{4.11}$$

$$\dot{\underline{\xi}}^*(t) = \mathbf{A}_c \underline{\xi}^*(t). \tag{4.12}$$

When $\mathbf{A}_c$ has no eigenvalues at the imaginary axis, $\underline{\xi}^*(t) = \underline{0}$ is the only solution of (4.12) satisfying $\underline{\xi}^*(t) = \underline{\xi}^*(t-\tau)\ \forall t$. Substituting $\underline{\xi}^*(t) = \underline{0}$ into (4.11) gives

$$\begin{aligned}\dot{\underline{x}}^*(t) = \big(\mathbf{A} + \mathbf{B}_a \mathbf{K}_s \mathbf{C}_a\big)\underline{x}^*(t) \\ + \mathbf{B}_t a_p \sum_{j=0}^{z-1} g_j\big(\phi_j(t)\big) h_{j,\mathsf{stat}}(t)^{x_F} \mathbf{S}(t) \begin{bmatrix} K_t \\ K_r \end{bmatrix}.\end{aligned} \tag{4.13}$$

Since the $h_{j,\mathsf{stat}}(t)$ and $\mathbf{S}(t)$ are periodic with period time τ, and $\mathbf{A} + \mathbf{B}_a \mathbf{K}_s \mathbf{C}_a$ has in general no eigenvalues at $il2\pi f_{tpe}$, $l \in \mathbb{Z}$, $\underline{x}^*(t)$ is a τ-periodic solution of the *closed-loop* system. The fact that $\mathbf{A}+\mathbf{B}_a \mathbf{K}_s \mathbf{C}_a$ has in general no eigenvalues at $il2\pi f_{tpe}$, $l \in \mathbb{Z}$, is due to the fact that, in general, the AMB actuator is designed such that the decrease in stiffness, due to the negative stiffness effect of a electromagnetic actuator, see [136], is significantly smaller than the stiffness of the spindle rotor. Hence, $\mathbf{A} + \mathbf{B}_a \mathbf{K}_s \mathbf{C}_a$ will typically exhibit eigenvalues in the open left-half complex plane. Note that this periodic solution differs from the periodic solution of the *open-loop* system without the AMB model given by (2.15), which is due to the fact that the nominal control action vanishes, i.e. $\underline{F}_a^*(t) = \mathbf{K}_i \underline{i}_c^*(t) = \mathbf{K}_i(\mathbf{C}_c \underline{\xi}^*(t) + \mathbf{D}_c \underline{y}^*(t)) = 0$.

Next, the equations of motions (4.1), (4.3) and (4.8) are linearised about the periodic solution $\underline{x}^*(t), \underline{\xi}^*(t)$. Hereto, consider the decompositions of the state vectors $\underline{x}(t)$ and $\underline{\xi}(t)$ as defined in (4.5) with $\underline{\xi}^*(t) = 0$. Then the linearised

closed-loop equations of motion, using the AMB actuator model, are given by

$$\begin{aligned}\dot{\tilde{\underline{x}}}(t) &= \big(\mathbf{A}+\mathbf{B}_a\mathbf{K}_s\mathbf{C}_a\big)\tilde{\underline{x}}(t)\\ &\quad+\mathbf{B}_t a_p\sum_{j=0}^{z-1} g_j\big(\phi_j(t)\big)\mathbf{H}_j(t)\mathbf{C}_t\big(\tilde{\underline{x}}(t)-\tilde{\underline{x}}(t-\tau)\big)\\ &\quad+\mathbf{B}_a\mathbf{K}_i(\mathbf{D}_c\mathbf{C}_a\tilde{\underline{x}}(t)+\mathbf{C}_c\tilde{\underline{\xi}}(t)),\\ \dot{\tilde{\underline{\xi}}}(t) &= \mathbf{A}_c\tilde{\underline{\xi}}(t)+\mathbf{B}_c\mathbf{C}_a\tilde{\underline{x}}(t)\end{aligned} \tag{4.14}$$

with $\mathbf{H}_j(t)$ as given in (2.17). From the linearised *closed-loop* equations of motion, presented above, it can be seen that, for controller design with perturbation feedback, the AMB can be modelled by the following linear model:

$$\tilde{\underline{F}}_a(t) = \mathbf{K}_i\tilde{\underline{i}}_c(t)+\mathbf{K}_s\tilde{\underline{v}}_a(t), \tag{4.15}$$

where $\mathbf{K}_i$ and $\mathbf{K}_s$ as given in (4.9) and (4.10), respectively.

4.3.3 Controller input signal: discussion

From the analysis using the linear actuator model, as presented above, it can be concluded that the SLD with active chatter controller (4.3) does not depend on the chosen controller input signal. This is due to the fact that the variable c, indicating whether full output feedback ($c = 0$) or perturbation feedback ($c = 1$) is applied, does not appear in the linearised equations of motion (see (4.7)). Moreover it is shown that the actuator forces, needed to stabilise the milling process, will be zero in steady state in case of perturbation feedback whereas the actuator forces will be non-zero in steady state in case of full output feedback. This result is exploited for the model incorporating the AMB model, where it is important to limit the actuator input current in order to avoid actuator saturation. Note that, as described in Section 4.2, the controller design will be based on a linearised model of the milling process. An important aspect from a practical point of view is the estimation of the periodic solution in case of perturbation feedback. The perturbation displacements $\tilde{\underline{v}}_a(t)$ can e.g. be obtained by using a chatter detection algorithm based on a parametric model of the milling process, as described in Section 3.2. The effect of the selection of the controller input signal on the required actuator forces will be further demonstrated by results from time domain simulations (TDS) in Section 4.6.

4.4 Modelling for control

The model of the milling process, discussed in Chapter 2, can readily be employed for stability analysis (i.e. determination of the SLD). However, the presence of time-delay and the explicit time-dependency of the right-hand side of

the DDE (4.1) (and in the linearised dynamics in (4.2)) complicates the employment of robust control synthesis techniques. Therefore, two model simplifications are introduced to construct a finite-dimensional, time-invariant model, which will be more suitable for controller design using μ-synthesis techniques as pursued in Section 4.5. Moreover, the effect of these model simplifications on the SLD is demonstrated.

First, the discussion will focus on an autonomous approximation of the linearised nonautonomous DDE describing the linearised perturbation milling dynamics given by (4.2) with $\underline{\tilde{F}}_a(t) = \mathbf{K}_a \underline{\tilde{z}}_c(t)$ for the case of the linear actuator model and with $\underline{\tilde{F}}_a(t) = \mathbf{K}_i \underline{\tilde{z}}_c(t) + \mathbf{K}_s \underline{\tilde{v}}_a(t)$ for the AMB model. A characteristic feature of a milling process is that the direction of the cutting forces is a function of the rotation angle $\phi_j(t)$. As a result, time-dependent functions appear in the describing model equations through the term $\mathbf{H}_j(t)$ in (4.2). In [6], a method is described which approximates $\mathbf{H}_j(t)$ by means of a Fourier series expansion. The number of harmonics to be considered for an accurate reconstruction of $\mathbf{H}_j(t)$ depends on the immersion conditions (which indicates the percentage of the tool diameter used during cutting) and the number of teeth in cut. In this work full immersion cuts are considered (i.e. the entire tool diameter is used for cutting). Then, as described in [5], it is sufficient to take the average (zero-order) component of the Fourier series expansion over one tooth passing, i.e.

$$\bar{\mathbf{H}} = \frac{1}{\tau} \int_0^{\tau} \sum_{j=0}^{z-1} \mathbf{H}_j(t) dt. \tag{4.16}$$

Since $\bar{\mathbf{H}}$ is valid only between the entry ϕ_s and exit ϕ_e angles of the cutter (i.e. when $g_j(\phi_j) = 1$), it becomes equal to the average value of $\mathbf{H}_j(t)$ at cutter pitch angle $\phi_p = 2\pi/z$:

$$\bar{\mathbf{H}} = \frac{1}{\phi_p} \int_{\phi_s}^{\phi_e} \sum_{j=0}^{z-1} \mathbf{H}_j(\phi) d\phi = \frac{z}{2\pi} \begin{bmatrix} \bar{H}_{xx} & \bar{H}_{xy} \\ \bar{H}_{yx} & \bar{H}_{yy} \end{bmatrix}, \tag{4.17}$$

where the integrated functions $\bar{H}_{xx}, \bar{H}_{xy}, \bar{H}_{yx}$ and $\bar{H}_{yy}$ can be determined analytically in case of a linear cutting model ($x_F = 1$, see [5]) and have to be computed numerically in case of an exponential cutting model ($x_F < 1$).

At this point a time-invariant DDE milling model is obtained, in which the dependency on the rotation angle $\phi_j(t)$ is eliminated, given as follows:

$$\begin{aligned} \dot{\underline{\tilde{x}}}(t) &= \mathbf{A} \underline{\tilde{x}}(t) + a_p \mathbf{B}_t \bar{\mathbf{H}} \mathbf{C}_t (\underline{\tilde{x}}(t) - \underline{\tilde{x}}(t-\tau)) + \mathbf{B}_a \underline{\tilde{F}}_a(t), \\ \underline{\tilde{v}}_a(t) &= \mathbf{C}_a \underline{\tilde{x}}(t). \end{aligned} \tag{4.18}$$

However, averaging the cutting forces may be a rather crude approximation. Therefore, the error in the stability lobes is examined in more detail for two different numbers of teeth on the cutting tool.

Table 4.1: Milling model parameters.

Parameter	Value	Parameter	Value
$m_{t,x} = m_{t,y}$	0.015 kg	K_t	462 [N/mm$^{(1+x_F)}$]
$m_{a,x} = m_{a,y}$	0.14 kg	K_r	38.6 [N/mm$^{(1+x_F)}$]
$\omega_{t,x} = \omega_{t,y}$	2350 Hz	x_F	0.744 [-]
$\omega_{a,x} = \omega_{a,y}$	1400 Hz	ϕ_s	0 [rad]
$\zeta_{t,x} = \zeta_{t,y}$	0.05 [-]	ϕ_e	π [rad]
$\zeta_{a,x} = \zeta_{a,y}$	0.12 [-]	f_z	0.2 [mm/tooth]
z	2/4 [-]		

In Figure 4.3, stability lobes diagrams and the error between the autonomous and nonautonomous model are given for cutters with two and four teeth. Hereto, the machine spindle-toolholder-tool dynamics is modelled by two decoupled subsystems (representing the dynamics in two (x,y) orthogonal directions perpendicular to the spindle axis) consisting of two mass-spring-damper systems to mimic the inherent compliance between actuator and tooltip, see Figure 4.4, with masses $m_{i,k},\ i \in \{a,t\},\ k \in \{x,y\}$, eigenfrequencies $\omega_{i,k} = \sqrt{(c_{i,k}/m_{i,k})},\ i \in \{a,t\},\ k \in \{x,y\}$, and dimensionless damping ratios $\zeta_{i,k} = b_{i,k}/2\sqrt{(c_{i,k}m_{i,k})},\ i \in \{a,t\},\ k \in \{x,y\}$. This is done in order to capture the inherent dynamics between the actuator/sensor system (denoted by subscript a) and the cutting tool (denoted by subscript t). The parameters of the machine spindle model and cutting force coefficients are listed in Table 4.1. Herein, the cutting model parameters ($K_t,\ K_r$ and x_F) are taken from [50] and spindle parameters are chosen such that these represent realistic machine spindle dynamics for high-speed milling machines as in [49]. It can be seen that for this typical case and for a two-fluted cutter, the peak of the lobe of the time-invariant model is shifted slightly to the right compared to the time-varying model. For the four-fluted cutter the error is (almost) zero (actually for a linear cutting force model, i.e. $x_F = 1$, it can be shown that for $z = 4$ the error becomes exactly zero). Hence, it can be concluded that, for the given parameters of the milling process, the time-invariant model is accurate enough for predicting the chatter stability boundary. However, it should be noted that the error between the chatter stability boundaries for the autonomous and nonautonomous models depends on the number of teeth on the cutter, the immersion percentage and the spindle speed.

Secondly, a finite-dimensional approximation of the time delay, using a Padé approximation, is applied (see also [21, 140] where a Padé approximation of the time-delay is applied for controller design in case of turning). Hereto, the delayed tool vibrations $\underline{\tilde{v}}_t(t-\tau) = \mathbf{C}_t\tilde{x}(t-\tau)$ are approximated using a Padé approximation and the resulting approximation is denoted by $\underline{\tilde{v}}_{pd}(t)$, such that $\underline{\tilde{v}}_t(t-\tau) = \mathbf{C}_t\tilde{x}(t-\tau) \approx \underline{\tilde{v}}_{pd}(t)$. The milling model in (4.2) with cutting force

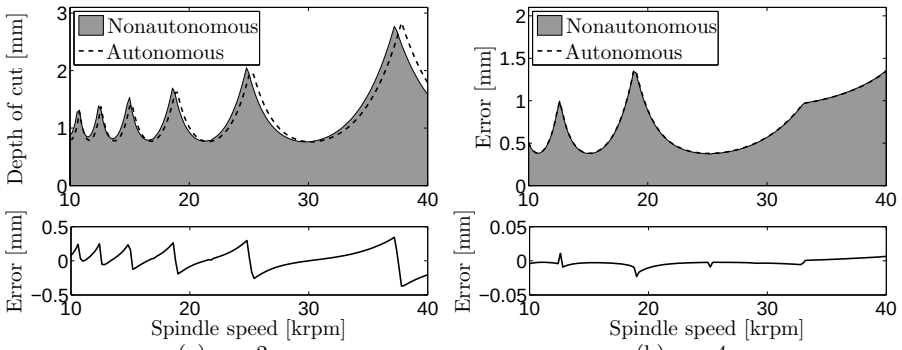

(a) $z = 2$. (b) $z = 4$.

Figure 4.3: Stability lobes diagram using a nonautonomous model (4.2) *and an approximated autonomous model* (4.18) *(dashed), with* $\underline{\tilde{F}}_a(t) = 0$ *and parameters as in Table 4.1 for a two- and four-fluted cutter.*

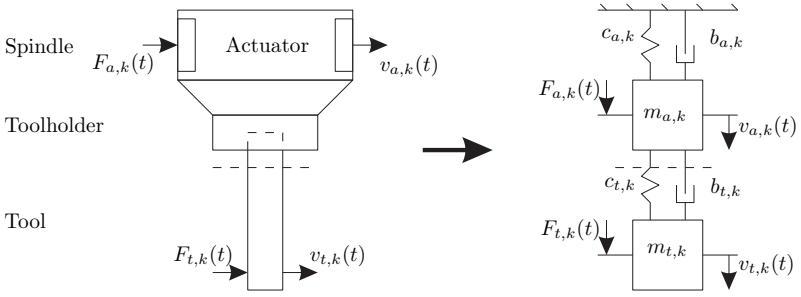

Figure 4.4: Schematic overview of spindle dynamics model, $k \in \{x, y\}$.
$\underline{F}_a, \underline{v}_a$*: forces displacements at actuator.*
$\underline{F}_t, \underline{v}_t$*: forces displacements at tooltip.*

---

averaging, defined in (4.17), and Padé approximation is given as follows:

$$\begin{bmatrix} \dot{\underline{\tilde{x}}}(t) \\ \dot{\underline{\tilde{x}}}_{pd}(t) \end{bmatrix} = \begin{bmatrix} \mathbf{A} + a_p \mathbf{B}_t \bar{\mathbf{H}} (\mathbf{C}_t - \mathbf{D}_{pd} \mathbf{C}_t) & -a_p \mathbf{B}_t \bar{\mathbf{H}} \mathbf{C}_{pd} \\ \mathbf{B}_{pd} \mathbf{C}_t & \mathbf{A}_{pd} \end{bmatrix} \begin{bmatrix} \underline{\tilde{x}}(t) \\ \underline{\tilde{x}}_{pd}(t) \end{bmatrix} + \begin{bmatrix} \mathbf{B}_a \\ \mathbf{0} \end{bmatrix} \underline{\tilde{F}}_a(t), \quad \underline{\tilde{v}}_a(t) = \mathbf{C}_a \underline{\tilde{x}}(t), \tag{4.19}$$

where $\mathbf{A}_{pd} \in \mathbb{R}^{2n_{pd}}, \mathbf{B}_{pd} \in \mathbb{R}^{2n_{pd} \times 2}, \mathbf{C}_{pd} \in \mathbb{R}^{2 \times 2n_{pd}}$ and $\mathbf{D}_{pd} \in \mathbb{R}^{2 \times 2}$ denote matrices of the state-space description of the Padé approximation. The size of these matrices depends on the chosen order n_{pd} for the Padé approximation. Since the delayed output vector $(\underline{\tilde{v}}_t(t - \tau))$ has two elements (x- and y-direction), the state-space description of the Padé approximation has two

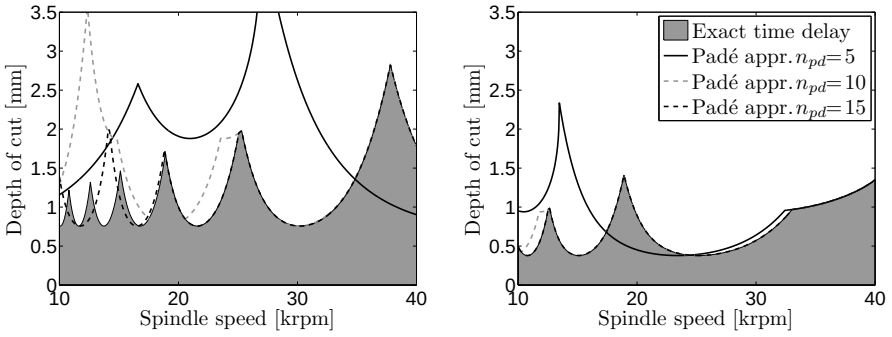

(a) $z = 2$. (b) $z = 4$.

Figure 4.5: Stability lobes diagram for the approximated autonomous milling process with Padé approximation of order n_{pd} (4.19) and the autonomous milling model with exact time delay (4.18) for two different number of teeth.

times the number of states of the Padé approximation order n_{pd}. The order of the Padé approximation will be based on a desired level of accuracy regarding the predicted chatter stability boundary using the model with Padé approximation. Hereto, in Figure 4.5 stability lobes diagrams are given for the autonomous model with time-delay given by (4.18) with $\underline{\tilde{F}}_a(t) = 0$, and (4.19) with $\underline{\tilde{F}}_a(t) = 0$ for different orders n_{pd} of the Padé approximant with the parameters of the model listed in Table 4.1. From the figure, it can be observed that, for increasing order n_{pd} of the Padé approximant, the error between the stability lobes determined using the exact delay term and the approximated delay term becomes smaller. Moreover, since the delay is inversely proportional to the spindle speed, the approximation becomes more accurate as the spindle speed increases (i.e. for small delays). Next to that, it can be observed that when the number of teeth on the cutting tool increases, a lower order for the Padé approximation may be selected for a desired accuracy. This can be explained by realising that the delay is inversely proportional with the number of teeth and the Padé approximants are good near the origin [60]. In this work the focus lies on relatively high spindle speeds (i.e. above 20 krpm). Hence, it is sufficient to choose the order of the Padé approximant for $z = 2$ to be $n_{pd} = 15$ while for $z = 4$ the order of the Padé approximation is chosen equal to $n_{pd} = 10$.

4.5 Robust controller design

In the previous section, a model has been derived which is suitable for robust controller design. Therefore, in this section, the actual controller design for an active chatter control methodology, which will alter the chatter stability boundary, is presented, such that stable operating points, of higher productivity can be attained while avoiding chatter.

4.5.1 Control objective

As outlined in the introduction of this chapter, the goal of the current work is to alter the SLD by means of an active control strategy. In other words, the aim is to design a controller such that the milling process is stabilised for a pre-defined area of working points (in terms of depth-of-cut a_p and spindle speed n) using limited control effort (i.e. satisfying a specified bound on the controller gain). This control problem can be cast into the generalised plant framework and solved using μ-synthesis techniques [142]. The remainder of this section will be devoted to deriving the generalised plant formulation for the active chatter control problem as stated in Section 4.2. The set of milling operations to be stabilised will be expressed as uncertainties in depth of cut a_p and spindle speed n.

4.5.2 Nominal model

Given the milling process, modelled for control as a finite-dimensional linear time-invariant differential equation in (4.19), see Section 4.4, a linear dynamic controller $\mathbf{K}$ will be designed with transfer function matrix

$$\mathbf{K}(s) = \begin{bmatrix} K_{xx}(s) & K_{xy}(s) \\ K_{yx}(s) & K_{yy}(s) \end{bmatrix}, \tag{4.20}$$

$s \in \mathbb{C}$, from controller input signal $\underline{y}(t) = \underline{v}_a(t) - c\underline{v}_a^*(t)$ to actuator input $\underline{i}_c(t)$ to effectively adapt the spindle dynamics. However, in contrast to most active chatter control methods discussed in Chapter 1, in this work not only the spindle dynamics are considered during the control design, but also the interaction between the spindle dynamics and the cutting forces (and therewith the regenerative effect responsible for chatter) is explicitly taken into account. It is expected that this is a more profound and promising method to make dedicated modifications to the SLD by means of feedback control.

Equation (4.19) together with the appropriate actuator model, i.e. $\underline{\tilde{F}}_a(t) = \mathbf{K}_a\underline{\tilde{i}}_c(t)$ for the linear actuator model or the AMB model as given by (4.15) and the controller input signal $\underline{y}(t) = \underline{v}_a(t) - c\underline{v}_a^*(t)$, gives the nominal plant model used during μ-synthesis. A block diagram of the closed-loop process is given in Figure 4.6.

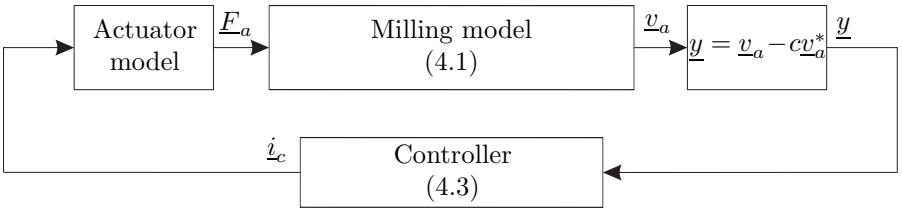

Figure 4.6: Block diagram of the closed-loop nominal milling process modelled for control.

4.5.3 Uncertainty modelling

This section describes the modelling of the uncertainties in the process parameters and spindle dynamics, which can be considered as a key step in achieving the control objective defined above: robust stability (i.e. chatter avoidance) in a predefined range of process parameters. The control design will be based on the (simplified) milling model (4.19) presented in the previous section.

4.5.3.1 Uncertainty in process parameter: depth of cut a_p

First, the uncertainty in depth of cut a_p is considered which is modelled as a parametric uncertainty. An important (practical) aspect is that robust control design should provide stability for small as well as (relatively) large values of the depth of cut. Hereto, the uncertain depth of cut is modelled such that it specifies a range from zero up to a maximum value $\bar{a}_p$, i.e. $a_p \in [0, \bar{a}_p]$. Let us define a real scalar uncertainty set $\Delta_{a_p} = \left\{\delta_{a_p} \in \mathbb{R} : |\delta_{a_p}| \leq 1\right\}$. The uncertainty for the depth of cut is then defined by

$$a_p \in \{a_p \in \mathbb{R} : a_p = \tfrac{1}{2}\bar{a}_p(1 + \delta_{a_p}), \delta_{a_p} \in \Delta_{a_p}\}, \tag{4.21}$$

where $\bar{a}_p$ is the maximal depth of cut for which stable cutting is desired.

4.5.3.2 Uncertainty in process parameter: spindle speed n

Next, the uncertainty model for the spindle speed is considered. As described before, the delay is inversely proportional to the spindle speed. Hence, uncertainty in spindle speed n is modelled as an uncertainty in the delay τ, where $\tau = \frac{60}{zn}$. Since a Padé approximation is a rational function of two polynomials in the Laplace operator s and delay τ, modelling the interval delay via a parametric uncertainty would result in an overall uncertainty of very large dimensions (due to the relatively large order of the Padé approximations).

Here an alternative approach will be presented. Hereto, note that for arbitrary frequency ω, the value set of the frequency-domain delay operator $e^{-i\omega\tau}$ for all $\tau \in [\underline{\tau}, \bar{\tau}]$ can be represented in the complex plane as a circular arc

extending along the unit circle. This time-delay interval can be approximated by choosing any pair of stable transfer functions $G_d(s)$ and $W_d(s)$ such that $G_d(s) + W_d(s)\Delta_d$, with $\Delta_d \in \mathbb{C}$ and $|\Delta_d| \leq 1$, covers the uncertainty set $e^{-i\omega\tau}$ with $\tau \in [\underline{\tau}, \bar{\tau}]$. Several alternatives exist to determine transfer function $G_d(s)$ and $W_d(s)$ satisfying these conditions. Chen and Knospe [21] propose to choose $G_d(s)$ and $W_d(s)$ such that at each frequency: 1) the arc length covered by the disk $G_d(s) + W_d(s)\Delta_d$ is nearly that of the delay element $e^{-i\omega\tau}$, for $\tau \in [\underline{\tau}, \bar{\tau}]$, and 2) the area of the disk lying outside the unit circle is minimised. Doing so results in a transfer function $G_d(s)$ which has twice the order of the chosen Padé approximation. Since the Padé approximation needed to accurately describe the delay term is already of a relatively high order (e.g. $n_{pd} = 15$ for $z = 2$, see Figure 4.5), the generalised plant will be of an even higher order which is not desired due to possible computational and implementation issues. Moreover, the size of the circle covering the circular arc of the delay uncertainty is rather large which is due to the fact that the area of the disk lying outside the unit circle is chosen to be minimised. This approach may therefore give conservative results as illustrated for the milling process in [163].

Hence, here a different approach is presented to model the delay uncertainty. In contrast to the approach as discussed above, the approach to model the delay uncertainty taken in this thesis is based on a Padé approximation of the nominal model. The total delay uncertainty interval is then overapproximated using a low-order transfer function which covers the circular arc of the delay uncertainty interval along the unit disk about the nominal delay. Hereto, consider the linearised autonomous milling model, given by (4.18), with a delay uncertainty only. Basically, this model can be represented by the following state-space model:

$$\begin{aligned} \dot{\underline{\tilde{x}}}(t) &= \mathbf{A}_0\underline{\tilde{x}}(t) + \mathbf{A}_1\underline{\tilde{x}}(t-\tau) + \mathbf{B}_a\underline{\tilde{F}}_a(t), \\ \underline{\tilde{v}}_a(t) &= \mathbf{C}_a\underline{\tilde{x}}(t). \end{aligned} \tag{4.22}$$

where $\mathbf{A}_0 = \mathbf{A} + a_p\mathbf{B}_t\bar{\mathbf{H}}\mathbf{C}_t$, $\mathbf{A}_1 = -a_p\mathbf{B}_t\bar{\mathbf{H}}\mathbf{C}_t$ and uncertainty set $\tau \in [\underline{\tau}, \bar{\tau}]$. It is easy to show that (4.22) can be written as a feedback interconnection between the dynamics

$$\begin{aligned} \dot{\underline{\tilde{x}}}(t) &= \mathbf{A}_0\underline{\tilde{x}}(t) + \mathbf{A}_1\underline{\tilde{x}}(t-\tau_0) - a_p\mathbf{B}_t\bar{\mathbf{H}}\underline{q}_d(t) + \mathbf{B}_a\underline{\tilde{F}}_a(t), \\ \underline{\tilde{v}}_t(t) &= \mathbf{C}_t\underline{\tilde{x}}(t), \\ \underline{\tilde{v}}_a(t) &= \mathbf{C}_a\underline{\tilde{x}}(t), \end{aligned} \tag{4.23}$$

and uncertainty term

$$\underline{q}_d(t) = \big(\mathcal{D}_\tau - \mathcal{D}_{\tau_0}\big)\underline{\tilde{v}}_t(t), \tag{4.24}$$

where, $\tau_0 = \frac{\bar{\tau}+\underline{\tau}}{2}$ and the delay operator $\mathcal{D}_{\tau_0}$ is defined as $\mathcal{D}_{\tau_0}\underline{x}(t) = \underline{x}(t-\tau_0)$. The representation of (4.24) in the Laplace domain can be given as

$$\underline{Q}_d(s) = \big(e^{-s\tau} - e^{-s\tau_0}\big)\underline{\tilde{V}}_t(s), \tag{4.25}$$

where $\underline{Q}_d(s)$, $\tilde{\underline{V}}_t(s)$ the Laplace transforms of $\underline{q}_d(t)$ and $\tilde{\underline{v}}_t(t)$, respectively. Let $\kappa(\omega)$ be the gain bound of the uncertainty operator (4.24) in the frequency domain, given as,

$$\kappa(\omega) := \max_{\tau \in [\underline{\tau},\ \bar{\tau}]} |e^{-i\omega\tau} - e^{-i\omega\tau_0}|. \tag{4.26}$$

Since the transfer function $\left(e^{-s\tau} - e^{-s\tau_0}\right)$ is analytic and bounded in the open right half of the complex plane, the $\mathcal{H}_\infty$-norm of $\left(e^{-s\tau} - e^{-s\tau_0}\right)$ can be determined by evaluating the transfer function on the imaginary axis, i.e. for $s = i\omega$. Consequently, in order to determine a bound on $\left(e^{-s\tau} - e^{-s\tau_0}\right)$, it should be determined for $s = i\omega$. It can be shown, see [71], that the upper bound $\kappa(\omega)$ on the delay uncertainty is represented as follows

$$\kappa(\omega) = \begin{cases} 2\sin\frac{\delta_\tau \omega}{2}, & \forall \omega,\ 0 \leq \omega \leq \pi/\delta_\tau \\ 2, & \forall \omega \geq \pi/\delta_\tau, \end{cases} \tag{4.27}$$

where $\delta_\tau = \frac{1}{2}(\bar{\tau} - \underline{\tau})$. The frequency-dependent upper bound $\kappa(\omega)$ on the delay uncertainty is not a rational function and can therefore not readily be used during controller synthesis. Hereto, in [169] rational transfer functions $\rho_l(s)$ for several orders $l = 1, 2, 3$ are derived such that $\kappa(\omega) \leq |\rho_l(i\omega)|$. Since, in this work, the high-speed milling process is considered, the delay intervals will be relatively small (typically of $\mathcal{O}(10^{-5})$ s. for typical spindle speed ranges of $\mathcal{O}(10^3)$ rpm for spindle speeds $n \geq 20000$ rpm). Using this fact, together with the fact that the dominant spindle dynamics resonances lie in general between $1 \cdot 10^3 \leq \frac{\omega_n}{2\pi} \leq 3 \cdot 10^3$ Hz, implies that typically $\omega \leq \pi/\delta_\tau$ and, consequently, an accurate approximation of the frequency-dependent upper bound $\kappa(\omega) = 2\sin\frac{\delta_\tau \omega}{2}$ is required. Moreover, from a numerical point of view, proper transfer functions $\rho_l(s)$ are desired. Then, based on the results in [169], $\rho_l(s)$ is chosen as

$$\rho_1(s) = \frac{\delta_\tau s}{\frac{\delta_\tau}{3.456}s + 1}, \tag{4.28}$$

which ensures a tight over bound of $\kappa(\omega)$ (by $|\rho_l(i\omega)|$) especially in the frequency region which is relevant in the case of high-speed milling, as is described above. Hence, by using the results presented above, the delay uncertainty is approximated by two rational transfer functions $G_d(s)$ and $W_d(s)$, where $G_d(s)$ is the Padé approximation of $e^{-s\tau_0}$ and $W_d(s) = \rho_1(s)$, with ρ_1 as in (4.28), such that:

$$\{\left(e^{-s\tau} - e^{-s\tau_0}\right),\ s \in \mathbb{C},\ \tau \in [\underline{\tau}, \bar{\tau}]\} \subseteq \{W_d(s)\Delta_d,\ s \in \mathbb{C},\ |\Delta_d| \leq 1\}. \tag{4.29}$$

4.5.3.3 Uncertainty in spindle dynamics

The final uncertainty model describes the uncertainty in the spindle dynamics. A common way of determining a model of the spindle dynamics is to perform

identification experiments on a machine spindle at a spindle speed of zero rpm, after which a parametric model is fit onto the experimentally obtained data [50, 135]. There will generally be a discrepancy between the parametric model and the physical system dynamics due to unmodelled dynamics. Moreover, the dynamics of the physical system may change under varying operating conditions. The most important effect is the stiffness change of the spindle which is influenced by the spindle speed due to varying centrifugal loads on the spindle bearings which results in a change of the eigenfrequencies of the milling spindle [84, 127].

In order to ensure robustness for variations in the spindle dynamics, uncertainty on these dynamics is taken into account during μ-synthesis. In this work, the uncertainty in spindle dynamics is modelled by means of parametric uncertainties in the natural frequencies $\underline{\omega}_n = 2\pi\underline{f}_n$ and the dimensionless damping ratios $\underline{\zeta}$. Hereto, the parametric uncertainties in the model parameters are formulated as:

$$\omega_{n,j} = \omega_{0,j}(1 + r_{\omega,j}\delta_{\omega,j}) \tag{4.30}$$

$$\zeta_j = \zeta_{0,j}(1 + r_{\zeta,j}\delta_{\zeta,j}), \tag{4.31}$$

where $\zeta_{0,j}, \omega_{n_0,j}$ are nominal values for the j-th spindle mode, with $j = 1, \ldots, n_u$ and $n_u \leq \frac{n_x}{2}$ the number of uncertain spindle modes under consideration and n_x the order of the spindle dynamics. Moreover, $r_{\omega,j}, r_{\zeta,j}$ are relative uncertainties related to the j-th uncertain spindle mode and $\delta_{\omega,j}$ and $\delta_{\zeta,j}$ are scalars satisfying $\delta_{\omega,j},\ \delta_{\zeta,j} \in \mathbb{R}$ and $|\delta_{\omega,j}|,\ |\delta_{\zeta,j}| < 1,\ \forall j \in \{1, \ldots, n_u\}$. Typical values of $r_{\omega,j}, r_{\zeta,j}$ lie in the order of $\mathcal{O}(10^{-2})$.

It should be noted that, by representing the uncertainty in the spindle dynamics as given in (4.30) and (4.31), it is assumed that the structure of the (nominal) model of the spindle dynamics is known. In general, a more extended uncertainty model of the machine dynamics may be necessary in order to incorporate unmodelled dynamics and imperfections due to measurement errors in the identification process, as will also be illustrated in Chapter 6. Note that it is possible to incorporate other uncertainty models in the μ-framework, see [142] for more detail on the modelling of uncertainties. However, for reasons of simplicity it is assumed that the parametric uncertainty model is sufficient to illustrate the feasibility of accounting for uncertainties in machine dynamics during the control design.

4.5.4 Performance requirement

This section discusses the specification of a performance requirement for the active chatter control design. In essence, the chatter control problem at hand is a robust stabilisation problem rather than a performance problem. As outlined in the problem statement in Section 4.2, the robust stability require-

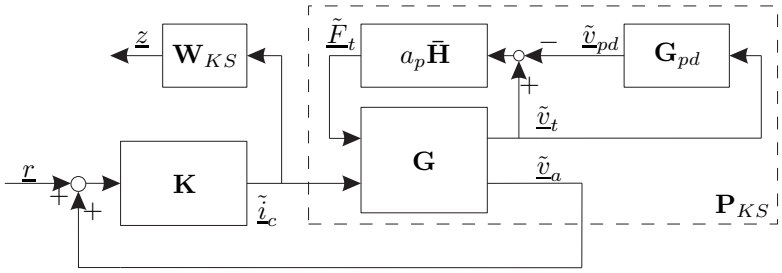

Figure 4.7: Block diagram of linearised approximated autonomous milling model with performance weighting.

ment has to be achieved with limited control effort, since actuator forces have to satisfy practical saturation limits (of e.g. AMB). Therefore, the control gain will be bounded during μ-synthesis, which reflects the most relevant performance requirement for chatter control. Limiting the control gain is done by applying an upper bound on the control sensitivity transfer function $\mathbf{KS}(s) = (\mathbf{I} - \mathbf{K}(s)\mathbf{P}_{KS}(s))^{-1}\mathbf{K}(s)$, where

$$\mathbf{P}_{KS}(s) = \begin{bmatrix}\mathbf{C}_a & \mathbf{0}\end{bmatrix}\left(s\mathbf{I} - \begin{bmatrix}\bar{\mathbf{A}} + a_p\mathbf{B}_t\bar{\mathbf{H}}(\mathbf{C}_t - \mathbf{D}_{pd}\mathbf{C}_t) & -a_p\mathbf{B}_t\bar{\mathbf{H}}\mathbf{C}_{pd} \\ \mathbf{B}_{pd}\mathbf{C}_t & \mathbf{A}_{pd}\end{bmatrix}\right)^{-1}\begin{bmatrix}\bar{\mathbf{B}}_a \\ \mathbf{0}\end{bmatrix},$$

gives the transfer function representation from $\underline{\tilde{i}}_c$ to $\underline{\tilde{v}}_a$ of the nominal plant given by (4.19). Here, the control sensitivity is defined as the transfer function from a input signal $\underline{r}(t)$ (which can e.g. be interpreted as measurement noise on the measured perturbation displacements $\underline{\tilde{v}}_a(t)$ entering the feedback loop) to the control input $\underline{i}_c(t)$. In addition, system- and input-matrices $\bar{\mathbf{A}}$ and $\bar{\mathbf{B}}_a$, of the spindle-actuator dynamics $\mathbf{G}(s)$ where

$$\mathbf{G}(s) = \begin{bmatrix}\mathbf{C}_t \\ \mathbf{C}_a\end{bmatrix}\left(s\mathbf{I} - \bar{\mathbf{A}}\right)\begin{bmatrix}\mathbf{B}_t & \bar{\mathbf{B}}_a\end{bmatrix}, \tag{4.32}$$

depend on the chosen actuator model. For the linear actuator model ($\underline{\tilde{F}}_a = \mathbf{K}_a\underline{\tilde{i}}_c$) $\bar{\mathbf{A}}$ and $\bar{\mathbf{B}}_a$ become:

$$\bar{\mathbf{A}} = \mathbf{A},\ \bar{\mathbf{B}}_a = \mathbf{B}_a\mathbf{K}_a. \tag{4.33}$$

For the linear AMB model, given in (4.15), these matrices are defined as follows:

$$\bar{\mathbf{A}} = \mathbf{A} + \mathbf{B}_a\mathbf{K}_s\mathbf{C}_a,\ \bar{\mathbf{B}}_a = \mathbf{B}_a\mathbf{K}_i, \tag{4.34}$$

where $\mathbf{K}_i$ and $\mathbf{K}_s$ are defined in (4.9) and (4.10), respectively. The bound on the control sensitivity is enforced by defining a weighting function $\mathbf{W}_{KS}(s)$, which will be described below, such that the performance output of the generalised plant is the weighted control sensitivity ($\mathbf{W}_{KS}(s)\mathbf{KS}(s)$). A schematic

overview of the closed-loop approximated autonomous milling model with performance weighting is given in Figure 4.7. Then, the problem in which it is aimed to find a μ-optimal controller $\mathbf{K}(s)$ which stabilises the milling process in the face of modelled uncertainties (in a_p, τ and the spindle dynamics) while minimising the peak magnitude of the weighted control sensitivity; that is a controller which achieves $\|\mathbf{W}_{KS}(s)\mathbf{KS}(s)\|_\infty < \gamma,\ \min \gamma \in \mathbb{R}$. Of course, minimising the weighted control sensitivity actually enforces a frequency-dependent upper bound on the magnitude of control gain $|\mathbf{K}(s)|$ rather than on the magnitudes of the actual control input $\underline{\tilde{i}}_c(t)$. Hence, by estimating the magnitude of the inputs to the controller, i.e. of the chatter-related tool displacements in x- and y-direction, an appropriate bound on the control gain can in practice be chosen such that the actuator forces are satisfying given saturation limits.

In this work, the weighting transfer function matrix $\mathbf{W}_{KS}(s)$ is chosen to be diagonal, because of the two-dimensional nature of the control input $\underline{i}_c(t)$, i.e. $\mathbf{W}_{KS}(s) = \mathrm{diag}(W_{KS}(s), W_{KS}(s))$. Moreover, its structure is chosen such that $W_{KS}(s)$ is a double lead-lag filter with high- and low-pass characteristics. This means that, for frequencies f between roll-off frequencies $f_{r,l} < f < f_{r,h}$, the control gain is limited by a certain value and that, for frequencies smaller than $f_{r,l}$ and larger than $f_{r,h}$, the inputs to the controller are attenuated in order to reduce the (undesired) influence of, firstly, a DC-component in the control force due to a DC component in the measured displacements in the case of full output feedback and, secondly, high-frequent measurement noise on the control action. This weighting function $W_{KS}(s)$ is written as:

$$W_{KS}(s) = K_p \frac{\frac{1}{2\pi f_{r,l}}s + 1}{\frac{1}{2\pi f_{p,l}}s + 1} \cdot \frac{\frac{1}{2\pi f_{r,h}}s + 1}{\frac{1}{2\pi f_{p,h}}s + 1}, \tag{4.35}$$

where K_p denotes the gain of the weighting function. Two poles, at frequencies $f_{p,l}$ and $f_{p,h}$ (such that $f_{p,l} < f_{r,l}$ and $f_{p,h} > f_{r,h}$), are added to obtain a proper weighting function, necessary for implementation. As often in robust control, $W_{KS}(s)$ is chosen in an iterative fashion.

4.5.5 Generalised plant formulation

Based on the discussion on uncertainty modelling and the specification of a performance requirement in the previous sections and the milling model for control, presented in Section 4.4, the control problem will be transformed into the generalised plant framework [142]. Figure 4.8 shows the configuration of this framework. The generalised plant $\mathbf{P}$ is a given system with three sets of inputs and three sets of outputs. The signal pair $\underline{p}, \underline{q}$ denote the in-/outputs of the uncertainty channel. The signal $\underline{r}$ represents an external input in which possible disturbances, measurement noise and reference inputs are stacked. The signal $\underline{\tilde{i}}_c$ is the control input. The output $\underline{z}$ can be considered as a performance

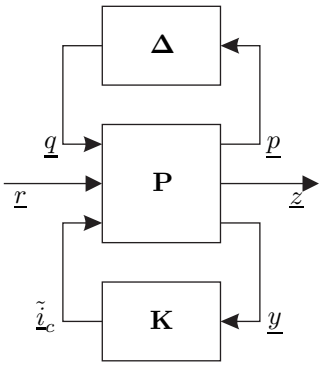

Figure 4.8: Generalised plant interconnection.

variable. In this case $\underline{z}$ will be considered as the weighted control input, i.e. $\underline{z}(s) = \mathbf{W}_{KS}(s)\tilde{\underline{i}}_c(s),\ s \in \mathbb{C}$, in order to limit the controller effort required for stabilising the uncertain milling process. The output $\underline{y}$, finally, is the measured output, and is available for feedback (i.e. $\underline{y} = \tilde{\underline{v}}_a$ in the case of perturbation feedback).

A block diagram of the generalised plant $\mathbf{P}$ and uncertainties can be found in Figure 4.9. In order to derive the generalised plant, first, consider the following state-space descriptions of the systems $G_d\mathbf{I}_2$, $W_d\mathbf{I}_2$, where $\mathbf{I}_n \in \mathbb{R}^{n\times n}$ and $\mathbf{W}_{KS}$, respectively:

$$G_d\mathbf{I}_2 \begin{cases} \dot{\underline{x}}_d(t) &= \mathbf{A}_d\underline{x}_d(t) + \mathbf{B}_d\tilde{\underline{v}}_t(t), \\ \underline{v}_d(t) &= \mathbf{C}_d\underline{x}_d(t) + \mathbf{D}_d\tilde{\underline{v}}_t(t), \end{cases} \tag{4.36}$$

$$W_d\mathbf{I}_2 \begin{cases} \dot{\underline{x}}_w(t) &= \mathbf{A}_w\underline{x}_w(t) + \mathbf{B}_w\tilde{\underline{v}}_t(t), \\ \underline{p}_d(t) &= \mathbf{C}_w\underline{x}_w(t) + \mathbf{D}_w\tilde{\underline{v}}_t(t), \end{cases} \tag{4.37}$$

$$\mathbf{W}_{KS} \begin{cases} \dot{\underline{x}}_{KS}(t) &= \mathbf{A}_{KS}\underline{x}_{KS}(t) + \mathbf{B}_{KS}\tilde{\underline{i}}_c(t), \\ \underline{z}(t) &= \mathbf{C}_{KS}\underline{x}_{KS}(t) + \mathbf{D}_{KS}\tilde{\underline{i}}_c(t), \end{cases} \tag{4.38}$$

where the size of $\mathbf{A}_d$ is chosen such that $\underline{v}_p(t) \approx \tilde{\underline{v}}_t(t - \tau_0)$. Next, consider the linearised autonomous milling model as described by (4.18) (including actuator model $\tilde{\underline{F}}_a = \mathbf{K}_a\tilde{\underline{i}}_c$ or AMB model (4.15)):

$$\begin{aligned} \dot{\tilde{\underline{x}}}(t) &= \bar{\mathbf{A}}\tilde{\underline{x}}(t) + a_p\mathbf{B}_t\bar{\mathbf{H}}\mathbf{C}_t(\tilde{\underline{x}}(t) - \tilde{\underline{x}}(t - \tau_0)) + \bar{\mathbf{B}}_a\tilde{\underline{i}}_c, \\ \tilde{\underline{v}}_a &= \mathbf{C}_a\tilde{\underline{x}}(t), \end{aligned} \tag{4.39}$$

with $\bar{\mathbf{A}}$ and $\bar{\mathbf{B}}_a$ as defined in (4.33) in case of the linear actuator model $\tilde{\underline{F}}_a = \mathbf{K}_a\tilde{\underline{i}}_c$ and as defined in (4.34) for the AMB model.

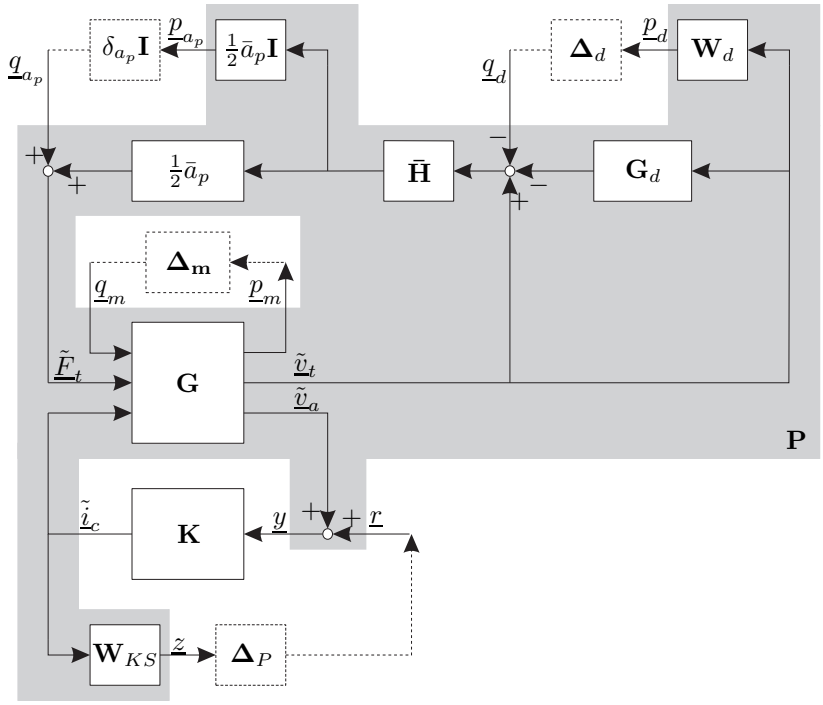

Figure 4.9: Block diagram of the generalised plant $\mathbf{P}$*, indicated by the grey area, and controller* $\mathbf{K}$ *and uncertainties* $\mathbf{\Delta}$*.*

Then, by adding the uncertainty and performance channel in-/output, denoted by $\underline{p}(t)$, $\underline{q}(t)$ and $\underline{r}(t)$, $\underline{z}(t)$, respectively to the system and rearranging terms the generalised plant $\mathbf{P}$ is given as follows :

$$\begin{aligned} \dot{\underline{x}}_P(t) &= \mathbf{A}_P\underline{x}_P(t) + \mathbf{B}_P\underline{u}_P(t), \\ \underline{v}_P(t) &= \mathbf{C}_P\underline{x}_P(t) + \mathbf{D}_P\underline{u}_P(t), \end{aligned} \tag{4.40}$$

with the state vector $\underline{x}_P(t) = [\tilde{\underline{x}}^T(t)\ \underline{x}_d^T(t)\ \underline{x}_w^T(t)\ \underline{x}_{KS}^T(t)]^T$, input vector $\underline{u}_P(t) = [\underline{q}^T(t)\ \underline{r}^T(t)\ \tilde{\underline{i}}_c^T(t)]^T$, output vector $\underline{v}_P(t) = [\underline{p}^T(t)\ \underline{z}^T(t)\ \underline{y}^T(t)]$. The uncertainty channel input $\underline{p}(t)$ and output $\underline{q}(t)$ are defined as

$$\underline{p}(t) = [\underline{p}_m^T(t)\ \underline{p}_d^T(t)\ \underline{p}_{a_p}^T(t)]^T, \text{ and } \underline{q}(t) = [\underline{q}_m^T(t)\ \underline{q}_d^T(t)\ \underline{q}_{a_p}^T(t)]^T,$$

where the subscripts m, d and a_p denote the input/output of the machine dynamics, delay and depth of cut uncertainty, respectively. The state-space

matrices of the generalised plant are defined as follows:

$$\mathbf{A}_P = \begin{bmatrix} \bar{\mathbf{A}} + \frac{1}{2}\bar{a}_p \mathbf{B}_t \bar{\mathbf{H}}(\mathbf{I} - \mathbf{D}_d)\mathbf{C}_t & -\frac{1}{2}\bar{a}_p \mathbf{B}_t \bar{\mathbf{H}} \mathbf{C}_d & \mathbf{0} & \mathbf{0} \\ \mathbf{B}_d \mathbf{C}_t & \mathbf{A}_d & \mathbf{0} & \mathbf{0} \\ \mathbf{B}_w \mathbf{C}_t & \mathbf{0} & \mathbf{A}_w & \mathbf{0} \\ \mathbf{0} & \mathbf{0} & \mathbf{0} & \mathbf{A}_{KS} \end{bmatrix}, \tag{4.41}$$

$$\mathbf{B}_P = \begin{bmatrix} \mathbf{B}_m & -\frac{1}{2}\bar{a}_p \mathbf{B}_t \bar{\mathbf{H}} & \mathbf{B}_t & \mathbf{0} & \bar{\mathbf{B}}_a \\ \mathbf{0} & \mathbf{0} & \mathbf{0} & \mathbf{0} & \mathbf{0} \\ \mathbf{0} & \mathbf{0} & \mathbf{0} & \mathbf{0} & \mathbf{0} \\ \mathbf{0} & \mathbf{0} & \mathbf{0} & \mathbf{0} & \mathbf{B}_{KS} \end{bmatrix}, \tag{4.42}$$

$$\mathbf{C}_P = \begin{bmatrix} \mathbf{C}_m & \mathbf{0} & \mathbf{0} & \mathbf{0} \\ \mathbf{D}_w \mathbf{C}_t & \mathbf{0} & \mathbf{C}_w & \mathbf{0} \\ \frac{1}{2}\bar{a}_p \bar{\mathbf{H}}(\mathbf{I} - \mathbf{D}_d)\mathbf{C}_t & -\frac{1}{2}\bar{a}_p \bar{\mathbf{H}} \mathbf{C}_d & \mathbf{0} & \mathbf{0} \\ \mathbf{0} & \mathbf{0} & \mathbf{0} & \mathbf{C}_{KS} \\ \mathbf{C}_a & \mathbf{0} & \mathbf{0} & \mathbf{0} \end{bmatrix}, \tag{4.43}$$

$$\mathbf{D}_P = \begin{bmatrix} \mathbf{0} & \mathbf{0} & \mathbf{0} & \mathbf{0} & \mathbf{0} \\ \mathbf{0} & \mathbf{0} & \mathbf{0} & \mathbf{0} & \mathbf{0} \\ \mathbf{0} & -\frac{1}{2}\bar{a}_p \bar{\mathbf{H}} & \mathbf{0} & \mathbf{0} & \mathbf{0} \\ \mathbf{0} & \mathbf{0} & \mathbf{0} & \mathbf{0} & \mathbf{D}_{KS} \\ \mathbf{0} & \mathbf{0} & \mathbf{0} & \mathbf{I} & \mathbf{0} \end{bmatrix}. \tag{4.44}$$

Herein, $\mathbf{B}_m$ and $\mathbf{C}_m$ denote the input/output matrices of the feedback interconnection between the nominal model of spindle dynamics and corresponding uncertainty, which is given as

$$\begin{aligned} \dot{\underline{x}}(t) &= \bar{\mathbf{A}}\underline{x}(t) + \mathbf{B}_m \underline{q}_m(t), \\ \underline{p}_m(t) &= \mathbf{C}_m \underline{x}(t), \\ \underline{q}_m(t) &= \mathbf{\Delta}_m \underline{p}_m(t), \end{aligned}$$

where the size of $\mathbf{B}_m$, $\mathbf{\Delta}_m$ and $\mathbf{C}_m$ depend on the number of uncertain spindle modes under consideration with

$$\begin{aligned} \mathbf{\Delta}_m = \{\mathrm{diag}\big(\delta_{\omega,j}\mathbf{I}_3, \delta_{\zeta,j}\mathbf{I}_1\big) : \delta_{\omega,j},\ \delta_{\zeta,j} \in \mathbb{R},\ |\delta_{\omega,j}|, |\delta_{\zeta,j}| < 1, \\ \forall j \in \{1, \ldots, n_u\}, \mathbf{I}_n \in \mathbb{R}^{n \times n}\} \end{aligned} \tag{4.45}$$

with n_u the number of uncertain spindle modes under consideration. Combining all the sources of uncertainty as described in Section 4.5.3, the total uncertainty block $\mathbf{\Delta}$ is given as:

$$\begin{aligned} \mathbf{\Delta} = \{\mathrm{diag}(\mathbf{\Delta}_m, \Delta_d \mathbf{I}_2, \delta_{a_p}\mathbf{I}_2) : \mathbf{I}_n \in \mathbb{R}^{n \times n}, \delta_{a_p} \in \mathbb{R}, \Delta_d \in \mathbb{C}, \\ |\Delta_d|, |\delta_{a_p}| < 1\} \end{aligned} \tag{4.46}$$

with $\mathbf{\Delta}_m$ as defined in (4.45). From the definition of the generalised plant $\mathbf{P}$ and corresponding uncertainty set $\mathbf{\Delta}$ it becomes clear that the control problem at

hand is a robust performance problem which contains structured uncertainties, i.e. the uncertainty $\mathbf{\Delta}$ is not a full complex matrix but has specific elements which contain uncertainties. Hence, it is recommended to solve the problem using μ-synthesis, which will be discussed in the following section.

4.5.6 Controller synthesis

In this section, the problem of finding controllers which satisfy the requirements as defined in Section 4.2, will be discussed. As discussed in the previous section, the control problem at hand is a robust performance problem. The problem is to find a controller $\mathbf{K}$ such that the $\mathcal{H}_\infty$-norm of the performance channel (i.e. the transfer function from $\underline{r}$ to $\underline{z}$) with the controller in closed-loop, becomes smaller than 1, for all allowed uncertainties $\mathbf{\Delta}$. As shown in [181], the robust performance problem can be transformed into a robust stability problem by adding an extra uncertainty block $\mathbf{\Delta}_P \in \mathbb{C}^{2\times 2}, \|\mathbf{\Delta}_P\|_\infty < 1$, associated with the performance channel, to the problem. A block diagram interpretation of the transformation can be found in [142, p. 318]. The newly obtained uncertainty block is then given as follows:

$$\hat{\mathbf{\Delta}} = \begin{bmatrix} \mathbf{\Delta} & \mathbf{0} \\ \mathbf{0} & \mathbf{\Delta}_P \end{bmatrix}. \tag{4.47}$$

Then robust stability can be tested by computing the structured singular value $\mu_{\hat{\mathbf{\Delta}}}$ of the interconnection of the generalised plant $\mathbf{P}$ and controller $\mathbf{K}$, denoted by $\mathbf{N}$ and defined in (4.50) below, with respect to the expanded uncertainty set $\hat{\mathbf{\Delta}}$, i.e.

$$\sup_{\omega\in\mathbb{R}} \mu_{\hat{\mathbf{\Delta}}}(\mathbf{N}) < 1. \tag{4.48}$$

For the definition of the structured singular value $\mu_{\hat{\mathbf{\Delta}}}$, see Appendix A. Herein, $\mathbf{N}$ is defined as the lower fractional transformation between $\mathbf{P}$ and $\mathbf{K}$. Consider the following decomposition of the transfer function matrix of the generalised plant $\mathbf{P}$,

$$\mathbf{P} = \begin{bmatrix} \mathbf{P}_{11} & \mathbf{P}_{12} \\ \mathbf{P}_{21} & \mathbf{P}_{22} \end{bmatrix}, \tag{4.49}$$

with

$$\begin{bmatrix} \underline{p} \\ \underline{z} \end{bmatrix} = \mathbf{P}_{11} \begin{bmatrix} \underline{q} \\ \underline{r} \end{bmatrix} + \mathbf{P}_{12}\tilde{\underline{i}}_c, \;\; \underline{y} = \mathbf{P}_{21} \begin{bmatrix} \underline{q} \\ \underline{r} \end{bmatrix} + \mathbf{P}_{22}\tilde{\underline{i}}_c.$$

Then the lower fractional transformation between $\mathbf{P}$ and $\mathbf{K}$, i.e. $\mathcal{F}_l(\mathbf{P},\mathbf{K})$, is defined as follows:

$$\mathbf{N} := \mathcal{F}_l(\mathbf{P},\mathbf{K}) = \mathbf{P}_{11} + \mathbf{P}_{12}\mathbf{K}(\mathbf{I} - \mathbf{P}_{22}\mathbf{K})^{-1}\mathbf{P}_{21}. \tag{4.50}$$

For more information on lower fractional transformations the reader is referred to [181]. Then, the optimisation problem of computing the μ-optimal controller $\mathbf{K}$ which minimises the structured singular value $\mu_{\hat{\mathbf{\Delta}}}$ with respect to uncertainty set $\hat{\mathbf{\Delta}}$, is defined as follows:

$$\min_{\mathbf{K}} \sup_{\omega \in \mathbb{R}} \mu_{\hat{\mathbf{\Delta}}}(\mathbf{N}) \tag{4.51}$$

with $\mathbf{N}$ as defined above. Unfortunately, the computation of $\mu_{\hat{\mathbf{\Delta}}}$ is in general a difficult problem [142]. However, an upper and lower bound on $\mu_{\hat{\mathbf{\Delta}}}$ may be computed. In most cases the upper bound approximation is used since this is a convex optimisation problem in the scaling matrices [142]. The upper bounds may be computed for purely complex uncertainty sets as well as mixed real/complex uncertainties [178]. However, the upper bound in case of mixed real/complex uncertainties may result in scaling matrices of relatively high order. It is well known that the order of the resulting controller is directly related to the order of the generalised plant (with scaling matrices) and the order of the controller cannot be restricted using standard controller synthesis algorithms [165]. As the generalised plant in this work is already of relatively high order (since a relatively high-order Padé approximation is needed to accurately approximate the time delay), the scalar uncertainties will be modelled as complex uncertainties. The additional conservatism introduced by considering only complex uncertainties during the controller design is accepted in order to avoid the design of a controller of even higher order. Then the complex uncertainty set $\hat{\mathbf{\Delta}}_c$ is given as follows:

$$\hat{\mathbf{\Delta}}_c = \begin{bmatrix} \mathbf{\Delta}_c & \mathbf{0} \\ \mathbf{0} & \mathbf{\Delta}_P \end{bmatrix}, \tag{4.52}$$

with

$$\begin{aligned} \mathbf{\Delta}_c = \{\mathrm{diag}(\delta_{\omega,j}\mathbf{I}_3, \delta_{\zeta,j}\mathbf{I}_1, \Delta_d\mathbf{I}_2, \delta_{a_p}\mathbf{I}_2) : \delta_{\omega,j}, \delta_{\zeta,j}, \delta_{a_p} \in \mathbb{C}, \Delta_d \in \mathbb{C}, \\ |\Delta_d|, |\delta_{\omega,j}|, |\delta_{\zeta,j}|, |\delta_{a_p}| < 1, \forall j \in \{1, \ldots, n_u\}, \mathbf{I}_n \in \mathbb{R}^{n \times n}\}. \end{aligned} \tag{4.53}$$

Then the optimisation problem (4.51) can be reformulated by using the upper bound on the complex structured singular value $\mu_{\hat{\mathbf{\Delta}}_c}$. The upper bound on $\mu_{\hat{\mathbf{\Delta}}_c}$ with complex uncertainties $\hat{\mathbf{\Delta}}_c$ is defined as follows:

$$\mu_{\hat{\mathbf{\Delta}}_c} \leq \min_{\mathbf{D}_\omega \in \boldsymbol{\mathcal{D}}} \bar{\sigma}(\mathbf{D}_\omega \mathbf{N} \mathbf{D}_\omega^{-1}), \tag{4.54}$$

with $\bar{\sigma}(\mathbf{N})$ the largest singular value of the matrix $\mathbf{N}$, $\boldsymbol{\mathcal{D}}$ the set of matrices $\mathbf{D}_\omega$ which commute with the uncertainty set $\hat{\mathbf{\Delta}}_c$, i.e. which satisfy $\mathbf{D}_\omega \hat{\mathbf{\Delta}}_c = \hat{\mathbf{\Delta}}_c \mathbf{D}_\omega$, see e.g. [117] for more details on the computation of lower and upper bounds on the complex structured singular value. Using the upper bound on $\mu_{\hat{\mathbf{\Delta}}_c}$ as

defined above, the optimisation problem (4.51) is relaxed as follows:

$$\min_{\mathbf{K}} \min_{\mathbf{D}\in\boldsymbol{\mathcal{H}}_\infty} \sup_{\omega\in\mathbb{R}} \bar{\sigma}(\mathbf{DND}^{-1}), \tag{4.55}$$

where $\boldsymbol{\mathcal{H}}_\infty$ denotes the set of functions that are analytic and bounded in the open right half plane. The optimisation problem (4.55) is normally iteratively solved for $\mathbf{K}$ and $\mathbf{D}$. This approach is known as D-K-iteration [181]. For a fixed scaling transfer matrix $\mathbf{D}$, the problem reduces to a standard $\mathcal{H}_\infty$ synthesis problem, which can be turned into a convex optimisation problem. The optimisation problem for a fixed controller matrix, i.e. the problem of determining the optimal scaling matrix $\mathbf{D}_\omega$ for a given frequency ω can also be recast in to a convex optimisation problem. Both the $\mathbf{D}$ as well as the $\mathbf{K}$ step in the D-K-iteration can be solved using algorithms from the Robust Control Toolbox of MATLAB [107].

4.5.7 Controller order reduction

Due to the relatively high order of the Padé approximation needed to accurately describe the delay term, the resulting controllers will be of relatively high order ($n_c > 30$), see [33]. As discussed above, the spindle dynamics typically has resonances lying between $1 \cdot 10^3 \leq \frac{\omega_n}{2\pi} \leq 3 \cdot 10^3$ Hz, which will generally result in relatively fast controller poles which in turn require relatively large sample frequencies in a digital implementation. Hence, for the purpose of the feasibility of the implementation of the proposed active chatter control methodology in practice, controller order reduction should be applied.

Balanced truncation is an order reduction procedure which is often applied to tackle such model reduction problems. However, balanced truncation can only be applied in case the system to be reduced is stable. The control synthesis procedure discussed in the previous section does, however, not guarantee the design of stable controllers. To deal with this fact, closed-loop balanced truncation can be applied, see [20].

The controller states which do not contribute significantly to the *closed-loop* input/output of the generalised plant will be removed from the controller using closed-loop balanced truncation. After that, robust performance for the closed-loop system with the reduced-order controller is evaluated by determining $\mu_{\boldsymbol{\Delta}_c}$-values. The acceptable amount of reduction is defined as the smallest controller order for which $\sup_{\omega\in\mathbb{R}} \mu_{\hat{\boldsymbol{\Delta}}_c} < 1$.

As already outlined above, the robust control problem under consideration has structured uncertainties, which will be solved via D-K-iteration. Hence, during closed-loop balanced truncation, the D-scaling matrices obtained during controller synthesis are absorbed into the generalised plant.

4.6 Results

In this section, the results for controller synthesis for a realistic model of a high-speed milling machine is addressed. In order to demonstrate the feasibility of the μ-synthesis approach proposed in the previous section, control design is performed for an illustrative example.

Hereto, consider the parameters of the milling process as given in Table 4.1. The spindle dynamics is modelled, as before, by two decoupled subsystems each consisting of a two mass-spring-damper model in order to capture the inherent compliance between the actuator/sensor system (with mass $m_{a,j},\ j = x, y$) and the cutting tool (with mass $m_{t,j},\ j = x, y$), see Figure 4.4.

The presentation of the results is organised as follows. Firstly, controllers will be synthesised considering the linear actuator model. Stability diagrams will be presented and the results will be compared to the results from time-domain simulations, using the milling model presented in Section 2.6. Secondly, a controller will be designed for the milling model including the AMB model as presented in Chapter 2.

4.6.1 Case study with a linear actuator model

The goal is to design controllers that stabilise milling operations (i.e. guarantee the avoidance of chatter), using the linear actuator model $\underline{F}_a(t) = \mathbf{K}_a \underline{i}_c(t)$, where for sake of simplicity $\mathbf{K}_a$ is chosen as, $\mathbf{K}_a = \mathbf{I}$, for two different ranges of spindle speed intervals, for a range of depth-of-cut a_p which should be as large as possible for a given performance requirement (i.e. for a given limitation of the control gain). Hereto, μ-synthesis (see Section 4.4) is employed within a bi-section scheme, where $\bar{a}_p$ is chosen as the optimisation parameters in the bi-section scheme. Moreover, a controller is designed that stabilises milling operations for a range of spindle speeds where the machine dynamics is uncertain.

The performance requirement, presented in the previous section, is used to limit the actuator forces. The choice of the gain K_p of the performance weighting W_{KS} in (4.35) will influence the maximum depth of cut $\bar{a}_p$ for which robust stability can be guaranteed. In practice, the choice of the gain K_p will be a design trade-off between the maximum achievable force generated by the actuator and the desired maximum achievable depth of cut $\bar{a}_p$. For this illustrative example, it is assumed that the actuator is able to deliver forces up to $1 \cdot 10^3$ N (which is the typical maximum force an AMB can deliver for the spindle under consideration [136]). For the spindle under consideration typical measured displacements $\underline{\tilde{v}}_a(t)$, related to the onset of chatter, are of the order of $1 \cdot 10^{-3}$ mm. Then, an upper bound on the control gain due to physical constraints of the actuator is set to $|\mathbf{K}(s)| = 1 \cdot 10^6$ N/mm and consequently K_p in (4.35) is set equal to $1 \cdot 10^{-6}$ mm/N. Moreover, the remaining parameters of the weighting filter $W_{KS}(s)$ are set to $f_{r,l} = 100$ Hz, $f_{r,h} = 7500$ Hz, $f_{p,l} =$

$1 \cdot 10^{-4}$ Hz and $f_{p,h} = 1 \cdot 10^{5}$ Hz, where the high-frequent roll-off frequency is set to approximately three times the largest eigenfrequency of the machine spindle dynamics and the additional poles are added such that, firstly, W_{KS} is well-posed and, secondly, the generalised plant fulfills the rank conditions typically made in the $\mathcal{H}_\infty$ problem, see [142, p. 354].

Controllers $\mathbf{K}(s)$ are designed for two different ranges of spindle speeds, namely a relatively small interval given as $n \in [27990, 28010]$ rpm and a relatively large interval given as $n \in [36000, 38000]$ rpm. Moreover, a four-fluted tool is considered. Consequently, as already discussed in Section 4.4, a 10-th order Padé approximation is used to approximate the time delay in the milling model. Controller synthesis using D-K-iteration yields a 42-th order controller for a maximal depth of cut of $\bar{a}_p = 2.67$ mm ($\sup_{\omega\in\mathbb{R}} \mu_{\hat{\mathbf{\Delta}}_c} = 0.969$) for $n \in [27990, 28010]$ rpm and a 50-th order controller for a maximal depth of cut of $\bar{a}_p = 2.89$ mm ($\sup_{\omega\in\mathbb{R}} \mu_{\hat{\mathbf{\Delta}}_c} = 0.979$) for $n \in [36000, 38000]$ rpm. The difference between the controller orders is due to a difference in the D-scales.

The controllers are of relatively high order, due to the relatively high-order Padé approximation needed to approximate the delay term. Hence, first the controller order will be reduces by applying closed-loop balanced truncation as discussed in Section 4.5.7. In Figure 4.10, the $\mu_{\hat{\mathbf{\Delta}}_c}$-value for different controller orders (after reduction) are depicted for the two ranges of spindle speeds. In general, closed-loop stability cannot be guaranteed after controller order reduction. Therefore, before determining the $\mu_{\hat{\mathbf{\Delta}}_c}$-value for a specific reduced-order controller, first stability of the nominal closed-loop system is checked. When the closed-loop system is stable the corresponding $\mu_{\hat{\mathbf{\Delta}}_c}$-value is determined. From these results, the lowest controller order is selected for which robust performance can be guaranteed, i.e. the lowest controller order for which $\sup_{\omega\in\mathbb{R}} \mu_{\hat{\mathbf{\Delta}}_c} < 1$. This yields a 24-th order controller for $n \in [27990, 28010]$ and a 18-th order controller for $n \in [36000, 38000]$ rpm. So, it can be concluded that a significant reduction of the controller order can be achieved while still guaranteeing robust stability and performance.

Frequency response functions (FRF) of the full- and reduced-order controllers together with the inverse of the frequency bound imposed on the control sensitivity (i.e. $W_{KS}^{-1}(s)$) are given in Figure 4.11. It can be seen that the resulting controllers exhibit highly dynamical characteristics indicated by the inverse notches in the FRF. Moreover, compared to the small spindle speed range ($n \in [27990, 28010]$ rpm), the (inverse) notch-like characteristics of the controller designed for the larger spindle speed range ($n \in [36000, 38000]$ rpm), exhibit more damping. Next, it can be concluded that the magnitude of the controllers do not exactly fulfill the imposed bound, which is due to the fact that the bound is imposed on the control sensitivity $\mathbf{KS}(s) = (\mathbf{I} - \mathbf{K}(s)\mathbf{P}_{KS}(s))^{-1}\mathbf{K}(s)$. Moreover, it can be seen that the full- and reduced-order controller have similar FRF magnitudes (therefore, the difference is hardly visible in Figure 4.11). Hence, it is expected that robust performance is maintained under controller-

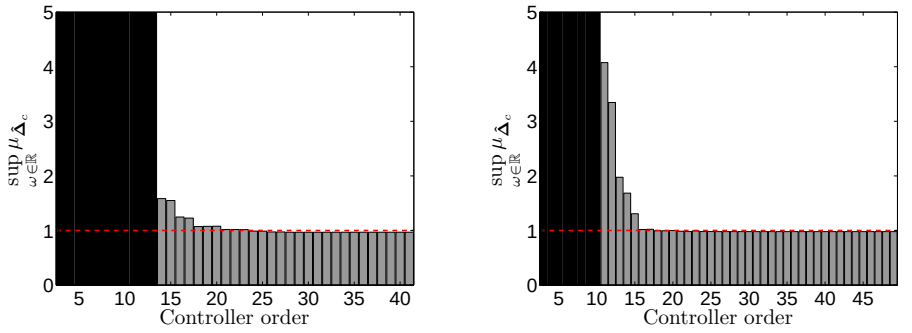

(a) $n \in [27990, 28010]$ rpm. (b) $n \in [36000, 38000]$ rpm.

Figure 4.10: Closed-loop $\mu_{\hat{\mathbf{\Delta}}_c}$-values for reduced controllers using closed-loop balanced truncation. Black bars indicate an unstable closed-loop.

order reduction. To verify whether robust performance is maintained, stability lobes diagrams (SLDs) are determined using the linearised non-autonomous milling model (Equation (4.2)), as outlined in Section 2.7, for the case with and without control. The resulting SLDs can be found in Figure 4.12. It can be seen that the SLD of the controlled milling are shaped such that it contains a lobe in the desired spindle speed range. Stability is ensured up to a depth of cut $a_{p,\mathsf{max}} = 2.91$ mm (an increase of approximately 660% compared to the case without control) and $a_{p,\mathsf{max}} = 3.37$ mm (an increase of approximately 250% compared to the case without control) where controllers are designed for $n \in [27990, 28010]$ rpm and $n \in [36000, 38000]$ rpm, respectively. Herein, $a_{p,\mathsf{max}}$ denotes the maximal achievable depth of cut in the SLD in the desired spindle speed range. Figure 4.12 clearly illustrates the power of the proposed approach, as the SLD is shaped locally to be able to increase a_p at a specific spindle speed (while avoiding chatter and satisfying a specified bound on the control gain). This is contrary to the application of active damping which lifts the SLD over the entire spindle speed range at the cost of high required levels of actuation energy. Whereas stability is increased at the desired spindle speeds, it decreases significantly at other spindle speeds. The characteristics of the controller design and its ability to shape the SLD in a dedicated fashion can be explained by further examining the controlled spindle dynamics.

The FRF of the closed-loop tool-tip spindle dynamics $\mathbf{G}_{tt,c}(s)$ (i.e. the FRF from $\underline{\tilde{F}}_t(t)$ to $\underline{\tilde{v}}_t(t)$) is given, together with the original (uncontrolled) spindle dynamics, in Figure 4.13. While the original (uncontrolled) spindle dynamics only has x- and y-components (due to decoupled spindle dynamics), the controlled machine dynamics also has off-diagonal components. This can be explained by the fact that controller design is performed using the complete

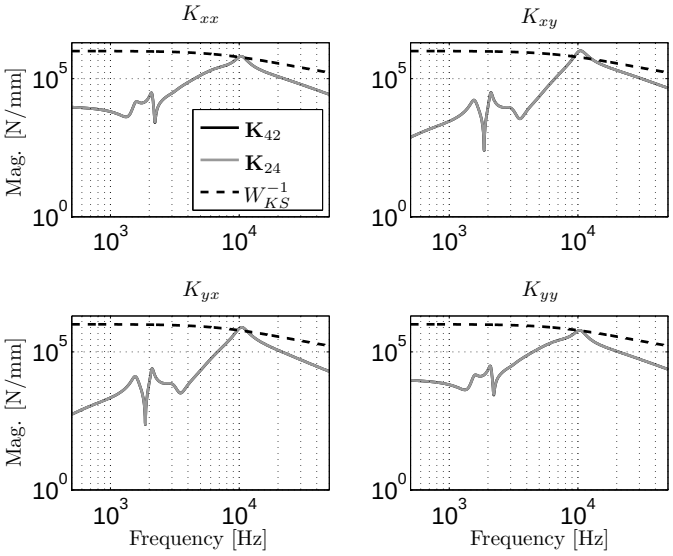

(a) $n \in [27990, 28010]$ rpm.

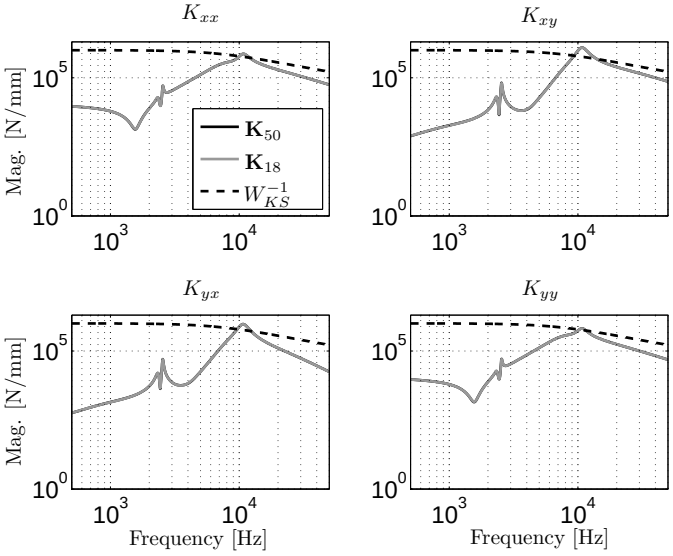

(b) $n \in [36000, 38000]$ rpm.

Figure 4.11: Magnitude of FRF *of the full-order (black) and reduced-order (grey) controllers obtained by D-K-iteration for two different range of spindle speeds $n \in [27990, 28010]$ and $n \in [36000, 38000]$ rpm. The difference between the controller orders is due to a difference in the D-scales.*

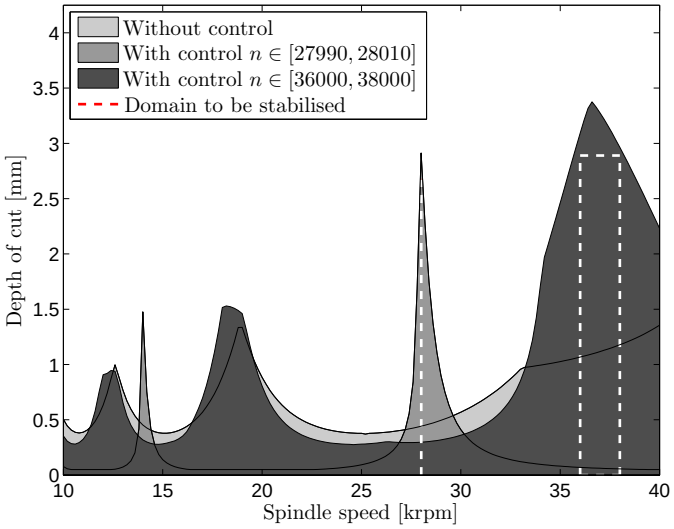

Figure 4.12: Stability lobes diagrams, determined using the linearised nonautonomous milling model (4.2)*, for reduced-order controllers designed for two different range of spindle speeds,* $n \in [27990, 28010]$ *and* $n \in [36000, 38000]$ *rpm.*

milling model where coupling between x- and y-direction is introduced by the cutting force model (resulting in a full matrix $\bar{\mathbf{H}}$ in (4.17) and consequently in a full 2×2 controller $\mathbf{K}(s)$, see also Figure 4.11).

A striking characteristic displayed in Figure 4.13 is the fact that the controller has tailored the spindle dynamics such that the resonances are shifted. For the small spindle speed range ($n \in [27990, 28010]$ rpm), a dominant weakly damped resonance can be seen which is located at $f = 1867$ Hz. A better damped resonance around $f = 2400$ Hz, which lies at the edge of the range of desired tooth passing frequencies, is created in case of the larger spindle speed range ($n \in [36000, 38000]$ rpm). As a matter of fact, the location of these resonances correspond to the tooth passing excitation frequencies $f_{tpe} = \frac{nz}{60}$ for milling operations within the defined spindle speed ranges (in this case $n = 28000$ rpm and $n = 36000$ rpm, respectively). Hence, it can be concluded that, in order to create a stability lobe at a certain spindle speed, the resonance frequency of the spindle dynamics should be set equal to the corresponding tooth passing excitation frequency, see also [8]. The fact that a closed-loop spindle resonance situated at a tooth-passing excitation frequency is beneficial for avoiding chatter can be explained as follows. In the milling process the highest depth of cut can be obtained (corresponding to a peak in the SLD) when the dynamic chip thickness $h_{j,\mathsf{dyn}}(t) = \underline{v}_t(t) - \underline{v}_t(t-\tau)$ is equal

to zero. This relation can be transformed to the frequency domain as follows:

$$\underline{H}_{j,dyn}(i\omega) = (1 - e^{-i\omega\tau})\underline{V}_t(i\omega) =: Q(i\omega)\underline{V}_t(i\omega), \tag{4.56}$$

where $\underline{H}_{j,dyn}(i\omega)$ and $\underline{V}_t(i\omega)$ are the Fourier transforms of $h_{j,\mathsf{dyn}}(t)$ and $\underline{v}_t(t)$, respectively. Hence, the difference between the tooltip displacements of the present and previous cut is actually characterised by a filter, denoted by $Q(i\omega)$, with zeros at $l\omega\tau = l\omega\frac{1}{f_{tpe}}$, $l = 0, 1, 2, \ldots$. Moreover, for the milling process, the dominant (chatter) frequency of the perturbation vibrations lies in general close to the eigenfrequency of the spindle dynamics [77]. Then, by designing the controller such that the closed-loop resonance is close to a tooth-passing frequency and due to the filter properties of the $Q(i\omega)$ (in particular the location of the zeros of $Q(i\omega)$ at f_{tpe}-related frequencies), the dynamic chip thickness is enforced to be zero at the desired spindle speed. This, in turn, results in a large depth of cut within the desired spindle speed range and a peak in the SLD at that spindle speed. So, by means of applying robust control design techniques, a controller is obtained which tailors the tooltip spindle dynamics, such that a resonance is created at a tooth passing harmonic which in turn results in a peak in the SLD. Comparing this with the analysis given for the spindle speed selection procedure, as discussed in Chapter 3, it can be seen that the line of reasoning is similar for both cases. The adaptive spindle speed selection control algorithm alters, in case of (onset) of chatter, the spindle speed, resulting in a change in the delay τ, and therewith the zeros of $Q(i\omega)$ are altered, whereas the active chatter control procedure, proposed in this chapter, alters the frequency content of $\underline{V}_t(i\omega)$ such that it matches the zeros of $Q(i\omega)$.

Next, controllers will be determined for a spindle speed range of $n \in [29000, 31000]$ rpm where, not only uncertainties in spindle speed and depth of cut are considered, but also the spindle dynamics are considered uncertain. This is an important aspect from a practical point of view, since, as described before, the spindle dynamics depends on the spindle speed. As before, the parameters of the milling process as given in Table 4.1 are considered, and the parameters of the weighting filter W_{KS} as defined above. It is assumed that the natural frequencies $\omega_{a,x}$, $\omega_{a,y}$ and the damping ratios $\zeta_{a,x}$, $\zeta_{a,y}$ may vary up to 5% of their nominal values. Hereto, consider the following definitions of the vector of natural frequencies $\underline{\omega}_{n,0}$ and dimensionless damping ratios $\underline{\zeta}_0$:

$$\underline{\omega}_{n,0} = \begin{bmatrix}\omega_{a,x} & \omega_{a,y} & \omega_{t,x} & \omega_{t,y}\end{bmatrix}^T, \ \underline{\zeta}_0 = \begin{bmatrix}\zeta_{a,x} & \zeta_{a,y} & \zeta_{t,x} & \zeta_{t,y}\end{bmatrix}^T.$$

Then, the relative uncertainty parameters are set as $r_{\omega,j} = r_{\zeta,j} = 0.05$ for $j = 1, 2$ in (4.30) and (4.31). D-K-iteration yields a controller of order 66 for a maximal depth of cut of $\bar{a}_p = 1.69$ mm ($\sup_{\omega\in\mathbb{R}} \mu_{\hat{\mathbf{\Delta}}_c} = 0.96$). After closed-loop balanced truncation the controller order can be reduced to 29 ($\sup_{\omega\in\mathbb{R}} \mu_{\hat{\mathbf{\Delta}}_c} = 0.97$). Stability lobes diagrams (SLDs) are determined using the reduced-order controller where 50 (randomly chosen) samples are taken

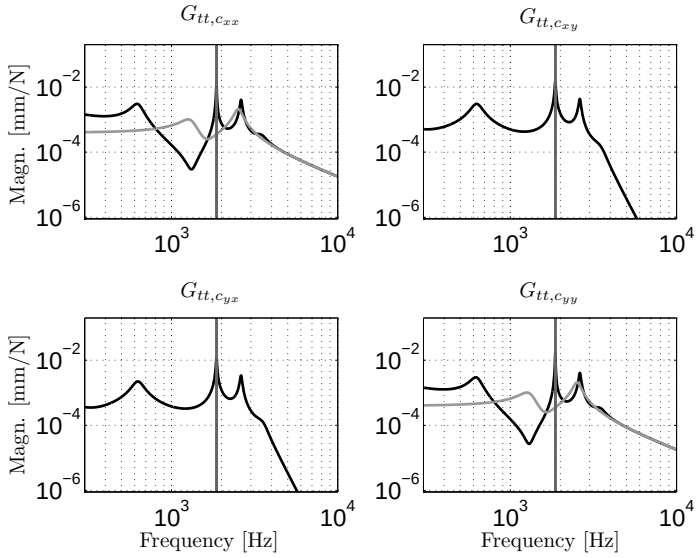

(a) $n \in [27990, 28010]$ rpm.

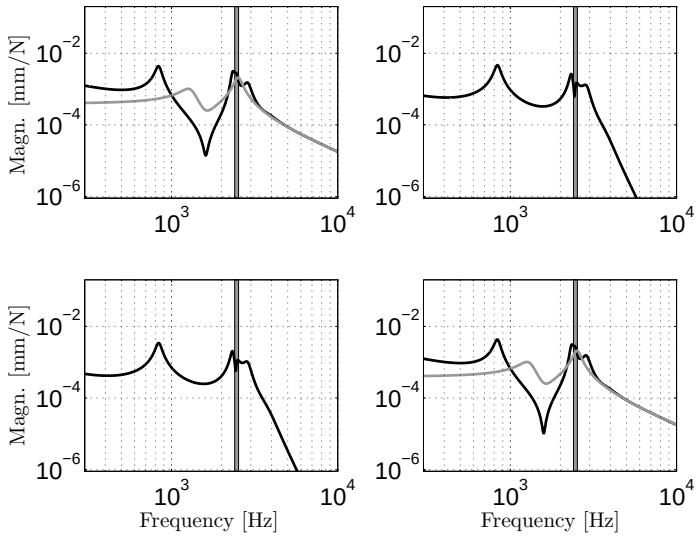

(b) $n \in [36000, 38000]$ rpm.

Figure 4.13: Controlled $\mathbf{G}_{tt,c}(i\omega)$ (black) and uncontrolled (open-loop) $\mathbf{G}_{tt}(i\omega)$ (grey) tooltip spindle dynamics for reduced-order controllers designed for the two different range of spindle speeds, $n \in [27990, 28010]$ and $n \in [36000, 38000]$ rpm. The interval of tooth passing excitation frequencies corresponding to the spindle speed range is indicated by the grey area.

from the uncertain spindle dynamics set. The results are gathered in Figure 4.14. From the stability lobes diagram, given in Figure 4.14(a), it can be seen that, again, the SLD (which, in this case, gives a range of stability boundaries, indicated by the grey area in Figure 4.14(a), due to the uncertain spindle dynamics) is altered such that the desired domain of stable operating points is stabilised (for any sample of the uncertain spindle dynamics in the uncertainty set). Due to the presence of the spindle dynamics uncertainty, the maximal depth of cut for which stability is guaranteed (in this case $\bar{a}_p = 1.69$ mm) will be lower than for the case without spindle dynamics uncertainty, which is as expected. Samples of the uncertain closed-loop tooltip spindle dynamics are given in Figure 4.14(b). Also the nominal spindle dynamics (i.e. the spindle dynamics for $r_{\omega,j} = r_{\zeta,j} = 0$ for $j = 1, 2$) with (solid) and without (dashed) control are given. As before, it can be seen that the closed-loop spindle dynamics is tailored such that a closed-loop resonance is situated at a tooth passing harmonic (in this case around 2000 Hz which is the tooth passing frequency at $n = 30000$ rpm) resulting in a peak in the SLD at the desired spindle speed interval. Moreover, it can be seen that the uncertain spindle speed modes are moved to a lower frequency region.

In the final part of this section, some results from time-domain simulations (TDS) will be discussed. Hereto, the nonlinear nonautonomous delay differential equations describing the total milling model, given by (4.1), have been implemented in MATLAB/SIMULINK [107]. The purpose of the TDS is to demonstrate the difference between the two different choices of feedback signal, i.e. using full output feedback ($c = 0$) and using perturbation feedback ($c = 1$), see Section 4.3. In order to apply perturbation feedback, the periodic solution $\underline{x}^*(t)$ has to be known. As already explained in Section 4.3, in case of perturbation feedback, the periodic solution of the closed-loop system becomes equal to the periodic solution of the open-loop system which is the solution of (2.15). To apply perturbation feedback in the TDS the ordinary differential equation (ODE) describing the periodic solution dynamics (i.e. Equation (2.15)) is included in the MATLAB/SIMULINK model. In practice, the perturbation displacements $\underline{\tilde{v}}_a(t)$ can be obtained by using a chatter detection algorithm based on a parametric model of the milling process, as described in Section 3.2.

The controller determined for the spindle speed range of $n \in [36000, 38000]$ rpm is used during the TDS. In order to compare the performance of the milling process with and without chatter control the simulation is performed for an operating point which is originally unstable, but is stabilised by means of control. Here, the operation point under consideration has the process parameters $n = 37000$ rpm and $a_p = 2$ mm, which is originally an unstable working point (see Figure 4.12). The results are gathered in Figures 4.15 and 4.16. Figure 4.15 presents the displacements at the tooltip with control off, control on with full output feedback ($c = 0$) and control on with perturbation feedback ($c = 1$). Furthermore, the τ-sampled tool displacements are depicted by dots.

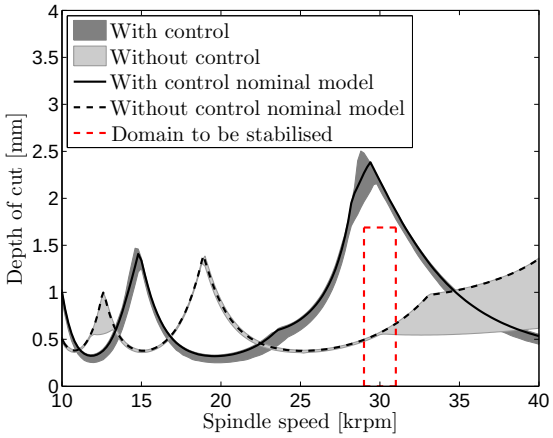

(a) Stability lobes diagram.

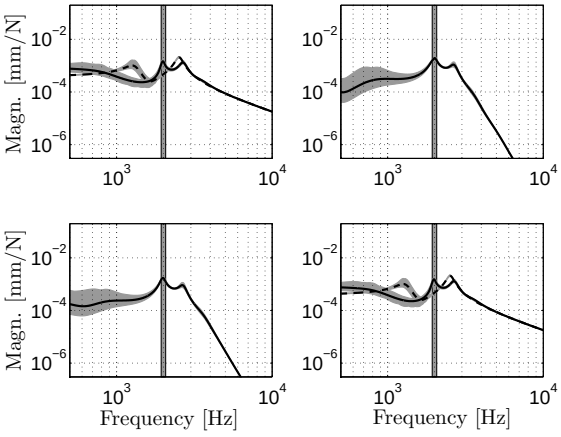

(b) Tooltip FRF.

Figure 4.14: Stability lobes diagram and controlled $\mathbf{G}_{tt,c}(i\omega)$ and uncontrolled (open-loop) $\mathbf{G}_{tt}(i\omega)$ tooltip spindle dynamics for reduced-order controllers designed for a range of spindle speeds, $n \in [29000, 31000]$, where the spindle dynamics is considered uncertain. Samples of the uncertain machine dynamics (grey) are used to determine SLD *and* FRFs*. Moreover, the nominal* FRF *and corresponding* SLD *(i.e. $r_{\zeta,j} = r_{\omega,j} = 0$ for $j = 1, 2$ in (4.30) and (4.31)) of the controlled (solid) and uncontrolled (dashed) tooltip spindle dynamics are given in black. The interval of tooth passing excitation frequencies corresponding to the spindle speed range is indicated by the grey box.*

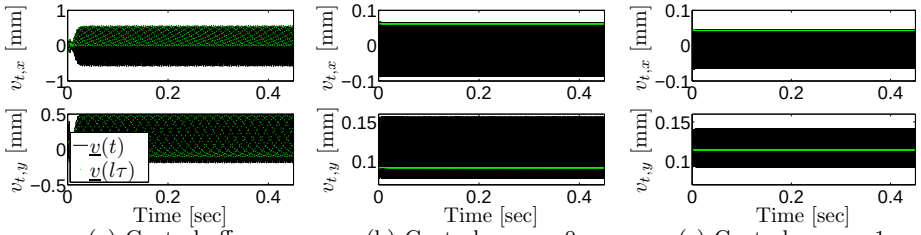

(a) Control off. (b) Control on, $c = 0$. (c) Control on, $c = 1$.

Figure 4.15: Displacements at the tooltip $\underline{v}_t(t)$ for a time-domain simulation performed for $n = 37000$ rpm and $a_p = 2$ mm where the controller designed for a spindle speed range of $n \in [36000, 38000]$ rpm is switched on and off. For the case where the controller is switched on, full output ($c = 0$) and perturbation feedback ($c = 1$) is considered.

When the control is switched off the periodic motion becomes unstable. It can be seen that in that case the displacement results in a quasi-periodic motion. When the controller is switched on, the motion for the initially unstable working point is stabilised, which can be seen from the τ-sampled displacements. Note that the stabilised motion is the τ-periodic non-chatter solution of the periodic DDE describing the milling process. Moreover, it can be seen that the amplitude of the displacements is considerably smaller for the case with active chatter control as compared to the uncontrolled case. It should be noted that the motions for the two cases where the controller is switched on differ. This is due to the fact that a different input signal is applied to the controller (either the full displacements or the perturbation motion are used as controller input signal). As shown in Section 4.3, in case of perturbation feedback, the resulting stable motion is equal to the open-loop periodic motion while this is not the case when full output feedback is applied. The difference between the two choices of the controller input signal can also be seen when regarding the actuator forces needed to stabilise the milling process, see Figure 4.16. It can be seen that, when perturbation feedback is applied, the actuator forces are (almost) zero. This is due to the fact that, when the milling operation is stable, the perturbations about the periodic solution are zero. Hence, the actuator forces will be zero in steady state. Since the nominal solution of the milling process is a periodic solution, the actuator forces will be nonzero for the full output feedback case. The results from time-domain simulations clearly demonstrate the benefit of applying perturbation feedback.

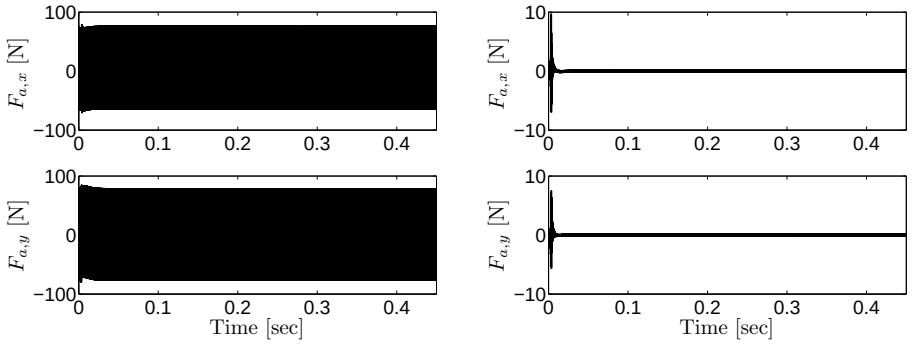

(a) Control on, $c = 0$. (b) Control on, $c = 1$.

Figure 4.16: Actuator forces $\underline{F}_a(t)$ for a time-domain simulation performed for $n = 37000$ rpm and $a_p = 2$ mm and full output ($c = 0$) and perturbation feedback ($c = 1$) is considered. The controller is designed for a spindle speed range of $n \in [36000, 38000]$ rpm.

4.6.2 Case study with an AMB model

Next, the results will be presented where controllers are determined to alter the chatter stability boundary while including the AMB model with perturbation feedback in the milling model, as presented in Section 2.5. The parameters of the AMB model are listed in Table 4.2 and are taken from [133]. The goal is to design a controller that stabilises milling operations for $n \in [30000, 32000]$ rpm, for a depth of cut which is as large as possible given the performance requirement on the control sensitivity **KS**. Hereto, again μ-synthesis is applied within a bi-section scheme. For an AMB it is important to limit the input current in order not to exceed the maximum amount of carrying force. Here, the bound on the input current is set to $i = 2$ A. Together with typical bearing displacements $\underline{\tilde{v}}_a(t)$, related to the onset of chatter, of approximately $1 \cdot 10^{-3}$ mm, K_p is set $1 \cdot 10^{-3}/2$ mm/A. Next, D-K-iteration yields a 36-th order controller for a maximal depth of cut of $\bar{a}_p = 2.18$ mm, where $\sup_{\omega \in \mathbb{R}} \mu_{\hat{\mathbf{\Delta}}_c} = 0.9915$. Closed-loop controller reduction yields a 16-th order controller, where $\sup_{\omega \in \mathbb{R}} \mu_{\hat{\mathbf{\Delta}}_c} = 0.9964$.

Frequency response functions (FRF) of the full- and reduced-order controllers together with the inverse of the frequency bound imposed on the control sensitivity (i.e. $W_{KS}^{-1}(s)$) are given in Figure 4.17. It can be seen that, as before, the resulting controllers exhibit highly dynamical characteristics indicated by the inverse notches in the FRF. Moreover, as before, the difference between the full- and reduced-order is hardly visible in Figure 4.17.

Using the reduced-order controller, the chatter stability boundary is determined using the linearised milling model with the AMB model as in (4.14).

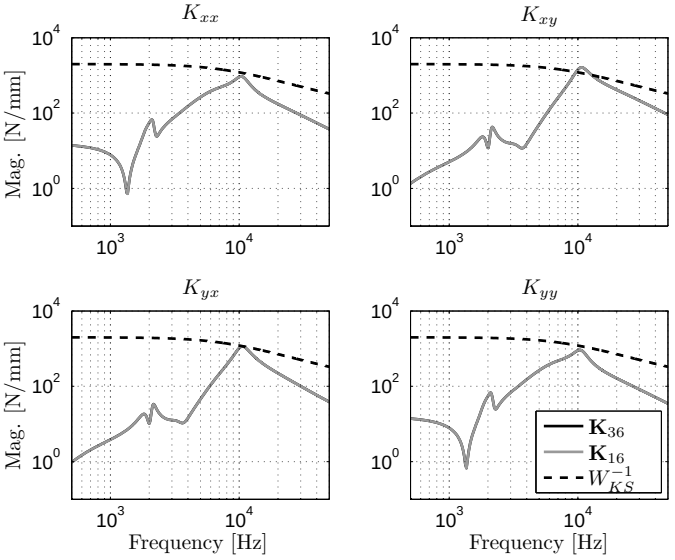

Figure 4.17: Magnitude of FRF *of the full-order (black) and reduced-order (grey) controllers obtained by D-K-iteration for the* AMB *model for a spindle speed range of* $n \in [30000, 32000]$ *rpm.*

Figure 4.18 gives the chatter stability boundary with and without control. It can be seen that, as for the case with the linear actuator model, the controller tailors the stability boundary such that a lobe is created at the desired spindle speed range. Stability is ensured up to a depth of cut of $a_{p,\max} = 2.663$, which leads to an improvement of approximately 239% compared to the case without control.

Time-domain simulations are performed for the actual milling model with the nonlinear bearing model, as presented in Section 2.5, using the reduced-order controller while considering perturbation feedback ($c = 1$). The results are shown in Figures 4.19 and 4.20 for $n = 31000$ rpm and $a_p = 2.0$ mm. Figure 4.19 gives the displacements at the tooltip in feed (x)- and normal (y)-direction with and without control. Furthermore, the τ-sampled displacements are shown by dots. It can be seen that without control, the amplitude of the displacements becomes relatively large (approximately 35 % of the tool radius which is chosen as 5 mm), which will result in the tool jumping in and out of cut resulting in an inferior workpiece quality. For the case with control, the motion is stable. This can be seen from the fact that the τ-sampled displacements remain constant. The actuator input currents are given in Figure 4.20. Due to the fact that perturbation feedback is applied, the (steady-state) actuator current, after some transients at the start of the simulation, are (almost)

Table 4.2: Parameters of the AMB *model, see [133].*

Parameter	Value	Unit
$k_{\mathsf{amb},x} = k_{\mathsf{amb},y}$	$1.2566 \cdot 10^{-5}$	$[\mathrm{Nm}^2/\mathrm{A}^2]$
i_0	2.5	[A]
v_0	$0.5 \cdot 10^{-3}$	[m]

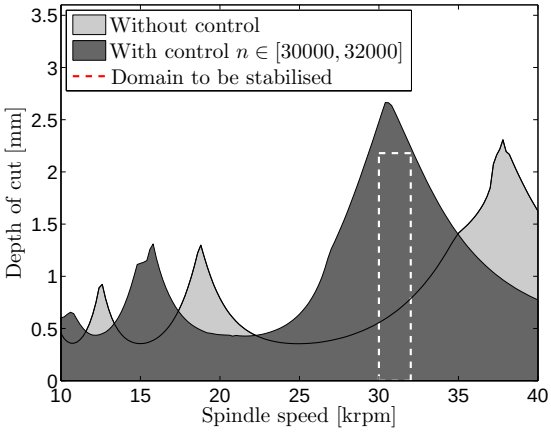

Figure 4.18: Stability lobes diagram for reduced order controller designed a range of spindle speeds, $n \in [30000, 320000]$ and using the AMB *model.*

zero. From the results of the time-domain simulations, it can be seen that the assumptions, for which the linear AMB model is a good approximation of the nonlinear AMB model, as discussed in 2.5, remain valid.

4.6.3 Discussion of the results

Based on the results discussed in this section, it can be concluded that the active chatter control design methodology, as proposed in this chapter, guarantees *a priori* stability for a pre-defined area of working-points. Such a strong guarantee of a priori stability is not yet available in chatter control literature for the milling process. Hereto, robust control techniques based on μ-synthesis are employed, which allow additional uncertainties in the model to be taken into account during controller design. Controllers obtained via D-K-iteration tailor the closed-loop spindle dynamics (e.g. uncertain spindle dynamics) in such a way that a resonance is situated near a tooth pass excitation frequency of the desired (range of) spindle speeds. As a result, the MRR of the process can be significantly increased in the desired range of operating points. Moreover,

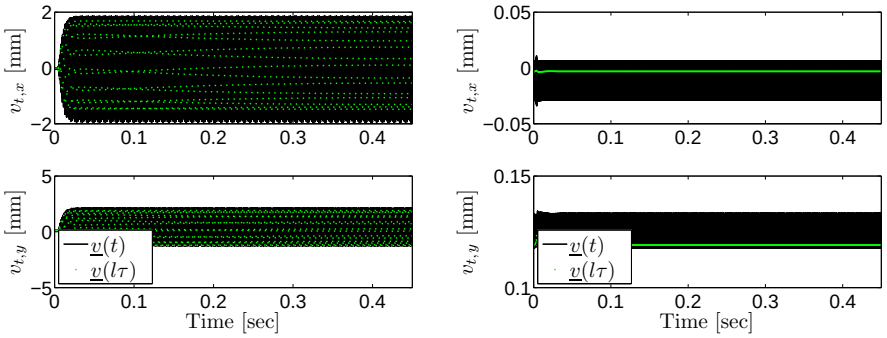

(a) Control off. (b) Control on, $c = 1$.

Figure 4.19: Displacements at the tooltip $\underline{v}_t(t)$ for a time-domain simulation performed for $n = 31000$ rpm and $a_p = 2$ mm with and without control using the nonlinear AMB model. The controller is designed for a spindle speed range of $n \in [30000, 32000]$ rpm.

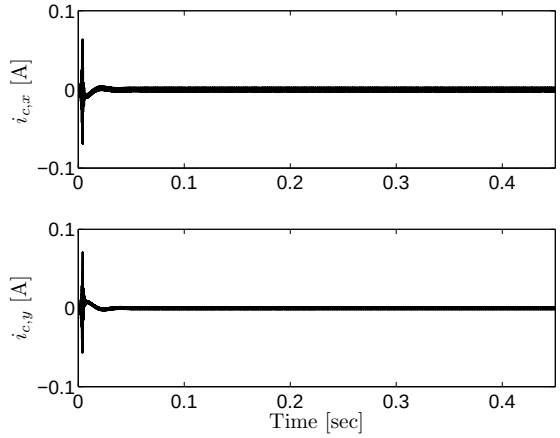

Figure 4.20: Actuator input currents $\underline{i}_c(t)$ for a time-domain simulation performed for $n = 31000$ rpm and $a_p = 2$ mm where perturbation feedback is considered. The controller is designed for a spindle speed range of $n \in [30000, 32000]$ rpm.

by means of time-domain simulations, it is shown that the required actuator forces, needed for stabilising the milling process, are zero in steady-state when perturbation feedback is applied.

4.7 Discussion

In this chapter, an active chatter control design methodology for the suppression of regenerative chatter in the high-speed milling process has been developed. The main purpose of the control design is the suppression of chatter (i.e. stabilisation of the milling process) in an a priori specified range of process parameters (spindle speed and depth of cut), such that working points of significantly higher productivity become feasible while avoiding undesirable chatter vibrations. Herein, the requirement for a priori stability guarantee for a predefined range of process parameters is cast into a robust stability requirement. Moreover, a performance requirement is imposed on the control sensitivity in order to limit the actuator forces. Existing chatter control strategies for the milling process cannot provide such a strong guarantee of a priori stability for a predefined range of working points. The control problem is solved via μ-synthesis using D-K-iteration. The resulting controllers tailor the closed-loop spindle dynamics in such a way that a resonance is situated near a tooth pass excitation frequency of the desired (range of) spindle speeds which results in a peak in the SLD at the desired (range of) spindle speeds. In addition, it is shown that the actuator forces, needed to stabilise the milling process, will be zero in steady state in case of perturbation feedback (i.e. only chatter vibrations are used as a feedback signal) whereas the actuator forces will be non-zero in steady state in case of full output feedback. This result is exploited for a milling model incorporating an active magnetic bearing model, where it is important to limit the actuator input current in order to avoid actuator saturation.

Results, for illustrative examples, clearly illustrate the power of the proposed control methodology. The chatter stability boundary is locally shaped to stabilise the desired range of working points. This is contrary to the application of active damping which lifts the SLD over the entire spindle speed range at the cost of high required levels of actuation energy. By means of illustrative examples it is shown that this control strategy can render working points of significantly higher productivity stable.

5

Fixed structure active chatter control design

5.1 Introduction

In the previous chapter, an active chatter control design methodology is presented that, by altering the machine dynamics, actively shapes the SLD. The control design procedure, based on μ-synthesis using a finite-dimensional time invariant approximation of the milling model, results in relatively high-order controllers due to the relatively high-order Padé approximation required to accurately approximate the delay term in the desired spindle speed range. As shown, the order of the controller can be reduced using closed-loop balanced truncation techniques. However, in general, no guarantees can be given regarding closed-loop stability and (robust) performance of the closed-loop system with the reduced-order controller obtained in this fashion.

Therefore, in this chapter a fixed structure control design methodology for time delay systems with structured uncertainties will be presented. More specifically, a design methodology, that results in fixed structure active chatter controllers for the milling process, is presented. The controller will be designed using μ-synthesis techniques for an infinite-dimensional model of the milling process, i.e. without approximation of the delay term in the milling model (as was employed in Chapter 4). The resulting linear fixed-structure controller is of fixed-order. Hence, the order of the controller can be directly imposed by the user.

Fixed-structure or fixed-order controller synthesis is an ongoing research field in the present day control engineering. It is desired to limit the complexity of the controller, due to e.g. hardware limitations which limit the sampling interval and the necessity for on-site tuning [105]. In general, a fixed-structure

control problem cannot be transformed into a convex optimisation problem. In [69], a model-based fixed-structure controller synthesis methodology based on linear matrix inequalities is presented, which may lead to computational issues for increasing complexity of the plant model. A fixed structure controller design using a data-based approach is presented in [65]. In [9], a fixed-structure $\mathcal{H}_\infty$ synthesis method for LTI systems is developed which avoids the use of Lyapunov techniques.

For time delay systems, results are often obtained using a Lyapunov-based approach, see e.g. [10, 56, 61]. An advantage of the Lyapunov approach is that it allows the incorporation of a more general class of uncertainties, such as time-varying uncertainties. However, the resulting optimisation problems are in the form of bi-linear matrix inequalities where the number of unknown variables in general grows quadratically with the number of states [9] which may lead to computational issues. Moreover, generally the application of a Lyapunov approach leads to conservative results. The usage of an eigenvalue based approach can overcome these disadvantages as explained in [109]. In [162], the algorithm presented in [15] is applied to the stabilisation problem for linear time-delay systems by tuning a finite number of controller parameters. The approach, as outlined in this chapter, can be seen as an extension of the work in [162] towards robust stabilisation of time-delay systems, for the case of the high-speed milling process, with structured uncertainties.

The chapter is organised as follows. First, the problem statement will be discussed in Section 5.2.1. Secondly, the generalised plant, for which the controllers will be designed, is presented in Section 5.2.2. After that, the algorithm for synthesising fixed structure active chatter controllers for the infinite-dimensional model describing the milling process in the presence of uncertainties will be presented in Section 5.2.3. In Section 5.3, the results of the fixed structure controllers, designed for the high-speed milling process using relatively simple models of the spindle-toolholder-tool dynamics, will be discussed. Finally, a discussion of the presented results will be given in Section 5.4.

5.2 Fixed structure active chatter control design

In this section, the fixed structure active chatter control design procedure based on an infinite-dimensional LTI model of the milling process will be described. First, the problem will be stated. Secondly, the generalised plant will be formulated. Finally, the fixed structure active chatter control synthesis algorithm will be presented.

5.2.1 Problem statement

Consider the linearised time-invariant uncertain model of the milling process with a linear actuator model, as derived in Section 4.4, given as follows:

$$\begin{aligned}\dot{\underline{\tilde{x}}}(t) &= (\mathbf{A} + a_p\mathbf{B}_t\bar{\mathbf{H}}\mathbf{C}_t)\underline{\tilde{x}}(t) - a_p\mathbf{B}_t\bar{\mathbf{H}}\mathbf{C}_t\underline{\tilde{x}}(t-\tau) + \mathbf{B}_a\mathbf{K}_a\underline{\tilde{i}}_c(t),\\ \underline{\tilde{v}}_a(t) &= \mathbf{C}_a\underline{\tilde{x}}(t).\end{aligned} \tag{5.1}$$

with uncertainty sets $a_p \in [0, \bar{a}_p]$ and $\tau \in [\underline{\tau}, \bar{\tau}]$, respectively, for the depth of cut and the delay. The aim of this chapter is to design a finite-dimensional linear controller $\mathbf{K}$ with controller input $\underline{y}(t) = \underline{v}_a(t) - c\underline{v}_a^*(t)$ as defined in Section 4.3 and controller output $\underline{\tilde{i}}_c(t)$, which guarantees:

- robust stability of $\underline{\tilde{x}} = \underline{0}$ for the given uncertainties in depth of cut a_p and time delay τ;
- performance by minimising the $\mathcal{H}_\infty$-norm of the control sensitivity $\mathbf{KS}$, where $\mathbf{KS}$ is the transfer function from an input $\underline{r}$ to controller output $\underline{\tilde{i}}_c$ (see also Figure 4.7 in Chapter 4).

Herewith, the actuator forces will be limited during the controller design, which is an important practical performance requirement. As in Chapter 4, it is assumed that the controller $\mathbf{K}$ has the following state-space description,

$$\begin{aligned}\dot{\underline{\xi}}(t) &= \mathbf{A}_c\underline{\xi}(t) + \mathbf{B}_c\underline{y}(t),\\ \underline{i}_c(t) &= \mathbf{C}_c\underline{\xi}(t) + \mathbf{D}_c\underline{y}(t),\end{aligned} \tag{5.2}$$

where $\mathbf{A}_c \in \mathbb{R}^{n_c\times n_c}$, $\mathbf{B}_c \in \mathbb{R}^{n_c\times 2}$, $\mathbf{C}_c \in \mathbb{R}^{2\times n_c}$ and $\mathbf{D_c} \in \mathbb{R}^{2\times 2}$ with n_c the order of the controller.

5.2.2 Generalised plant formulation

In order to solve the problem stated in the previous section, i.e. in order to design the fixed structure controller $\mathbf{K}$ which ensures robust stability and performance of the milling process, the control problem is cast into the generalised plant formulation. Figure 5.1 shows the schematic configuration employed in this framework. The generalised plant $\mathbf{P}$ is a given system with three sets of inputs and three sets of outputs. The signal pair $\underline{p}, \underline{q}$ denote the in-/outputs of the uncertainty channel. The signal $\underline{r}$ represents an external input in which possible disturbances, measurement noise and reference inputs are stacked. The signal $\underline{\tilde{i}}_c$ is the control input. The output $\underline{z}$ can be considered as a performance variable. In this case, $\underline{z}$ will be considered as the weighted control input, see Figure 4.7 in Chapter 4, in order to limit the controller effort required for stabilising the uncertain milling process. The output $\underline{y}$, finally, is the measured output, and is available for feedback. In general, the generalised plant $\mathbf{P}$ contains a mathematical model of the plant to be controlled (i.e. the nominal plant,

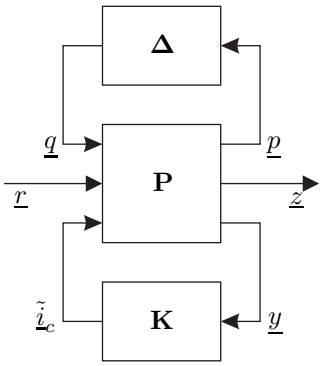

Figure 5.1: Generalised plant interconnection.

given by (5.1) with $a_p = \frac{1}{2}\bar{a}_p$ and $\tau = \tau_0$, where $\tau_0 = \frac{\bar{\tau}+\underline{\tau}}{2}$) and one or more weighting filters. These weighting filters are included in order to specify the desired shapes of the closed-loop transfer function from $\underline{r}$ to $\underline{z}$. The remainder of this section describes the transformation of the uncertain plant (5.1) into the generalised plant framework, whereas the next section presents the actual optimisation problem for fixed structure controller design.

In Section 4.5, an elaborate discussion regarding modelling uncertainties in the depth of cut a_p and spindle speed n is given. In this chapter, the same methodology for uncertainty modelling is followed. Hence, the uncertainty sets as defined in Section 5.2.1 are given as follows:

$$a_p = \tfrac{1}{2}\bar{a}_p(1+\delta_{a_p}), \qquad \tau = \tau_0 + \delta_\tau, \tag{5.3}$$

where $\bar{a}_p$ is the maximal depth of cut for which stable cutting is desired, $\delta_{a_p} \in \mathbb{C}$, $|\delta_{a_p}| \leq 1$ and $\delta_\tau \in \frac{\bar{\tau}-\underline{\tau}}{2}[-1,1]$. Moreover, in this case, the performance output is chosen as the weighted control input $\underline{z}(s) = \mathbf{W}_{KS}(s)\underline{\tilde{i}}_c(s)$, $s \in \mathbb{C}$, where $\mathbf{W}_{KS}$ is a stable weighting filter with the following state-space realisation:

$$\begin{aligned} \dot{\underline{x}}_{KS}(t) &= \mathbf{A}_{KS}\underline{x}_{KS}(t) + \mathbf{B}_{KS}\underline{\tilde{i}}_c(t), \\ \underline{z}(t) &= \mathbf{C}_{KS}\underline{x}_{KS}(t) + \mathbf{D}_{KS}\underline{\tilde{i}}_c(t). \end{aligned} \tag{5.4}$$

Substituting (5.3) in (5.1) and by adding the performance channel in-/output to the system and rearranging terms, the state-space representation of the

generalised plant $\mathbf{P}$ is given as follows:

$$\begin{aligned}\dot{\underline{x}}_P(t) &= \mathbf{A}_{P,0}\underline{x}_P(t) + \mathbf{A}_{P,1}\underline{x}_P(t-\tau_0) + \mathbf{B}_P \begin{bmatrix}\underline{q}(t)\\ \underline{r}(t)\\ \tilde{\underline{i}}_c(t)\end{bmatrix}\\ \begin{bmatrix}\underline{p}(t)\\ \underline{z}(t)\\ \underline{y}(t)\end{bmatrix} &= \mathbf{C}_{P,0}\underline{x}_P(t) + \mathbf{C}_{P,1}\underline{x}_P(t-\tau_0) + \mathbf{D}_P \begin{bmatrix}\underline{q}(t)\\ \underline{r}(t)\\ \tilde{\underline{i}}_c(t)\end{bmatrix}\end{aligned} \tag{5.5}$$

with the state vector $\underline{x}_P(t) = [\tilde{\underline{x}}^T(t)\ \underline{x}_{KS}^T(t)]^T$ and the uncertainty channel input $\underline{p}(t)$ and output $\underline{q}(t)$ are defined as

$$\underline{p}(t) = [\underline{p}_1^T(t)\ \underline{p}_2^T(t)]^T, \underline{q}(t) = [\underline{q}_1^T(t)\ \underline{q}_2^T(t)]^T.$$

Using the decomposition of $\underline{p}(t)$ and $\underline{q}(t)$ as defined above, the state-space matrices of the generalised plant are defined as follows:

$$\mathbf{A}_{P,0} = \begin{bmatrix}\mathbf{A}_0 & \mathbf{0}\\ \mathbf{0} & \mathbf{A}_{KS}\end{bmatrix}, \tag{5.6}$$

$$\mathbf{A}_{P,1} = \begin{bmatrix}\mathbf{A}_1 & \mathbf{0}\\ \mathbf{0} & \mathbf{0}\end{bmatrix}, \tag{5.7}$$

$$\mathbf{B}_P = \left[\begin{array}{cc|cc} -\frac{1}{2}\bar{a}_p\mathbf{B}_t\bar{\mathbf{H}} & \mathbf{B}_t\bar{\mathbf{H}} & \mathbf{0} & \bar{\mathbf{B}}_a\\ \mathbf{0} & \mathbf{0} & \mathbf{0} & \mathbf{B}_{KS}\end{array}\right], \tag{5.8}$$

$$\mathbf{C}_{P,0} = \left[\begin{array}{cc} \mathbf{0} & \mathbf{0}\\ \frac{1}{2}\bar{a}_p\mathbf{C}_t & \mathbf{0}\\ \hline \mathbf{0} & \mathbf{C}_{KS}\\ \mathbf{C}_a & \mathbf{0}\end{array}\right], \tag{5.9}$$

$$\mathbf{C}_{P,1} = \left[\begin{array}{cc} \mathbf{C}_t & \mathbf{0}\\ -\frac{1}{2}\bar{a}_p\mathbf{C}_t & \mathbf{0}\\ \hline \mathbf{0} & \mathbf{0}\\ \mathbf{0} & \mathbf{0}\end{array}\right], \tag{5.10}$$

$$\mathbf{D}_P = \left[\begin{array}{cc|cc} \mathbf{0} & \mathbf{0} & \mathbf{0} & \mathbf{0}\\ -\frac{1}{2}\bar{a}_p\mathbf{I} & \mathbf{0} & \mathbf{0} & \mathbf{0}\\ \hline \mathbf{0} & \mathbf{0} & \mathbf{0} & \mathbf{D}_{KS}\\ \mathbf{0} & \mathbf{0} & \mathbf{I} & \mathbf{0}\end{array}\right], \tag{5.11}$$

where $\mathbf{A}_0 := \mathbf{A} + \frac{1}{2}\bar{a}_p\mathbf{B}_t\bar{\mathbf{H}}\mathbf{C}_t$, $\mathbf{A}_1 := -\frac{1}{2}\bar{a}_p\mathbf{B}_t\bar{\mathbf{H}}\mathbf{C}_t$ and $\bar{\mathbf{B}}_a := \mathbf{B}_a\mathbf{K}_a$. In the following discussion also the transfer function description of the generalised plant will be used. The transfer function description of the generalised plant $\mathbf{P}$ is given as follows:

$$\mathbf{P}(s) = \left(\mathbf{C}_{P,0} + \mathbf{C}_{P,1}e^{-s\tau_0}\right)\left[s\mathbf{I} - \mathbf{A}_{P,0} - \mathbf{A}_{P,1}e^{-s\tau_0}\right]^{-1}\mathbf{B}_P + \mathbf{D}_P, \tag{5.12}$$

$s \in \mathbb{C}$. The (structured) uncertainty channel is then given as follows:

$$\begin{aligned} \underline{q}_1(t) &= (\mathcal{D}_{\delta_\tau} - 1)\,\underline{p}_1(t), \\ \underline{q}_2(t) &= \delta_{a_p}\underline{p}_2(t), \end{aligned} \tag{5.13}$$

where the operator $\mathcal{D}_\tau$ is defined as $\mathcal{D}_\tau \underline{x}(t) = \underline{x}(t-\tau)$. Let $\mathbf{\Delta}(s)$ denote the Laplace transform of the uncertainty term (5.13), such that $\underline{q}(s) = \mathbf{\Delta}(s)\underline{p}(s)$ with

$$\mathbf{\Delta}(s) = \begin{bmatrix} (e^{-s\delta_\tau} - 1)\mathbf{I}_2 & \mathbf{0} \\ \mathbf{0} & \delta_{a_p}\mathbf{I}_2 \end{bmatrix}. \tag{5.14}$$

with identity matrix $\mathbf{I}_n \in \mathbb{R}^{n\times n}$. Based on the definition of the generalised plant $\mathbf{P}$, as given above, it can be seen that the control problem at hand is a robust performance problem. The problem is to find a controller $\mathbf{K}$, as in (5.2), such that the $\mathcal{H}_\infty$ norm of the performance channel (i.e. the transfer function from $\underline{r}$ to $\underline{z}$) with the controller in closed-loop, becomes smaller than 1, for all allowed uncertainties $\mathbf{\Delta}$. As discussed in Section 4.5.6 and [181], the robust performance problem can be transformed into a robust stability problem by adding an extra uncertainty block $\mathbf{\Delta}_P \in \mathbb{C}^{2\times 2}$, $\|\mathbf{\Delta_P}\|_\infty \leq 1$, associated with the performance channel, to the problem. A block diagram interpretation of the transformation can be found in [142, p. 318]. The newly obtained uncertainty block is then given as follows:

$$\hat{\mathbf{\Delta}} = \begin{bmatrix} \mathbf{\Delta} & \mathbf{0} \\ \mathbf{0} & \mathbf{\Delta}_P \end{bmatrix}. \tag{5.15}$$

Then robust stability can be tested by computing the structured singular value of the interconnection of the generalised plant $\mathbf{P}$ and controller $\mathbf{K}$, denoted by $\mathbf{N}$, with respect to the expanded uncertainty set $\hat{\mathbf{\Delta}}$, i.e.

$$\sup_{\omega\in\mathbb{R}} \mu_{\hat{\mathbf{\Delta}}}(\mathbf{N}(i\omega)) < 1. \tag{5.16}$$

Herein, $\mathbf{N}$ is defined as the lower fractional transformation between $\mathbf{P}$ and $\mathbf{K}$. Consider the following decomposition of the generalised plant $\mathbf{P}$:

$$\mathbf{P} = \begin{bmatrix} \mathbf{P}_{11} & \mathbf{P}_{12} \\ \mathbf{P}_{21} & \mathbf{P}_{22} \end{bmatrix}. \tag{5.17}$$

Then the lower fractional transformation between $\mathbf{P}$ and $\mathbf{K}$, i.e. $\mathcal{F}_l(\mathbf{P},\mathbf{K})$, is defined as follows:

$$\mathbf{N} := \mathcal{F}_l(\mathbf{P},\mathbf{K}) = \mathbf{P}_{11} + \mathbf{P}_{12}\mathbf{K}(\mathbf{I} - \mathbf{P}_{22}\mathbf{K})^{-1}\mathbf{P}_{21}. \tag{5.18}$$

However, as can be seen from the definition of the uncertainty, given in the Laplace domain in (5.14), the term $e^{-s\delta_\tau} - 1$ depends on $s \in \mathbb{C}$. As illustrated in

Section 4.5.3.2, the delay uncertainty $e^{-s\delta_\tau}-1$ can be upperbounded by a (non-rational) frequency-dependent upper bound $\kappa(i\omega)$, which is over-approximated by a frequency-dependent norm-bounded rational transfer function $\rho_1(s)\mathbf{I}_2$ with state-space realisation:

$$\begin{aligned}\dot{\underline{x}}_\rho(t) &= \mathbf{A}_\rho \underline{x}_\rho(t) + \mathbf{B}_\rho \bar{\underline{q}}_1(t),\\ \underline{q}_1(t) &= \mathbf{C}_\rho \underline{x}_\rho(t) + \mathbf{D}_\rho \bar{\underline{q}}_1(t).\end{aligned} \tag{5.19}$$

Or stated differently:

$$|e^{-i\omega\delta\tau}-1| \leq \kappa(i\omega) \leq |\rho_1(i\omega)|,\ \forall \delta_\tau \in [\underline{\tau}-\tau_0, \bar{\tau}-\tau_0]. \tag{5.20}$$

Then, the robust performance requirement given by (5.16) can be refined by applying the small-μ theorem as presented in [155]. As before, assume that $\mathbf{N}$ is internally stable, then for all $\|\hat{\underline{\mathbf{\Delta}}}\|_\infty \leq 1$ the interconnection $\mathcal{F}_u(\mathbf{N}, \hat{\underline{\mathbf{\Delta}}})$ is well-posed, internally stable and $\|\mathcal{F}_u(\mathbf{N}, \hat{\underline{\mathbf{\Delta}}})\|_\infty < 1$ if and only if

$$\sup_{\omega\in\mathbb{R}} \mu_{\hat{\underline{\mathbf{\Delta}}}}\big(\mathbf{L}(i\omega)\mathbf{N}(i\omega)\big) < 1, \tag{5.21}$$

where

$$\mathbf{L}(i\omega) = \mathrm{diag}\big(\rho_1(i\omega)\mathbf{I}_2, \mathbf{I}_2, \mathbf{I}_2\big), \tag{5.22}$$

and

$$\hat{\underline{\mathbf{\Delta}}} = \mathbf{L}^{-1}\hat{\mathbf{\Delta}}. \tag{5.23}$$

Using the robust stability test in (5.21), instead of (5.16), will in general lead to less conservative results, due to the fact that the upper bound on the delay is explicitly taken into account in the generalised plant formulation. The statements above define the tools to evaluate robust performance using robust stability analysis.

5.2.3 Fixed structure controller synthesis

Based on the discussion in the previous section, it becomes clear that the design of a controller guaranteeing robust performance requires the following optimisation problem to be solved:

$$\begin{aligned}&\min_{\mathbf{K}} \sup_{\omega\in\mathbb{R}} \mu_{\hat{\underline{\mathbf{\Delta}}}}\big(\mathbf{LN}\big),\\ &\text{subject to } \Psi(\mathbf{K}) < 0,\end{aligned} \tag{5.24}$$

with $\mathbf{L}$ as in (5.22), $\mathbf{P}$ the generalised plant, given in transfer function matrix description in (5.12), $\mathbf{K}$ the controller to be designed, and $\Psi(\mathbf{K})$ the spectral abscissa function of the closed-loop system defined as:

$$\Psi(\mathbf{K}) := \sup\{\mathrm{Re}(\lambda) : \det(\lambda\mathbf{I} - \bar{\mathbf{A}}_0 - \bar{\mathbf{A}}_1 e^{-\lambda\tau_0}) = 0\}, \tag{5.25}$$

where

$$\bar{\mathbf{A}}_0 = \begin{bmatrix} \mathbf{A} + \frac{1}{2}\bar{a}_p \mathbf{B}_t \bar{\mathbf{H}} \mathbf{C}_t & \mathbf{0} \\ \mathbf{0} & \mathbf{0} \end{bmatrix} + \begin{bmatrix} \bar{\mathbf{B}}_a & \mathbf{0} \\ \mathbf{0} & \mathbf{I} \end{bmatrix} \begin{bmatrix} \mathbf{D}_c & \mathbf{C}_c \\ \mathbf{B}_c & \mathbf{A}_c \end{bmatrix} \begin{bmatrix} \mathbf{C}_a & \mathbf{0} \\ \mathbf{0} & \mathbf{I} \end{bmatrix},$$
$$\bar{\mathbf{A}}_1 = \begin{bmatrix} -\frac{1}{2}\bar{a}_p \mathbf{B}_t \bar{\mathbf{H}} \mathbf{C}_t & \mathbf{0} \\ \mathbf{0} & \mathbf{0} \end{bmatrix}.$$

The constraint on the objective function, defined above, is a necessary condition to guarantee the existence of the $\mathcal{H}_\infty$-norm of $\mathbf{N}$ along with stability of the closed-loop feedback system, see also [181].

The robust performance requirement in (5.21) is satisfied when the objective function becomes smaller than one. As described in the previous chapter, it is in general difficult to calculate $\mu_{\underline{\hat{\mathbf{\Delta}}}}$. However, an upper bound on $\mu_{\underline{\hat{\mathbf{\Delta}}}}$ can be obtained by calculating the scaled $\mathcal{H}_\infty$ norm of $\big(\mathbf{LN}\big)$ [181]. Since the uncertainties are modelled by complex uncertainties see (5.15) and (5.14), as described in the previous chapter, a reasonable approach to solve the problem is to apply D-K-iteration, see [181]. Hereby, the optimisation problem is given as follows:

$$\begin{aligned} &\min_{\mathbf{K}} \inf_{\mathbf{D} \in \boldsymbol{\mathcal{H}}_\infty} \|\mathbf{DLND}^{-1}\|_\infty, \\ &\text{subject to } \Psi(\mathbf{K}) < 0, \end{aligned} \tag{5.26}$$

which is iteratively solved for $\mathbf{K}$ and $\mathbf{D}$. Herein,

$$\|\mathbf{DLND}^{-1}\|_\infty = \sup_{\omega \in \mathbb{R}} \bar{\sigma}\big(\mathbf{D}(i\omega)\mathbf{L}(i\omega)\mathbf{N}(i\omega)\mathbf{D}(i\omega)^{-1}\big),$$

$\boldsymbol{\mathcal{H}}_\infty$ denotes the set of functions that are analytic and bounded in the open right half plane, and, the structure of $\mathbf{D}$ is chosen such that $\mathbf{D}$ commutes with the uncertainty set $\underline{\hat{\mathbf{\Delta}}}$, i.e. satisfy $\mathbf{D}\underline{\hat{\mathbf{\Delta}}} = \underline{\hat{\mathbf{\Delta}}}\mathbf{D}$. See e.g. [117] for more detail on the computation of lower and upper bounds on the complex structured singular value. For a given $\mathbf{K}$, the problem of finding the scaling matrix $\mathbf{D}$ can be turned into convex optimisation problem which is generally solved pointwise in the frequency domain (e.g. by using the `mussv` command from the Robust Control Toolbox of MATLAB [107], which uses the algorithm presented in [179]). Since in this chapter fixed structure controllers are considered, the problem of finding $\mathbf{K}$, for a given $\mathbf{D}$, in general results in a nonconvex, nonsmooth, constrained optimisation problem, given as follows:

$$\begin{aligned} &\min_{\mathbf{K}} f(\mathbf{K}), \\ &\text{subject to } \Psi(\mathbf{K}) < 0. \end{aligned} \tag{5.27}$$

with

$$f(\mathbf{K}) := \sup_{\omega \in \mathbb{R}} \bar{\sigma}\big(\mathbf{D}(i\omega)\mathbf{L}(i\omega)\mathcal{F}_l(\mathbf{P}(i\omega), \mathbf{K}(i\omega))\mathbf{D}(i\omega)^{-1}\big). \tag{5.28}$$

The nonsmooth dependence of the objective function (5.27) on the controller parameters of $\mathbf{K}$ typically occurs when the maximum of the objective function is located at two (or more) different frequencies. Due to the nonsmoothness of (5.27), standard optimisation algorithms cannot be used to determine the parameters of controller $\mathbf{K}$, since they tend to chatter about a nonsmooth surface. Instead, nonsmooth optimisation techniques, based on bundle methods, will be used. Bundle methods, see [68, 173], collect a number n_g of subgradients,

$$\nabla f(\underline{K}_{p,i}),\ \underline{K}_{p,i} \in \underline{K}_p + \epsilon_s \mathbb{B},\ i \in \{1, n_g\}, \tag{5.29}$$

to find an approximate for the Clarke subdifferential $\partial f(\underline{K}_p)$, defined as [25]

$$\partial f(\underline{K}_p) = \text{conv}\{\lim_{j\to\infty} \nabla f(\underline{K}_{p,j}) : \underline{K}_{p,j} \to \underline{K}_p, \nabla f(\underline{K}_{p,j}) \text{ exists}\}, \tag{5.30}$$

where $\text{conv}(Q)$ denotes the convex hull of Q. Herein, with a slight abuse of notation, $\underline{K}_p \in \mathbb{R}^{n_K}$ represents the parameter vector describing the controller $\mathbf{K}$, with n_K the number of controller parameters, $\epsilon_s > 0$ and $\mathbb{B}$ the n_K-dimensional open unit ball. Note that, when the function $f(\underline{K}_p)$ is smooth, the subdifferential $\partial f(\underline{K}_p)$ reduces to the gradient $\nabla f(\underline{K}_p)$. Using bundle methods, an approximate $\bar{\partial} f(\underline{K}_p)$ for the Clarke subdifferential $\partial f(\underline{K}_p)$ will be constructed.

The key idea behind bundle methods is that the continuous objective function is differentiable *almost everywhere*. Burke *et al.* [15] present a gradient bundle method, called gradient sampling, where the user specifies, for given controller parameters $\underline{K}_p$, the objective function $f(\underline{K}_p)$ in (5.27) and the gradient $(\nabla f(\underline{K}_p))$ at the parameter value $\underline{K}_p$, when the objective function is differentiable at $\underline{K}_p$. In this way, the user only has to specify one subgradient instead of the entire subdifferential, which is in general a difficult task. The gradient $\nabla f(\underline{K}_p)$ can either be determined analytically or numerically, e.g. using finite difference techniques [115]. Here, the gradient $\nabla f(\underline{K}_p)$ is determined using finite difference techniques as this appeared more robust as opposed to an analytically determined gradient. At each iteration, the gradient of the objective function is determined for n_g randomly generated values for the parameters characterising the state-space realisation of the controller, within sampling radius ϵ_s, of the current evaluation point. Denote the collection of the gradients by $\mathbf{G}_d$, defined as,

$$\mathbf{G}_d = \left[\nabla f(\underline{K}_{p,\epsilon_s,1}), \nabla f(\underline{K}_{p,\epsilon_s,2}), \ldots, \nabla f(\underline{K}_{p,\epsilon_s,n_g})\right] \tag{5.31}$$

with $\underline{K}_{p,\epsilon_s,i} = \underline{K}_p + \epsilon_s \underline{B}_i$, $i = 1, \ldots, n_g$, where the vectors $\underline{B}_1, \underline{B}_2, \ldots, \underline{B}_{n_g}$ are sampled independently and uniformly from $\mathbb{B}$ and n_g the number of sampled gradients. The approximate subdifferential $\bar{\partial} f(\underline{K}_p)$ is then obtained as follows:

$$\bar{\partial} f(\underline{K}_p) = \text{conv}(\mathbf{G}_d). \tag{5.32}$$

Based on the bundled gradients a local descent direction $\underline{d}$ is determined, where $-\underline{d}$ is the convex combination of the sampled gradients whose 2-norm, i.e. $\|\underline{d}\|_2$ is minimised [14]. This leads to solving the following (constrained) quadratic program:

$$\begin{aligned} &\min_{\underline{\alpha}} \underline{\alpha}^T \mathbf{G}_d^T \mathbf{G}_d \underline{\alpha}, \\ &\text{subject to} \quad \sum_{i=1}^{n_g} \alpha_i = 1. \\ &\qquad\qquad \alpha_i \geq 0, \end{aligned} \tag{5.33}$$

where $\underline{\alpha} = \begin{bmatrix} \alpha_1, \alpha_2, \ldots, \alpha_{n_g} \end{bmatrix}^T$. The descent direction is then obtained as $\underline{d} = -\mathbf{G}_d \underline{\alpha}$. In this way, when the optimisation approaches a nonsmooth manifold, in which e.g. a steepest descent based algorithm will jam, the bundle algorithm is able to use the information from both sides of the nonsmooth manifold to *turn the corner* and make progress towards the minimiser [14].

The gradient sampling algorithm, can be used to locally minimise the nonsmooth, nonconvex objective functions. In general, the gradient sampling algorithm is quite expensive per iteration. Therefore, Lewis and Overton have developed a hybrid algorithm for nonsmooth optimisation (HANSO) [93]. First, the BFGS method (named after its inventors Broyden, Fletcher, Goldfarb, and Shannon), a quasi-Newton algorithm, with an inexact line search algorithm based on weak Wolfe conditions is employed (see [115] for detail on BFGS and line search methods). When the BFGS algorithm finds a minimiser (i.e. when the norm of descent direction $\|\underline{d}\|_2$ becomes smaller than a pre-defined tolerance d_{tol}), the optimisation is stopped. In the event that, at a certain iteration, the Wolfe conditions are not satisfied, which indicates that the optimisation is near a nonsmooth manifold, the gradient sampling algorithm is employed where the sampling radius is adaptively reduced, see [15]. The details of the algorithm are listed below, when the full algorithm of finding fixed structure controllers for the considered time delay system with structured uncertainties is discussed.

The hybrid optimisation algorithm HANSO, as discussed above, is in general applied to finite-dimensional systems with continuous objective functions. However, as shown in [109, Chp. 9], the $\mathcal{H}_\infty$-norm of a system with time-delay exhibits continuity properties and is differentiable almost everywhere which allows the application of HANSO for the present system.

From (5.27), it can be seen that the problem of finding a fixed structure controller which guarantees robust performance of the milling process is actually a *constrained* optimisation problem. However, HANSO is only able to deal with unconstrained optimisation problems. The constrained optimisation problem can, however, be converted to an unconstrained optimisation problem using a penalty method, see [99]. An alternative method would be to e.g. use a barrier method. An advantage of the application of a barrier method is that

the parameters will never leave the feasible set of parameters (i.e. the set of parameters for which the constraint is satisfied). However, an important aspect of the fixed-order controller synthesis procedure is the choice of the initial controller parameters. Starting values for the fixed-structured controller synthesis procedure can be generated by considering reduced-order controllers obtained via the (full-order) controller-synthesis procedure from Chapter 4. In general no guarantees can be given regarding closed-loop stability of the closed-loop system for the reduced-order controller. Then, it may happen that the initial starting parameters lie outside the feasible set. A penalty function approach is able to deal with this situation. The constrained objective function (5.27) is replaced with the following unconstrained (nonsmooth) objective function:

$$\min_{\mathbf{K}} \bar{f}(\underline{K}_p), \tag{5.34}$$

where $\bar{f}(\underline{K}_p) = f(\underline{K}_p) + \gamma \max\big(0, \Psi(\underline{K}_p)\big)$, where again a slight abuse of notation is introduced, and γ is a positive constant. The value of γ is in general iteratively chosen, see [115] for rules on how to choose γ.

During an optimisation step, in order to evaluate the objective function (5.34) for given $\mathbf{K}$ and $\mathbf{D}$, the (scaled) $\mathcal{H}_\infty$-norm of $\mathbf{DL}\mathcal{F}_l(\mathbf{P},\mathbf{K})\mathbf{D}^{-1}$ as well as spectral abscissa $\Psi(\underline{K}_p)$, defined in (5.25), need to be calculated. Since, in this case, the system is infinite-dimensional (due to the presence of the time-delay), the standard Hamiltonian approach to calculate the $\mathcal{H}_\infty$-norm, as presented in [13], cannot be used. Recently, in [62] a method is presented to compute the $\mathcal{H}_\infty$-norm of a stable time-delay system with transfer function representation

$$\mathbf{G}(s) = \mathbf{C}\big(s\mathbf{I} - \mathbf{A}_0 - \mathbf{A}_1 e^{-s\tau}\big)^{-1}\mathbf{B} + \mathbf{D}. \tag{5.35}$$

Unfortunately, as can be seen from (5.12), the transfer function description of the generalised plant is not in the form of (5.35). Hence, here the $\mathcal{H}_\infty$-norm will be determined by calculating the singular values of $\mathbf{D}(i\omega)\mathbf{L}(i\omega)\mathcal{F}_l(\mathbf{P}(i\omega),\mathbf{K}(i\omega))\mathbf{D}(i\omega)^{-1}$ pointwise across a grid of frequencies $\underline{\omega} = \big[\omega_1, \omega_2, \ldots, \omega_N\big]^T$. The spectral abscissa is determined using the DDE-BIFTOOL [44] software package, which can be used to determine the right-most characteristic roots of a LTI system with time-delays. More information about computation of characteristic roots for time-delay systems can be found in [109].

Based on the discussion above, the following algorithm is presented to solve the fixed structure robust control synthesis problem for LTI time-delay systems with structured uncertainties.

Algorithm 5.1:
Given $\mathbf{D} = \mathbf{I}$, $\underline{K}_p = \underline{K}_p^0$, with $\underline{K}_p^0$ the initial vector of controller parameters, a positive constant γ and frequency grid vector $\underline{\omega} = \big[\omega_1, \omega_2, \ldots, \omega_N\big]^T$:

1. Find minimiser $\underline{K}_p^*$ which leads to the controller $\mathbf{K}^*$ to minimise the nonsmooth objective function $\bar{f}(\underline{K}_p)$:

a. run the BFGS algorithm with inexact line search algorithm starting from $\underline{K}_p = \underline{K}_p^0$;

b. **if** $\|\underline{d}\|_2 < d_{\mathsf{tol}}$ **then**
continue to step 2,
else
if inexact line search fails **then**
continue to step c.
end if
end if

c. initialise the gradient sampling algorithm by starting with the controller parameters $\underline{K}_p$ obtained from BFGS and choose a sampling radius ϵ_s and set the counter $g_{\mathsf{iter}} = 0$ in combination with the desired number of gradient sampling reduction steps g_{max};

d. Compute n_g gradients $\nabla \bar{f}(\underline{K}_{p,\epsilon_s,i})$, $\underline{K}_{p,\epsilon_s,i} = \underline{K}_p + \epsilon_s \underline{B}_i$, $i = 1, \ldots, n_g$, where $\underline{B}_1, \underline{B}_2, \ldots, \underline{B}_{n_g}$ are sampled independently and uniformly from $\mathbb{B}$;

e. compute descent direction $\underline{d} = -\arg\min\{\|\underline{d}\|_2 : \underline{d} \in \bar{\partial} \bar{f}(\underline{K}_p)\}$, with $\bar{\partial} \bar{f}(\underline{K}_p) = \mathrm{conv}\big([\nabla \bar{f}(\underline{K}_{p,\epsilon_s,1}), \nabla \bar{f}(\underline{K}_{p,\epsilon_s,2}), \ldots, \nabla \bar{f}(\underline{K}_{p,\epsilon_s,n_g})]\big)$;

f. determine step length t by applying the inexact line search algorithm with weak Wolfe conditions and update the controller parameter vector via $\underline{K}_p^{i+1} = \underline{K}_p^i + td$;

g. **if** $\|\underline{d}\|_2 > d_{\mathsf{tol}}$ **then**
go back to step d,
else
if $\|\underline{d}\|_2 < d_{\mathsf{tol}}$ and $g_{\mathsf{iter}} = g_{\mathsf{max}}$ **then**
continue to step 2,
else
reduce the sampling radius by setting $\epsilon_s = 0.1\epsilon_s$ and increase the counter g_{iter}, $g_{\mathsf{iter}} = g_{\mathsf{iter}} + 1$ and return to step d
end if
end if

2. Determine minimiser $\mathbf{D}^*$ to minimise $\bar{\sigma}\big(\mathbf{DL}\mathcal{F}_l(\mathbf{P}, \mathbf{K}^*)\mathbf{D}^{-1}\big)$ pointwise across frequency vector $\underline{\omega}$;

3. Calculate approximate maxima on $\mu_{\underline{\hat{\mathbf{\Delta}}}}$ by substituting $\mathbf{D}^*$ and $\mathbf{K}^*$ into (5.34) and evaluate for the given frequency grid $\underline{\omega}$;

4. Correct approximate maxima on $\mu_{\underline{\hat{\mathbf{\Delta}}}}$ using local optimisation strategy to find ω^* such that:

$$\sup_{\omega\in\mathbb{R}} \bar{\sigma}\big(\mathbf{D}^*(i\omega)\mathbf{L}(i\omega)\mathbf{N}^*(i\omega)\mathbf{D}^{*-1}(i\omega)\big) = \bar{\sigma}\big(\mathbf{D}^*(i\omega^*)\mathbf{L}(i\omega^*)\mathbf{N}^*(i\omega^*)\mathbf{D}^{*-1}(i\omega^*)\big),$$

with $\mathbf{N}^* = \mathcal{F}_l(\mathbf{P}, \mathbf{K}^*)$;

5. Stop when $\sup_{\omega\in\mathbb{R}} \mu_{\underline{\hat{\mathbf{\Delta}}}} = 1$. If $\sup_{\omega\in\mathbb{R}} \mu_{\underline{\hat{\mathbf{\Delta}}}} \neq 1$ compare $\sup_{\omega\in\mathbb{R}} \mu_{\underline{\hat{\mathbf{\Delta}}}}$ with previous obtained bound and stop when difference becomes smaller than user-defined tolerance, otherwise set $\mathbf{D} = \mathbf{D}^*$ and return to step 1.

The local optimisation strategy in step 4 of the algorithm presented above, corrects the upper bound on the structured singular value for a fixed controller $\mathbf{K}$ for the frequency grid $\underline{\omega}$. The optimisation strategy tries to find a local maximum of the (scaled) largest singular value by adjusting the scaling function $\mathbf{D}$ for a fixed controller $\mathbf{K}$. The optimisation problem is solved using the BFGS quasi-Newton implementation in the `fminunc` command from the optimisation toolbox in MATLAB.

5.3 Results

In this section, the results of the application of the fixed structure control synthesis algorithm, presented in the previous section, to the robust chatter control problem will be presented. Firstly, the static output feedback case will be considered in Section 5.3.1. Secondly, dynamic output feedback controllers will be designed in Section 5.3.2. The parameters of the milling model, considered in this section, are given in Table 4.1.

5.3.1 Static output feedback

In this section, a static output feedback controller ($n_c = 0$, in (5.2)) will be designed for the uncertain time-delay system (5.1). Moreover, a linear cutting model is considered (i.e. $x_F = 1$). A static output feedback can also be realised using a passive control strategy. However, the goal of this section is to illustrate the working principle of the fixed-structure control design approach. The structure of the controller matrix is chosen such that it has a similar structure as the averaged cutting force matrix $\bar{\mathbf{H}}$ which can be written as the sum of a diagonal matrix $k\mathbf{I}$ and a skew-symmetric matrix for a linear cutting model with full immersion cutting, see [5, page 107]. Then, the controller matrix is assumed to have a similar structure as the averaged cutting force matrix $\bar{\mathbf{H}}$ and therewith only two controller parameters need to be synthesised, i.e. the controller matrix structure is given as

$$\mathbf{K} = \mathbf{D}_c = \begin{bmatrix} k_1 & -k_2 \\ k_2 & k_1 \end{bmatrix}, \tag{5.36}$$

with the unknown controller parameter vector $\underline{K}_p = \begin{bmatrix} k_1 & k_2 \end{bmatrix}^T$. In this way the computational effort of the controller synthesis is reduced. Moreover, it allows for a graphical representation of the results.

The static output feedback controller is designed such that it stabilises milling operations between $n \in [36000, 38000]$ rpm, for a depth of cut which is as large as possible given the performance requirement on the control sensitivity **KS** as defined in Section 4.5.4, with a static performance weighting $W_{KS} = K_p$, where $K_p = 1 \cdot 10^{-6}$ mm/N. Moreover, the parameter of the penalty function is set to $\gamma = 100$ and the initial sampling radius $\epsilon_s = 0.1$.

Starting at the initial controller parameters $k_1 = k_2 = 0$, the fixed structure controller synthesis algorithm, as presented in Section 5.2.3, solves the constrained optimisation problem (5.27) by iterating over $\mathbf{D}$ and $\mathbf{K}$. The algorithm converges after three D-K steps resulting in $\sup_{\omega \in \mathbb{R}} \bar{\sigma}\big(\mathbf{D}(i\omega)\mathbf{L}(i\omega)\mathbf{N}(i\omega)\mathbf{D}^{-1}(i\omega)\big) = 0.9911$ therewith guaranteeing robust performance for milling operations between $n \in [36000, 38000]$ rpm up to a depth of cut of $\bar{a}_p = 2.4375$ mm.

In Figure 5.2(a), the values of the objective function during the K-step, i.e. $\sup_{\omega \in \mathbb{R}} \bar{\sigma}\big(\mathbf{D}_l \mathbf{L} \mathbf{N} \mathbf{D}_l^{-1}\big) + \gamma \max\big(0, \Psi(\mathbf{K})\big)$ with $l = 1, 2, 3$ the index of the corresponding D-scale matrices $\mathbf{D}_l$, are given as function of iteration number. Moreover, the evolution of the feedback gains k_1 and k_2 during the K-steps are given in Figure 5.2(b). The obtained feedback gains that guarantee robust performance of the the milling process for the desired uncertainties are given as

$$\begin{aligned} k_1 &= 10072.7 \text{ N/mm}, \\ k_2 &= -24.70908 \text{ N/mm}, \end{aligned}$$

from which it can be seen that the controller parameters are smaller than the inverse of the bound W_{KS}^{-1} posed on the control sensitivity **KS**. A contour plot of the objective function (5.34) for $\mathbf{D} = \mathbf{I}$ is given in Figure 5.3. Moreover, the path of controller synthesis (in the first K optimisation step, i.e. $l = 1$) is given in the feedback gain parameter space. It can be seen that the optimisation moves towards the (local) minimum of the objective function for the given D-scaling. In Figure 5.4, a contour plot is depicted where the upper bound on $\sup_{\omega \in \mathbb{R}} \mu_{\underline{\mathbf{\Delta}}}\big(\mathbf{L}(i\omega)\mathbf{N}(i\omega)\big)$ is calculated for several values of k_1 and k_2. Moreover, the path of the fixed structure controller synthesis algorithm in the feedback gain parameter space is given, where the end point of each K-step in the D-K-iteration process are indicated by a circle. From the contour plot, it can be seen that the during the D-K-iteration the optimisation converges to a (local) minimum thereby guaranteeing robust performance of the milling process. During the second D-K-step the optimisation moves along a nonsmooth boundary of the objective function. In the same figure, the evaluation of the objective function by using the default BFGS algorithm for smooth functions (see [115, Chp. 6], invoked using `fminunc` from MATLAB) is given in grey. It

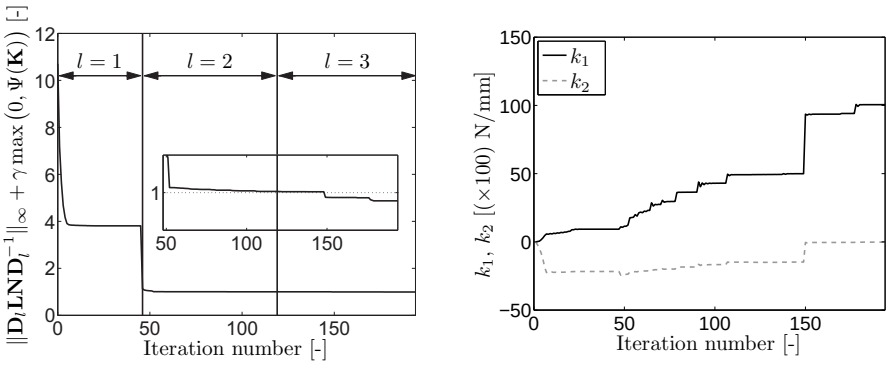

(a) Objective function. (b) Feedback gains.

Figure 5.2: Objective function in K-step of algorithm (left) and feedback gains k_1 and k_2 (right) as a function of iteration number.

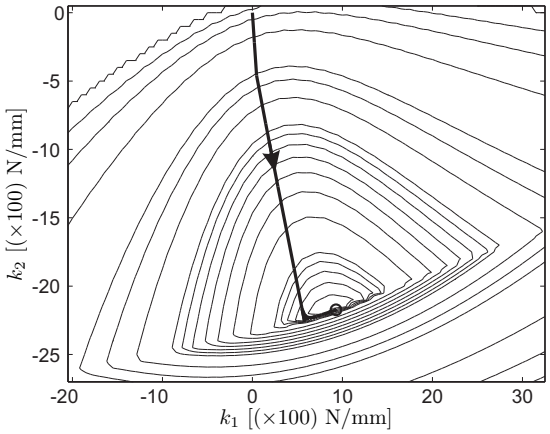

Figure 5.3: Contour plot of objective function (5.34) for fixed D-scales $\mathbf{D} = \mathbf{I}$, $\gamma = 100$ together with optimisation result during the first K-step of the algorithm. The circle indicates the parameter values obtained at the end of the first K-step.

---

can be seen that the standard BFGS algorithm gets stuck exactly at a non-smooth boundary of the objective function (A nonsmooth boundary can be distinguished from the nonsmoothness of a contour).

In Figure 5.5, the frequency response functions of open-loop and closed-loop tooltip dynamics are given. The closed-loop tooltip dynamics are determined using the static-output feedback controller as determined in the present section.

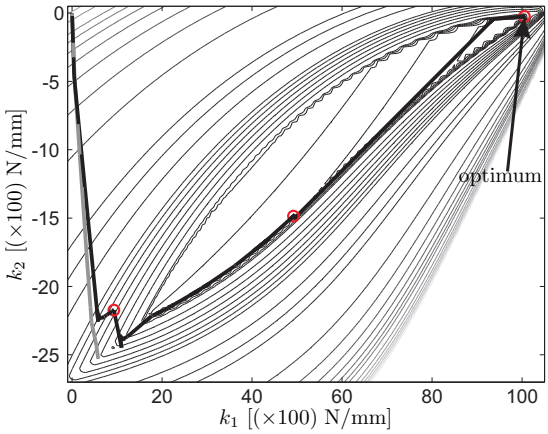

Figure 5.4: Contour plot of objective function $\sup_{\omega\in\mathbb{R}} \mu_{\underline{\hat{\mathbf{\Delta}}}}\big(\mathbf{L}(i\omega)\mathbf{N}(i\omega)\big)$ *together with optimisation result using Algorithm 5.1 (black) and standard* BFGS *(grey) during three D-K-iterations of the algorithm. The circles indicate the end of each K-step.*

It can be seen that the static-output controller alters the tooltip dynamics such that the first resonance in the tooltip dynamics is shifted to a lower frequency range. The second resonance is altered such that it lies inside the area of desired tooth passing excitation frequencies, which is beneficial for stability as will be illustrated below and also has been discussed in the results of the previous chapter.

Next, SLDs are determined for the original linearised time-variant model of the milling process (Eq. (4.2)), as outlined in Section 2.7, with and without the static output controller. The SLD is given in Figure 5.6. It can be seen that the controller synthesis algorithm has created a peak in the SLD exactly at the desired spindle speed range. In this case, this is realised by altering the closed-loop spindle dynamics, as presented above, such that the second resonance, which lies in the desired range of spindle speeds, becomes dominant for chatter in the desired range of spindle speeds. For the open-loop SLD, the first resonance limits the maximum achievable depth of cut for spindle speeds above approximately $n = 33000$ rpm. Using the static output feedback controller the depth of cut, in the considered spindle speed range, can be increased from $a_{p,\mathsf{max}} = 1.595$ mm to $a_{p,\mathsf{max}} = 3.042$ mm ($\bar{a}_p = 2.4375$ mm) which is an increase of more than 90%. Based on the discussion above, it can be concluded that the proposed controller synthesis strategy is able to effectively alter the SLD such that productivity is significantly increased. This is even accomplished for the least number of controller parameters. In the next section, fixed structure controllers will be synthesised using dynamic output feedback controllers.

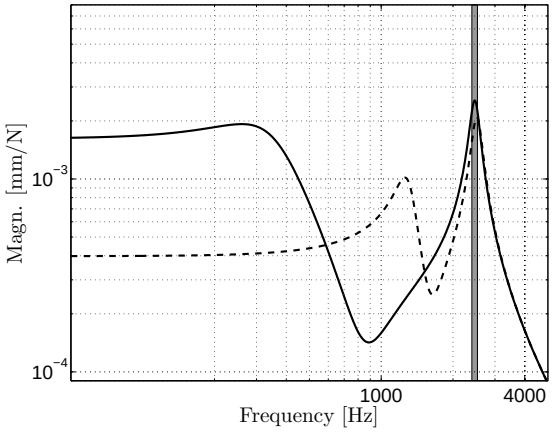

(a) Feed direction.

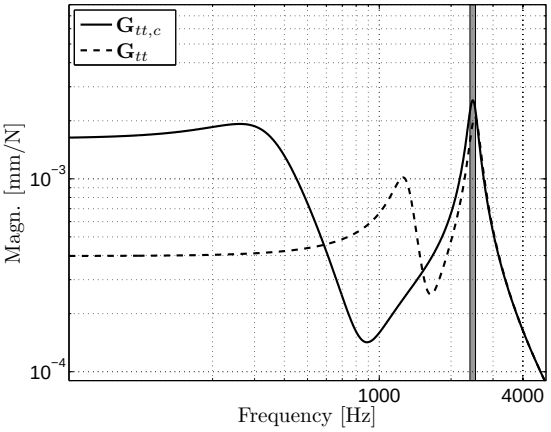

(b) Normal direction.

Figure 5.5: Controlled $\mathbf{G}_{tt,c}(i\omega)$ (solid) and uncontrolled (open-loop) $\mathbf{G}_{tt}(i\omega)$ (dashed) tooltip spindle dynamics for the static-output controller designed for a range of spindle speeds, $n \in [36000, 38000]$ rpm. The interval of tooth passing excitation frequencies corresponding to the spindle speed range is indicated by the grey area.

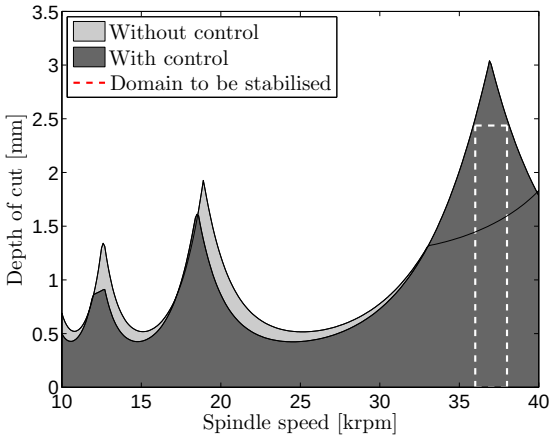

Figure 5.6: Stability lobes diagram with and without static output feedback controller.

5.3.2 Dynamic output feedback

The previous section illustrated the working principle of the proposed controller design method using a static output feedback controller with two controller parameters. In this section, the results will be presented by synthesising dynamic output controllers as defined by (5.2) for $x_F < 1$.

The dynamic output feedback controller will be designed such that milling operations between $n \in [34000, 36000]$ rpm are stabilised, for a depth of cut which is as large as possible given the performance requirement on the control sensitivity **KS** as given defined in Section 4.5.4. Here, the performance weighting W_{KS} is chosen similarly as in the previous chapter, i.e.

$$W_{KS}(s) = K_p \frac{\frac{1}{2\pi f_{r,l}} s + 1}{\frac{1}{2\pi f_{p,l}} s + 1} \cdot \frac{\frac{1}{2\pi f_{r,h}} s + 1}{\frac{1}{2\pi f_{p,h}} s + 1}, \tag{5.37}$$

with $K_p = 1 \cdot 10^{-6}$ mm/N, $f_{r,l} = 100$ Hz, $f_{r,h} = 7500$ Hz, $f_{p,l} = 1 \cdot 10^{-2}$ Hz and $f_{p,h} = 2 \cdot 10^4$ Hz. As before, the parameter of the penalty function is set to $\gamma = 100$ and the initial sampling radius is chosen as $\epsilon_s = 0.1$.

As the controller synthesis problem at hand is in general a nonconvex problem, an important aspect of the fixed-order controller synthesis procedure is the choice of the initial controller parameters $\underline{K}_p^0$ describing the initial controller transfer matrix $\mathbf{K}_0$. Here, the initial controller parameters will be based on the reduced controller obtained via the (full-order) μ-synthesis procedure as presented in Chapter 4.

In order to reduce the number of optimisation variables (i.e. controller parameters), the initial controller, obtained by reducing a full-order controller de-

Table 5.1: Results from fixed structure controller synthesis for three different controller orders, $\bar{a}_p$ denotes the maximal depth of cut for which robust performance can be guaranteed, $a_{p,\mathsf{max}}$ denotes the maximal depth of cut in the SLD *for desire spindle speed interval.*

n_c [-]	$\mu_{\underline{\hat{\mathbf{\Delta}}}}$ [-]	$\bar{a}_p$ [mm]	$a_{p,\mathsf{max}}$
0	0.9816	1.1875	1.845
2	0.9809	2.0469	2.579
4	0.9865	2.25	2.805

termined using the μ-synthesis procedure from Chapter 4, is transformed to the modal canonical form (herewith the system matrix $\mathbf{A}_c$ of the reduced-order controller has the real Jordan form). After the transformation the controller's system matrix $\mathbf{A}_c$ is a block diagonal matrix, i.e. $\mathbf{A}_c = \mathrm{diag}(\mathbf{A}_{c,1}, \ldots, \mathbf{A}_{c,n_{\mathbb{C}}/2+n_{\mathbb{R}}})$, with $n_{\mathbb{C}}$ the number of complex eigenvalues and $n_{\mathbb{R}}$ the number of real eigenvalues, and

$$\mathbf{A}_{c,l} = \lambda_l, \text{ for } \lambda_l \in \mathbb{R}, \tag{5.38}$$

and

$$\mathbf{A}_{c,l} = \begin{bmatrix} \mathrm{Re}(\lambda_l) & \mathrm{Im}(\lambda_l) \\ -\mathrm{Im}(\lambda_l) & \mathrm{Re}(\lambda_l) \end{bmatrix}, \text{ for } \lambda_l \in \mathbb{C}, \tag{5.39}$$

where λ_l is the solution of $\det(\lambda_l \mathbf{I} - \mathbf{A}_c) = 0$. Note that in this case it is assumed that the eigenvalues have algebraic multiplicity one. Three fixed structure controllers are synthesised, namely for $n_c = 0$ (i.e. static-output feedback), $n_c = 2$ and $n_c = 4$, using the algorithm as presented in Section 5.2.3. The algorithm has to optimise 4 parameters in case of $n_c = 0$, 16 parameters in case of $n_c = 2$ and 28 parameters in case of $n_c = 4$. The results after five D-K-steps are listed in Table 5.1. As before, SLDs are computed with the obtained fixed structure controllers and without control using the linearised time-variant model of the milling process (Equation (4.2)), as outlined in Section 2.7. The corresponding results are given in Figure 5.7. For completeness, the maximal achievable depth of cut $a_{p,\mathsf{max}}$ from the SLD in the desired spindle speed range is listed in Table 5.1. From the figure, it can be seen that for the case where $n_c = 0$ the fixed structure controller indeed alters the SLD. The peak of the lobe is approximately located at $n = 37000$ rpm, which is outside the domain of desired spindle speeds. In this case, based on the SLD, the depth of cut can be increased from $a_{p,\mathsf{max}} = 1.067$ mm to 1.845 mm which is a gain of approximately 73%. In order to shift the peak of the lobe to another spindle speed, the controller needs to have more complexity (freedom), which is obtained by increasing the controller order. For the dynamic fixed structure controllers with $n_c = 2$ and $n_c = 4$ it can be seen that the SLD is altered such that a lobe is created

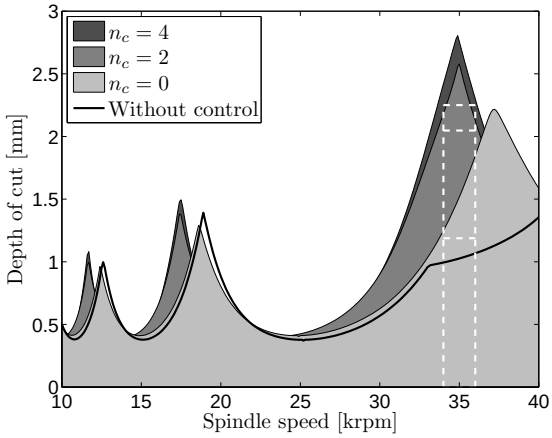

Figure 5.7: Stability lobes diagram for the structured dynamic output feedback controllers for three $0, 2$ *and* 4 *controller states, respectively, and without control. The area for which robust stability is guaranteed is indicated by the dashed boxes, see also Table 5.1.*

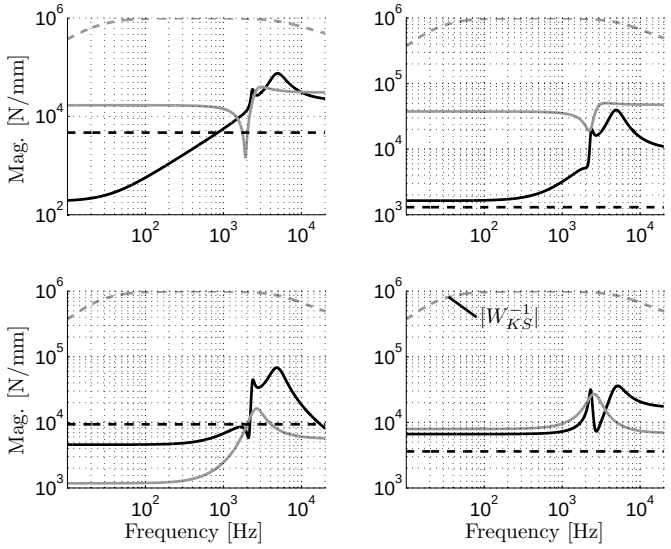

Figure 5.8: Magnitude of the fixed structure controller for $n_c = 0$ *(black dashed),* $n_c = 2$ *(grey solid) and* $n_c = 4$ *(black solid) controller states which stabilises the milling process for* $n \in [34000, 36000]$ *rpm. Also the magnitude of the inverse of the performance weighting function* W_{KS} *is given.*

at the desired spindle speed interval. It can be seen that by increasing the order of the fixed structure controller, the area for which robust stability is guaranteed is increased. In this case, based on the SLD, the depth of cut can be increased from $a_{p,\max} = 1.067$ mm to $a_{p,\max} = 2.579$ for $n_c = 2$ and to $a_{p,\max} = 2.805$ for $n_c = 4$, which leads to an increase of approximately 142% and 163%, respectively. The obtained depth of cut $\bar{a}_p$ for which robust performance can be guaranteed is smaller for the fixed structure controller as compared to the higher-order controller designed using the approach outlined in Chapter 4. This is as expected since less parameters are available to tune for the fixed structure controller. On the contrary, the fixed structure controller synthesis is based on the model of the milling process without the necessity of a high-order approximation of the time delay.

The resulting fixed structure controllers are given in Figure 5.8. From the figure, it can be seen that the controllers designed for $n_c = 2$ and $n_c = 4$ are dynamic MIMO controllers with notch characteristics, which show similar behaviour as the controllers obtained using the μ-synthesis procedure exploited in Chapter 4.

The closed-loop tooltip dynamics in both x- and y-direction are given in Figure 5.9. In the same figure, the interval of tooth passing excitation frequencies f_{tpe} associated with the spindle speed interval $n \in [34000, 36000]$ rpm is indicated. It can be seen that the controller, designed for $n_c = 0$, is unable to shift the second resonance into the frequency range of desired tooth passing excitation frequencies. As described above, this is due to the limited complexity of the controller. For the dynamic fixed structure controllers with $n_c = 2$ and $n_c = 4$ it can be seen that the controllers alter the closed-loop tooltip spindle dynamics such that the second resonance is shifted such that it is located inside the desired uncertainty range of f_{tpe}.

5.4 Discussion

This chapter presented a methodology to directly synthesise fixed structure controllers which guarantee robust stability and performance of the high-speed milling process (i.e. the avoidance of chatter in a predefined area of depth of cut a_p and spindle speed n). It is shown that the resulting optimisation problem is a nonsmooth constrained optimisation problem which can be transformed to an unconstrained nonsmooth optimisation problem using a penalty function. The unconstrained optimisation problem is solved using D-K-iteration. The K-step is solved by utilising a dedicated nonsmooth optimisation algorithm based on bundle methods. An important aspect of the fixed-order controller synthesis procedure is the choice of the initial controller parameters. Starting values for the fixed-structured controller synthesis procedure can be generated by considering reduced-order controllers obtained via the (full-order) controller-synthesis procedure from Chapter 4. From the results, it can be seen that it is possi-

ble to synthesise fixed structure controllers for the high-speed milling process that guarantee robust stability (i.e. avoidance of chatter) for given ranges of the depth of cut and spindle speed. This leads to a slight performance degradation, in terms of achievable maximum depth of cut $\bar{a}_p$ for which robust performance can be guaranteed, as compared to the procedure presented in Chapter 4. However, with the approach as presented in this chapter it is possible to synthesis controllers for systems with a time-delay without the necessity of a (possibly) high-order approximation of the delay term. From the perspective of practical implementation, it is clearly desirable to be able to design relatively low-order controllers guaranteeing robust chatter-free machining.

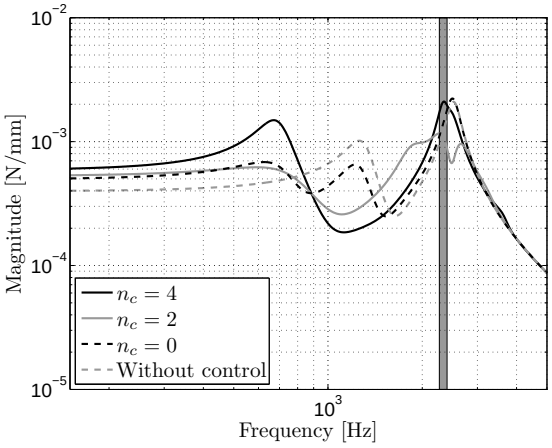

(a) x-direction.

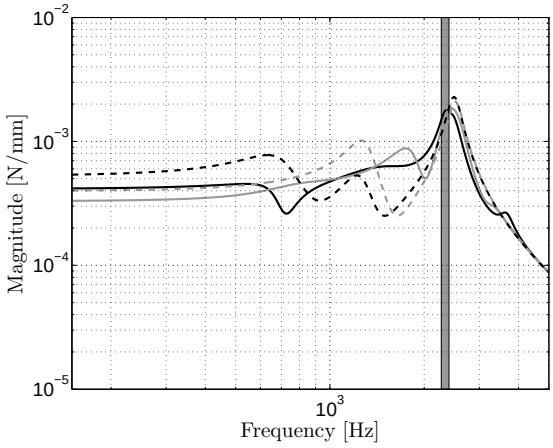

(b) y-direction.

Figure 5.9: Controlled $\mathbf{G}_{tt,c}(i\omega)$ and uncontrolled $\mathbf{G}_{tt}(i\omega)$ tooltip spindle dynamics in x- and y-direction for fixed structure controller for $n_c = 0$, $n_c = 2$ and $n_c = 4$ states designed for a spindle speed interval $n \in [34000, 36000]$ rpm. The interval of tooth passing excitation frequencies corresponding to the spindle speed range is indicated by the grey area.

6

Active chatter control: experimental results

6.1 Introduction

In Chapters 4 and 5, an active chatter controller design methodology has been presented which shapes the stability lobes diagram (SLD) such that a predefined domain of working points in terms of spindle speed n and depth of cut a_p is stabilised. The main goal of this chapter is to illustrate the working principle of the active chatter control procedure in practice. Hereto, the active chatter control strategy, as presented in Chapter 4, will be used to design controllers for an actual high-speed milling spindle which is equipped with an active magnetic bearing (AMB). The controller designs in Chapters 4 and 5 are based on relatively simple models of the spindle dynamics. In reality, however, the models of the spindle dynamics will be rather complex (see e.g. [19, 94]). It will be shown that it is possible to apply the active control strategy to more complex models of the spindle-actuator dynamics. As a consequence of the higher complexity of the model of the spindle dynamics, the controllers will be more complex (i.e. of higher order) and should be implemented in a real-time control environment with a relatively high sampling frequency. Moreover, there

The experiments that will be presented in this chapter are performed in close-cooperation with the Institut für Produktionsmanagement, Technologie und Werkzeugmaschinen (PTW) of the Technische Universität Darmstadt, Germany, and, more specifically Prof. Dr.-Ing. Eberhard Abele and Dipl.-Ing. Andreas Schiffler.

will be a difference between the actual spindle-actuator dynamics and the identified model of the setup. This implies that uncertainties need to be included in the spindle-actuator model in order to accurately describe the experimental setup which may deteriorate the attainable performance of the controller design. These challenges will be faced in this chapter while applying the developed controller design methodology in practice.

The experimental setup that will be considered in the present chapter will be presented in Section 6.2. In Section 6.3, parameters of the cutting force model and a model of the spindle-actuator dynamics will be determined experimentally. Moreover, an uncertainty model for the spindle-actuator dynamics will be derived and the SLD without control will be presented. Then, using the obtained (uncertain) model of the experimental setup, two different controllers will designed in Section 6.4. Based on a closed-loop model-based stability analysis, results using the obtained controllers in combination with the model of the experimental setup will be discussed in Section 6.5. Next, actual closed-loop milling operations will be presented with the designed controllers in Section 6.6. Finally, a discussion regarding the obtained experimental results will be presented in Section 6.7.

6.2 Experimental Setup

As described above, in this chapter controllers will be designed for an actual high-speed milling spindle which is equipped with an AMB. The experimental setup, which will be used throughout this chapter, is designed and realised at the Institut für Produktionsmanagement, Technologie und Werkzeugmaschinen (PTW) of the Technische Universität Darmstadt, Germany. In Figure 6.1, a photo and schematic overview of the spindle with integrated AMB can be found. It can be seen that the active magnetic bearing is integrated in the spindle and is placed between the front bearings and the toolholder. In this way, the setup can serve as a testbed for a proof of principle in order to test the active chatter control strategy in practice. The specifications of the spindle and AMB, taken from [82], are listed in Table 6.1. The same spindle with integrated AMB has been used in [82] for chatter control using active damping techniques.

6.3 Identification of the experimental setup

The active chatter control synthesis procedure, presented in Chapter 4, is a model-based controller design procedure. Hence, a model of the experimental setup is required for the purpose of controller design. First, the parameters of the cutting force model will be identified. Secondly, a parametric model of the spindle and actuator dynamics will be determined experimentally. Thirdly, uncertainties in the spindle dynamics will be modelled. Finally, the SLD of the

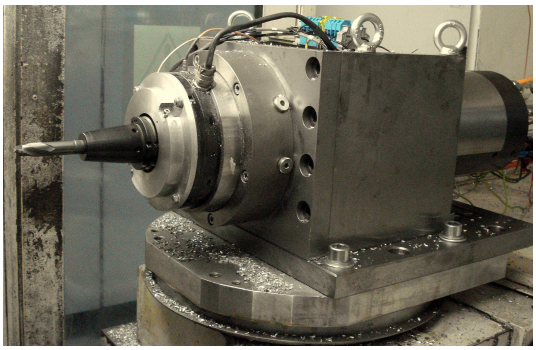

(a) Photo.

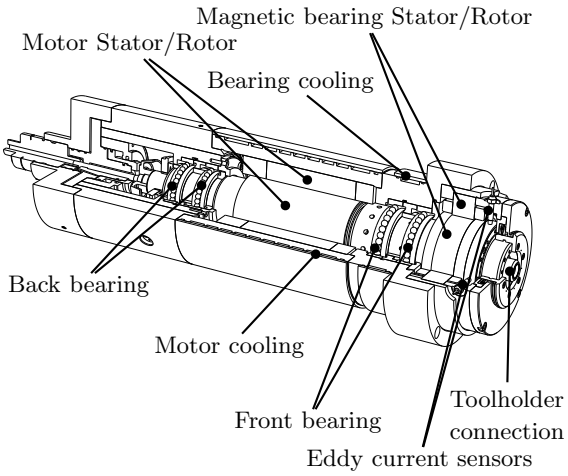

(b) Schematic representation.

Figure 6.1: The experimental setup. An active magnetic bearing (AMB) is integrated into a machine spindle between the front bearings and toolholder connection. Source: Institut für Produktionsmanagement, Technologie und Werkzeugmaschinen (PTW), Technische Universität Darmstadt, Germany.

experimental setup will be determined through dedicated milling experiments as well as using the obtained model.

Table 6.1: Specifications of the experimental setup.

Spindle	
max. Power	80 kW
max. spindle speed	24000 rpm

AMB	
number of poles	8
nominal airgap	0.4 mm
pre-magnetising current	5 A
max. input current	10 A
max. static force	600 N
Bandwidth current controller	1000 Hz

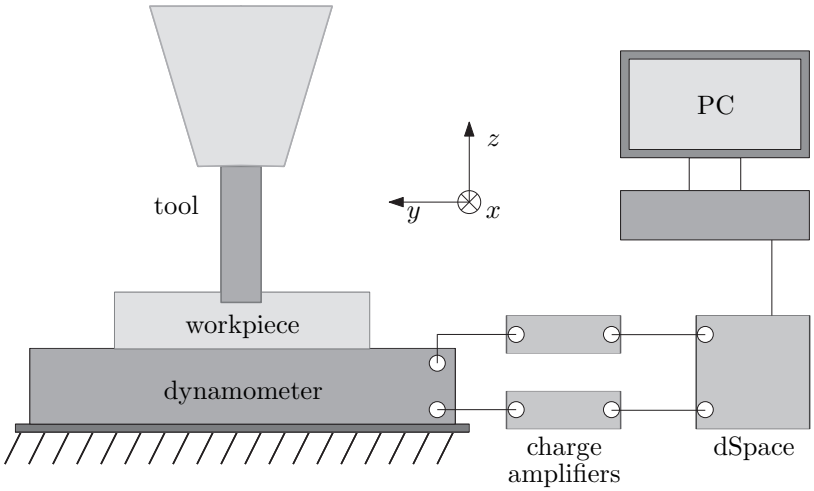

Figure 6.2: Schematic representation of the setup for measuring cutting forces.

6.3.1 Identification of the cutting force model parameters

Cutting tests have been performed to experimentally identify the parameters, K_t, K_r and x_F of the cutting force model (2.6), presented in Section 2.4. Hereto, full immersion cuts in aluminum 7075 have been performed while measuring the cutting forces using a dynamometer (Kistler 9257A). A schematic representation of the measurement setup can be found in Figure 6.2. The cutter, used during the experiments, is a two-fluted cutter which has a diameter of $d = 16$ mm, a shaft length of 72 mm and a helix angle greater than zero.

Table 6.2: Estimated parameters of cutting force model obtained after fitting model to measured cutting forces.

K_t [N/mm$^{1+x_F}$]	K_r [N/mm$^{1+x_F}$]	x_F [-]
585.0038	210.0388	0.7654

Cuts are made for a spindle speed of 8000 rpm. The spindle speed is chosen such that the frequency content of the measured cutting forces (which consists of the spindle speed and tooth passing excitation frequencies and higher harmonics, see Chapter 2) is significantly lower than the eigenfrequency of the dynamometer (which is approximately 2.3 kHz).

The parameters are obtained by fitting the model on the experimentally obtained cutting forces in feed and normal direction, denoted by $F_{t,x_{\text{meas}}}$ and $F_{t,y_{\text{meas}}}$, respectively, using least squares optimisation. Hereto, the approach as outlined in [49] is used. By plotting the forces in normal direction as function of the forces in feed direction, an ellipse can be fitted to the data. The data is represented as function of the angle θ, where θ is defined as the angle to the feed direction. By choosing a grid for θ, with $\Theta := \left[\theta_1, \theta_2, \ldots, \theta_i, \ldots, \theta_N\right]^T$, with $\theta_i \in [0, 2\pi]$, $\forall i \in \{1, N\}$, and averaging the measured cutting forces to this grid (as shown in Figure 6.3), the following objective function is minimised, see [49]:

$$\sum_{\theta_i \in \Theta} \left(\sqrt{F_{t,x_{\text{meas}}}(\theta_i)^2 + F_{t,y_{\text{meas}}}(\theta_i)^2} - \sqrt{F_{t,x}(\theta_i)^2 + F_{t,y}(\theta_i)^2} \right)^2. \tag{6.1}$$

In Figure 6.4, the measured cutting forces along with the fitted model are given. The corresponding parameters are listed in Table 6.2. From the figures it can be seen that the fitted model differs somewhat from the measured cutting forces. The main difference is due to runout of the spindle/tool combination (i.e. the geometric axis of rotation does not equal the axis of rotation). However, as described in [49] the sensitivity of the SLD with respect to the cutting force parameters is much smaller as compared to the spindle dynamics. Therefore, the fit of the parameters is considered sufficiently accurate.

6.3.2 Identification of the spindle-actuator dynamics

Next, the nominal model of the spindle and actuator dynamics is determined experimentally. The model consists of four inputs (the input voltage to the current controller which drives the AMB and the force acting at the tooltip in feed (x)- and normal (y)-direction) and four outputs (displacements in feed (x)- and normal (y)-direction measured at the AMB location and the tooltip). In order to determine the frequency response functions (FRF), corresponding to this input/output set, of the experimental setup, the tooltip is excited using

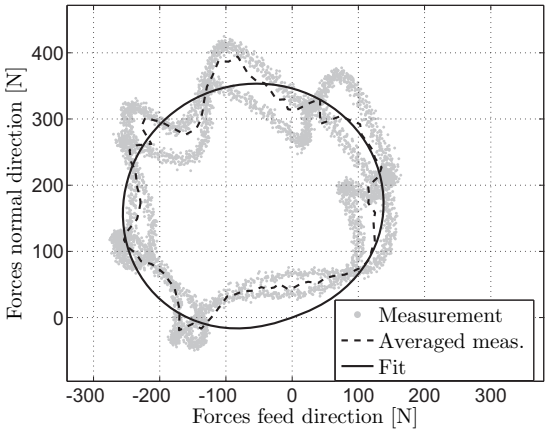

Figure 6.3: Measured and fitted cutting forces, where the cutting forces in normal direction are plotted as function of the cutting forces in feed direction.

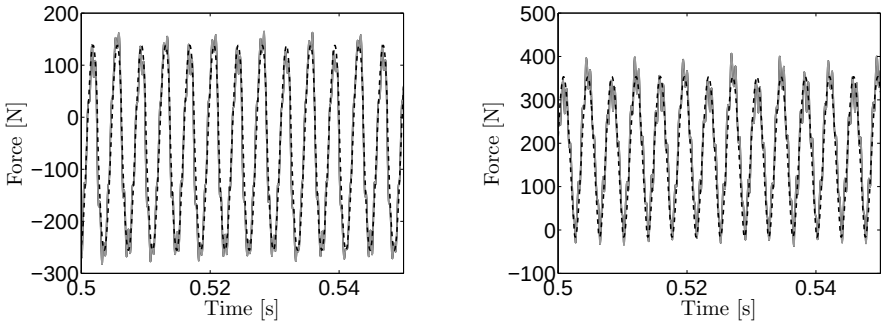

(a) Feed direction.

(b) Normal direction.

Figure 6.4: Cutting force measurements (grey) and fitted cutting force model (black dashed) for a spindle speed of 8000 *rpm, depth of cut of* 2 *mm, feed per tooth* 0.2 *mm.*

---

an impulse hammer (PCB 086C04) while the accelerations at the tooltip are measured using a B&K 4520 accelerometer and AMB displacements are measured using the eddy current sensors (SKF CMSS 65). The FRF matrix $\mathbf{G}$ of the spindle dynamics is defined as follows:

$$\mathbf{G}(i\omega) = \begin{bmatrix} \mathbf{G}_x(i\omega) & \mathbf{0} \\ \mathbf{0} & \mathbf{G}_y(i\omega) \end{bmatrix}, \tag{6.2}$$

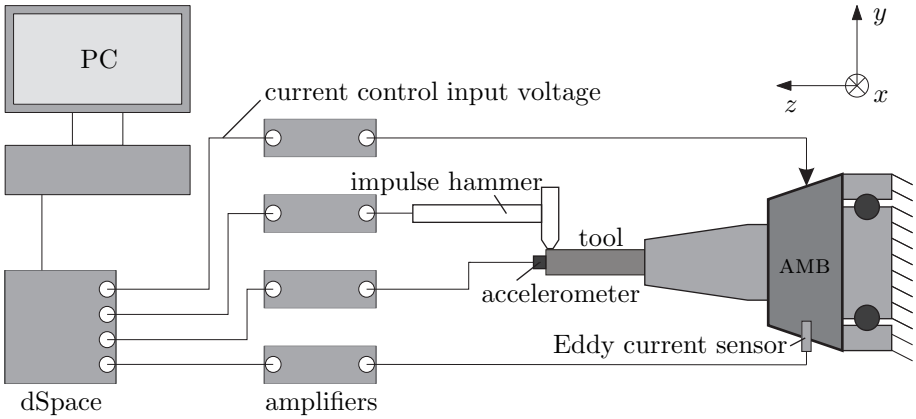

Figure 6.5: Schematic representation of the setup for identification of the spindle-actuator dynamics.

with

$$\mathbf{G}_x(i\omega) = \begin{bmatrix} \mathbf{G}_{tt,x}(i\omega) & \mathbf{G}_{ta,x}(i\omega) \\ \mathbf{G}_{at,x}(i\omega) & \mathbf{G}_{aa,x}(i\omega) \end{bmatrix}, \ \mathbf{G}_y(i\omega) = \begin{bmatrix} \mathbf{G}_{tt,y}(i\omega) & \mathbf{G}_{ta,y}(i\omega) \\ \mathbf{G}_{at,y}(i\omega) & \mathbf{G}_{aa,y}(i\omega) \end{bmatrix}.$$

Herein, $\mathbf{G}_{kl,x}(i\omega)$ (and $\mathbf{G}_{kl,y}(i\omega)$) denote the FRF with output k and input l, where t and a indicate tooltip and bearing excitation/response, respectively. In Figure 6.5, a schematic representation of the experimental setup for identification of the spindle actuator model is given. Since the controller design will be based on a linear model, it is important to limit the input current of the AMB, due to the nonlinear relation between input current and force/displacements [136]. Here, the AMB is excited using a Pseudo Random Binary Sequence (PRBS), which is a periodic sequence that has constant amplitude, see [121] for more details. Since frequency-domain identification techniques are used and, moreover, the controller design is based on linear design techniques, the amplitude of the PRBS signal is chosen such that the AMB works in the linear operation domain. Here the amplitude is set to 1 V. Since it is difficult to perform hammer tests for a rotating spindle, all the experiments are conducted at stand-still. It is well known, that the dynamics of a spindle depends on the spindle speed, see e.g. [2, 127]. However, the spindle speed dependency of the experimental setup will be identified and modelled by including uncertainty to the spindle-actuator dynamics during controller design, which is discussed in the next section.

Based on the measured data, a parametric model is fitted to the obtained frequency response functions. In principle, the conducted experiments are single input multiple output (SIMO) experiments. By using a curve fitting approach in the frequency domain instead of a time-domain approach, the

number of data points can be considerably reduced. Since, the model of the spindle-actuator dynamics consists of two-decoupled MIMO systems (in x- and y-direction), a multivariable identification approach is used to obtain the parameters of the model. In this way, a model of relatively lower order is obtained as compared to an approach where a parametric model is fitted to each single SISO FRF. The multivariable model is described using polynomial matrix fraction descriptions as described in [18]. The parameters of the model are determined using Sanathanan-Koerner (SK) iteration, see [131]. Hereto, the *freqid* toolbox in MATLAB is employed [17]. The order of the parametric model is chosen such that,

1. the difference between the modelled and measured the frequency response functions is as small as possible;
2. the model is internally stable.

In Figures 6.6 and 6.7, the amplitude and phase of the measured frequency response functions (FRFs) and corresponding parametric models in feed (x)- and normal (y)-direction, respectively, are given. The corresponding coherence plots can be found in Appendix B. It can be seen that, especially near resonances, the fitted frequency response data and experimental data are quite comparable. The accuracy of the fit highly depends on the selected model order and the chosen frequency-dependent weighting functions. Here, the inverse of the amplitude data is used as weighting function during the parameter fitting procedure. The presented parametric model has a total of 30 states (14 in feed direction and 16 states in normal direction). The difference in order between x- and y-direction is due to the appearance of an extra resonance around 500 Hz in the y-direction. The order of the model is considerably lower as compared to a model which would have been obtained by fitting each SISO FRF independently.

6.3.3 Identification of spindle-actuator dynamics uncertainties

In [49], it has been concluded that the sensitivity of the SLD with respect to the spindle dynamics is considerably larger than the sensitivity as compared to the parameters of the cutting force model. Consequently, during the controller design, uncertainties in the spindle-actuator model, as obtained in the previous section, will be included. Based on the discussion in the previous section, the following sources can be considered as the most critical type of uncertainties in the model of the spindle-actuator dynamics:

- uncertainty due to spindle speed dependent dynamics;
- uncertainty due to unmodelled dynamics;
- uncertainty due to temperature effects.

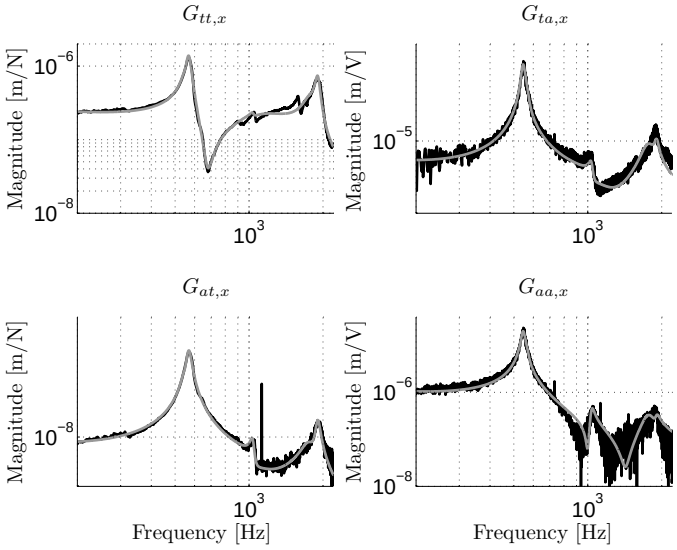

(a) Amplitude.

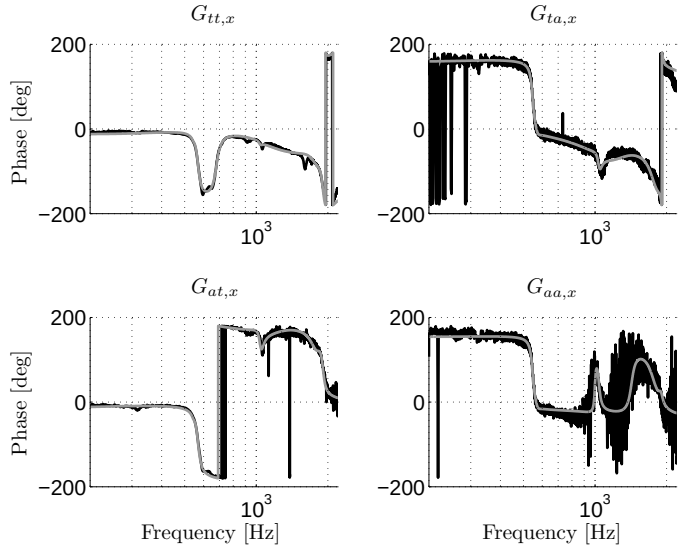

(b) Phase.

Figure 6.6: Frequency response measurements (black) and fitted parametric model (grey) in feed (x) direction. $G_{kl,x}(i\omega)$ reflects the FRFs *with output k and input l where t and a indicate tooltip and bearing excitation/response, respectively.*

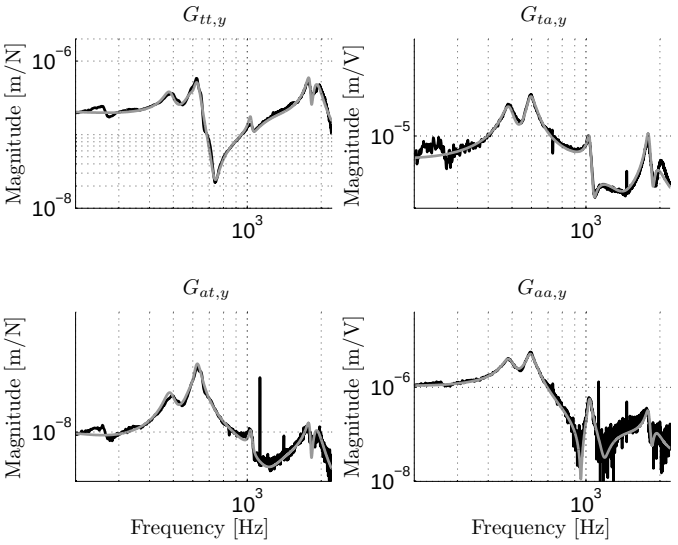

(a) Amplitude.

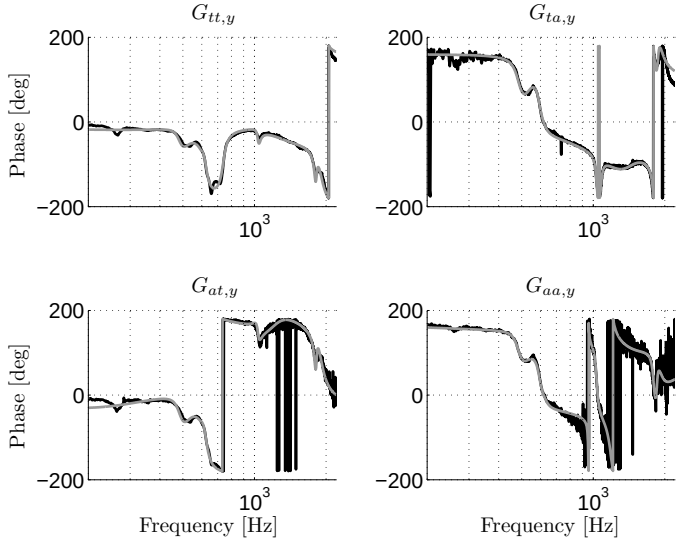

(b) Phase.

Figure 6.7: Frequency response measurements (black) and fitted parametric model (grey) in normal (y) direction. $G_{kl,y}(i\omega)$ reflects the FRFs *with output k and input l where t and a indicate tooltip and bearing excitation/response, respectively.*

Firstly, the uncertainty due to spindle speed dependent dynamics is known for rotor dynamic systems. The spindle speed dependency arises due to gyroscopic effects in the rotor and the spindle speed dependent bearing stiffness [127], which results in a change of the low-frequent stiffness and a change in the eigenfrequencies of the spindle-actuator dynamics. The change in the low-frequent stiffness is compensated for by scaling the nominal model of the spindle-actuator dynamics, presented in Section 6.3.2. This is justified by the fact that the change in stiffness can be estimated reasonably well. The scaling factor $\nu_{s,k}$ is determined by dividing the average value of the magnitude of the measured FRF $\mathbf{G}_{aa,k,n}$ (which is the only FRF from (6.2) that can be measured for a rotating spindle) from input voltage of the current controller to measured displacements $\underline{v}_a(t)$ at spindle speed n by the average value of magnitude of the FRF $\mathbf{G}_{aa,k,0}$ measured at standstill over a certain frequency range $\Omega \in \{\omega_1, \omega_2\}$, i.e.

$$\nu_{s,k} = \frac{\sum\limits_{\omega_i \in \Omega} |G_{aa,k,n}(i\omega_i)|}{\sum\limits_{\omega_i \in \Omega} |G_{aa,k,0}(i\omega_i)|}, \tag{6.3}$$

where $k \in \{x, y\}$ and Ω should be chosen in the (low)-frequency domain where the stiffness effects are present. The scaling factor may differ for both feed and normal direction. After obtaining the scaling factors the scaled model is obtained as

$$\mathbf{G}_{s,x} = \nu_{s,x}\mathbf{G}_x, \quad \mathbf{G}_{s,y} = \nu_{s,y}\mathbf{G}_y. \tag{6.4}$$

In order to deal with changing eigenfrequencies due spindle speed induced uncertainty, parametric uncertainties will be used to consider uncertain spindle modes. Uncertainty in resonances is often modelled as a parametric uncertainty in the eigenvalue λ of the system matrix $\mathbf{A}$ of the system. One way to do this is to transform the representation of the system matrix to the modal canonical form (herewith the system matrix $\mathbf{A}$ of the system is in the real Jordan form). After the transformation, the system matrix $\mathbf{A}$ is a block diagonal matrix, i.e. $\mathbf{A} = \text{diag}(\mathbf{A}_1, \mathbf{A}_2, \ldots, \mathbf{A}_{n_\mathbb{C}+n_\mathbb{R}})$, with $n_\mathbb{C}$ the number of complex eigenvalues of $\mathbf{A}$ and $n_\mathbb{R}$ the number of real eigenvalues of $\mathbf{A}$, and

$$\mathbf{A}_l = \lambda_l, \text{ for } \lambda_l \in \mathbb{R}, \tag{6.5}$$

and

$$\mathbf{A}_l = \begin{bmatrix} \text{Re}(\lambda_l) & \text{Im}(\lambda_l) \\ -\text{Im}(\lambda_l) & \text{Re}(\lambda_l) \end{bmatrix}, \text{ for } \lambda_l \in \mathbb{C}. \tag{6.6}$$

Note that in this case it is assumed that the eigenvalues have algebraic multiplicity one, which is typically the case for a parametric model based on a curve

fitting procedure. Then a parametric uncertainty $\delta_{\omega,l} \in \mathbb{C}, |\delta_{\omega,l}| < 1$ can be introduced such that the uncertain mode is modelled as $\mathbf{A}_{l,\delta} = \mathbf{A}_l(1 + r_l\delta_{\omega,l})$ with scaling parameter r_l. However, in this way the uncertainty $\delta_{\omega,l}$ becomes a repeated scalar uncertainty, which results in an increase of the D-scales in case of μ-synthesis which in turn leads to an increase of the controller order. To overcome this problem, Kern [82] exploits a similarity transformation $\mathbf{T}_l$ such that

$$\tilde{\mathbf{A}}_l = \mathbf{T}_l^{-1}\mathbf{A}_l\mathbf{T}_l = \begin{bmatrix} 0 & 1 \\ -\omega_{n,l}^2 & -2\zeta_l\omega_{n,l} \end{bmatrix}. \tag{6.7}$$

Then, by applying a parametric uncertainty $\delta_{\omega,l}$ to the undamped eigenfrequency $\omega_{n,l}$ (since it is assumed that the uncertainty arises due to a change of the bearing stiffness [2, 127]), the uncertain system matrix $\tilde{\mathbf{A}}_{l,\delta}$ is given as

$$\tilde{\mathbf{A}}_{l,\delta} = \begin{bmatrix} 0 & 1 \\ -\omega_{n,l}^2(1 + r_l\delta_{\omega,l})^2 & -2\zeta_{n,l}\omega_{n,l}(1 + r_l\delta_{\omega,l}) \end{bmatrix}. \tag{6.8}$$

By assuming that the term $\omega_{n,l}^2(r_l\delta_{\omega,l})^2$ is small, which is in general the case since r_l is typically chosen in the order of 10^{-2}, (6.8) can be approximated as follows [82]:

$$\tilde{\mathbf{A}}_{l,\delta} \simeq \tilde{\mathbf{A}}_l + \begin{bmatrix} 0 \\ r_l \end{bmatrix} \delta_{\omega,l} \begin{bmatrix} -2\omega_{n,l}^2 & -2\zeta_l\omega_{n,l} \end{bmatrix}. \tag{6.9}$$

As a result, the uncertainty $\delta_{\omega,l}$ becomes a single parametric uncertainty per uncertain eigenfrequency $\omega_{n,l}$, which in turn will result in a controller with a lower order as compared to the case where a parametric uncertainty was applied to (6.6).

Secondly, the uncertainty due to unmodelled dynamics is mainly due to the limited order of the parametric model which results in a deviation between the measured and modelled FRFs at higher frequencies. Moreover, at high frequencies the signal to noise ratio of the eddy current sensors becomes small, as can be seen from the measured FRFs in Figures 6.6 and 6.7. Therewith, the structure of the model at high frequencies is unknown and the uncertainty is modelled using a (frequency-dependent) dynamic additive uncertainty.

Finally, temperature changes are mainly due to an increase of heat generated by the motor as well as due to friction at the interface between raceways and balls in the bearings. This will result in heat generation in the bearings and shaft housing which in turn results in a change in the bearing pre-load [94]. The incorporation of temperature effects in the uncertainty model is difficult. Therefore, in this chapter, all the experiments are performed for a warm spindle and it is assumed that small changes in the temperature are captured by the parametric uncertainties at the eigenfrequencies. The spindle is considered warm when the motor temperature, a variable available in the motor-drive software, has stabilised.

Table 6.3: Parameters of the uncertain spindle modes in both x- and y-direction.

$\omega_{n,l}/2/\pi$ [Hz]	509	545	562	577	596
r_l [-]	0.04	0.04	0.04	0.04	0.04

In order to determine the uncertainties in the spindle-actuator dynamics of the experimental setup, FRFs from AMB input voltage to eddy current displacements $\underline{v}_a(t)$ have been measured for several spindle speeds. In this case, only the response at the bearing location can be measured. In Figure 6.8, the amplitudes of the measured FRFs in feed and normal direction are given for several spindle speeds. First, the scaling parameters $\nu_{s,x}$ and $\nu_{s,y}$, to compensate for the change in the low-frequent stiffness, are determined. Hereto, the average value of the magnitude of the measured FRF at $n = 18$ krpm $\mathbf{G}_{aa,k,18}$ is divided by the averaged value of the magnitude of the FRF at standstill $\mathbf{G}_{aa,k,0}$ for $k \in \{x, y\}$. The interval Ω in (6.3) is chosen as $\Omega = 2\pi[20, 250]$ rad/s. This results in scaling parameters $\nu_{s,x} = 1.4506$ and $\nu_{s,y} = 1.8182$. This implies that there is a significant change in the stiffness due to the spindle speed dependent dynamics, as can also be observed from Figure 6.8. From now on, when a reference to the nominal model is made, it implies the model in which the scaling is absorbed.

From Figure 6.8, it can also be seen that the first bending mode (which lies around 550 Hz) shifts as a function of the spindle speed. Moreover, it can be seen that especially at frequencies above approximately 800 Hz the structure of the model (which is determined using measured data at stand still) does not match the measured FRFs. Based on these results, it is chosen to model the uncertainties on the eigenfrequencies of the model around 550 Hz by parametric uncertainties and to add an additive uncertainty to cope with the differences observed at higher frequencies. From 6.8, it can be seen that the uncertainty in the model, especially at higher frequencies is rather large for the setup under consideration. This may limit the maximal achievable depth of cut during the controller synthesis. It should be noted, however, that such large uncertainties are typically not present in spindles used in commercial milling machines.

In Table 6.3, the parameters of the uncertain eigenfrequencies are listed for both the feed (x)- as the normal (y)-direction. Samples of the uncertain modelled machine dynamics (where the additive uncertainty is not included in the uncertain model) along with the additive uncertainty bound are given in Figure 6.8. It can be seen that the measured spindle speed dependent spindle-actuator dynamics lie inside the uncertainty set of the uncertain model of the spindle-actuator model.

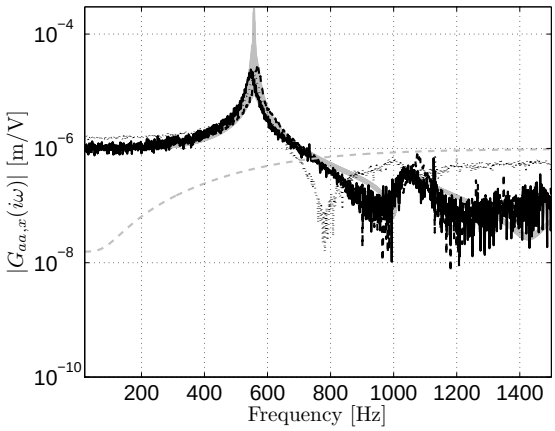

(a) feed direction.

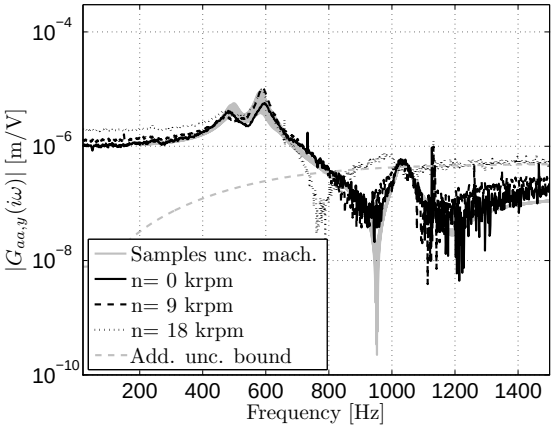

(b) normal direction.

Figure 6.8: Frequency response data for bearing excitation experiments for several spindle speeds.

6.3.4 Stability lobes diagram

Before discussing the controller design, first, stability lobes diagrams (SLD) are calculated using the linearised non-autonomous model of the milling process without control, as presented in Chapter 2, along with the obtained parameters for the cutting force model and the *nominal* scaled parametric models of the spindle-actuator dynamics as presented in Sections 6.3.1 and 6.3.2, respectively. The SLD is also determined experimentally. Hereto, cuts in aluminum 7075

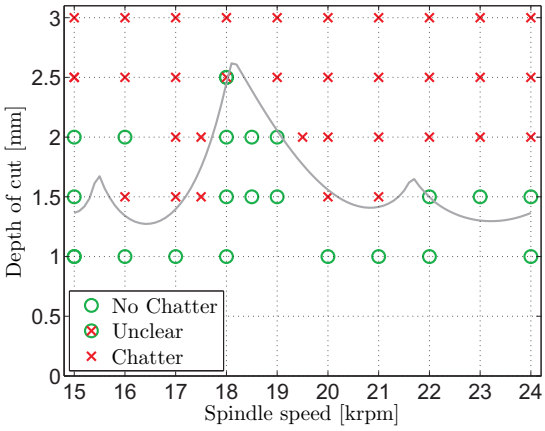

Figure 6.9: Experimental (o,x) and (nominal) model-based (grey line) stability lobes diagram of the experimental setup.

have been made with the experimental setup as described in Section 6.2 for several spindle speeds and depth of cuts. Based on a visible inspection of the workpiece and the observed sound during the cut, a cut is marked with or without chatter. The resulting experimentally obtained SLD and the model-based SLD, calculated using the semi-discretisation method, are presented in Figure 6.9. It can be seen that the calculated SLD fits sufficiently well to the experimentally obtained SLD. Hence, the model of the described in this section will be used for controller synthesis, which will be discussed in the following section.

6.4 Controller design

The model of the experimental setup has been presented in the previous section. In this section, active chatter controllers will be designed which will guarantee robust stability of the milling process for a predefined domain of operating points. The controllers are designed using the procedure as presented in Chapter 4. Herewith, the linearised non-autonomous infinite-dimensional model of the milling process is approximated by a linear autonomous finite-dimensional model, which is suitable for control, by averaging the cutting forces and using a Padé approximation to approximate the time-delay as described in Section 4.4. Moreover, as described in Section 4.5.4, the goal is to determine controllers which guarantee robust stability for a pre-defined domain of operating points in terms of spindle speed n and depth of cut a_p while limiting the level of the actuator forces. This is realised by, firstly, using the perturbation vibrations

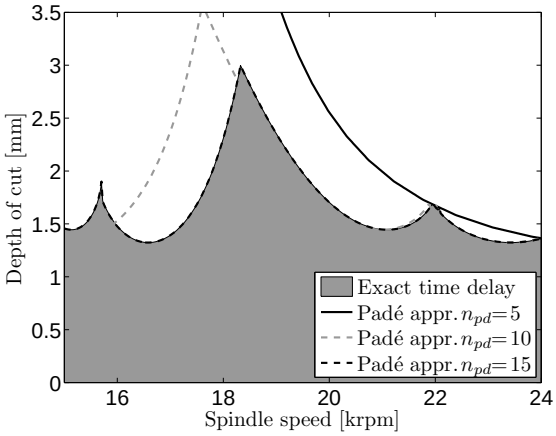

Figure 6.10: Stability lobes diagrams for the approximated autonomous milling model with Padé approximation of order n_{pd} and the milling model with exact time delay for the model of the setup.

$\underline{\tilde{v}}_a(t)$ about the periodic solution $\underline{v}_a^*(t)$ as a controller input signal (see Section 4.3), and, secondly, by enforcing a bound on the control sensitivity function **KS** using weighting function W_{KS} (see Section 4.5.4). It has been shown that the problem can be cast into the generalised plant framework (see Section 4.5.5) and solved using μ-synthesis techniques in the form of D-K-iteration.

As such, before being able to determine controllers **K**, the order of the Padé approximation that will be used to approximate the time-delay in the milling model needs to be selected and the performance weighting function W_{KS} which limits the controller sensitivity function should be specified.

In order to select the order of the Padé approximation, SLDs are determined using the linearised autonomous model of the milling process, given by (4.18) in Chapter 4, and the autonomous model with Padé approximation as given by (4.19). Herein, the scaled nominal model (i.e. without uncertainty) of the spindle-actuator dynamics, as discussed in Section 6.3.2, is used for calculating the stability lobes diagrams. The resulting SLDs for several orders of the Padé approximation are given in Figure 6.10. Similar observations as discussed in Section 4.4 can be made regarding the error between the SLD for the model with exact time-delay and the milling model with approximated time-delay and the order of the approximation. Since the delay is inversely proportional to the spindle speed, the approximation becomes more accurate as the spindle speed increases (i.e. for small delays). Based on the results in Figure 6.10, a Padé approximation of order $n_{pd} = 15$ is selected in order to accurately approximate the delay term in the milling model.

Next, the weighting on the control sensitivity function is defined. As de-

scribed in Section 6.2, the bandwidth of the current controller is limited. In addition, for an AMB it is important to limit the input current in order to avoid saturation of the current [136]. Moreover, as described above, it is desired to limit the input current to the linear operating range of the bearing. Hereto, the structure of the weighting function W_{KS} is chosen as follows

$$W_{KS}(s) = K_p \frac{\frac{1}{(2\pi f_r)^2}s^2 + \frac{\beta_r}{2\pi f_r}s + 1}{\frac{1}{(2\pi f_p)^2}s^2 + \frac{\beta_p}{2\pi f_p}s + 1} \cdot \frac{\frac{1}{(2\pi f_r)^2}s^2 + \frac{\beta_r}{2\pi f_r}s + 1}{\frac{1}{(2\pi f_p)^2}s^2 + \frac{\beta_p}{2\pi f_p}s + 1}. \tag{6.10}$$

Based on the reasoning above, the variables of the weighting function are chosen as follows: $f_r = 1300$ Hz, $f_p = 5000$ Hz, $\beta_r = \beta_p = 0.7$ and $K_p = 2.0 \cdot 10^{-5}$ mm/V. Consequently, W_{KS} has a high-pass characteristic which will enforce roll-off in the controller above the roll-off frequency f_r. The choice of the gain K_p is a trade-off between the ability to shape the SLD and the maximum current that can be applied to the AMB. Moreover, since perturbation feedback will be applied, the actuator forces will be already significantly smaller than in the case where full output feedback is applied (see Section 4.6). This makes it possible to choose K_p more freely.

Based on the SLD of the uncontrolled system, as presented in Section 6.3.4 in Figure 6.9, it can be seen that the productivity of the system measured in terms of the material removal rate (MRR), can be significantly increased when the critical depth of cut is increased in the spindle speed range above 20000 rpm. To this end, two controllers for a single spindle speed of $n = 23000$ rpm have been designed. The first controller is designed where the uncertainty in the spindle-actuator model is not included in the controller synthesis, whereas, for the second controller the uncertainty in the spindle-actuator dynamics is included in the controller design. For the latter case, the uncertainty in the spindle-actuator dynamics is modelled as described in Section 6.3.3. The controllers are designed by employing D-K-iteration with a bi-section scheme to find the largest depth of cut $\bar{a}_p$ such that the structured singular value $\mu_{\hat{\mathbf{\Delta}}_c}(\mathbf{N})$, where $\mathbf{N}$ is defined as the lower fractional transformation between generalised plant $\mathbf{P}$, defined by (4.40) and controller $\mathbf{K}$ (see Section 4.5.6) with respect to uncertainty set $\hat{\mathbf{\Delta}}_c$ is smaller than one (i.e. $\sup_{\omega\in\mathbb{R}} \mu_{\hat{\mathbf{\Delta}}_c}(\mathbf{N}) < 1$) and robust performance of the closed-loop milling process can be guaranteed. Recall, from (4.52), that the uncertainty set $\hat{\mathbf{\Delta}}_c$ is defined as

$$\hat{\mathbf{\Delta}}_c = \begin{bmatrix} \mathbf{\Delta}_c & \mathbf{0} \\ \mathbf{0} & \mathbf{\Delta}_P \end{bmatrix}, \tag{6.11}$$

with $\mathbf{\Delta}_P \in \mathbb{C}^{2\times 2}$, $\|\mathbf{\Delta}_P\|_\infty < 1$ and $\mathbf{\Delta}_c$ is obtained for the case without spindle-actuator dynamics uncertainty

$$\mathbf{\Delta}_c = \{\delta_{a_p}\mathbf{I}_2 : \mathbf{I}_n \in \mathbb{R}^{n\times n}, \delta_{a_p} \in \mathbb{C}, |\delta_{a_p}| < 1\}, \tag{6.12}$$

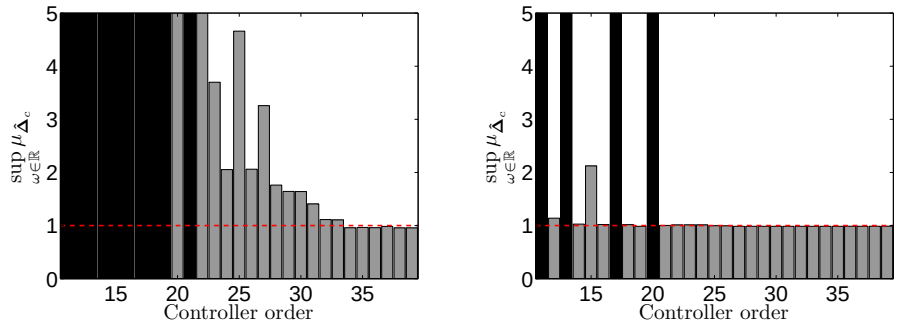

(a) Without spindle-actuator uncertainty.

(b) With spindle-actuator uncertainty.

Figure 6.11: Closed-loop $\mu_{\hat{\mathbf{\Delta}}_c}$-values for reduced-order controllers calculated with and without spindle-actuator uncertainty, using closed-loop balanced truncation. Black bars indicate an unstable closed-loop.

and for the case with spindle-actuator dynamics uncertainty included in the controller design

$$\begin{aligned}\mathbf{\Delta}_c = \{\mathrm{diag}(\delta_{\omega,l}\mathbf{I}_1, \delta_{a_p}\mathbf{I}_2) : \delta_{\omega,l}, \delta_{a_p} \in \mathbb{C}, |\delta_{\omega,l}|, |\delta_{a_p}| < 1, \\ \mathbf{I}_n \in \mathbb{R}^{n\times n}, l \in \{1,\ldots,5\}\}.\end{aligned} \tag{6.13}$$

As described in Section 4.5.6, $\mu_{\hat{\mathbf{\Delta}}_c}(\mathbf{N})$ is determined by calculating the upper bound on $\mu_{\hat{\mathbf{\Delta}}_c}(\mathbf{N})$ as defined in (4.54).

Controller synthesis using D-K-iteration without including uncertainty in the spindle-actuator dynamics yields a 104-th order controller for a maximal depth of cut $\bar{a}_p = 2.69$ mm ($\mu_{\hat{\mathbf{\Delta}}_c} = 0.946$). After applying closed-loop model reduction techniques as described in Section 4.5.7, the controller order is reduced to 34 with $\sup_{\omega\in\mathbb{R}} \mu_{\hat{\mathbf{\Delta}}_c} = 0.9582$ and, consequently, robust performance is guaranteed for the reduced-order controller. Values of $\sup_{\omega\in\mathbb{R}} \mu_{\hat{\mathbf{\Delta}}_c}$ for several controller orders (after reduction) are given in Figure 6.11(a). The controller with uncertainty in the spindle-actuator dynamics included in the synthesis yields a 98-th order controller for a depth of cut $\bar{a}_p = 2$ mm ($\sup_{\omega\in\mathbb{R}} \mu_{\hat{\mathbf{\Delta}}_c} = 0.989$). Closed-loop model reduction yields a 19-th order controller with $\sup_{\omega\in\mathbb{R}} \mu_{\hat{\mathbf{\Delta}}_c} = 0.9859$ and, as previously discussed, robust performance is guaranteed for the reduced-order controller. Values of $\sup_{\omega\in\mathbb{R}} \mu_{\hat{\mathbf{\Delta}}_c}$ for several controller orders are given in Figure 6.11(b). It can be seen that by including uncertainty in the spindle-actuator dynamics model, the maximal depth of cut $\bar{a}_p$ for which robust performance of the milling system can be guaranteed is smaller than for the case where no uncertainty in the spindle-actuator dynamics model is included in the controller design. This was also concluded from the results in Chapter 4. This result is as expected, since a controller is designed which should ren-

der the closed-loop milling model stable for an entire (uncertain) set of models describing the spindle-actuator dynamics. Magnitude plots of the high-order and reduced-order controllers are given in Figure 6.12. It can be seen that the resulting controllers exhibit highly dynamical characteristics indicated by the inverse notches in the FRF. Whereas for the case without spindle-actuator dynamics uncertainty, the full- and reduced-order controller have similar FRF magnitudes (hence the difference is hardly visible in Figure 6.12(a)), the FRF magnitudes for the full-order and reduced-order controller differ significantly for the case where spindle-actuator dynamics is included in the controller synthesis. In the next section, SLDs will be determined using the reduced-order controllers for both cases.

6.5 Closed-loop model-based stability analysis

Based on the controllers, obtained using D-K-iteration in the previous section, in this section, the results of a closed-loop model-based stability analysis will be discussed. Hereto, SLD diagrams will be determined using the linearised non-autonomous model of the milling model (Equation (2.13)), as outlined in Section 2.7, with the cutting force model parameters and spindle-actuator dynamics model as described in Section 6.3 and the controllers as obtained in the previous section. The resulting closed-loop model-based SLDs along with the open-loop and experimentally obtained SLD, as already presented in Section 6.3.4, are given in Figure 6.13.

From the closed-loop SLD calculated using the controller without uncertainty in the spindle-actuator dynamics included, as given in Figure 6.13(a), it can be seen that the SLD is shaped such that a peak at the desired spindle speed of $n = 23000$ rpm is created. In this way, the depth of cut can be increased from $a_{p,\mathsf{max}} = 1.30$ mm in the uncontrolled case to a depth of cut of $a_{p,\mathsf{max}} = 2.84$ mm ($\bar{a}_p = 2.69$ mm) in the case with active chatter control, where $a_{p,\mathsf{max}}$ denotes the maximal depth of cut in the SLD at $n = 23000$ rpm, which is an increase of 118%.

When the spindle-speed uncertainty model is included in the controller design, the SLD is altered in a different way as compared to the case with no spindle-actuator uncertainty included in the controller design. This can be seen from the SLD in Figure 6.13(b). It can be clearly seen, that in this case the controller is unable to create a peak at the desired location. This is due to the fact that in order to create a peak in the SLD the closed-loop eigenfrequency needs to be altered (by the controller). However, due to the uncertainty in the eigenfrequency the resulting controller cannot tailor the eigenfrequency such that it is shifted to the tooth-passing excitation frequency. Consequently, the peak in the SLD is not located at the desired spindle speed. Despite this fact, it can be seen that the resulting SLD is lifted at the desired spindle speed. In this case the depth of cut can be increased to $a_{p,\mathsf{max}} = 2.23$ mm ($\bar{a}_p = 2$ mm),

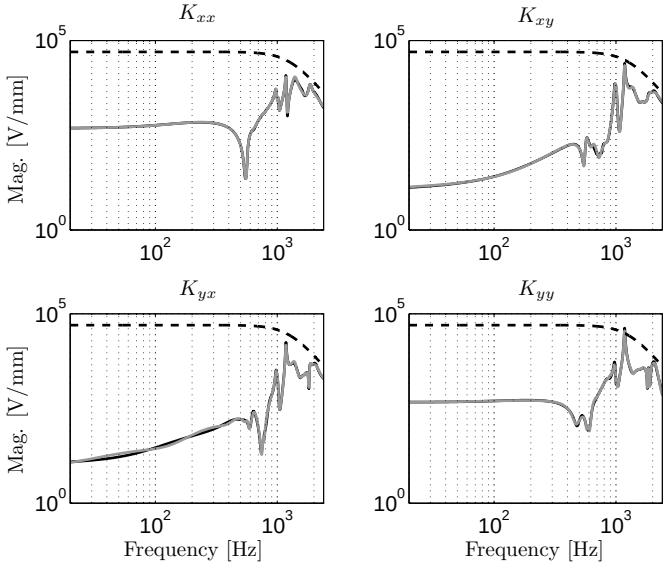

(a) Without spindle-actuator uncertainty.

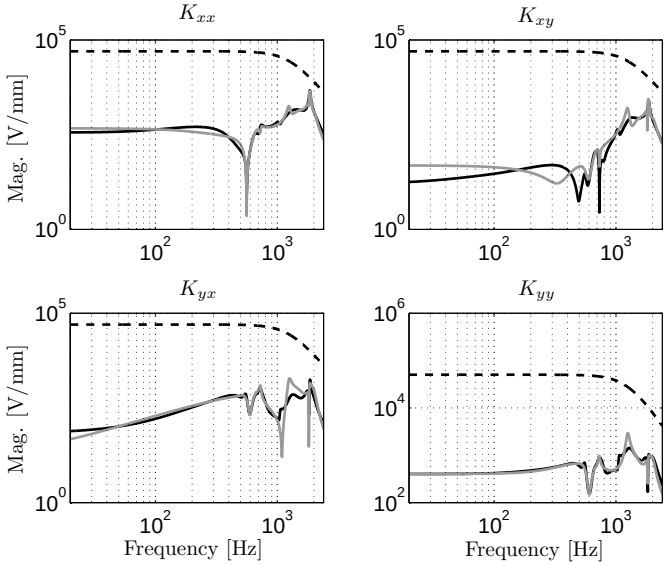

(b) With spindle-actuator uncertainty.

Figure 6.12: Magnitude of the FRF *for the full-order (black) and reduced-order (grey) controllers obtained from D-K-iteration for the case with and without spindle-actuator uncertainty along with the inverse of the performance weighting function W_{KS} (dashed).*

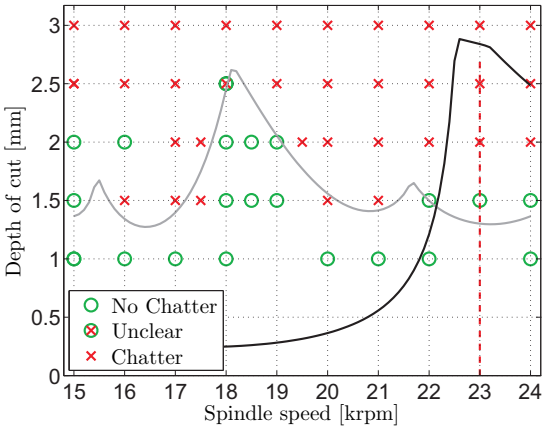

(a) Without spindle-actuator uncertainty.

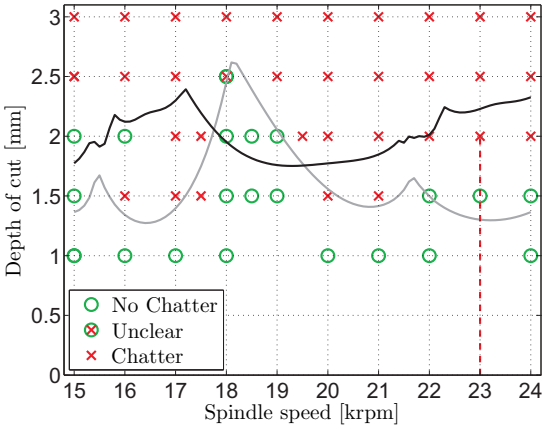

(b) With spindle-actuator uncertainty.

Figure 6.13: Experimental (o, x) SLD *and model-based (solid lines)* SLD *of the open-loop system (grey) and the closed-loop system for reduced-order controllers (black) obtained from D-K-iteration with and without spindle-actuator uncertainty, using the nominal spindle dynamics. The domain of stable operating points as guaranteed by the μ-synthesis is given by the dashed line.*

---

which is an increase of approximately 71% as compared to the case without active chatter control.

To explain the difference between the two control design cases in more

detail, FRFs of the closed-loop tooltip dynamics are given in Figure 6.14. The open-loop and closed-loop tooltip dynamics are calculated using the nominal model of the spindle-actuator dynamics. For the case that the uncertainty in the model of the spindle-actuator dynamics is not included in the controller design, it can be seen that the eigenfrequency related to the first bending mode of the spindle is shifted to the first tooth-passing excitation frequency. As discussed above, this leads to a peak in the SLD at the desired spindle speed of 23000 rpm which is beneficial for stability, i.e. the robustness of the milling process against chatter. For the controller where the uncertainty model of the spindle-actuator dynamics model is included in the controller design, it can be seen that the closed-loop tooltip dynamics of the closed-loop system in the feed (x)-direction is almost similar as the open-loop dynamics. The resonance related to the first bending mode of the spindle-actuator model is slightly damped. For the normal (y)-direction the resonance shifted towards the first harmonic of the tooth passing excitation frequency and is also damped considerably as compared to the open-loop tooltip dynamics. It is well known that damping the resonances affects the chatter stability boundary over the entire spindle speed range as can be seen from the SLD in Figure 6.13(b).

From the results presented in this section, it can be concluded that when the spindle-actuator dynamics has little or no uncertainty, the SLD can be altered such that a peak is created at the desired spindle speed interval, even for relatively complex models of the spindle-actuator dynamics. However, in the controller design a trade-off between performance (in terms of maximal achievable depth of cut) and the amount of uncertainty in the spindle-actuator model has to be made. In the next section, the controllers will be implemented on the actual setup and closed-loop milling tests will be performed.

6.6 Experimental results

In the final part of this chapter, the controllers, as designed in Section 6.4, will be implemented on the experimental setup. Hereto, the controllers are implemented using hardware and software from dSpace [38], see Figure 6.15 where a block diagram of the implementation of the controller is given. Recall from Chapter 4 that the controllers are designed in a continuous-time domain setting. Real-time workshop of MATLAB [107] can be used to convert SIMULINK models of the controllers to C-code which is then loaded onto the dSpace hardware and executed in real-time. At each sampling instant a numerical integration algorithm calculates the controller output. Here a sampling frequency of 10 kHz is chosen. The choice of the sampling frequency is a trade-off between the ability to implement controllers of relatively high-order (due to the number of calculations needed at each time instant) and the accurate discrete-time approximation of the continuous-time controller in the digital control environment to prevent performance degradation. As already described above, the

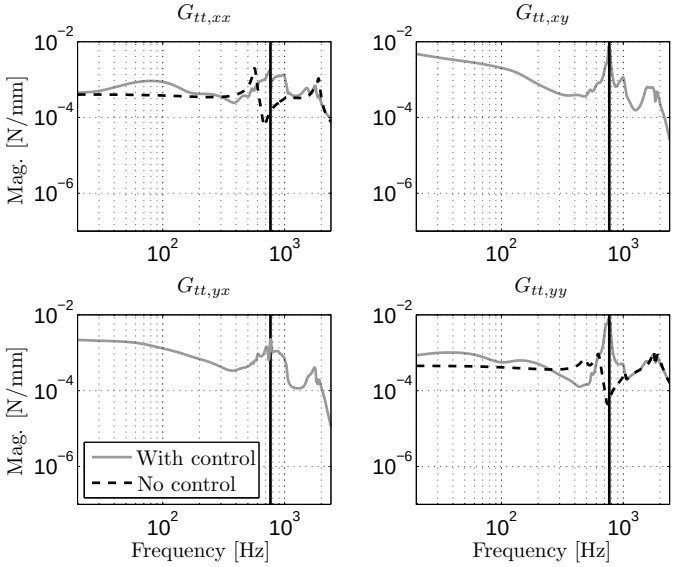

(a) Without spindle-actuator uncertainty.

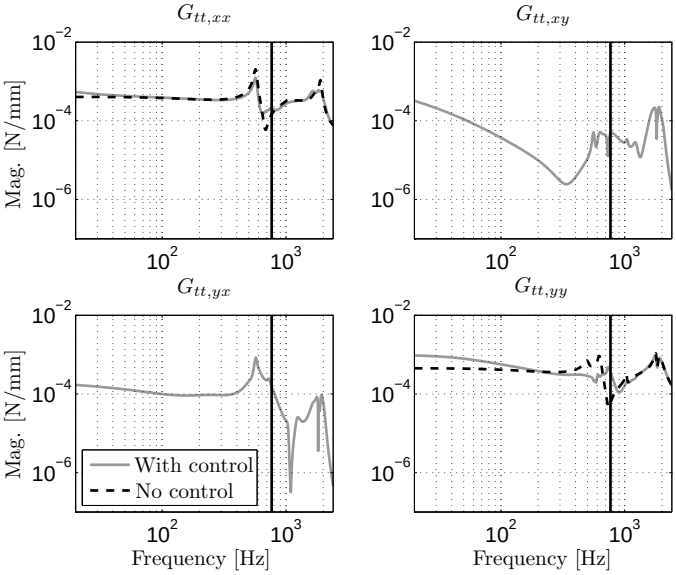

(b) With spindle-actuator uncertainty.

Figure 6.14: Magnitudes of the open-loop FRF $\mathbf{G}_{tt}(i\omega)$ *(dashed) and closed-loop* FRF $\mathbf{G}_{tt,c}(i\omega)$ *(grey) of the spindle-actuator dynamics at the tooltip. The first harmonic of the tooth passing excitation frequency is indicated by the vertical bar.*

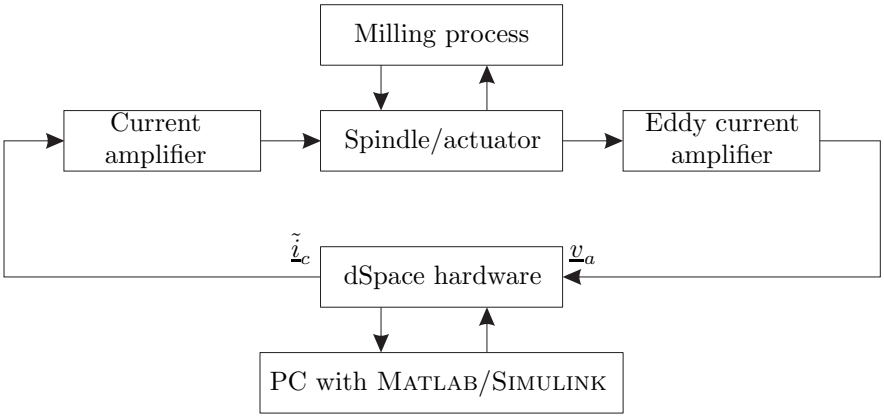

Figure 6.15: Block diagram of the implementation of the controller on the experimental setup.

input current to the AMB should be limited in order to prevent the AMB from saturating. In Section 4.3, it has been shown that by using perturbation feedback (i.e. the controller output is determined using the perturbation vibrations $\tilde{\underline{v}}_a(t)$ about the periodic solution $\underline{v}_a^*(t)$ as controller input signal) the actuator forces will be significantly smaller as compared to the case where the total measured displacements $\underline{v}_a(t)$ are used as a input signal to the controller. In order to determine the perturbation vibrations, an online estimation algorithm as presented in Chapter 3, which is based on the NLMS algorithm, can be used. A similar estimation algorithm, based on a recursive least square algorithm is presented in [83]. It should be noted that by applying an online estimation algorithm in closed-loop with the controller and the plant, closed-loop stability may not be guaranteed. This can be realised by considering the fact that the estimation algorithm can be seen as a kind of observer and no separation principle has been developed (yet) for this type of observer/controller design combination in case of a system which can be described by a set of nonlinear time-varying delay-differential equations.

Next, the controllers will be implemented on the actual setup and milling tests will be performed. Unfortunately, the controller which is designed without including the uncertainty model of the spindle-actuator dynamics in the controller design, does not render the closed-loop system stable. The output of the controller grows unbounded and results in saturation of the AMB input current. This result can be due to various reasons. First of all, since the controller is designed without including uncertainty in the spindle-actuator dynamics, the spindle-actuator dynamics may be, at the time of this experiment, such that the closed-loop system is unstable. Secondly, as already mentioned in Chapter 4, the controller design does not guarantee a priori that the synthesised con-

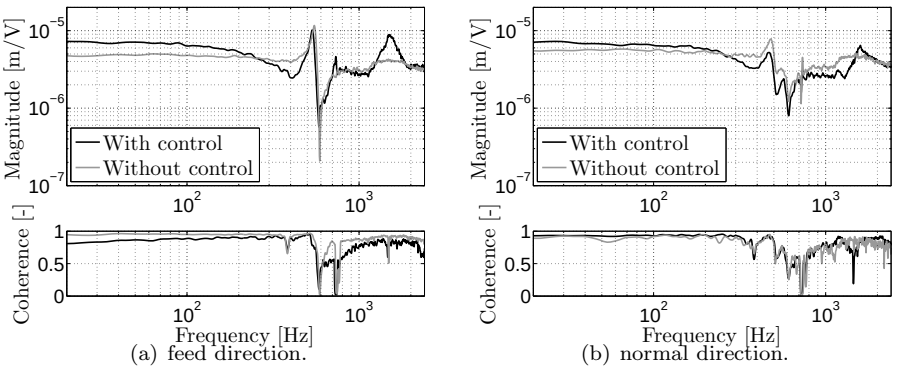

Figure 6.16: Magnitude and coherence of the measured closed-loop process sensitivity and open-loop FRF *from current controller input voltage to measured bearing displacements where the spindle is rotating at $n = 23000$ rpm.*

trollers are stable by itself. In this case, the controller without spindle-actuator uncertainty included in the design, has unstable poles which are not desired from a practical viewpoint [69].

Finally, the controller designed with uncertainty in the spindle-actuator dynamics taken into account, is implemented on the experimental setup. With this controller it is possible to perform milling tests where perturbation feedback is applied by filtering the spindle speed harmonics from the measured displacements using the recursive least squares algorithm from [83]. Herewith, the first spindle speed harmonic and the first three tooth passing excitation frequencies are filtered from the displacements $\underline{v}_a(t)$ measured using the eddy current sensors. Before the results from a milling test are presented, first measurements are performed to determine the process sensitivity FRF of the closed-loop system in both feed and normal direction. The obtained FRFs are compared to measurements of the open-loop plant. Hereto, the AMB is excited using a PRBS signal with amplitude 2 A, for a rotating spindle at $n = 23000$ rpm while measuring the response using the eddy current sensors. The resulting magnitudes of the FRFs in feed and normal direction are given in Figure 6.16 (note that in this case the tooltip dynamics, which are of interest for calculating the SLD, cannot be measured since the spindle is rotating). From the figures it can be seen that the controller alters the spindle dynamics, where the first bending mode of the spindle is damped (this is especially noticeable in the normal direction) and a resonance is created at approximately 1510 Hz which is close to the second harmonic of the tooth passing excitation frequency ($2f_{tpe} = 2 \cdot \frac{2 \cdot 23000}{60} \approx 1533$ Hz). Moreover, it can be seen that the stiffness of

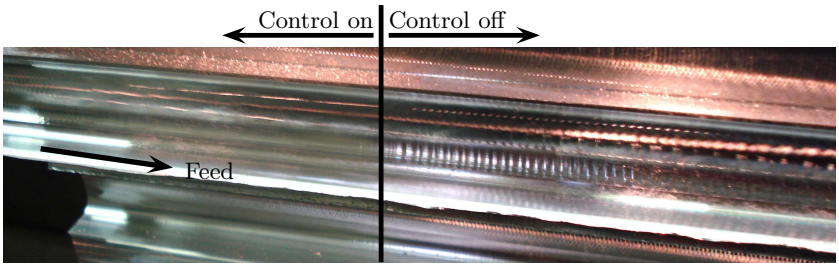

Figure 6.17: Photo of the workpiece where a cut is made at $n = 23000$ rpm for a depth of cut of $a_p = 2.5$ mm, where in the first part of the cut the controller is on and is switched off after approximately 100 mm.

---

the system is decreased.

Next, a full immersion cutting test has been performed at 23000 rpm for a depth of cut of 2.5 mm using the controller with spindle-actuator uncertainty included in the controller design. Notice that chatter occurs for the open-loop at this depth of cut, see Figure 6.9. At the start of the cut, the controller is switched on. When the cutter is approximately 100 mm inside the material (in feed direction), the controller is switched off. After switching the controller off, chatter marks become visible on the workpiece. A picture of a part of the resulting workpiece is given in Figure 6.17. It can be seen that, at the start of the cut, no chatter marks are visible on the workpiece, whereas, chatter marks appear on the workpiece when the controller has been switched off. The output $\underline{\tilde{i}}_c(t)$ generated by the controller is given in Figure 6.18(a). With the controller switched on, the amplitude of the controller output is about 1.8 A, which is smaller than the maximal allowed controller output of 5 A (the maximum allowed controller output is given by subtracting the pre-magnetising current in Table 6.1 from the maximal current input as listed in Table 6.1, see also [136]). The perturbation displacements $\underline{\tilde{v}}_a(t)$, estimated using the recursive estimation algorithm as described in [83], are given in Figure 6.18(b). From the estimated perturbation vibrations $\underline{\tilde{v}}_a(t)$ no significant decrease in amplitude can be seen between the case with the controller switched on and the controller switched off.

Therefore, the power spectral density (PSD) plot of the estimated perturbation vibrations $\underline{\tilde{v}}_a(t)$ in the feed (x) direction are considered in Figure 6.19(a). For sake of clarity, also the PSD of the measured displacements $\underline{v}_a(t)$ in the feed direction are given in Figure 6.19(b). It can be seen that the amplitude of the first spindle speed harmonic and first three tooth passing excitation frequencies are significantly reduced in the PSD of the estimated perturbation vibrations. This reduces the total amount of actuator forces necessary to stabilise the pro-

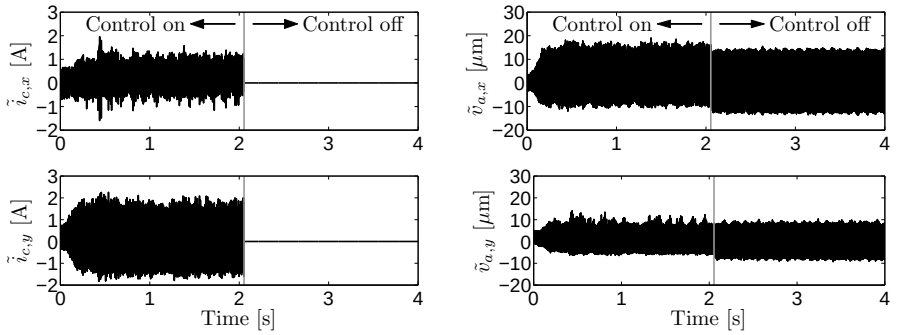

(a) Controller output.

(b) Estimated bearing perturbation displacements.

Figure 6.18: Controller output $\underline{\tilde{i}}_c(t)$ (in ampere) and estimated perturbation vibrations $\underline{\tilde{v}}_a(t)$ (in μm) for a cut made at $n = 23000$ rpm for a depth of cut of $a_p = 2.5$ mm where along the cut the controller is switched off.

cess. Next to spindle speed harmonics, other frequencies are present in the PSD. At approximately 570 Hz a dominant frequency can be seen in the PSD, which is related to the first resonance of the spindle-actuator system. It can be seen that for the case with control the amplitude of this frequency is reduced with almost 50% as compared to the case without control. Around the second harmonic of the tooth passing excitation frequency (i.e. around 1500 Hz) a clear difference in the PSD for the case with and without can be seen. For the case with control a relatively wide peak in the PSD can be seen around 1500 Hz. This frequency is related to a new created resonance at the second harmonic of the tooth passing excitation frequency as can be seen from the magnitude of the measured closed-loop spindle-actuator dynamics in Figure 6.16. As discussed in Section 2.8, in the case without chatter the PSD contains spindle speed related frequencies as well as the damped natural frequencies of the spindle dynamics, whereas chatter frequencies appear around each spindle speed harmonic when chatter occurs. Due to the fact that the spindle system, considered in this chapter, has multiple resonances it is difficult to distinguish from the PSD whether the typical chatter frequencies are present in the measured vibration signal. However, from the resulting workpiece in Figure 6.17 it is evident that for the case with control no chatter marks are visible on the workpiece, whereas, for the case without control chatter marks are clearly visible on the workpiece.

Resuming it can be said that, based on the results presented in this chapter, the working principle of the active chatter control design methodology has been

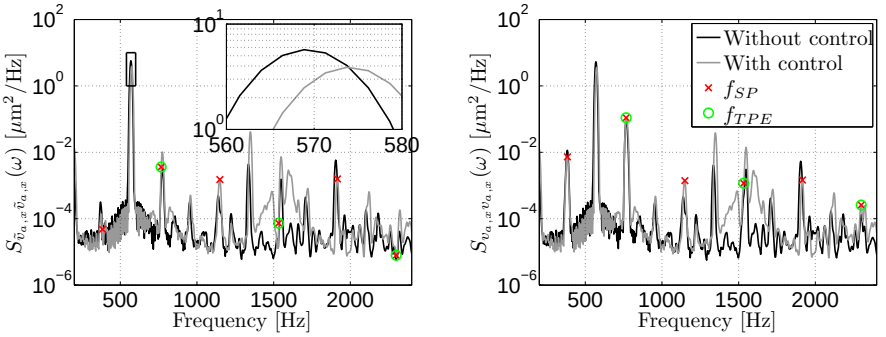

(a) Estimated perturbation vibrations.

(b) Measured displacements.

Figure 6.19: Power spectral density of the estimated perturbation vibrations $\underline{\tilde{v}}_a$ and measured displacements $\tilde{v}_a$ in feed (x) direction for a cut made at $n = 23000$ rpm for a depth of cut of $a_p = 2.5$ mm.

illustrated in practice. With active chatter control for a single spindle speed, the depth of cut could be increased to 2.5 mm which is an increase of approximately 66% as compared to the experimentally uncontrolled obtained SLD in Figure 6.9 at the same spindle speed.

However, more research is necessary for the further validation of the methodology for future implementation in commercial milling machines. In order to design controllers based on the active chatter control methodology for the experimental setup under consideration uncertainties needed to be incorporated into the controller design which significantly limits the performance of the obtained controller, as illustrated in this section. One way to decrease the amount of uncertainties is the dedicated identification of the model of the experimental setup at the spindle speed for which controllers need to be designed (as opposed to identifying the spindle dynamics at standstill). Identification of spindle-speed dependent spindle-actuator dynamics is difficult due to the fact that the tooltip response cannot be measured directly. Receptance coupling techniques, as e.g. discussed in [45, 111, 134], where the spindle-actuator dynamics are determined for a specific spindle speed and (a model of) the tool/toolholder dynamics is coupled afterwards to the obtained spindle-actuator dynamics, can be applied. Although receptance coupling techniques seem to work well for simple models of the spindle-actuator dynamics, more research is necessary for more complex spindle-actuator dynamics as discussed in [171]. Moreover, while the experimental setup as used in this chapter can serve as a testbed to provide a proof of principle of the active chatter control methodology, it cannot be readily used in a machine shop. This is mainly due to the relatively large uncertainties present in the setup under consideration, as discussed in

Section 6.3.3. Hereto, a new dedicated spindle design with integrated actuator should be pursued which is better suitable for application in commercial milling machines.

6.7 Discussion

The goal of this chapter has been to illustrate the working principle of the active chatter control strategy on an actual milling spindle with integrated (AMB) actuator. A milling spindle with an integrated active magnetic bearing, located between the front bearing and the toolholder connection, is used to provide the proof of principle. From the experimental results, presented in this chapter, it can be concluded that the active chatter control methodology, developed in this thesis, can indeed be applied to design controllers which alter the SLD such that a pre-defined domain of working points is stabilised, even for (more) complex (models of the) spindle-actuator dynamics. A milling test illustrates that with active chatter control at a specific spindle speed, the productivity, for the spindle considered in this chapter, can be increased by approximately 66% as compared to the case without active chatter control. The increase of productivity (i.e. the MRR) is limited, firstly, due to the fact that the identification of the model of the spindle-actuator dynamics can only be performed for a non-rotating spindle, and, secondly, due to the fact that the spindle-actuator dynamics varies significantly due to, amongst others, temperature effects. Both effects require that uncertainties in the model of the spindle-actuator dynamics need to be taken into account during controller design, resulting in a limited increase of the productivity as compared to the case where no uncertainties in the spindle-actuator model are included in the controller design. Therefore, a trade-off has to be made between the performance of the controller (in terms of maximal achievable depth of cut) and the amount of uncertainty included in the controller design. The uncertainties in the spindle dynamics are rather large for the typical spindle under consideration in this chapter. Therefore, it is recommended to pursue a new dedicated spindle design with integrated actuator which is better suitable for application in commercial milling machines.

7

Conclusions and recommendations

The occurrence of the vibrational instability phenomenon chatter limits the performance (in terms of the material removal rate (MRR)) of cutting techniques, such as the high-speed milling (HSM) process. Chatter should therefore be avoided at all times. A machinist can select (chatter-free) working points based on the knowledge of stability lobes diagram (SLD). The choice of the working point typically aims at a high productivity while possibly complying with additional cutting speeds requirements. In order to guarantee a chatter-free high-speed milling operation, which, firstly, is robust for changing process conditions and, secondly, renders working points with a higher MRR feasible, two chatter control approaches have been developed in this thesis.

The first chatter control strategy, presented in Chapter 3, ensures a robust (chatter-free) milling operation, despite changing process conditions, such as temperature changes and wear of the spindle and tool, by automatic adaptation of spindle speed and feed. The second control strategy, presented in Chapters 4, 5 and 6, enables dedicated shaping of the stability lobes diagram in a selective spindle speed range such that working points, in terms of spindle speed and depth of cut, of higher MRR become feasible while avoiding chatter.

In Section 7.1, the main conclusions of the work presented in this thesis will be discussed. Recommendations for future research will be presented in Section 7.2.

7.1 Conclusions

The conclusions of this thesis are categorised based on the two chatter control strategies.

Chatter control by automatic spindle speed selection

The conclusions regarding chatter control by automatic adaptation of spindle speed and feed, as presented in Chapter 3, are given as follows:

- The automatic spindle speed selection algorithm requires an early detection of the onset of chatter and, moreover, an accurate estimation of the (dominant) chatter frequency. A novel, computationally efficient, detection algorithm is presented which detects chatter before chatter marks appear on the workpiece. A computationally efficient algorithm is a prerequisite for chatter detection, since chatter develops typically within 100 ms in the case of HSM. Additionally, the detection algorithm provides an accurate estimate of the (dominant) chatter frequency, which is necessary for the automatic spindle speed selection control algorithm.

- When chatter is detected, spindle speed and feed setpoints are generated such that stable (chatter-free) machining is guaranteed. Two approaches are discussed in Section 3.3. In the first approach, which is a common approach in literature on chatter control by spindle speed selection, the spindle speed is adjusted such that a tooth passing excitation frequency becomes equal to the dominant chatter frequency. While this results in bounded chatter vibrations, the vibrations are not likely to be minimised. Therefore, in this work, a second approach, based on extremum seeking control, is presented, which automatically minimises the cutter vibrations by adaptation of the spindle speed.

- Experiments on a state-of-the-art high-speed milling machine have been performed in Section 3.4 to validate the working principle of the chatter detection and automatic spindle speed selection control algorithm in practice. Results illustrate that both spindle speed selection approaches ensure the avoidance of chatter. Consequently, spindle speed selection guarantees a robust high-speed milling operation, such that working points high up in a lobe may be selected, which results in a high material removal rate, without the occurrence of chatter. Whereas the first approach only guarantees a robust machining operation, the second approach also minimises the total chatter vibrations.

Active chatter control design

The conclusions regarding the active chatter control design, as presented in Chapters 4, 5 and 6, are given as follows:

- A (model-based) active chatter control methodology has been developed which is able to shape the stability lobes diagram in a selective range of spindle speeds, such that chatter free high-speed milling operations can be a priori guaranteed for a predefined domain of operating points. As a result, working points of a higher material removal rate become feasible while avoiding chatter. Such a strong guarantee of a priori stability for a predefined domain of operating points does not yet exist in active chatter control in the case of milling. This is contrary to the application of active

damping which lifts the SLD over the entire spindle speed range at the cost of high required levels of actuation energy. The requirement of a priori stability for a predefined range of process parameters is cast into a robust stability requirement. Hereto, the spindle speed and depth of cut are treated as uncertainties. In addition, uncertainties in the spindle dynamics, due to spindle-speed dependent dynamics, can be included in the controller design.

- The controller effort, needed to stabilise milling operations is limited during the controller design. Firstly, a comprehensive analysis has been presented where, based on an appropriate choice of the controller input signal, it is illustrated that the actuator forces can be significantly reduced. Secondly, a bound on the actuator forces is incorporated in the controller design by including a bound on the controller sensitivity as a performance criterion.

- The dynamics of the milling model, as discussed in Chapter 2, is modelled as a set of nonlinear time-varying delay differential equations. The presence of the time-delay and the explicit time-dependency of the milling model complicates the controller design. Hereto, in Chapter 4, a simplified (finite-dimensional, autonomous) linearised milling model is derived where the time delay is approximated using a Padé approximation and the cutting forces are averaged over the tooth path. Then the control problem is solved via μ-synthesis using D-K-iteration. Results for illustrative examples, clearly illustrate the power of the proposed control methodology. The chatter stability boundary is locally shaped to stabilise the desired range of working points. This is contrary to the application of active damping which lifts the SLD over the entire spindle speed range at the cost of high required levels of actuation energy. The controllers tailor the closed-loop spindle dynamics in such a way that a resonance is situated near a tooth pass excitation frequency of the desired (range of) spindle speeds which results in a peak in the SLD at the desired (range of) spindle speeds.

- The active chatter control methodology, based on a simplified linearised milling model, results in controllers which are of relatively high order due to the relatively high order of the Padé approximation necessary to accurately describe the delay term in the desired range of spindle speeds. To alleviate the burden of controller complexity, which is important for digital implementation, the order of the controller is reduced by applying closed-loop balanced truncation techniques.

- A disadvantage of the employment of controller order reduction by closed-loop balanced truncation is that in general no guarantees can be given regarding closed-loop stability and (robust) performance of the closed-loop

system. To overcome this drawback, a fixed structure active chatter control procedure is presented in Chapter 5. The fixed structure controller design is based on the infinite-dimensional model of the milling process, i.e. without approximating the time-delay term. In this way, low-order controllers can be designed which is beneficial from an implementation perspective. Results, for both static and dynamic output feedback, show that even for low-order controllers it is possible to alter the SLD, in a dedicated fashion, such that a peak in the SLD is created in the desired range of spindle speed range. This illustrates the effectiveness of the fixed structure controller design methodology.

- Some similarities and differences can be distinguished between the two active chatter control methodologies presented in Chapters 4 and 5. Firstly, both control design approaches are based on μ-synthesis techniques and the related optimisation problems are solved using D-K-iteration. Secondly, the fixed-structured chatter control design is based on the model without any delay approximation, whereas the controller design in Chapter 4 is based on a linear model with approximation of the delay. Thirdly, the μ-synthesis for the finite-dimensional model of the milling process leads to high-order controllers while the fixed-structure controller design procedure results in linear controllers of fixed-order. Fourthly, no uncertainty in the spindle dynamics is included in the fixed-structure control design procedure, yet. Finally, standard tools from robust control theory can be applied in case of active chatter control for the finite-dimensional model of the milling process to determine controllers of high-order, which may be required for active chatter control in case of complex spindle dynamics. However, it may be computationally challenging to determine high-order controllers using the fixed-order active chatter control methodology.

- Experiments have been performed to validate the working principle of the active chatter control strategy (of Chapter 4) in practice. Hereto, a milling spindle with an integrated active magnetic bearing, located between the front bearing and the toolholder connection, is considered. Based on the obtained experimental results, it can be stated that the active chatter control methodology, as presented in this thesis, can indeed be applied to design controllers, which alter the SLD such that a predefined domain of working points is stabilised, even for (more) complex (models of the) spindle-actuator dynamics and relatively high levels of uncertainty therein. Results from milling tests underline this conclusion. By using the active chatter controller, designed for a specific spindle speed, working points with a higher material removal rate become feasible while avoiding chatter.

- The rational behind of the automatic spindle speed selection algorithm,

presented in Chapter 3, and the active chatter control methodologies, presented in Chapters 4 and 5, are actually similar. Both approaches aim to set the dynamic chip thickness equal to zero. The spindle speed selection algorithm alters, in case of (onset) of chatter, the spindle speed, such that a tooth-passing excitation frequency is set (equal or close to) the dominant chatter frequency, which results in the dynamic chip thickness to be zero. The active chatter control methodology, alters the spindle dynamics such that an eigenfrequency is set to a tooth passing excitation frequency, and, as a result the dynamic chip thickness becomes equal to zero, which is beneficial for stability.

Summarising, it can be said that, with the chatter control methodologies, as presented in this thesis, robust (chatter-free) high-speed milling operations can be performed with a significant increase in productivity as compared to the case without chatter control. Firstly, the application of the automatic in-process spindle speed selection algorithm, ensures robust machining despite changing process conditions, such as temperature changes in the spindle and wear of the tool. In this way, working points high up in a lobe may be chosen which results in an increase of the MRR, as compared to the case where a working point is chosen which is stable for all spindle speeds. Secondly, the application of the active chatter control methodology, as presented in this thesis, enables the possibility to alter the SLD in a specific range of spindle speeds. Therewith, working points of a high depth of cut can be rendered feasible (chatter-free) which results in a significant increase in the MRR.

7.2 Recommendations

In this final section, recommendations for future research are given. Firstly, recommendations regarding the automatic spindle speed selection algorithm will be given. Secondly, recommendations regarding the active chatter control design methodologies will be discussed.

Chatter control by automatic spindle speed selection

Recommendations for future research regarding the automatic spindle speed selection chatter controller design are given below:

- The chatter detection and control methodology that, by automatic adaptation of spindle speed and feed, ensures robust (chatter-free) milling operations, as presented in Chapter 3, requires the selection/tuning of the parameters of the detection and control algorithm. In general, these parameters will differ for each milling machine/spindle/workpiece combination. Moreover, the tuning of the parameters can be a challenging task. Therefore, a methodology to automatically select the parameters of the

detection and control algorithm would be highly beneficial to successfully implement the chatter control strategy in a machine shop environment.

- In the experimental results of Chapter 3, it has been discussed that there is a relatively large delay present in the chatter control loop. The delay is caused by the fact that the spindle speed and feed override on the hand terminal are used as an input to the spindle speed and feed controllers of the milling machine. The spindle speed and feed override has a relatively low priority in the control loop of a milling machine which, in turn, results in a delay in the control loop. Although chatter is detected before chatter marks are present on the workpiece, due to the relatively large delay, some small chatter marks may still appear on the workpiece during the spindle speed transition. Therefore, in order to reduce the delay in the chatter control loop, the spindle speed and feed setpoint should be directly supplied to the internal spindle speed and feed controllers of the milling machine.

Active chatter control design

Recommendations for future research on active chatter control design are given below:

- The active chatter control design, presented in Chapters 4, 5 and 6, has been based on an autonomous model of the milling process (after averaging of the time-varying cutting model). While the autonomous model is a good approximation of the non-autonomous model for high immersion levels, it may not be sufficient for active chatter controller design at low immersion levels. Therefore, for cuts at a low immersion level, the time-varying term in the milling model should be taken into account during controller design. Hereto, e.g. Lyapunov-based techniques for robust stabilising controller design may be exploited.

- In order to limit the amount of actuator forces needed to stabilise the milling process in a pre-defined domain of working points, perturbation feedback can be applied. Hereto, the (nominal) periodic solution of the milling process is subtracted from the total (measured) vibrations. An alternative approach might be to apply Pyragas type feedback (see [125, 126]), where the delayed total (measured) vibrations are subtracted from the total (measured) vibrations at the present time.

- The working principle of the active chatter control strategy, presented in Chapter 4, has been illustrated using a milling spindle where an active magnetic bearing is integrated in the spindle (see Chapter 6). In addition, controllers should be designed for the more complex spindle-actuator

dynamics of the experimental setup, using the controller design methodology from Chapter 5. For more complex spindle dynamics, controllers with a relatively large number of parameters are probably required to be able to shape the SLD, which may lead to computational issues in the fixed structure controller design. In addition, uncertainty in the spindle dynamics should be included in the fixed structure controller design methodology.

- The obtainable increase in performance (i.e. MRR) for the experimental setup is limited, firstly, due to the fact that the identification of the model of the spindle-actuator dynamics can only be performed for a non-rotating spindle, and, secondly, due to the fact that the spindle-actuator dynamics varies significantly due to, amongst others, temperature effects. These effects require that relatively large uncertainties are included in the controller design, which results in a limited increase of the material removal rate. Consequently, in order to improve the performance of the active chatter control design for more complex models of the spindle dynamics even further, the amount of uncertainty that needs be included during the controller design should be decreased. Hereto, first, the model should be based on experiments that are performed for a rotating spindle in the range of spindle speeds for which the controller will be designed. However, in general, it is difficult to measure the tooltip response for a rotating spindle. Receptance coupling techniques can be used to couple the experimental model of the spindle-actuator dynamics, obtained for a certain spindle speed, to a model of the tool dynamics (e.g. obtained using finite-element modelling based techniques). Although receptance coupling techniques seem to work well for simple models of the spindle-actuator dynamics, more research is necessary for more complex spindle-actuator dynamics [171].

- The amount of the uncertainties in the spindle, due to e.g. temperature effects, are rather large in the specific spindle employed in the experiments in Chapter 6. Therefore, a new dedicated spindle design with integrated actuator should be pursued which is better suitable for application of active chatter control in commercial milling machines. The spindle design should focus on the implementation of an actuator which enables the implementation of the active chatter control strategies, as presented in this thesis, without diminishing the stiffness as compared to a spindle without the additional actuator.

A

The structured singular value

This section, briefly introduces the definition of the structured singular value. The discussion in this section is based on the work in [181]. A more elaborate discussion regarding the structured singular value and its computation can be found in [117, 142, 181]. Consider an uncertain system $\mathbf{L}$, modelled as the feedback interconnection between (nominal) stable plant $\mathbf{N}$ and stable uncertainty term $\mathbf{\Delta}$, as given in Figure A.1.

A common interest in robust stability problems is the size of the uncertainty $\mathbf{\Delta}$ which destabilises the system. The closed-loop system $\mathbf{L}$ becomes unstable if $\det(\mathbf{I} - \mathbf{N}\mathbf{\Delta}) = 0$. Based on the small-gain theorem, the closed-loop system $\mathbf{L}$ is internally stable when

$$\|\mathbf{L}\| < 1, \tag{A.1}$$

where $\|\mathbf{L}\|$ denotes the norm induced by the signal norm which guarantees $\|AB\| \leq \|A\|\|B\|$. A common norm induced by the signal norm, which is also used in this thesis, is the $\mathcal{H}_\infty$-norm. Then, when both $\mathbf{N}$ and $\mathbf{\Delta}$ are stable, the feedback interconnection between $\mathbf{N}$ and $\mathbf{\Delta}$ is internally stable for all $\mathbf{\Delta}$, if and only if,

$$\|\mathbf{N}\|_\infty < \gamma, \text{ with } \|\mathbf{\Delta}\|_\infty \leq \frac{1}{\gamma} \tag{A.2}$$

with γ a constant such that $\gamma > 0$ and

$$\|\mathbf{N}\|_\infty := \sup_{\mathrm{Re}(s)>0} \bar{\sigma}(\mathbf{N}(s)) = \sup_{\omega\in\mathbb{R}} \bar{\sigma}(\mathbf{N}(i\omega)). \tag{A.3}$$

Herein, $\bar{\sigma}(\mathbf{N})$ denotes the largest singular value of $\mathbf{N}$. The last equality in (A.3) is due to the fact that $\mathbf{N}(s)$ is assumed stable and therewith is analytic and bounded in the open-right half complex plane. Then, as described in [181], for any s for which $\mathrm{Re}(s) > 0$, the system $\mathbf{L}$ is at the edge of stability when the largest singular value of $\mathbf{N}$ equals:

$$\bar{\sigma}(\mathbf{N}) = \frac{1}{\min\{\bar{\sigma}(\mathbf{\Delta}) : \det(\mathbf{I} - \mathbf{N}\mathbf{\Delta}) = 0, \mathbf{\Delta} \text{ is unstructured}\}}. \tag{A.4}$$

Next, a similar line of reasoning can be followed when the uncertainty term has a certain structure. The smallest destabilising structured complex uncertainty

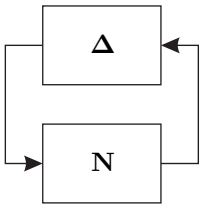

Figure A.1: Feedback interconnection between nominal plant $\mathbf{N}$ *and uncertainty term* $\mathbf{\Delta}$.

$\mathbf{\Delta}$ is defined, by generalising the concept of the largest singular value, as follows:

$$\mu_{\mathbf{\Delta}}(\mathbf{N}) = \frac{1}{\min\{\bar{\sigma}(\mathbf{\Delta}) : \det(\mathbf{I} - \mathbf{N}\mathbf{\Delta}) = 0, \mathbf{\Delta} \text{ is structured}\}}. \tag{A.5}$$

If $\det(\mathbf{I} - \mathbf{N}\mathbf{\Delta}) \neq 0$ for all $\mathbf{\Delta}$ then $\mu_{\mathbf{\Delta}} = 0$. Then, from the definition of the structured singular value $\mu_{\mathbf{\Delta}}$, the feedback interconnection between $\mathbf{N}$ and $\mathbf{\Delta}$ is internally stable for all $\|\mathbf{\Delta}\|_\infty \leq 1/\gamma$, if and only if,

$$\sup_{\mathrm{Re}(s)>0} \mu_{\mathbf{\Delta}}(\mathbf{N}(s)) = \sup_{\omega \in \mathbb{R}} \mu_{\mathbf{\Delta}}(\mathbf{N}(i\omega)) < \gamma. \tag{A.6}$$

Hence, the value $\mu_{\mathbf{\Delta}}(\mathbf{N})$ defines the inverse of the smallest value of the norm of structured complex $\mathbf{\Delta}$, i.e. $\bar{\sigma}(\mathbf{\Delta})$, for which the closed-loop system $\mathbf{L}$ becomes unstable.

B

Additional figures of the experiments

In this appendix the coherence plots of the identification measurements of the spindle-actuator dynamics with the experimental setup, as presented in Chapter 6, are given.

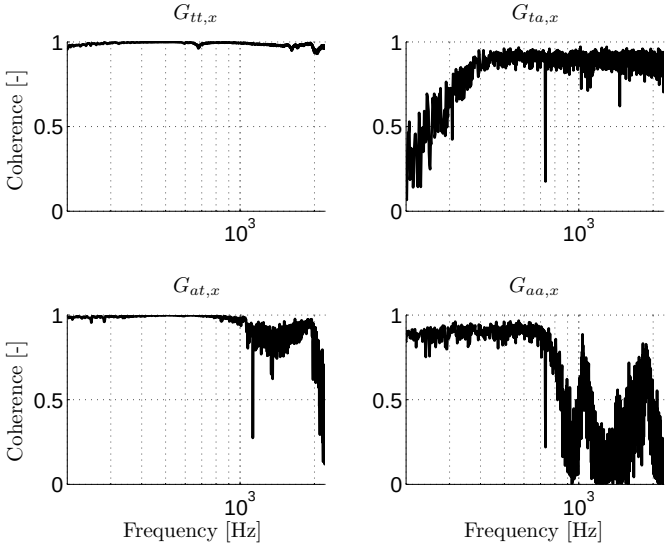

(a) x-direction.

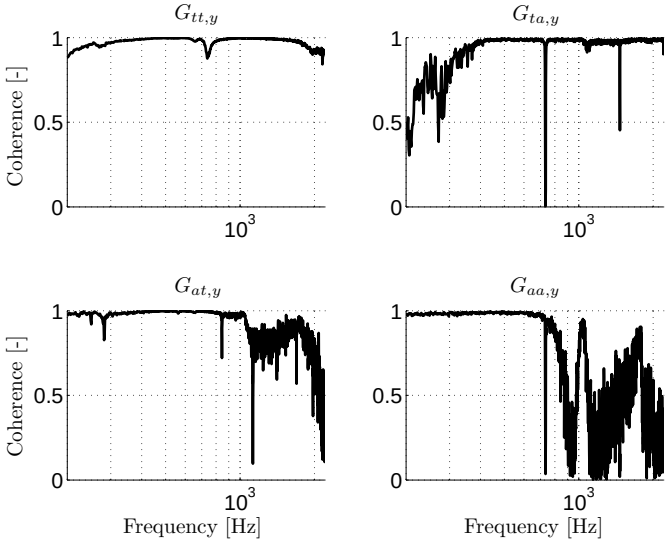

(b) y-direction.

Figure B.1: Coherence plots of the frequency response measurements of the spindle-actuator dynamics. $G_{kl,x}(i\omega)$ and $G_{kl,y}(i\omega)$ reflect the FRFs *with output k and input l where t and a indicate tooltip and bearing excitation/response, respectively.*

Bibliography

[1] E. Abele and U. Fiedler. Creating stabiltiy lobe diagrams during milling. *Annals of the CIRP*, 53(1):309–312, 2004.

[2] E. Abele, M. Kreis, and M. Roth. Electromagnetic actuator for in process non-contact identification of spindle-tool frequency respons functions. In *CIRP 2nd International Conference on High Performance Cutting*, Vancouver, Canada, 2006. paper no. 103.

[3] E. Abele, Y. Altintas, and C. Brecher. Machine tool spindle units. *CIRP Annals - Manufacturing Technology*, 59(2):781–802, 2010.

[4] E. Al-Regib, J. Ni, and S.H. Lee. Programming spindle speed variation for machine tool chatter suppression. *International Journal of Machine Tools and Manufacture*, 43(12):1229–1240, 2003.

[5] Y. Altintas. *Manufacturing automation*. Cambridge University Press, Cambridge, UK, 2000.

[6] Y. Altintas and E. Budak. Analytical prediction of stability lobes in milling. *Annals of the CIRP*, 44(1):357–362, 1995.

[7] Y. Altintas and P.K. Chan. In-process detection and suppression of chatter in milling. *International Journal of Machine Tools and Manufacture*, 32(3): 329–347, 1992.

[8] Y. Altintas and M. Weck. Chatter stability of metal cutting and grinding. *CIRP Annals - Manufacturing Technology*, 53(2):619–642, 2004.

[9] P. Apkarian and D. Noll. Nonsmooth H_∞ synthesis. *IEEE Transactions on Automatic Control*, 51(1):71–86, 2006.

[10] S.C. Bengea, X. Li, and R.A. DeCarlo. Combined controller-observer design for uncertain time delay systems with application to engine idle speed control. *Journal of Dynamic systems, Measurement and Control*, 126(4):772–780, 2004.

[11] K. Bickraj, M. Demutgul, I.N. Tansel, B. Kaya, and B. Ozcelik. Detection of the development of chatter in end milling operations using index based reasoning (ibr). In *ECTC 2008, 2008 ASME Early Career Technical Conference*, Miami, Florida, USA, October 3-4 2008. ASME.

[12] W. Bouzid. Cutting parameter optimization to minimize production time in high speed turning. *Journal of Materials Processing Technology*, 161(3):388–395, 2005.

[13] N.A. Bruinsma and M. Steinbuch. A fast algorithm to compute the H_∞-norm of a transfer function matrix. *Systems & Control Letters*, 14(4):287–293, 1990.

[14] J.V. Burke, A.S. Lewis, and M.L. Overton. Two numerical methods for optimizing matrix stability. *Linear Algebra and its Applications*, 351-352:117–145, 2002.

[15] J.V. Burke, A.S. Lewis, and M.L. Overton. A robust gradient sampling algorithm for nonsmooth, nonconvex optimization. *SIAM Journal on Optimization*, 15(3):751–779, 2005.

[16] E.A. Butcher, O.A. Bobrenkov, E. Bueler, and P. Nindujarla. Analysis of milling stability by the Chebyshev collocation method: algorithm and optimal stable immersion levels. *Journal of Computational and Nonlinear Dynamics*, 4(3): 1–12, 2009.

[17] R.A. de Callafon. *FREQID: a graphical user interface for frequency domain identification*. University of California, San Diego, USA, September 2000.

[18] R.A. de Callafon, D. de Roover, and P.M.J. Van den Hof. Multivariable least squares frequency domain identification using polynomial matrix fraction descriptions. In *Proceedings of the 35th IEEE conference on Decision and Control*, volume 2, pages 2030–2035, Kobe, Japan, 1996.

[19] Y. Cao and Y. Altintas. Modeling of spindle-bearing and machine tool systems for virtual simulation of milling operations. *International Journal of Machine Tools and Manufacture*, 47:1342–1350, 2007.

[20] C. Ceton, P.M.R. Wortelboer, and O.H. Bosgra. Frequency weighted closed-loop balanced reduction. In *Proceedings of the 2nd European Control Conference, Groningen, the Netherlands*, volume 2, pages 697–701, 1993.

[21] M. Chen and C.R. Knospe. Control approaches to the suppression of machining chatter using active magnetic bearings. *IEEE Transactions on Control Systems Technology*, 15(2):220–232, 2007.

[22] Y. Chen, X.G. Wang, C. Sun, F. Devine, and C.W. De Silva. Active vibration control with state feedback in woodcutting. *Journal of Vibration and Control*, 9(6):645–664, 2003.

[23] T. Choi and Y.S. Shin. On-line chatter detection using wavelet-based parameter estimation. *Journal of Manufacturing Science and Engineering*, 125(1):21–28, 2003.

[24] B. Chung, S. Smith, and J. Tlusty. Active damping of structural modes in high-speed machine tools. *Journal of Vibration and Control*, 3(3):279–295, 1997.

[25] F.H. Clarke, Y.S. Ledyaev, R.J. Stern, and P.R. Wolenski. *Nonsmooth analysis and control theory*, volume 178 of *Graduate texts in mathematics*. Springer, New York, 1998.

[26] T.R. Comstock, F.S. Tse, and J.R. Lemon. Application of controlled mechanical impedance for reducing machine tool vibrations. *Journal of Engineering for Industry*, 91(4):1057–1062, 1969.

[27] N.H. Cook. Self-excited vibrations in metal cutting. *Journal of Engineering for Industry*, 81:183–186, 1959.

[28] T. Delio. Method of controlling chatter in a machine tool. US patent no. 5,170,358, 1992.

[29] T. Delio, J. Tlusty, and S. Smith. Use of audio signals for chatter detection and control. *Journal of Engineering for Industry*, 114(2):146–157, 1992.

[30] B. Denkena, O. Gümmer, C. Will, and F. Hackelöer. Compensation of static and dynamic tool deflections during milling processes by an adaptronic spindle system. In *2nd International Conference "Innovative Cutting Processes & Smart Machining"*, Cluny, France, 22-23 October 2008.

[31] N.J.M. van Dijk, N. van de Wouw, H. Nijmeijer, R.P.H. Faassen, E.J.J. Doppenberg, and J.A.J. Oosterling. Real-time detection and control of chatter in the high-speed milling process. In *2nd International Conference "Innovative Cutting Processes & Smart Machining"*, Cluny, France, 22-23 October 2008.

[32] N.J.M. van Dijk, E.J.J. Doppenberg, R.P.H. Faassen, N. van de Wouw, J.A.J. Oosterling, and H. Nijmeijer. Automatic in-process chatter avoidance in the high-speed milling process. *Journal of Dynamic systems, Measurement and Control*, 132(3):031006 (14 pages), 2010.

[33] N.J.M. van Dijk, N. van de Wouw, E.J.J. Doppenberg, J.A.J. Oosterling, and H. Nijmeijer. Chatter control in the high-speed milling process using μ-synthesis. In *Proceedings of the American Control Conference*, pages 6121–6126, Baltimore, MD, USA, 30 June - 2 July 2010.

[34] N.J.M. van Dijk, N. van de Wouw, E.J.J. Doppenberg, J.A.J. Oosterling, and H. Nijmeijer. Robust active chatter control in the high-speed milling process. *IEEE Transactions on Control Systems Technology*, 2010. Submitted.

[35] Y. Ding, L. Zhu, X. Zhang, and H. Ding. A full-discretization method for prediction of milling stability. *International Journal of Machine Tools and Manufacture*, 50(5):502–509, 2010.

[36] J.L. Dohner, T.D. Hinnerichs, J.P. Lauffer, C.M. Kwan, M.E. Regelbrugge, and N. Shankar. Active chatter control in a milling machine. In *Proceedings of SPIE*, volume 3044, pages 281–294, 1997.

[37] J.L. Dohner, J.P. Lauffer, T.D. Hinnerichs, N. Shankar, M.E. Regelbrugge, C.M. Kwan, R. Xu, B. Winterbauer, and K. Bridger. Mitigation of chatter instabilities in milling by active structural control. *Journal of Sound and Vibration*, 269(1-2):197–211, 2004.

[38] dSpace Gmbh. URL `http://www.dspace.de`.

[39] C. Duque. Adaptive gradient lattice prediction of a multichannel iir system in adaptive optics. Master's thesis, Delft University of Technology, Delft, the Netherlands, 2008.

[40] A.H. El-Sinawi and R. Kashani. Improving surface roughness in turning using optimal control of tool's radial position. *Journal of Materials Processing Technology*, 167(1):54–61, 2005.

[41] S. Ema and E. Marui. Suppression of chatter vibration of boring tools using impact dampers. *International Journal of Machine Tools and Manufacture*, 40 (8):1141–1156, 2000.

[42] K. Eman and S.M. Wu. A feasibility study of on-line identification of chatter in turning operations. *Journal of Engineering for Industry*, 102:315–321, 1980.

[43] K.F Eman. Identification and control of chatter in turning. In *computer-based factory automation, 11th conference on production research and technology*, pages 413–417, Pittsburgh, PA, 1984.

[44] K. Engelborghs, T. Luzyanina, and G. Samaey. *DDE-BIFTOOL v. 2.00: A MATLAB package for bifurcation analysis of delay differential equations*. TW Report 330, Department of Computer Science, Katholieke Universiteit Leuven, Belgium, 2001.

[45] A. Ertürk, H.H. Özgüven, and E. Budak. Analytical modeling of spindle-tool dynamics on machine tools using Timoshenko beam model and receptance coupling for the prediction of tool point FRF. *International Journal of Machine Tools and Manufacture*, 46:1901–1912, 2006.

[46] Eurostat. Annual detailed enterprise statistics on manufacturing subsections df-dn and total manufacturing (nace rev.1.1 d). Online, `http://appsso.eurostat.ec.europa.eu/nui/show.do?dataset=sbs_na_2a_dfdn`, Visited on November 4 2010.

[47] Eurostat. Glossary:value added at factor cost. Online, `http://epp.eurostat.ec.europa.eu/statistics_explained/index.php/Glossary:Value_added_at_factor_cost`, Visited on November 4 2010.

[48] European Commission; Eurostat. *European Business: Facts and Figures 2009*. Office for Official Publications of the European Communities, Luxembourg, 2009.

[49] R.P.H. Faassen. *Chatter prediction and control for high-speed milling: modelling and experiments*. PhD thesis, Eindhoven University of Technology, Eindhoven, the Netherlands, 2007.

[50] R.P.H. Faassen, N. van de Wouw, J.A.J. Oosterling, and H. Nijmeijer. Prediction of regenerative chatter by modelling and analysis of high-speed milling. *International Journal of Machine Tools and Manufacture*, 43(14):1437–1446, 2003.

[51] R.P.H. Faassen, E.J.J. Doppenberg, N. van de Wouw, J.A.J. Oosterling, and H. Nijmeijer. Online detection of the onset and occurrence of machine tool chatter in the milling process. In *CIRP 2nd international conference on high performance cutting*, Vancouver, Canada, 2006. paper no. 23.

[52] R.P.H. Faassen, N. van de Wouw, H. Nijmeijer, and J.A.J. Oosterling. An improved tool path model including periodic delay for chatter prediction in milling. *Journal of Computational and Nonlinear Dynamics*, 2(2):167–179, 2007.

[53] M. Farkas. *Periodic motions*. Springer-Verlag, Berlin, 1994.

[54] R.L. Fittro and C.R. Knospe. μ-control of a high speed spindle thrust magnetic bearing. In *International Conference on Control Applications*, volume 1, Kohala Coast-Island of Hawaï, Hawaï, USA, 22-27 August 1999. IEEE.

[55] R.L. Fittro and C.R. Knospe. Rotor compliance minimization via μ-control of active magnetic bearings. *IEEE Transactions on Control Systems Technology*, 10(2):238–249, 2002.

[56] E. Fridman and U. Shaked. Delay-dependent stability and H_∞ control: Constant and time-varying delays. *International Journal of Control*, 76(1):48–60, 2003.

[57] A. Ganguli, A. Deraemaeker, M. Horodinca, and A. Preumont. Active damping of chatter in machine tools - demonstration with a 'hardware-in-the-loop' simulator. *Proceedings of the Institution of Mechanical Engineers, Part I: Journal of Systems and Control Engineering*, 219(5):359–369, 2005.

[58] A. Ganguli, A. Deraemaeker, I. Romanescu, M. Horodinca, and A. Preumont. Simulation and active control of chatter in milling via a mechatronic simulator. *Journal of Vibration and Control*, 12(8):817–848, 2006.

[59] D.J. Glaser and C.L. Nachtigal. Development of a hydraulic chambered, actively controlled boring bar. *Journal of Engineering for Industry*, 101(3):362–368, 1979.

[60] G.H. Golub and C.F. van Loan. *Matrix Computations*. John Hopkins University Press, Baltimore, third edition, 1996.

[61] K. Gu and S.-I. Niculescu. Survey on recent results in the stability and control of time-delay systems. *Journal of Dynamic systems, Measurement and Control*, 125(2):158–165, 2003.

[62] S. Gumussoy and W. Michiels. Computing $\mathcal{H}_\infty$ norms of time-delay systems. In *Joint 48th IEEE Conference on Decision and Control and 28th Chinese Control Conference*, pages 263–268, Shanghai, China, 16-18 December 2009.

[63] R.S. Hahn. Design of lanchester damper for eliminattion of metal-cutting chatter. *Transactions of the ASME*, 73:331–335, 1951.

[64] J. Hale and S.M. Verduyn Lunel. *Introduction to functional differential equations*. Springer-Verlag, New York, USA, 1993.

[65] A.J. Den Hamer. *Data-driven optimal controller synthesis: a frequency domain approach*. PhD thesis, Eindhoven University of Technology, Eindhoven, the Netherlands, 2010.

[66] S. Haykin. *Adaptive filter theory*, volume 4th Edition. Prentice Hall, Englewood Cliffs, NJ, USA, 2002.

[67] N. Hennes and M. Queins. Machine tools for high performance cutting of aircraft components. In *2nd international conference on high performance cutting*, Vancouver, Canada, June 2006. CIRP. paper no. 118.

[68] J.-B. Hiriart-Urruty and C. Lemaréchal. *Convex analysis and minimization algorithms II: advanced theory and bundle methods*. Springer-Verlag, Berlin, 1993.

[69] C.W.J Hol. *Structured controller synthesis for mechanical servo-systems*. PhD thesis, Delft University of Technology, Delft, the Netherlands, 2006.

[70] T. Hoshi, N. Sakisaka, I. Moriyama, M. Sato, A. Higashimoto, and T. Tokunaga. Study for practical application of fluctuating speed cutting for regenerative chatter control. *Annals of the CIRP*, 26(1 - 2):175–179, 1977.

[71] Y.-P. Huang and K. Zhou. Robust stability of uncertain time-delay systems. *IEEE Transactions on Automatic Control*, 45(11):2169–2173, 2000.

[72] T. Insperger. *Stability analysis of periodic delay-differential equations modeling machine tool chatter*. PhD thesis, University of Budapest, Budapest, Hungary, 2002.

[73] T. Insperger and G. Stépán. Stability of the milling process. *Periodica Polytechnica, Mechanical Engineering*, 44(1):47–57, 2000.

[74] T. Insperger and G. Stépán. Stability analysis of turning with periodic spindle speed modulation via semi-discretisation. *Journal of Vibration and Control*, 10: 1835–1855, 2004.

[75] T. Insperger and G. Stépán. Updated semi-discretization method for periodic delay-differential equations with discrete delay. *International Journal for Numerical Methods in Engineering*, 61(1):117–141, 2004.

[76] T. Insperger, G. Stépán, and N. Sri Namachchivaya. Comparison of the dynamics of low immersion milling and cutting with varying spindle speed. In *ASME International Design Engineering Technical Conferences*, Pittsburgh, PA, USA, September 2001. paper no. DETC2001/VIB-21616.

[77] T. Insperger, G. Stépán, P.V. Bayly, and B.P. Mann. Multiple chatter frequencies in milling processes. *Journal of Sound and Vibration*, 262(2):333–345, 2003.

[78] T. Insperger, B.P. Mann, T. Surmann, and G. Stépán. On the chatter frequencies of milling processes with runout. *International Journal of Machine Tools and Manufacture*, 48(10):1081–1089, 2008.

[79] F. Ismail and E.G. Kubica. Active suppression of chatter in peripheral milling, part I: A statistical indicator to evaluate the spindle speed modulation method. *International Journal of Advanced Manufacturing Technology*, 10(5):299–310, 1996.

[80] K. Jemielniak and A. Widota. Suppression of self-excited vibration by the spindle speed variation method. *International Journal of Machine Tool Design and Research*, 24(3):207–214, 1984.

[81] T. Kalmár-Nagy and F. C. Moon. *Nonlinear dynamics of production systems*, chapter Mode-coupled regenerative machine tool vibrations, pages 129–151. Wiley-VCH, 2004.

[82] S. Kern. *Erhöhung der prozessstabilität durch aktive dämpfung von frässpindeln mittels elektromagnetischer aktoren*. PhD thesis, Technische Universität Darmstadt, Darmstadt, Germany, 2009.

[83] S. Kern, C. Ehmann, R. Nordmann, M. Roth, A. Schiffler, and E. Abele. Active damping of chatter vibrations with an active magnetic bearing in a motor spindle using μ-synthesis and an adaptive filter. In *The 8th International Conference on Motion and Vibration Control*, Daejeon, Korea, 2006.

[84] S. Kern, A. Schiffler, R. Nordmann, and E. Abele. Modelling and active damping of a motor spindle with speed-dependent dynamics. In *9th International conference of vibrations in rotating machinery*, University of Exeter, Exeter, Great Britain, 8-10 September 2008.

[85] S. Kern, A. Schwung, and R. Nordmann. Gain-scheduling approaches for active damping of a milling spindle with speed-dependent dynamics. In *9th International conference on motion and vibration control*, München, Germany, 15-18 September 2008.

[86] N.H. Kim, D. Won, and J.C. Ziegert. Numerical analysis and parameter study of a mechanical damper for use in long slender endmills. *International Journal of Machine Tools and Manufacture*, 46(5):500–507, 2006.

[87] C.R. Knospe. Active magnetic bearings for machining applications. *Control Engineering Practice*, 15(3):307–313, 2007.

[88] C.R. Knospe, R.L. Fittro, and L.S. Stephens. Control of a high speed machining spindle via μ-synthesis. In *Proceedings of the 1997 IEEE International Conference on Control Applications*, pages 912–917, Hartford, CT, USA, October 5-7 1997. IEEE.

[89] E.G. Kubica and F. Ismail. Active suppression of chatter in peripheral milling, part II: Application of fuzzy control. *International Journal of Advanced Manufacturing Technology*, 12(4):236–245, 1996.

[90] C.M. Kwan, H. Xu, C. Lin, L. Haynes, J. Dohner, M. Regelbrugge, and N. Shankar. H_∞ control of chatter in octahedral hexapod machine. In *Proceedings of the American Control Conference*, volume 2, pages 1015–1016, Albuquerque, NM, USA, June 1997.

[91] J.H. Kyung and C.W. Lee. Controller design for a magnetically suspended milling spindle based on chatter stability analysis. *JSME International journal series C: Dynamics, control, robotics and design manufacturing*, 46(2):416–422, 2003.

[92] E.C. Lee, C.Y. Nian, and Y.S. Tarng. Design of a dynamic vibration absorber against vibrations in turning operations. *Journal of Materials Processing Technology*, 108:278–285, 2001.

[93] A.S. Lewis and M.L. Overton. Hybrid algorithm for nonsmooth optimization (HANSO). online, 2010. URL `http://www.cs.nyu.edu/faculty/overton/software/hanso/index.html`.

[94] H. Li and Y.C. Shin. Integrated dynamic thermo-mechanical modeling of high speed spindles, part 1: Model development. *Journal of Manufacturing Science and Engineering*, 126(1):148–158, 2004.

[95] M. Liang, T. Yeap, and A. Hermansyah. A fuzzy system for chatter suppression in end milling. *Proceedings of the Institution of Mechanical Engineers, Part B: Journal of Engineering Manufacture*, 218(4):403–417, 2004.

[96] S.C. Lin, R.E. DeVor, and S.G. Kapoor. The effects of variable speed cutting on vibration control in face milling. *Journal of Engineering for Industry*, 112 (1):1–11, 1990.

[97] K.J. Liu and K.E. Rouch. Optimal passive vibration control of cutting process stability in milling. *Journal of Materials Processing Technology*, 28(1-2):285–294, 1991.

[98] L. Ljung. *System identification: theory for the user*. Prentice Hall, Upper Saddle River, NJ, USA, 2nd edition, 1999.

[99] D.G. Luenberger. *Linear and nonlinear programming*, volume 116 of *International Series in Operations Research & Management Science*. Springer, 3rd edition, 2008.

[100] C.A. Van Luttervelt, T.H.C. Childs, I.S. Jawahir, F. Klocke, P.K. Venuvinod, Y. Altintas, E. Armarego, D. Dornfeld, I. Grabec, J. Leopold, B. Lindstrom, D. Lucca, T. Obikawa, Shirakashi, and H. Sato. Present situation and future trends in modelling of machining operations progress report of the cirp working group 'modelling of machining operations. *CIRP Annals-Manufacturing Technology*, 47(2):587–624, 1998.

[101] O. Maeda, Y. Cao, and Y. Altintas. Expert spindle design system. *International Journal of Machine Tools and Manufacture*, 45(4-5):537–548, 2005.

[102] B.P. Mann, N.K. Garg, K.A. Young, and A.M. Helvey. Milling bifurcations from structural asymmetry and nonlinear regeneration. *Nonlinear Dynamics*, 42(4):319–337, 2005.

[103] M.A. Marra, K.E. Rouch, S.G. Tewani, and B.L. Walcott. Vibration control for machining using H_∞ techniques. In *Proceedings of the IEEE Southeastcon '95 Conference*, pages 436–442, Raleigh, NC, USA, 1995.

[104] M.A. Marra, B.L. Walcott, K.E. Rouch, and S.G. Tewani. H_∞ vibration control for machining using active dynamic absorber technology. In *Proceedings of the 1995 American Control Conference*, volume 1, pages 739–743, Seattle, WA, USA, 1995.

[105] I. Maruta, T.-H. Kim, and T. Sugie. Fixed-structure H_∞ controller synthesis: A meta-heuristic approach using simple constrained particle swarm optimization. *Automatica*, 45(2):553–559, 2009.

[106] G. Mason and M. Berg. Linear time-invariant milling models applicable to chatter suppression system design. *Systems Analysis Modelling Simulation*, 43 (2):201–217, 2003.

[107] The MathWorks, Inc. URL `http://www.mathworks.com`.

[108] H.E. Merritt. Theory of self-excited machine-tool chatter. *Journal of Engineering for Industry*, 87(4):447–454, 1965.

[109] W. Michiels and S.-I. Niculescu. *Stability and stabilization of time-delay systems: an Eigenvalue-based approach*. SIAM, Philadelphia, USA, 2007.

[110] G. Morgan, R. Qi Cheng, Y. Altintas, and K. Ridgway. An expert troubleshooting system for the milling process. *International Journal of Machine Tools and Manufacture*, 47(9):1417–1425, 2007.

[111] M.R. Movahhedy and J.M. Gerami. Prediction of spindle dynamics in milling by sub-structure coupling. *International Journal of Machine Tools and Manufacture*, 46(3-4):243–251, 2006.

[112] C. Nachtigal. Design of a force feedback chatter control system. *Journal of Dynamic systems, Measurement and Control*, 94(1):5–10, 1972.

[113] K. Nagaya, J. Kobayasi, and K. Imai. Vibration control of milling machine by using auto-tuning magnetic damper and auto-tuning vibration absorber. *International Journal of Applied Electromagnetics and Mechanics*, 16(1-2):111–123, 2002.

[114] R. Neugebauer, B. Denkena, and K. Wegener. Mechatronic systems for machine tools. *Annals of the CIRP*, 56(2):657–686, 2007.

[115] J. Nocedal and S.J. Wright. *Numerical optimization*. Springer, second edition, 2006.

[116] M. Omar, K. Hussain, and S. Wright. Simulation study of an agile high-speed machining system for automotive cylinder heads. *Proceedings of the Institution of Mechanical Engineers, Part B: Journal of Engineering Manufacture*, 213(5): 491–499, 1999.

[117] A. Packard and J. Doyle. The complex structured singular value. *Automatica*, 29(1):71–109, 1993.

[118] G. Pan, H. Xu, C.M. Kwan, C. Liang, L. Haynes, and Z. Geng. Modeling and intelligent chatter control strategies for a lathe machine. *Control Engineering Practice*, 4(12):1647–1658, 1996.

[119] J.C. Pan and C.Y. Su. Chatter suppression with adaptive control in turning metal via application of piezoactuator. In *Proceedings of the 40th IEEE Conference on Decision and Control*, volume 3, pages 2436–2441, Orlando, FL, 2001.

[120] G. Park, M.T. Bement, D.A. Hartman, R.E. Smith, and C.R. Farrar. The use of active materials for machining processes: A review. *International Journal of Machine Tools and Manufacture*, 47(15):2189–2206, 2007.

[121] R. Pintelon and J. Schoukens. *System identification : a frequency domain approach*. IEEE Press, New York, NY, USA, 2001.

[122] J.R. Pratt and A.H. Nayfeh. Design and modeling for chatter control. *Nonlinear Dynamics*, 19(1):49–69, 1999.

[123] J.R. Pratt and A.H. Nayfeh. Chatter control and stability analysis of a cantilever boring bar under regenerative cutting conditions. *Philosophical transactions of the royal society A: mathematical, physical and engineering sciences*, 359(1781):759–792, 2001.

[124] A. Preumont. *Vibration Control of Active StructuresAn Introduction*. Kluwer Academic Publishers, Dordrecht, the Netherlands, 2002.

[125] K. Pyragas. Continuous control of chaos by self-controlling feedback. *Physics Letters A*, 170(6):421–428, 1992.

[126] K. Pyragas, V. Pyragas, and H. Benner. Delayed feedback control of dynamical systems at a subcritical hopf bifurcation. *Physical Review E - Statistical, Nonlinear, and Soft Matter Physics*, 70(5):056222–1–056222–4, 2004.

[127] M. Rantatalo, J. Aidanpä, B. Göransson, and P. Norman. Milling machine spindle analysis using fem and non-contact spindle excitation and response measurement. *International Journal of Machine Tools and Manufacture*, 47 (7-8):1034–1045, 2007.

[128] A. Rashid and C.M. Nicolescu. Design and implementation of tuned viscoelastic dampers for vibration control in milling. *International Journal of Machine Tools and Manufacture*, 48(9):1036–1053, 2008.

[129] M. Ries, S. Pankoke, and K. Gebert. Increase of material removal rate with an active hsc milling spindle. In *Adaptronic congress*, Göttingen, Germany, 3-4 May 2006.

[130] J. Saffury and E. Altus. Optimized chatter resistance of viscoelastic turning bars. *Journal of Sound and Vibration*, 324(1-2):26–39, 2009.

[131] C. Sanathanan and J. Koerner. Transfer function synthesis as a ratio of two complex polynomials. *IEEE Transactions on Automatic Control*, 8(1):56–58, 1963.

[132] A.H. Sayed. *Fundamentals of Adaptive Filtering*. John Wiley & Sons Inc., Hobroken, NJ, USA, 2003.

[133] A. Schiffler. Einsatz eines aktiven magnetlagers an einer motorspindel zur systemidentifikation wahrend der hpc-bearbeitung. Master's thesis, Technische Universität Darmstadt, Darmstadt, Germany, 2006.

[134] T.L. Schmitz and K.S. Smith. *Machining Dynamics: frequency response to improved productivity*. Springer, New York, NY, USA, 2009.

[135] T.L. Schmitz, J.C. Ziegert, and C. Stanislaus. A method for predicting chatter stability for systems with speed-dependent spindle dynamics. In *Transactions of the North American Manufacturing Research Institute of SME*, volume 32, pages 17–24, 2004.

[136] G. Schweitzer, H. Bleuler, and A. Traxler. *Active magnetic bearings : basics, properties and applications of active magnetic bearings*. Zürich : Verlag der Fachvereine, 1994.

[137] D.J. Segalman and J.M. Redmond. Method and apparatus for suppressing regenerative instability and related chatter in machine tools. patent no. US 6,189,426 B1, 20 Feb. 2001.

[138] S.E. Semercigil and L.A. Chen. Preliminary computations for chatter control in end milling. *Journal of Sound and Vibration*, 249(3):622–633, 2002.

[139] J.S. Sexton and B.J. Stone. The stability of machine with continuously varying spindle speed. *Annals of the CIRP*, 27(1):321–326, 1978.

[140] M. Shiraishi, K. Yamanaka, and H. Fujita. Optimal control of chatter in turning. *International Journal of Machine Tools and Manufacture*, 31(1):31–43, 1991.

[141] N.D. Sims. Vibration absorbers for chatter suppression: A new analytical tuning methodology. *Journal of Sound and Vibration*, 301(3-5):592607, 2007.

[142] S. Skogestad and I. Postlethwaite. *Multivariable feedback control: analysis and design*. John Wiley & Sons Ltd., Chichester, England, second edition, 2005.

[143] S. Smith and T. Delio. Sensor-based chatter detection and avoidance by spindle speed. *Journal of Dynamic systems, Measurement and Control*, 114(3):486–492, 1992.

[144] S. Smith and J. Tlusty. Update on high-speed milling dynamics. *Journal of Engineering for Industry*, 112(2):142–149, 1990.

[145] S. Smith and J. Tlusty. Stabilizing chatter by automatic spindle speed regulation. *Annals of the CIRP*, 41(1):433–436, 1992.

[146] S. Smith and J. Tlusty. Current trends in high-speed machining. *Journal of Manufacturing Science and Engineering*, 119(4B):664–666, 1997.

[147] E. Soliman and F. Ismail. Chatter suppression by adaptive speed modulation. *International Journal of Machine Tools and Manufacture*, 37(3):355–369, 1997.

[148] E. Soliman and F. Ismail. A control system for chatter avoidance by ramping the spindle speed. *Journal of Manufacturing Science and Engineering*, 120(4): 674–683, 1998.

[149] N. Sri Namachchivaya and Beddini. Spindle speed variation for the suppression of regenerative chatter. *Journal of Nonlinear Science*, 13(3):265–288, 2003.

[150] G. Stépán. Modelling nonlinear regenerative effects in metal cutting. *Philosophical transactions of the royal society A: mathematical, physical and engineering sciences*, 359(1781):739–757, 2001.

[151] Y.S. Tarng and T.C. Li. The change of spindle speed for the avoidance of chatter in end milling. *Journal of Materials Processing Technology*, 41(2):227–236, 1994.

[152] Y.S. Tarng, J.Y. Kao, and E.C. Lee. Chatter suppression in turning operations with a tuned vibration absorber. *Journal of Materials Processing Technology*, 105(1):55–60, 2000.

[153] F.W. Taylor. On the art of cutting metals. In *Transactions of the ASME*, volume 28, pages 31–350, 1906.

[154] S.G. Tewani, K.E. Rouch, and B.L. Walcott. Study of cutting process stability of a boring bar with active dynamic absorber. *International Journal of Machine Tools and Manufacture*, 35(1):91–108, 1995.

[155] A.L. Tits and V. Balakrishnan. Small-μ theorems with frequency-dependent uncertainty bounds. *Mathematics of Control, Signals, and Systems*, 11(3):220–243, 1998.

[156] J. Tlusty. *Manufacturing processes and equipmant*. Prentice Hall, Upper Saddle River, New Jersey, USA, 2000.

[157] J. Tlusty and M. Polacek. The stability of machine tools against self-excited vibrations in machining. In *ASME International Research in Production Engineering*, pages 465–474, Pittsburgh, PA, USA, 1963.

[158] J. Tlusty, W. Zaton, and F. Ismail. Stability lobes in milling. *Annals of the CIRP*, 32(1):309–313, 1983.

[159] S.A. Tobias. *Machine-tool vibration*. Blackie and Son, London, 1965.

[160] S.A. Tobias and W. Fishwick. The chatter of lathe tools under orthogonal cutting. *Transactions of the ASME*, 80:1079–1088, 1958.

[161] C.K. Toh. Design, evaluation and optimisation of cutter path strategies when high speed machining hardened mould and die materials. *Materials and Design*, 26(6):517–533, 2005.

[162] J. Vanbiervliet, K. Verheyden, W. Michiels, and S. Vandewalle. A nonsmooth optimisation approach for the stabilisation of time-delay systems. *ESAIM: Control, Optimisation and Calculus of Variations*, 14(3):478–493, 2008.

[163] T.A.C. Verschuren. Active chatter control in high-speed milling using μ-synthesis. Master's thesis, Eindhoven University of Technology, Eindhoven, the Netherlands, 2009.

[164] J. Vivancos, C.J. Luis, L. Costa, and J.A. Ortíz. Optimal machining parameters selection in high speed milling of hardened steels for injection moulds. *Journal of Materials Processing Technology*, 155-156:1505–1512, 2004.

[165] M. van de Wal, G. van Baars, F. Sperling, and O. Bosgra. Multivariable feedback control design for high-precision wafer stage motion. *Control Engineering Practice*, 10(7):739–755, 2002.

[166] M. Wang and R. Fei. Chatter suppression based on nonlinear vibration characteristic of electrorheological fluids. *International Journal of Machine Tools and Manufacture*, 39(12):1925–1934, 1999.

[167] M. Wang and R. Fei. On-line chatter detection and control in boring based on an electrorheological fluid. *Mechatronics*, 11(7):779–792, 2001.

[168] M. Wang, T. Zan, Y. Yang, and R. Fei. Design and implementation of nonlinear tmd for chatter suppression: An application in turning processes. *International Journal of Machine Tools and Manufacture*, 50(5):474–479, 2010.

[169] Z.-Q. Wang, P. Lundström, and S. Skogestad. Representation of uncertain time delays in the H_∞ framework. *International Journal of Control*, 59(3):627–638, 1994.

[170] M. Weck, E. Verhaag, and M. Gather. Adaptive control for face-milling operations with strategies for avoiding chatter-vibrations and for automatic cut distribution. *Annals of the CIRP*, 24(1):405–409, 1975.

[171] T.A.M. Wegman. Efficient chatter prediction in high-speed milling. Master's thesis, Eindhoven University of Technology, Eindhoven, the Netherlands, 2010.

[172] M. Wiercigroch and E. Budak. Sources of nonlinearities, chatter generation and suppression in metal cutting. *Philosophical Transactions of the Royal Society of London. Series A: Mathematical, Physical and Engineering Sciences*, 359 (1781):663–693, 2001.

[173] P. Wolfe. A method of conjugate subgradients for minimizing nondifferentiable functions. In M.L. Balinski and P. Wolfe, editors, *Nondifferentiable optimization*, volume 3 of *Mathematical programming study*, pages 145–173. Elsevier, Amsterdam, the Netherlands, 1975.

[174] F. Yang, B. Zhang, and J. Yu. Chatter suppression via an oscillating cutter. *Journal of Manufacturing Science and Engineering*, 121(1):54–60, 1999.

[175] F. Yang, B. Zhang, and J. Yu. Chatter suppression with multiple time-varying parameters in turning. *Journal of Materials Processing Technology*, 141(3): 431–438, 2003.

[176] Y. Yang, J. Muñoa, and Y. Altintas. Optimization of multiple tuned mass dampers to suppress machine tool chatter. *International Journal of Machine Tools and Manufacture*, 50(9):834–842, 2010.

[177] A. Yilmaz, E. Al-Regib, and J. Ni. Machine tool chatter suppression by multi-level random spindle speed variation. *Journal of Manufacturing Science and Engineering*, 124(2):208–216, 2002.

[178] P.M. Young. *Robustness with parametric and dynamic uncertainty.* PhD thesis, California institute of technology, Pasadena, California, USA, 1993.

[179] P.M. Young, M.P. Newlin, and J.C. Doyle. Practical computation of the mixed μ problem. In *Proceedings of the American Control Conference*, volume 3, pages 2190–2194, Chicago, IL, USA, 1992.

[180] Y. Zhang and N.D. Sims. Milling workpiece chatter avoidance using piezoelectric active damping: A feasibility study. *Smart materials and structures*, 14(6): N65–N70, 2005.

[181] K. Zhou, J.C. Doyle, and K. Glover. *Robust and Optimal Control.* Prentice Hall, Upper Saddle River, NJ, USA, 1996.

[182] J.C. Ziegert, C. Stanislaus, T.L. Schmitz, and R. Sterling. Enhanced damping in long slender end mills. *Journal of Manufacturing Processes*, 8(1):39–46, 2006.

Dankwoord

Aan alles komt een eind. Zo ook aan het schrijven van dit proefschrift. De laatste woorden die ik schrijf aan dit proefschrift wil ik dan ook gebruiken om een aantal mensen te bedanken die hebben bijgedragen aan de totstandkoming van dit proefschrift.

Allereerst wil ik mijn promotor Henk Nijmeijer bedanken voor de kans die hij mij heeft gegegeven om dit project in zijn groep uit te voeren. Henk, bedankt voor je enthousiasme, commentaar, vertrouwen en steun gedurende de afgelopen jaren.

Ten tweede, wil ik mijn co-promotor Nathan van de Wouw bedanken. Nathan, iedere promovendus kan zich gelukkig prijzen met jou als begeleider. Dankzij je gedetailleerde commentaar op elke versie van het proefschrift is het geworden zoals het er nu ligt. Je tomeloze inzet, kennis van zaken, oog voor detail en bovenal de plezierige discussies heb ik als uitermate waardevol ervaren.

I would like to thank the members of the core committee, Okko Bosgra, Wim Michiels and Yusuf Altintas, for their careful reading of the thesis and their valuable comments.

Daarnaast wil ik Han Oosterling, Ed Doppenberg en Douwe-Jan IJlst van TNO Industrie en Techniek bedanken voor alle hulp tijdens mijn onderzoek. Ed wil ik in het bijzonder bedanken voor zijn hulp bij de detectie en regelstrategie zoals gepresenteerd in Hoofdstuk 3 en de hulp tijdens de bezoeken aan Darmstadt. Daarnaast wil ik Douwe-Jan IJlst bedanken voor de hulp tijdens de experimenten zoals besproken in Hoofdstuk 3.

The experimental work, presented in Chapter 6, is performed in close-cooperation with the Institut für Produktionsmanagement, Technologie und Werkzeugmaschinen (PTW) of the Technische Universität Darmstadt, Germany, and, more specifically Prof. Dr.-Ing. Eberhard Abele and Dipl.-Ing. Andreas Schiffler. Andreas, thank you for your help with the experimental setup and your valuable time. I really enjoyed our discussions regarding chatter and the experimental setup. Good luck finishing your thesis!

Dank ook aan alle leden van de IOP begeleidingscommissie voor de waardevolle discussies en inzichten tijdens de halfjaarlijkse voortgangsbijeenkomsten. Veel nuttig werk is ook verricht door een aantal afstudeerders, Tom Verschuren en Theo Wegman. Bedankt voor jullie inzet en bijdrage aan het project.

Ik wil alle (oud)-collega's van DCT bedanken voor de nodige afleiding tijdens het koffiehalen, conferenties, 24-uurs meetingen etc. Petra en Lia, bedankt voor alle gezelligheid en organisatie van de 24-uurs meetingen, DCT-uitjes en alle andere zaken die voor ons vaak zo onzichtbaar zijn. In het bijzonder wil ik ook mijn (oud)-kamergenoten bedanken, Ronald, Niels, Bart en Viet, voor de gezellige discussies tussen het werk door. Ronald, in het bijzonder wil ik jou

bedanken voor je hulp tijdens het eerste half jaar van mijn promotieonderzoek.

Vanzelfsprekend wil ik ook mijn vrienden en familie bedanken voor hun interesse in mijn onderzoek, gezelligheid en de nodige afleiding. In het bijzonder wil ik mijn ouders bedanken voor het vertrouwen en de mogelijkheid die ze mij hebben geboden om mijn eigen weg te zoeken. Als laatste wil ik mijn lieve vriendin Joke bedanken. Je staat altijd voor me klaar. Mede dankzij jou steun en liefde is het gelukt om dit proefschrift af te ronden.

Niels van Dijk
December, 2010.

Curriculum vitæ

Niels van Dijk was born on March 8, 1981 in Deurne, the Netherlands. He completed his secondary school at Peellandcollege, Deurne, in 2000, after which he started his study Mechanical Engineering at the Eindhoven University of Technology (TU/e), the Netherlands. As part of his study he went for an external internship to the Netherlands Organisation for Applied Scientific Research TNO, where he worked on "Adaptive friction compensation of an inertia supported by MoS_2 solid-lubricated bearing". He received his M.Sc. degree in Mechanical Engineering from the Eindhoven University of Technology (TU/e) in 2006. The title of his M.Sc. project was "Generic trajectory generation for industrial manipulators" and was part of the NewMotion project performed in cooperation with Bosch Rexroth and FEI Company.

Since September 2006 he has been working as a Ph.D. student in the Dynamics and Control group at the department of Mechanical Engineering of the Eindhoven University of Technology. His research project is part of the SenterNovem-IOP project "Active high precision machining processes for milling" on the control of the chatter instability phenomenon in the milling process in cooperation with the Netherlands Organisation for Applied Scientific Research TNO. The results of the research are presented in this thesis.